Modelling and Simulation of Solid Fuel Particle Conversion

Zur Erlangung des akademischen Grades eines
DOKTORS DER INGENIEURWISSENSCHAFTEN (DR.-ING.)

von der KIT-Fakultät für Chemieingenieurwesen und Verfahrenstechnik des
Karlsruher Instituts für Technologie (KIT)
genehmigte

DISSERTATION

von
Tien Duc Luu, M.Sc.

Tag der mündlichen Prüfung:	25. Juli 2025
Erstgutachter:	Prof. Dr. Oliver T. Stein
Zweitgutachter:	Prof. Dr.-Ing. Gregor Wehinger

Summary

Climate change remains a critical environmental challenge, primarily driven by greenhouse gas emissions from human activities. Fossil fuel combustion, particularly coal, remains a major source of these emissions. Despite its negative impact on the environment and human health, coal remains widely used to meet growing energy demands, mainly in developing nations. Common strategies to mitigate the emissions include the improvement of the coal combustion process and adopting alternative solid fuels. Low- to zero-carbon fuels such as biomass and iron are promising options, because they can be integrated into existing coal power plant infrastructure. However, a detailed understanding of the solid fuel combustion process remains crucial. In this regard, numerical tools like computational fluid dynamics (CFD) play an important role by providing valuable insights into combustion systems.

In CFD, reactive turbulent gas-solid multiphase systems are typically modelled using the Euler-Lagrange (EL) approach, which offers a good trade-off between computational efficiency and accuracy. In this framework, the gas phase is treated as a continuum, while solid particles are represented as discrete Lagrangian point-particles, with explicitly modelled boundary layers. The objective of this work is to re-evaluate the EL framework for different types of solid fuel particles. The study begins by evaluating the applicability of the EL approach for biomass combustion through comparison with more costly but more accurate boundary layer-resolved simulations. This assessment identifies the validity range of the EL model and recommends coarse-graining strategies for scenarios that fall outside this range. Building on these insights, a more complex case involving turbulence-chemistry-particle interactions is explored for coal. Here, a multiphase flamelet/progress variable model is coupled with a Large Eddy Simulation and the good agreement with experimental measurements confirms the accuracy of the approach. The final part of this thesis extends the EL framework to iron, presenting a first-of-its-kind investigation into the ignition and combustion of iron particle clouds under shear-driven turbulence. These simulations were conducted using carrier-phase direct numerical simulation and provided initial insights into the interplay between turbulence and the ignition and combustion behaviour of both monodisperse and polydisperse iron particle clouds.

In this context, this thesis investigates the numerical models for different types of pulverised solid fuels. The aim is to give insights that support the optimisation of combustion systems and contribute to a cleaner, more efficient and more sustainable energy future.

Kurzfassung

Der Klimawandel stellt nach wie vor eine der größten Herausforderungen für die Umwelt dar, die hauptsächlich auf den von Menschen verursachten Ausstoß von Treibhausgasemissionen zurückzuführen ist. Die Verbrennung fossiler Brennstoffe, insbesondere Kohle, ist eine der Hauptquellen für den Ausstoß dieser Emissionen. Trotz der negativen Auswirkungen auf die Umwelt und die menschliche Gesundheit wird Kohle in großem Umfang zur Deckung des wachsenden Energiebedarfs, vor allem in Entwicklungsländern, eingesetzt. Die gängigsten Ansätze zur Verringerung der Treibhausgasemissionen sind die Verbesserung des Kohleverbrennungsprozesses und der Einsatz von alternativen festen Brennstoffen. Alternative feste Brennstoffe wie Biomasse und Eisen sind vielversprechende Optionen, da diese kohlenstoffarm/kohlenstofffrei verbrennen und in die bestehende Infrastruktur von Kohlekraftwerken integriert werden können. Dennoch ist ein detailliertes Verständnis des Verbrennungsprozesses von festen Brennstoffen unabdingbar für Optimierungsansätze. In diesem Zusammenhang spielen numerische Werkzeuge wie die numerische Strömungsmechanik (CFD) eine wichtige Rolle, da sie wertvolle Erkenntnisse zur Verbesserung der Effizienz und Nachhaltigkeit von Verbrennungssystemen liefern können.

In der CFD werden reaktive turbulente Gas-Feststoff-Mehrphasensysteme in der Regel mit dem Euler-Lagrange-Ansatz (EL) modelliert. Dieser bietet einen guten Kompromiss aus Berechnungseffizienz und Berechnungsgenauigkeit. In diesem Ansatz wird die Gasphase typischerweise als Kontinuum betrachtet, während die Feststoffpartikel als diskrete Lagrange-Punktpartikel angenommen und somit ihre Grenzschichten explizit modelliert werden. Das Ziel dieser Arbeit ist es, den EL-Ansatz für verschiedene Arten von Feststoffpartikeln neu zu bewerten. Die Studie beginnt mit der Bewertung des Anwendungsbereiches des EL-Ansatzes für die Verbrennung von Biomasse durch den Vergleich mit aufwändigeren, aber genaueren grenzschichtaufgelösten Simulationen. Diese Bewertung dient dazu, den Gültigkeitsbereich des EL-Ansatzes zu identifizieren und empfiehlt die Anwendung von Coarse-Graining-Strategien für Szenarien, die außerhalb dieses Bereichs liegen. Aufbauend auf diesen Erkenntnissen wird ein komplexerer Fall aufgesetzt, der die Wechselwirkungen zwischen Turbulenz, Chemie und Feststoffpartikeln anhand der Kohleverbrennung untersucht. Hierbei wird ein mehrphasiger Tabellierungsansatz verwendet, der mit einer Large-Eddy-Simulation gekoppelt ist. Die gute Übereinstimmung der Simulationsergebnisse mit den experimentellen Messungen bestätigt die Gültigkeit des Ansatzes. Im letzten Teil der Dis-

sertation wird der EL-Ansatz auf Eisenpartikel erweitert. Dabei wird die erstmalige Untersuchung der Zündung und Verbrennung von Eisenpartikelwolken in schergetriebener Turbulenz vorgestellt. Diese Simulationen werden mithilfe der direkten numerischen Simulation der Trägerphase durchgeführt und liefern erste Einblicke in das Zusammenspiel zwischen Turbulenz und Zünd- und Verbrennungsverhalten sowohl monodisperser als auch polydisperser Eisenpartikelwolken.

In diesem Zusammenhang werden in dieser Dissertation die numerischen Methoden zur Simulation verschiedener Arten von pulverisierten Festbrennstoffen untersucht. Ziel ist es, Erkenntnisse zu gewinnen, die die Optimierung von Verbrennungssystemen unterstützen und dazu beitragen, eine saubere, effizientere und nachhaltigere Energienutzung voranzutreiben.

Acknowledgements

This thesis represents the work I conducted during my time as a PhD student at the Institute for Combustion Technology (ITV) at the University of Stuttgart (2019-2023) and the Engler-Bunte-Institute (EBI) - Department Combustion Technology (VBT) - Simulation of Reacting Thermo-Fluid Systems (TFS) at the Karlsruhe Institute of Technology (2023-2025).

First and foremost, I would like to express my deepest gratitude to my supervisor, Prof. Dr. Oliver Thomas Stein, for the opportunity to complete my PhD under his guidance. His continuous support, encouragement and trust allowed me to freely develop and present our work at leading international conferences and workshops. I am especially thankful for the insightful discussions and constructive feedback that were essential to the success of this thesis. I sincerely appreciated the time and effort he spent throughout this journey. Furthermore, as we were both still living in Stuttgart and commuting by train to Karlsruhe, I truly appreciated and enjoyed our pleasant conversations during that time.

I would like to gratefully thank Prof. Dr. Andreas Kronenburg from ITV at the University of Stuttgart for providing me with the opportunity to begin my PhD journey. I have always been grateful for the possibilities he opened for me. His support and scientific advice led to many fruitful discussions that greatly enriched this work.

I would also like to thank Prof. Dr.-Ing. Gregor Wehinger for his interest in my work and for kindly agreeing to report on this thesis.

I would like to extend my thanks to all my colleagues who supported me during my PhD time. From EBI-VBT/TFS: Shiqi, Rishabh, Julia, David and Fabian. From ITV: Ali, Max, Weitao, Jonas, Jan, Marvin, Nadja, Sergio, Anjul, Jacqueline, Daniel, Christian, Nils, Bosen and Songbai. Your contributions, both academic and personal, made the past few years truly memorable.

Moreover, I want to thank all my project collaborators. From the Technical University of Darmstadt: Henrik, Hendrik, Xu, Sebastian, Daniel, Didi, Johannes, Arne and Prof. Dr.-Ing. Christian Hasse. From the Norwegian University of Science and Technology: Jingyuan, Tian and Prof. Terese Løvås. From Karlsruhe: Gabriel, Prof. Dr.-Ing. Bettina Frohnapfel and Maurizio from Rome. Your input and collaboration have generously contributed to my work.

Additional thanks go to Ricarda (ITV), Annika and Patricia (EBI-VBT/TFS) for taking care of administrative matters, and to Andreas for his efforts in maintaining and developing the new IT infrastructure at EBI-VBT/TFS.

Finally, I would like to express my sincere gratitude to my family and friends for their continued support and belief in me throughout my PhD journey.

"The whole of science is nothing more than a refinement of everyday thinking"
- Albert Einstein

List of Publications

Parts of this thesis have been published in archival literature and are included here without modifications from their original published form.

The relevant papers are:

1. Luu T. D., Zhang J., Gärtner J. W., Meng S., Kronenburg A., Li T., Løvås T. and Stein O. T. *Single particle conversion of woody biomass using fully-resolved and Euler–Lagrange coarse-graining approaches.* Fuel 368 (2024) 131600. https://doi.org/10.1016/j.fuel.2024.131600

2. Luu T. D., Shamooni A., Stein O. T., Kronenburg A., Popp S., Nicolai H., Schneider H., Wen X. and Hasse C. *Flame characterisation of gas-assisted pulverised coal combustion using FPV-LES.* Proceedings of the Combustion Institute 39 (2023) 3249-3258. https://doi.org/10.1016/j.proci.2022.07.080

3. Luu T. D., Shamooni A., Kronenburg A., Braig D., Mich J., Nguyen B.-D., Scholtissek A., Hasse C., Thäter G., Carbone M., Frohnapfel B. and Stein O. T. *Carrier-Phase DNS of Ignition and Combustion of Iron Particles in a Turbulent Mixing Layer.* Flow, Turbulence and Combustion 112 (2024) 1083-1103. https://doi.org/10.1007/s10494-023-00526-y

4. Luu T. D., Shamooni A., Kronenburg A., Braig D., Mich J., Nguyen B.-D., Scholtissek A., Hasse C., Thäter G., Carbone M., Frohnapfel B. and Stein O. T. *Carrier-phase DNS study of particle size distribution effects on iron particle ignition in a turbulent mixing layer.* Proceedings of the Combustion Institute 40 (2024) 105297. https://doi.org/10.1016/j.proci.2024.105297

Contents

List of Figures

List of Tables

Nomenclature

Latin symbols

Symbol	Description	Unit
A	Surface	m^2
A_r	Pre-exponential factor	var.
A, B	Mixture fraction ratios	-
a_k	Weighting factor	-
B_{corr}	Blowing correction	-
B_M, B_T	Spalding mass and heat transfer	-
C	Equation constants	-
C_{norm}	Normalised progress variable	-
$c_{i,j}$	Weighting factor coefficient	-
c_k	Species concentration	mol/m^3
c_{p}	Specific heat capacity	J/(kg K)
D	Diffusion conductance	var.
d	Diameter	m
d_i	Grey gas i weighting factor	-
E_a	Activation energy	kJ/mol
F	Mass flux per unit area	$kg/(m^2\ s)$
$F(.)$	Function	
G	Incident radiation	W/m^2
$G(.)$	Filter function	-
g	Gravity	m/s^2
H_{norm}	Normalised total enthalpy	-
H_{vap}	Heat of evaporation	J/kg
h	Heat transfer coefficient	$W/(m^2\ K)$
h_f	Specific enthalpy of formation	J/kg
h_s	Specific sensible enthalpy	J/kg
h_t	Specific total enthalpy	J/kg
$I(r, s)$	Radiation intensity	W/sr

I_b	Black body intensity	W/m^2
k	Turbulent kinetic energy	m^2/s^2
k_i	Grey gas i absorption coefficient	-
K_r	Equilibrium constant	-
k_r	Reaction rate constant	var.
k_f	Forward reaction rate constant	var.
k_b	Backward reaction rate constant	var.
k_{cond}	Thermal conductivity	W/(m K)
L	Characteristic length	m
l	Length scale	m
M	Molar mass	kg/kmol
MR	Molar ratio of H_2O to CO_2	-
m	Mass	kg
N	Total number	-
n	Normal vector	-
p	Pressure	N/m^2
Q-factor	Proximate analysis Q-factor	-
$\dot{Q}$	Heat flux	W/m^2
r	Radial position	m
R	Char conversion reaction rate	var.
R_u	Universal gas constant	J/(mol K)
S_a	Internal surface area	m^2
S_{ij}	Strain rate	1/s
S_{O_2}	Stoichiometric mass of oxygen	-
$\dot{S}$	Source term	var.
s	Radiation direction	-
s_L	Laminar burning velocity	m/s
T	Temperature	K
t	Time	s
u	Velocity	m/s
V	Volume	m^3
W_k	Reactant/Product species	-
W_α	Atomic weight	kg/kmol
X_k	Molar fraction	-
Y_c	Progress variable	var.
Y_k	Species mass fraction	-
Z	Mixture fraction	-

Greek symbols

Symbol	Description	Unit
α	Thermal diffusivity	m^2/s
α_1, α_2	Splitting coefficients	-
$\beta(.)$	Scattering phase function	-
δ_{ij}	Kronecker delta	-
δ_L	Laminar flame thickness	m
ϵ	Turbulent dissipation rate	m^2/s^3
ε	Emissivity	-
η	Kolmogorov scale	m
η_{eff}	Effectiveness factor	-
θ	Porosity	-
θ_r	Eulerian radiation temperature	K
κ	Absorption/Emission coefficient	-
λ	Taylor scale	m
μ	Dynamic viscosity	Pa s
ν	Kinematic viscosity	m^2/s
ν', ν''	Stoichiometric coefficients	-
ρ	Density	kg/m^3
σ	Stefan-Boltzmann constant	$W/(m^2\ K^4)$
σ_s	Scattering coefficient	-
τ	Tortuosity	-
τ_{con}	Convective heat transfer time scale	1/s
τ_{ij}	Viscous stress tensor	N/m^2
τ_p	Particle relaxation time	s
ϕ	Arbitrary variable	var.
ϕ_T	Thiele modulus	-
$\dot{w}$	Reaction rate	kg/s
w_i	Weighting factors	-
Γ	Diffusion coefficient	m^2/s
Δ	Cell size	m
Φ	Equivalence ratio	-
Ω	Solid angle	sr
ζ_α	Elemental mass fraction	-

Superscripts

Symbol	Description
β	Arrhenius temperature exponent
m	Molar-based quantity
max	Maximum
min	Minimum
*	Filtered physical space

Subscript

Symbol	Description
0	Initial
ash	Ash
b	Burned
boil	Boiling
C	Cell
char	Char
cog	Char off-gas
con	Convection
cond	Conductivity
const	Constant
cont	Continuous
crit	Critical
disp	Dispersed
dry	Drying
eff	Effective
η	Kolmogorov scale
f	Film
FC	Fixed carbon
filt	Filtered
fuel	Fuel
g	Gas
gas	Light gas
het	Heterogeneous
int	Integral scale
init	Initial

i, j, m	Indices
k	Species k
λ	Taylor scale
m	Mean
moist	Moisture
melt	Melting
norm	Normalised
ox	Oxidiser
p	Particle
pil	Pilot
prox	Proximate analysis
r	Reaction
rad	Radiation
ref	Reference
s	Surface
(s)	Solid
stoic	Stoichiometric
t	Turbulence
tar	Tar
u	Unburned
vol	Volatile
VM	Volatile matter

Abbreviations

Symbol	Description
CFD	Computational fluid dynamics
CG	Coarse-graining
CMC	Conditional moment closure
CP-DNS	Carrier-phase DNS
DNS	Direct numerical simulation
EBU	Eddy break-up model
EDC	Eddy dissipation concept
EDM	Eddy dissipation model
EL	Euler-Lagrange
FC	Fixed carbon

FDM	Finite difference method
FEM	Finite element method
FPV	Flamelet/Progress variable
FR-DNS	Fully-resolved DNS
FVM	Finite volume method
LES	Large eddy simulation
LHS	Left-hand side
MMC	Multiple mapping conditioning
ODE	Ordinary differential equation
PBC	Pulverised biomass combustion
PCC	Pulverised coal combustion
PDF	Probability density function
RANS	Reynolds-Averaged Navier-Stokes
RHS	Right-hand side
RSM	Reynolds stress model
RTE	Radiative transport equation
SFC	Solid fuel combustion
SGS	Sub-grid scale
URANS	Unsteady RANS
VM	Volatile matter
WSGGM	Weighted-sum-of-grey-gas

Dimensionless numbers

Symbol	Description
Bi	Biot number
Da^*	Normalised Damköhler number
Le	Lewis number
Nu	Nusselt number
Pr	Prandtl number
Re	Reynolds number
Sc	Schmidt number
Sh	Sherwood number

Operators

Symbol	Description
$<\bar{}>$	Time-averaged, Filter operation
$<'>$	Time-averaged, Filter operation fluctuation
$<\tilde{}>$	Favre-averaged, Favre-filtered
$<''>$	Favre-averaged, Favre-filtered fluctuation
$d/d(.)$	Ordinary differential operator
$\partial/\partial(.)$	Partial differential operator

1 Introduction

1.1 Motivation

Climate change has become one of the most significant environmental challenges facing the modern world. It involves long-term changes in global temperature and weather patterns. Such changes can be attributed to natural and human-driven causes. Natural variability of climate results from internal (e.g. redistribution of energy) and external (e.g. sun and volcanic activity, changes in the orbit) forcing. However, the impact of natural climate variability tends to have minimal influence on longer time scales. Over the entire historical period from 1850 to 2020, natural variability is estimated to have contributed between $\pm 0.23\,^{\circ}\mathrm{C}$ to the observed global temperature change [1]. Compared to the natural causes, human activities are the main driving force of climate change. The numbers given in the following refer to global averages since regional warming in certain regions (e.g. the Arctic region) is considerably higher. Since the 1850s (pre-industrial era), a substantial increase in the atmospheric concentrations of greenhouse gases, i.e. CO_2, CH_4 and N_2O [2, 3], has been observed with a measured global temperature change of $1.45\,^{\circ}\mathrm{C}$ in 2023 [4]. After deducting the temperature change by natural causes, this leads to a human-driven temperature change of approximately $1.22-1.68\,^{\circ}\mathrm{C}$. The United Nations has outlined a hypothetical scenario of what could occur with a global temperature increase above 1.5 degrees. The scientists and reviewers unanimously agreed, in line with the Paris Agreement, that limiting the global temperature rise to no more than 1.5 degrees would help to prevent severe climate consequences and ensure a liveable environment on earth [5].

The global greenhouse gas emissions can be attributed to the five economic sectors of energy, agriculture, industry, waste, and land-use change and forestry [6]. The energy sector is the most significant contributor, accounting for 75.5 % of total emissions, with CO_2 making up three-fourths of all greenhouse gases [2]. In 2023, the burning of fossil fuels such as coal (24.87 %), oil (29.78 %) and natural gas (21.89 %) of the energy mix was necessary to meet the global primary energy consumption [7, 8], with a share of almost 80 % [9]. Over the next few decades, global energy demand is expected to increase, driven by industrial growth in both developing and developed countries and a rising world population. According to the International Energy Agency [9], demand for fossil fuels will peak by 2030 before declining to a total share of 58 % by 2050, mainly due to the decrease in coal and the increase in clean

energy technologies. While clean energy technologies from renewable sources, such as wind and solar, are carbon-free, their geographical limitations and the intermittency of solar power cannot continuously meet the energy demands of high-consumption regions. Therefore, the demand for natural gas and oil is predicted to have the same share in 2050 as today due to their reliability, the relatively robust gas prices and the irreplaceable use of oil for aviation and petrochemical sectors.

However, coal power plants still play an important role because of their significant use in high-demand countries like China and India. Coal encounters less competition in the energy-intensive industrial sectors, such as iron, steel and cement. It is a reliable technology with high energy content and cost-effectiveness, especially in regions where alternative energy sources are either too expensive or unavailable. Another crucial factor is the potential for disruption of oil and gas supplies because of geopolitical uncertainties, leading to shortages and higher prices. Near-term disruptions were the COVID-19 pandemic, the Russian-Ukraine crisis, Middle East conflicts and elections in countries (e.g. USA, India, Russia and Iran). A strong correlation between global coal demand and oil/gas prices is observed. Historically, advanced economies consumed more coal per capita than emerging markets and developing economies. But, this trend has shifted in recent years, as advanced economies have decommissioned coal plants or reduced their usage, while many emerging markets and developing economies have built new coal power plants to meet growing energy demands.

Regardless of the advantages of coal combustion and its essential role in developing economies and the industrial sector, it causes the most negative impacts on both human health and the environment compared to all other energy sources [10]. Coal is the energy source that typically releases higher amounts of nitrogen oxides (NO_x), sulfur dioxide (SO_2), carbon dioxide (CO_2), heavy metals, and particulate matter per unit of energy than other fuels. The release of significant pollutants impacts flora, fauna and air quality. In addition CO_2 contributes directly to global warming, as outlined above [11, 12].

Mitigating climate change and global warming requires actions to reduce or prevent greenhouse gas emissions from human activities, particularly the CO_2 emissions from coal combustion. This is crucial for meeting the goals of the Paris Agreement and achieving a climate-neutral economy by 2050, as set out by the European Union. Several options are available, with the most common approach being the use of alternative fuels or optimising the coal combustion process to achieve the desired goal.

A typical replacement of coal is the use of renewable biomass. Solid biomass is considered a promising renewable alternative to coal due to the opportunity of using existing supply chains, infrastructure and proven power generation technology. Furthermore, it offers the possibility of retrofitting existing coal power plants with reasonable effort [13].

In recent years, an innovative way to replace coal as a fuel involves the use of pulverised iron within the existing infrastructure of coal power plants [14]. The approach follows the idea of developing a sustainable, circular, carbon-free energy economy system to store energy from renewable sources (iron oxide reduction) and to use it on demand in power plants to produce heat and electricity (iron oxidation) [15, 16].

Optimising the combustion process of solid fuels requires more profound insights into the underlying physical and chemical processes of solid fuel combustion (SFC). Understanding the complex interactions between turbulence, chemistry and heat transfer is necessary for identifying opportunities to improve burner designs or combustion conditions and processes. Achieving higher combustion efficiencies helps to reduce greenhouse gas emissions and minimises environmental impact.

Nowadays, computational fluid dynamics (CFD) has become increasingly important for conducting comprehensive investigations into combustion processes. CFD employs numerical analysis to solve systems involving fluid flow, heat transfer, solid particles and chemical reactions. The development of computers through the years has led to a drastic increase in the performance of processors so that computational costs have been reduced. This has opened the way to a wider use of numerical simulation in industrial and research areas. With numerical simulation, fundamental analyses are adaptable and can be applied to any SFC process. It serves as a valuable tool for gaining deeper insights into the complex combustion dynamics and interactions between the flow field and particles.

In this context, this thesis examines the applicability of numerical methods to various pulverised solid fuel types (such as coal, biomass and iron). It aims to provide valuable insights that can help optimise combustion systems. These insights encourage contributions towards the development of a cleaner, more efficient and more sustainable energy economy.

1.2 State of the art

Solid fuel types

Solid fuels are materials that remain in a solid state at room temperature and can react with oxygen to generate heat. Coal is the most well-known solid fuel. During the pulverised coal combustion (PCC) process, coal undergoes the major thermo-physical stages: (i) heat-up, (ii) drying, (iii) devolatilisation, (iv) homogeneous gas combustion, and (v) heterogeneous oxidation. Biomass, another commonly used solid fuel, follows the same stages during pulverised biomass combustion (PBC). However, biomass generally has a higher moisture content than coal, causing stage (ii) to be more dominant. Due to the similar conversion processes and the release of volatile gases in stage (iii), coal and biomass can be classified as volatile-containing solid fuels. In contrast, the combustion of pulverised metal fuels, such as iron, differs from

coal and biomass. The conversion of metal fuels is reduced to the stages of (i) heat-up and (v) heterogeneous oxidation. Without stage (iii), metal fuels can be classified as non-volatile solid fuels.

Turbulence modelling approaches

Combustion systems involving solid fuel particles typically operate under turbulent flow conditions. Turbulence affects the flow-chemistry-particle interaction and can further enhance the heat and momentum transfer. However, it can also lead to reduced effects in these transfers, e.g. through local flame extinction. Such changes in the interaction of the gas and solid phase can substantially influence the global ignition and SFC behaviour. Various modelling approaches are available for studying turbulent flows in the context of numerical simulation. The three main approaches are the direct numerical simulation (DNS), large eddy simulation (LES) and Reynolds-Averaged Navier-Stokes (RANS). Each approach aims to resolve turbulent motions across different scales. DNS resolves all relevant scales and offers high accuracy but comes with a substantial computational cost. LES finds a compromise between accuracy and computational costs by resolving the largest turbulence scales while modelling the smaller scales. In contrast, RANS only computes time-averaged flow quantities, making it a more computationally efficient approach compared to DNS and LES.

For two-phase flows, various scientists have conducted studies on fully-resolved (FR) DNS of solid fuel particles in the past. In FR-DNS, the computational grid resolves all relevant gradients, including the particle boundary layers. Mass, momentum, and heat are exchanged at the interface between the gas and solid phase. This exchange is typically realised through a set of boundary conditions. While this approach is highly accurate, it comes with significant computational costs, limiting its use to single particles [17–25] and small particle groups [26–32]. These investigations focus on the aspects of ignition [17, 19], Reynolds number [18], transport processes [20, 22, 23], oxygen dependency [18, 19, 25], detailed kinetics [21, 24], pollutant formation [24], interaction effects [26–32] as well as flame propagation and burning behaviour [27–32] in laminar flows. Such FR-DNSs of solid fuel particles give detailed descriptions of the physical phenomena occurring around the particle. These insights help to understand the physical processes and provide valuable data for deriving sub-models that can be used for LES or carrier-phase DNS (CP-DNS), as discussed next.

Unlike FR-DNS, the CP-DNS approach offers a good balance between accuracy and efficiency. All relevant turbulence scales are resolved in the CP-DNS, whereas particles are assumed to be Lagrangian point-particles. This assumption helps to overcome the FR-DNS limitation of only focusing on single particles and small particle groups, allowing for the study of larger particle clouds. However, as a result of the point-particle assumption, the mass, momentum, and heat transfer across the particle boundary layer need to be modelled.

CP-DNS of solid fuel particles has gained significant popularity in recent years [33–47]. The authors of [33,34,36] conducted the first CP-DNS studies on a simplified coal jet flame with reduced kinetics. Subsequent research shifted the focus to more canonical studies but incorporated higher complexity in the physical processes. These studies applied CP-DNS to examine homogeneous isotropic turbulence [35,37,46], shear-driven turbulence [35,37–44,47], pollutant formation [42,43], detailed homogeneous and heterogeneous kinetics [44] and solid particle clustering effects [45–47]. Despite the advancements in computational capabilities over the past few years, the high computational costs of CP-DNS limit its use to primarily canonical studies.

However, applications involving large-scale and complex geometries, a wide range of turbulent scales, numerous solid fuel particles and interphase coupling processes with detailed homogeneous and heterogeneous chemistry are highly relevant to the industry and require numerical investigation. For this purpose, LES has been established as a reliable tool. By modelling smaller turbulence scales in LES, it is possible to use a larger grid size than DNS or CP-DNS for numerical studies, which helps to reduce computational costs. The foundational work of Kurose and Makino [48] from the early 2000s marks the beginning of LES-SFC research. Since then, several research groups have employed LES-SFC to conduct studies on various scales [49–78]. Some of these studies focus on turbulent jet flames at lab-scale [51, 53, 55, 56, 58, 59, 62, 67, 70], as well as lab-/large-scale furnaces [49, 50, 52, 54, 57, 60, 61, 68, 69, 72–80], semi-industrial scale furnaces [63–66, 71] and industrial scale furnaces [81]. The wide range of studies and their good predictive accuracy compared with experimental measurements demonstrate the potential of LES in SFC. This positive trend gives hope for future developments of more detailed combustion models and conducting full-scale simulations, eventually leading to more efficient and cleaner combustion systems.

RANS simulations take a different approach by solving only the time-averaged flow field. This concept is computationally less demanding, which makes it interesting for trend predictions [82–88]. However, RANS simulations are limited by not capturing the unsteady nature of turbulent flows, which leads to inaccuracies in regions where unsteady and fluctuating behaviour is dominant [50, 52, 54, 57, 60, 79, 89, 90].

Chemistry modelling approaches

The combustion of pulverised solid fuel is characterised by strong interactions between the flow field, chemical reactions and solid particles. To accurately capture the highly dynamic behaviour of ignition and combustion, the flow-chemistry-particle interaction must be precisely reproduced in numerical simulations. Solid fuel particles may release a complex mixture of light gases and tars to the gas phase. Subsequently, the reaction of these species needs

to be described by a set of reaction equations (reaction mechanism). A detailed description of the reaction mechanism for solid fuel particles can consist of hundreds of species and thousands of reactions, which makes it computationally very expensive. Therefore, directly solving the species transport equations for all species is unfeasible and requires modelling techniques. These combustion models are based on different assumptions. Commonly used combustion models for SFC are the eddy break-up model (EBU) [91] and eddy dissipation model (EDM) [92]. Both models assume that the mixing time scale controls the reaction rate (infinitely fast chemistry). Other fast chemistry combustion models are the conserved scalar approach and chemical equilibrium assumption. The eddy dissipation concept model (EDC) [93] extends the EBU and EDM models to account for more complex chemistry. The simplified assumption of infinitely fast chemistry in EBU and EDM has the disadvantage of not accounting for chemical non-equilibrium (important for pollutant formation) and over-estimating flame temperature and fuel consumption. To overcome the limitation of these models, several advanced combustion models have been developed in the past few years. The most prominent models are the transported probably density function (PDF) [94], the conditional moment closure (CMC) [95], the multiple mapping conditioning (MMC) [96] and the flamelet [97] approach. The tabulated flamelet model is a well-established combustion modelling approach with limited cost that has been widely used for single-phase combustion in the past. One major improvement of the flamelet model is the flamelet/progress variable (FPV) approach [98] for capturing the flame dynamics by introducing a tracking scalar to describe the extent of chemical reaction. Since the proposed application of the FPV model with SFC [62], it has become very popular in recent years and led to various studies [43, 64, 66, 68, 70, 72, 73, 75, 77, 78, 99–101].

Gas-solid interactions

The coupling between gas phase and solid particles needs to be precisely described in the context of numerical modelling of multiphase gas-solid systems. The most accurate gas-solid coupling method is the FR approach [17–32]. Here, mass, momentum, energy and species exchange are realised at the boundary interface between the gas and solid phase. As mentioned before, this method is highly accurate but associated with very high computational cost. A good trade-off between accuracy and computational cost for dispersed gas-solid systems is the two-way Euler-Lagrange (EL) approach. The standard EL approach treats the bulk gas phase as a continuum, whereas the solid particles are treated as dispersed Lagrangian point-particles, assuming that the particle boundary layer is modelled. The interaction between the point-particle and continuum occurs through the exchange of information between them. The solid particles retrieve the gas phase data of mass, momentum, energy and species from the local Eulerian cell (Δ) in which they are located. Conversely, the reverse coupling, from

the solid particles to the gas phase, is implemented through a set of source terms applied to the local Eulerian cell. However, conflicting requirements arise for a reliable EL approach. The Eulerian cell needs to be sufficiently large to capture the relevant physics (e.g. small-scale turbulence) while ensuring that the Lagrangian particle diameter (d_p) is much smaller than the Eulerian cell size, i.e. $d_p/\Delta \ll 1$. For some solid fuel particles, e.g. biomass, the ratio of d_p/Δ is of order one or even larger, invalidating the standard EL approach. This may result in overestimated coupling interactions, which can cause unphysical behaviour and/or lead to simulation instabilities [102, 103]. This issue has been investigated in several studies [37, 104–110] where coarse-graining (CG) methods have been developed, which consider a larger volume of the gas phase. The current development of CG methods can be categorised into the particle centroid method, divided particle volume method, statistical kernel method and two-grid method [105]. These methods take a different approach but have the same objective of distributing the particle source terms to more than just the local Eulerian cell and considering a larger fluid volume than the local cell to retrieve the far-field gas phase information.

This section has highlighted important studies on SFC in turbulent flows. Although extensive research has been conducted, several scientific questions remain unresolved or insufficiently explored. This work aims to address some of these open issues.

1.3 Thesis objectives

As already outlined in the previous section, many researchers have studied the numerical simulation of multiphase reactive flows with solid fuels in the EL context in the past. However, some shortcomings and unknowns in this field are still present today and will be addressed in this thesis. The aim of this thesis is to numerically re-examine the Euler-Lagrange approach for gas-solid multiphase systems for different types of solid fuel particles.

The main research objectives of the presented thesis are as follows:

1. *Determining the applicability range of Euler-Lagrange approaches for volatile-containing solid fuel particles in laminar flow:*
   The Euler-Lagrange approach has been widely applied in several numerical studies in the past for SFC, but its applicability range has not been substantially quantified. In the first research objective, a methodology to compare the Euler-Lagrange approach with fully-resolved DNS is developed. The applicability range of the EL approach is demonstrated and correction methods are suggested if the approach is no longer valid.

2. *Accurate LES modelling of the complex turbulence-chemistry-particle interaction phenomena occurring in the combustion of volatile-containing solid fuels:*
   A case with significant complex turbulence-chemistry-particle interaction is studied in the second research objective. A pre-tabulated flamelet look-up table approach is developed and applied to explore the combustion of solid fuel particles in a piloted swirling combustion chamber at high Reynolds number.

3. *Extending the modelling framework to study the ignition and combustion of innovative non-volatile solid fuels (metals) in the CP-DNS context:*
   The third research objective extends the Euler-Lagrange numerical framework of volatile-containing to non-volatile solid fuels and studies the ignition and combustion behaviour of iron particles in shear-driven turbulence. For this purpose, a new numerical solver with sub-models needs to be developed and validated.

1.4 Thesis outline

This thesis is divided into six chapters. Chapter 2 reviews the theoretical and physical background of multiphase reacting flows with solid fuel particles and describes the underlying processes of pulverised solid fuel combustion. The incorporation of theoretical and physical aspects into numerical models is described in Chapter 3. Chapter 4 presents an overview of the numerical methods and solution procedure of multiphase gas-solid systems in the OpenFOAM framework. The studies and results of the investigated research objectives are presented in Chapter 5. Chapter 6 concludes the thesis and gives an outlook for further studies.

2 Theoretical background

This chapter provides the theoretical and physical background necessary to understand the complexity of reactive multiphase gas-solid systems, which is the main focus of this thesis. First, the general governing equations for a pure gas phase description are presented briefly, followed by the extensions required to describe a multiphase system. Afterwards, some insights into the physics of combustion are given. Then, turbulence phenomena are discussed, including their energy spectrum and length scales. Lastly, an overview of the various types of pulverised solid fuels and their characteristics is provided. This chapter follows mostly these textbooks [111–116]. For more detailed derivations and explanations, the reader is encouraged to refer to the textbooks.

2.1 Multiphase reacting flows

In most engineering problems, a reactive fluid can be assumed as a continuum. Therefore, only the effects on the macroscopic scale are of interest, whereas molecular motions can be neglected. On the macroscopic scale, the fluid can be fully characterised by its density, velocity, pressure, temperature and their changes in space and time. For reacting flows, additional species governing equations are needed to describe the change of the gas mixture. In the context of multiphase flows, two or more phases are present. The description of each phase can be either continuous or dispersed. The continuum assumption can be applied to two or more phases, provided that distinct interfaces separate them. Alternatively, the dispersed approach can be used, in which a freely moving dispersed phase with a volume V_{disp} is surrounded by a continuous flow field with volume V_{cont} that fulfils the requirement of $V_{\text{disp}}/V_{\text{cont}} \leq$ 5e-4 [117]. A dispersed phase typically consists of fluid particles (e.g. droplets or bubbles) or solid particles (e.g. coal, biomass or iron). The main subject of this thesis is the numerical treatment of dispersed solid fuel particles in a continuous gas mixture.

2.1.1 Gas phase governing equations

The conservation laws for mass, momentum and energy are typically expressed as governing equations of fluid flow. They describe the spatial and temporal evolution of density,

velocity, pressure and temperature. In this section, the three-dimensional and unsteady governing equations for a non-reactive single gas phase are briefly presented. These equations are presented in differential form and are applied to compressible flows at low Mach numbers.

Mass conservation

The mass conservation equation (continuity equation) is derived by applying a mass balance to a finite control volume dV. According to the law of mass conservation, mass can neither be created nor destroyed. As a result, the total mass flow into and out of the control volume must equal the mass change rate due to density changes. The continuity equation for a single gas phase is given as

$$\frac{\partial \rho}{\partial t} + \frac{\partial (\rho u_i)}{\partial x_i} = 0 \tag{2.1}$$

with subscript $< i >$ and later $< j, m >$ indicating the coordinate directions. The first term in Eq. (2.1) represents the change of the gas density ρ with time t and the second term the convective mass transport with velocity u_i in the spatial coordinate direction x_i. The density is evaluated from the ideal gas law, which is acceptable for small pressure changes as

$$\rho = \frac{p\,M}{R_u\,T} \tag{2.2}$$

where p is the pressure, M the molar mass, R_u the universal gas constant and T the temperature.

Momentum conservation

The momentum equation is based on Newton's second law and states that all forces acting on a finite control volume must equal to its rate of momentum change. The momentum conservation equation is expressed as

$$\frac{\partial (\rho u_i)}{\partial t} + \frac{\partial (\rho u_i u_j)}{\partial x_j} = -\frac{\partial p}{\partial x_i} + \frac{\partial \tau_{ij}}{\partial x_j} + \rho g_i \tag{2.3}$$

Similar to the continuity equation, the first and second term on the left-hand side (LHS) indicates the change of momentum over time and through convective transport. The terms on the right-hand side (RHS) describe all the external forces acting on the control volume. Considered are the pressure p, the viscous stresses τ_{ij} and gravitational force ρg_i. Assuming that a Newtonian fluid is present, the viscous stress tensor can be modelled as

$$\tau_{ij} = \mu \left(\frac{\partial u_j}{\partial x_i} + \frac{\partial u_i}{\partial x_j} \right) - \frac{2}{3} \mu \frac{\partial u_m}{\partial x_m} \delta_{ij} \quad \text{with} \quad \delta_{ij} = \begin{cases} 0 & \text{if } i \neq j \\ 1 & \text{if } i = j \end{cases} \tag{2.4}$$

where μ is the dynamic viscosity and δ_{ij} is the Kronecker delta.

Energy conservation

For non-reactive single-phase flows, the energy conservation is important for accounting for temperature changes resulting from boundary effects (e.g. preheated walls) or heat transfer phenomena (e.g. radiation). The energy equation is based on the first law of thermodynamics, which states that the rate of energy change in a control volume equals the total net rate of heat and work changes. The energy equation can be expressed in various forms [113]. In this thesis, the formulation of the sensible enthalpy h_s, defined as $h_s = h_t - h_f$ (= total enthalpy − enthalpy of formation), is used to account for energy conservation. Assuming a unity Lewis number $\mathrm{Le} = \alpha/D$, with thermal diffusivity α and mass diffusivity D, and approximating the heat flux using Fourier's law leads to the following formulation

$$\frac{\partial(\rho h_s)}{\partial t} + \frac{\partial(\rho h_s u_j)}{\partial x_j} = \frac{\partial}{\partial x_j}\left(\frac{\mu}{\mathrm{Pr}}\frac{\partial h_s}{\partial x_j}\right) + \dot{S}_{\mathrm{rad}}. \tag{2.5}$$

The terms on the LHS represent the unsteady and convection components of the sensible enthalpy transport, respectively. The changes in enthalpy are caused by heat conduction/diffusion (first RHS term) and by radiative heat transfer $\dot{S}_{\mathrm{rad}}$. The Prandtl number is calculated as $\mathrm{Pr} = \mu c_p/k_{\mathrm{cond}}$ with c_p the specific heat capacity and k_{cond} the thermal conductivity.

2.1.2 Reactive multiphase extensions

The governing equations described in Sec. 2.1.1 address the conservation of mass, momentum, and energy for a non-reactive single gas phase system. However, for a system that includes the combustion of pulverised solid fuels, it is necessary to adapt these equations to account for a reactive system with multiple species in the gas phase and to consider the interactions between the gas and solid phases. The set of governing equations for a reactive multiphase system is represented as

$$\frac{\partial \rho}{\partial t} + \frac{\partial(\rho u_i)}{\partial x_i} = \dot{S}_{\rho,p} \tag{2.6}$$

$$\frac{\partial(\rho u_i)}{\partial t} + \frac{\partial(\rho u_i u_j)}{\partial x_j} = -\frac{\partial p}{\partial x_i} + \frac{\partial}{\partial x_j}\left[\mu\left(\frac{\partial u_j}{\partial x_i} + \frac{\partial u_i}{\partial x_j}\right) - \frac{2}{3}\mu\frac{\partial u_m}{\partial x_m}\delta_{ij}\right] + \rho g_i + \dot{S}_{u,p} \tag{2.7}$$

$$\frac{\partial(\rho h_s)}{\partial t} + \frac{\partial(\rho h_s u_j)}{\partial x_j} = \frac{\partial}{\partial x_j}\left(\frac{\mu}{\mathrm{Pr}}\frac{\partial h_s}{\partial x_j}\right) + \dot{S}_{\mathrm{rad}} + \dot{\omega}_{h_s} + \dot{S}_{h_s,p} \tag{2.8}$$

$$\frac{\partial(\rho Y_k)}{\partial t} + \frac{\partial(\rho Y_k u_j)}{\partial x_j} = \frac{\partial}{\partial x_j}\left(\frac{\mu}{\mathrm{Sc}}\frac{\partial Y_k}{\partial x_j}\right) + \dot{\omega}_k + \dot{S}_{Y_k,p} \tag{2.9}$$

where the thermophysical properties (e.g. ρ, μ) are now multicomponent properties. Equations (2.1), (2.3) and (2.5) have been extended with the source terms of $\dot{S}_{\rho,p}$, $\dot{S}_{u,p}$ and $\dot{S}_{h_s,p}$, respectively, to account for the interphase transfers of mass, momentum and energy between gas and solid phase. Due to the chosen definition of sensible enthalpy, it is necessary to include a homogeneous chemical reaction term $\dot{\omega}_{h_s}$, to address heat sources and sinks arising from exothermic and endothermic reactions. The continuity equation in Eq. (2.6) considers the conservation of total mass, however, it does not account for the conversion of species $< k >$ among each other, which occurs in reactive flows. To address this issue, a set of species conservation equations for species $k = 1, \ldots, n$ is introduced in Eq. (2.9). Differentiation between the species is achieved by using the species mass fraction $Y_k = m_k/m_t$, which is defined as the ratio of the mass of the individual species m_k to the total mass of the mixture m_t. Additionally, species conservation includes the term $\dot{S}_{Y_k,p}$ for the interphase exchange between gas and solid phases. Furthermore, it considers the production and consumption of the species mass fraction Y_k via the homogeneous chemical reaction rate $\dot{\omega}_k$. The Schmidt number is evaluated as $\mathrm{Sc} = \mu/(\rho D)$.

2.2 Combustion

Combustion is a thermochemical process that converts chemical into thermal energy. A combustion process typically involves a fuel and an oxidiser, which are mixed and burned. The heat released by the exothermic reaction leads to an increase in temperature, which can be used in various engineering applications.

2.2.1 Chemical kinetics

A combustion process occurs when different species exchange/rearrange atoms through collisions. During this process, chemical bonds are broken and new bonds are formed. A simple way of describing combustion is to assume it only involves a single global reaction. However, it is well-known that the combustion process does not consist of just one reaction step but involves multiple intermediate steps. These intermediate steps are called elementary reactions. Reaction mechanisms consist of a series of elementary reactions. Each of these elementary reactions can be described in the following general form

$$\sum_{k=1}^{N_k} \nu'_{kr} W_k \rightleftharpoons \sum_{k=1}^{N_k} \nu''_{kr} W_k \quad \text{with} \quad r = 1, 2, \ldots, N_r \tag{2.10}$$

where ν'_{kr} and ν''_{kr} are the stoichiometric coefficients of reactant and product species, here denoted as W_k, in the reaction r. N_r describes the total number of reactions and N_k describes

the number of species participating in the reaction mechanism. The total molar reaction rate, indicated by superscript $< m >$, of a species k is given by the sum of its forward and backward reaction rates in every reaction r as

$$\dot{\omega}_k^m = \frac{dc_k}{dt} = \sum_{r=1}^{N_r} \left(\nu''_{kr} - \nu'_{kr}\right) \left[k_{f,r} \prod_{k=1}^{N_k} c_k^{\nu'_{kr}} - k_{b,r} \prod_{k=1}^{N_k} c_k^{\nu''_{kr}}\right]. \tag{2.11}$$

Here, $c_k = (\rho Y_k)/M_k$ is the species concentration, M_k the species molar mass, and $k_{f,r}$ and $k_{b,r}$ are the forward and backward reaction rate constant of reaction r, respectively. The specific reaction rate constants k_r are expressed by the Arrhenius law

$$k_r = A_r T^{\beta_r} \exp\left(-\frac{E_{a,r}}{R_u T}\right) \tag{2.12}$$

with A_r the pre-exponential factor, β_r the temperature exponent, $E_{a,r}$ the activation energy and R_u the universal gas constant. The equilibrium constant K_r relates the forward and backward reaction rate constants as

$$K_r = \frac{k_{f,r}}{k_{b,r}}. \tag{2.13}$$

The homogeneous chemical reaction rate $\dot{\omega}_k$ in the species conservation equation, (see Eq. (2.9)), arises from the expression

$$\dot{\omega}_k = \dot{\omega}_k^m M_k \tag{2.14}$$

which closes the species conservation equation for a pure gas reacting system. The heat release rate from chemical reactions in Eq. (2.8) is given by

$$\dot{\omega}_{h_s} = \sum_{k=1}^{N_k} h_{f,k} \dot{\omega}_k \tag{2.15}$$

with $h_{f,k}$ denoting the heat of formation of species k.

The field of combustion consists of a wide range of topics and applications. Depending on the use case, different types of fuel are utilised. The more complex the fuel is, the more reactions are needed to describe the dynamics of the chemical system accurately. A detailed reaction mechanism can include hundreds of chemical species and thousands of reactions. In such a detailed mechanism, the net reaction rate of each species must be calculated as shown in Eq. (2.14). Since chemical species may participate in multiple reactions, this leads to a large set of ordinary differential equations (ODEs), which can be computationally expensive to solve. Various strategies have been employed in the past to address the chemical kinetics of complex fuels effectively. One popular method is the development of reduced mechanisms, which aim to replicate the dynamics of a more detailed mechanism by focusing on the reaction equations of key major and minor species. Another approach involves not directly solving

the ODEs but instead using simpler models, e.g. flamelet, to describe the chemical state.

2.2.2 Combustion regimes

Combustion processes are typically classified based on the mixing state between fuel and oxidiser before entering the combustion chamber, which can be either premixed or non-premixed. However, combustion is a complex process that involves the interplay of mass and heat transfer, chemical kinetics, fluid dynamics, turbulence-chemistry interaction and radiative heat transfer. As a result, combustion in practical applications is often described as multi-regime, as it cannot be classified as purely premixed or non-premixed due to inhomogeneities or partial premixing. Nonetheless, based on the idealised assumptions of premixed and non-premixed flames, different modelling approaches have been developed depending on the specific combustion regimes, as shown in Fig. 2.1.

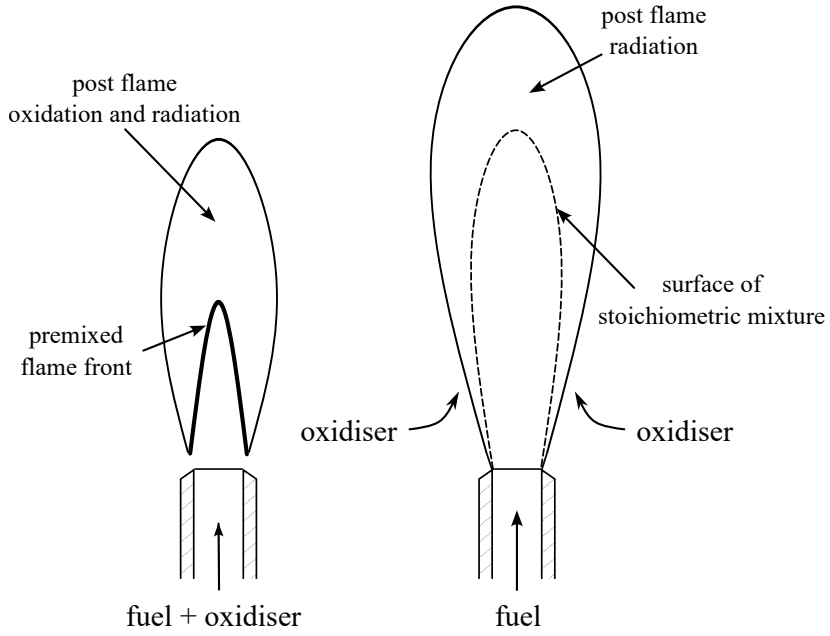

Figure 2.1: Schematic illustration of a premixed and non-premixed flame setup. Adapted from [112].

2.2.2.1 Premixed combustion

In premixed combustion fuel and oxidiser are homogeneously mixed before entering the combustion chamber and prior to ignition. A typical example of premixed combustion is a Bunsen flame operated in premixed mode, i.e. when fuel and air are injected jointly through the burner nozzle, see Fig. 2.1 (left). The primary advantage of the premixed combustion regime lies in the precise control of the operating conditions, which directly affect the flame

speed and structure. The combustion conditions are usually controlled by the equivalence ratio Φ, which is defined as

$$\Phi_u = \left.\frac{(m_{\mathrm{ox}}/m_{\mathrm{fuel}})_{\mathrm{stoic}}}{(m_{\mathrm{ox}}/m_{\mathrm{fuel}})}\right|_u = \left.\frac{(Y_{\mathrm{ox}}/Y_{\mathrm{fuel}})_{\mathrm{stoic}}}{(Y_{\mathrm{ox}}/Y_{\mathrm{fuel}})}\right|_u \tag{2.16}$$

where m_{ox} and m_{fuel} are the masses of oxidiser and fuel respectively and Y_{ox} and Y_{fuel} represent their corresponding mass fractions. Subscript $<\mathrm{stoic}>$ refers to stoichiometric condition, while $<u>$ and later $<b>$ indicates unburned and burned mixture state, respectively. According to Eq. (2.16), an equivalence ratio of $\Phi_u = 1$ represents a stoichiometric mixture, $\Phi_u > 1$ a fuel-rich mixture and $\Phi_u < 1$ a fuel-lean mixture. Although stoichiometric conditions ($\Phi_u = 1$) are ideal, fuel-lean mixtures ($\Phi_u < 1$) are commonly used to ensure complete combustion of the fuel. However, the presence of a homogeneous and flammable mixture results in a higher explosion risk. On the other hand, homogeneous mixing of fuel and oxidiser enables spatially uniform combustion zones. This leads to a flame front, which can be considered as a thin interface, separating the unburned from the burned mixture, as illustrated in Fig. 2.2.

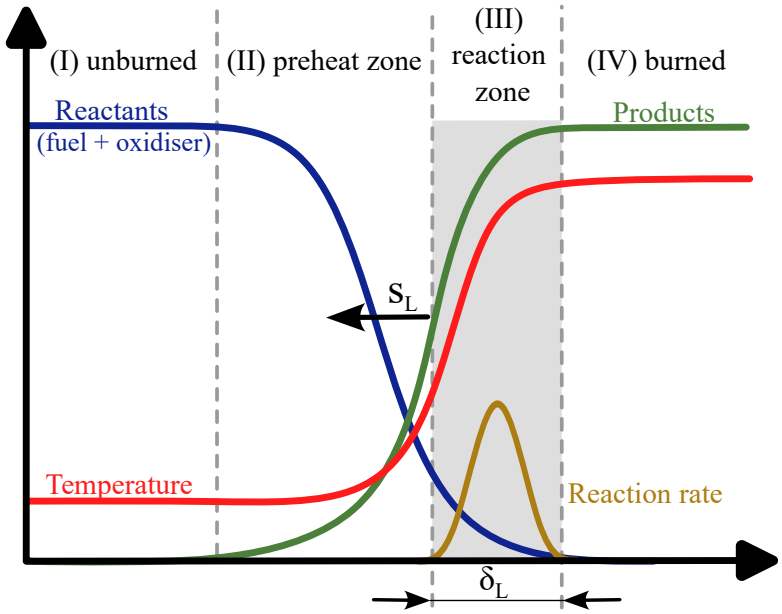

Figure 2.2: Schematic illustration of a stationary premixed flame structure.

In the ideal case (without curvature), the flame front propagates normally towards the unburned mixture with a characteristic laminar burning velocity s_L and a laminar flame thickness of δ_L. The flame structure can be divided into four distinct regions. The regions are namely (I) the unburned, (II) the preheat zone, (III) the reaction zone and (IV) the burned regions. A preheat zone is established due to heat conduction from the reaction zone, leading to a continuous preheating of the unburned mixture. In the reaction zone,

chemical reactions occur and the majority of heat is released.

In premixed flames, the chemical reaction progress is typically described using a progress variable Y_c. The definition of Y_c is not fixed and may vary depending on the chosen reference quantities or modelling approach. The only requirement for the progress variable is that it must be monotonic throughout the entire flame. A common approach is to use temperature as an indicator for the progress variable (i.e. $Y_c = F(T_u, T_b)$). However, a more general expression is the use of a linear combination of species mass fractions $Y_c = \sum a_k \cdot Y_k$, where a_k represents a weighting factor for species k. Suitable Y_k are intermediate species (e.g. CO) and combustion products (e.g. H_2O). To ensure the progress variable is bounded between 0 and 1, a normalisation procedure is applied as

$$Y_{c,\text{norm}} = C_{\text{norm}} = \frac{Y_c - Y_{c,u}}{Y_{c,b} - Y_{c,u}} \tag{2.17}$$

with $Y_{c,\text{norm}} = 0$ standing for unburned and $Y_{c,\text{norm}} = 1$ for fully-burned mixtures.

2.2.2.2 Non-premixed combustion

Non-premixed combustion is characterised by the separate introduction of fuel and oxidiser into the combustion chamber, where they mix and react. This mode of combustion is prevalent in many practical applications. Typical examples include counterflow flames, where fuel and oxidiser are fed in opposing directions and jet flames, where fuel is injected into an ambient oxidising environment. Combustion will occur in regions where the local mixture reaches a stoichiometric condition. Insufficient mixing can result in incomplete combustion or flame quenching. The structure of a typical non-premixed flame is illustrated in Fig. 2.3. The

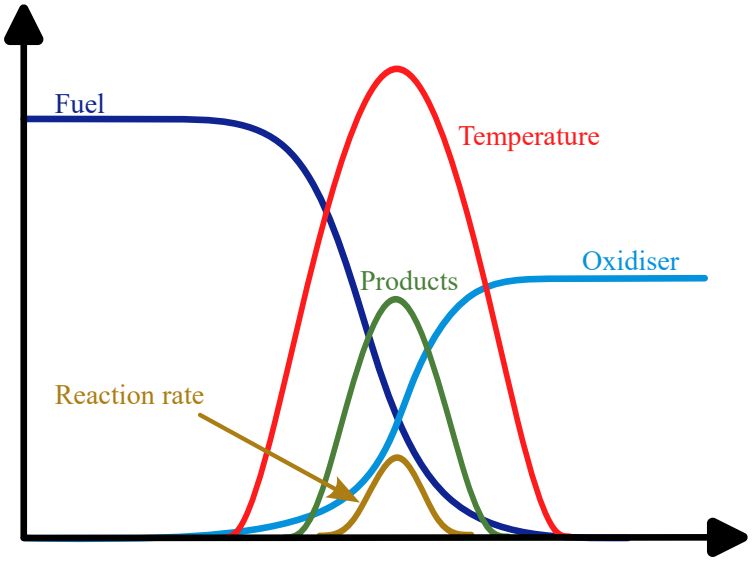

Figure 2.3: Schematic illustration of a stationary non-premixed flame structure.

maximum heat release and peak temperature in a non-premixed flame occur where fuel and oxidiser mix in stoichiometric proportions. On either side of this region, the mixture becomes fuel-rich or fuel-lean, corresponding to the injection of fuel and oxidiser streams, respectively. The mixing process is governed by molecular and turbulent diffusion, which is why non-premixed flames are also referred to as diffusion flames. Unlike premixed combustion, non-premixed flames lack characteristic properties such as laminar flame speed or flame thickness, as their behaviour is dominated by mixing rather than reaction kinetics. In this regime, the mixing rate is typically slower than the chemical reaction rate, making mixing the rate-limiting step that controls the overall flame. As a result, diffusion flames are often described by a *mixture fraction*. The mixture fraction is a conserved scalar that describes the local composition based on the mixing of fuel and oxidiser as

$$Z = \frac{m_{\text{fuel}}}{m_{\text{fuel}} + m_{\text{ox}}} \tag{2.18}$$

The mixture fraction is a useful variable because it is defined to be zero ($Z = 0$) for a pure oxidiser stream and unity ($Z = 1$) for a pure fuel stream. During combustion, the original fuel and oxidiser species undergo different stages of conversion, making it challenging to directly track their individual mass contributions. However, since chemical elements are conserved throughout the reaction, the mixture fraction can instead be defined in terms of elemental mass fractions. To account for this, Bilger [118] proposed a generalised formulation of the mixture fraction based on conserved elemental species for systems involving hydrocarbon fuels (i.e. C, H and O) and oxygen as

$$Z = \frac{2\zeta_{\text{C}}/W_{\text{C}} + \zeta_{\text{H}}/2W_{\text{H}} - 2(\zeta_{\text{O}} - \zeta_{\text{O,ox}})/W_{\text{O}}}{2\zeta_{\text{C,fuel}}/W_{\text{C}} + \zeta_{\text{H,fuel}}/2W_{\text{H}} + 2\zeta_{\text{O,ox}}/W_{\text{O}}} \tag{2.19}$$

with W_α the atomic weight of element α. The elemental mass fraction ζ_α is defined as

$$\zeta_\alpha = \sum_{k=1}^{N_k} \frac{a_{k,\alpha} W_\alpha}{M_k} Y_k. \tag{2.20}$$

Here, $a_{k,\alpha}$ denotes the number of atoms of element α in species k. Equation (2.19) is valid throughout the entire computational domain, making it useful for tracking the mixture composition. Alternatively, rather than calculating the mixture fraction from elemental mass fractions using Eq. (2.19), it is also common to treat the mixture fraction as a transported scalar as

$$\frac{\partial(\rho Z)}{\partial t} + \frac{\partial(\rho Z u_j)}{\partial x_j} = \frac{\partial}{\partial x_j}\left(\frac{\mu}{\text{Sc}}\frac{\partial Z}{\partial x_j}\right). \tag{2.21}$$

Furthermore, the primary concept behind the mixture fraction is that the thermochemical state of a non-premixed flame can be expressed as a function of the mixture fraction. Thus, determining the mixture fraction alone is sufficient to characterise the flame.

It is important to note that the mixture fraction transport equation for single phase flows does not contain any chemical source term, as it is based on the conservation of chemical elements, which remain unchanged by chemical reactions. However, when extended to multiphase flows, see Sec. 3.4.2, the presence of multiple fuel streams necessitates modifications to this formulation.

2.3 Turbulence

Fluid flows are present in nearly every aspect of daily life and play an important role in solving various engineering challenges. In general, these flows can be classified into two types, namely laminar and turbulent. To determine which flow regime is present, the Reynolds number serves as a key characteristic parameter with

$$\mathrm{Re} = \frac{u \cdot L}{\nu} \tag{2.22}$$

where u is the characteristic fluid velocity, L the characteristic length scale and ν the kinematic viscosity of the fluid. The Reynolds number can also be interpreted as the ratio between inertial and viscous forces. When the Reynolds number remains below a critical threshold ($\mathrm{Re} < \mathrm{Re}_{\mathrm{crit}}$), the flow stays laminar. However, once Re exceeds this critical value, the destabilising inertial forces dominate over the stabilising viscous forces, leading to the transition from laminar to turbulent flow. Laminar flow is characterised by smooth, orderly motion in stratified layers, where the fluid moves predominantly in one direction without chaotic or random fluctuations. Such flows can be fully described by the governing equations introduced in Sec. 2.1.1 and in simple scenarios, may even be solved analytically. In contrast, turbulent flow is defined by unsteady, irregular, and chaotic behaviour. The motion of eddies in turbulent regimes is three-dimensional and unpredictable. Although the same fundamental equations presented in Sec. 2.1.1 can also express turbulent flows, their complexity makes analytical solutions impractical. Instead, numerical approaches such as the finite volume method (FVM) in CFD must be employed to analyse and solve them. More details will be explained later in Secs. 3.1 and 4.2. Turbulent flows are a multiscale phenomenon and are characterised by a wide range of spatial and temporal scales, enabling effective mixing and transport of heat, mass and momentum. Despite the seemingly chaotic nature of turbulence, coherent structures such as vortices or eddies can still be identified. Their behaviour reveals an underlying order governed by the multiscale energy distribution

of the flow. One of the defining mechanisms of turbulence is vortex stretching. Large eddies interact with the mean flow, extracting energy and becoming elongated. As these eddies stretch, they become unstable and break down into smaller eddies, a phenomenon known as the energy cascade. This concept, introduced by [119], describes how energy is transferred from the largest eddies to progressively smaller ones. Those eddies differ in characteristic length, velocity and time scale. The different length scales and their associated energy content is illustrated in Fig. 2.4. The large eddies are governed by the geometry and/or the

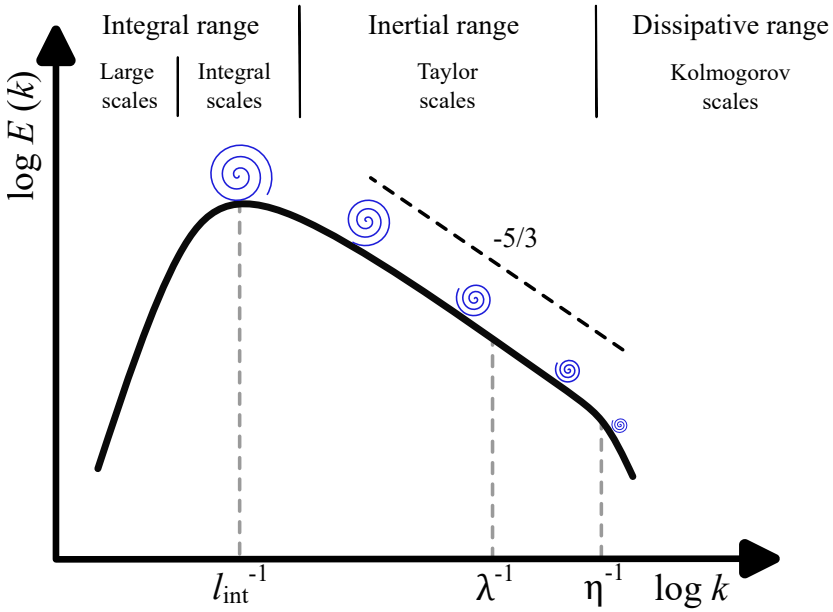

Figure 2.4: Schematic illustration of the turbulent kinetic energy spectrum E over the wavenumber k. Adapted from [112].

boundaries of the flow and are primarily influenced by convective forces. These integral scale eddies are associated with low wavenumbers and high kinetic energy. Their characteristic length, velocity and time scales can be estimated as

$$l_{\text{int}} = \frac{k^{3/2}}{\epsilon}, \qquad u_{\text{int}} = k^{1/2}, \qquad t_{\text{int}} = \frac{l_{\text{int}}}{u_{\text{int}}} = \frac{k}{\epsilon} \tag{2.23}$$

with k the turbulence kinetic energy and ϵ the turbulence dissipation rate. Both quantities are calculated as

$$k = \frac{1}{2}\left(\overline{u_i' u_i'}\right), \qquad \epsilon = \overline{\tau_{ij}\frac{\partial u_i'}{\partial x_j}} \quad \text{with} \quad \tau_{ij} = \mu\left(\frac{\partial u_j}{\partial x_i} + \frac{\partial u_i}{\partial x_j}\right) - \frac{2}{3}\mu\frac{\partial u_m}{\partial x_m}\delta_{ij}. \tag{2.24}$$

Here, overbar $<^{-}>$ and superscript $<'>$ denote time-averaged and fluctuating quantities, respectively. τ_{ij} represents the viscous stress tensor. As energy cascades down to smaller structures, the eddies become increasingly isotropic and are eventually dominated by viscous

effects. In the inertial sub-range of the energy spectrum, the slope typically follows a $-5/3$ trend, which reflects the systematic transfer of energy across different scales. The characteristic length in this spectrum is referred to as the Taylor scale. An approximation of the characteristic scales is given as

$$\lambda = \left(\frac{10\nu k}{\epsilon}\right)^{1/2}, \qquad u_\lambda = \left(\frac{2}{3}k\right)^{1/2}, \qquad t_\lambda = \frac{l_\lambda}{u_\lambda} = \left(\frac{15\nu}{\epsilon}\right)^{1/2}. \tag{2.25}$$

This energy cascade continues until it reaches the smallest scales of motion, known as the Kolmogorov scales. At these microscopic scales, viscous dissipation converts the remaining turbulent kinetic energy into thermal energy. The Kolmogorov scales are identified by the following expressions

$$\eta = \left(\frac{\nu^3}{\epsilon}\right)^{1/4}, \qquad u_\eta = (\nu\epsilon)^{1/4}, \qquad t_\eta = \frac{l_\eta}{u_\eta} = \left(\frac{\nu}{\epsilon}\right)^{1/2}. \tag{2.26}$$

The energy cascade is fundamental to turbulence modelling and has a direct impact on it. Further details are given in Sec. 3.1.

2.4 Pulverised solid fuels

Pulverised solid fuel combustion is still one of the most widespread technologies for power generation, industrial heating and potentially future energy systems. Prior to the combustion process, the solid fuel is finely ground into micrometre-sized particles, also known as pulverisation. The advantage of pulverisation lies in the significantly increased surface area compared with larger particles, which allows for more efficient combustion, i.e. faster ignition and improved heat release, thereby enhancing thermal efficiency and overall energy conversion. Based on their volatile content, pulverised solid fuels can generally be classified into volatile and non-volatile fuels.

2.4.1 Volatile-containing solid fuels

Conventional fossil fuels like coal and renewable sources like biomass are classified as volatile-containing solid fuels. A classification of solid fuels is often based on the atomic ratios of oxygen-to-carbon (O/C) and hydrogen-to-carbon (H/C), as shown in the van Krevelen Diagram in Fig. 2.5.

Coal is a combustible sedimentary rock formed from ancient plant matter that has undergone peatification and coalification. In prehistoric swamp environments, plant material accumulated to form peat, which was subsequently buried by geological processes, such as

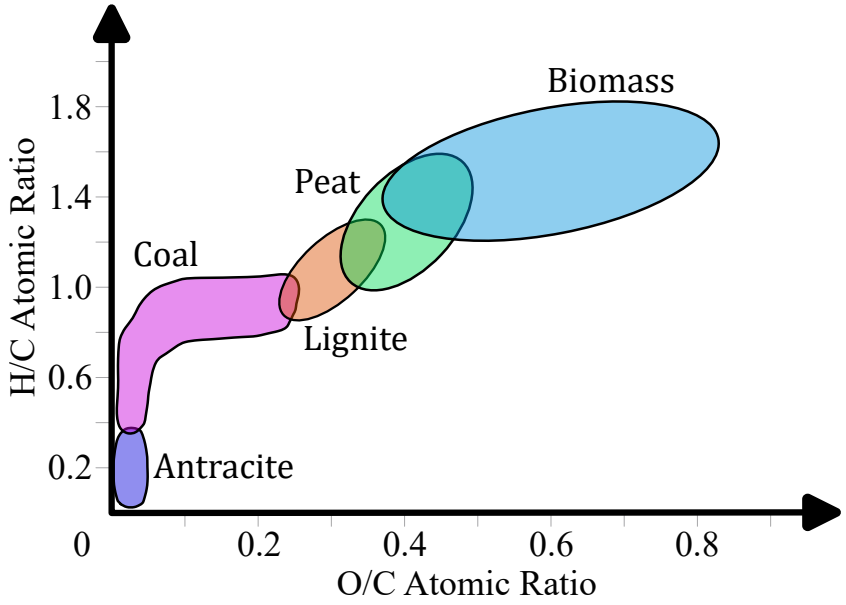

Figure 2.5: Classification of solid fuels in the Van Krevelen diagram by the hydrogen/carbon and oxygen/-carbon ratios. Adapted from [120].

crustal movement and flooding. Over millions of years, the combined effects of pressure, temperature, and time have converted the peat into coal due to coalification. The extent of coalification determines the specific properties of coal, resulting in different coal types with various moisture, volatile matter and energy content. To effectively characterise different coals, they are sub-classified by ranks, which reflects the degree of coalification. The typical classification includes four ranks (from low to high), namely lignite, sub-bituminous, bituminous and anthracite. Identification and assigning coal to the specific rank is determined by proximate and ultimate analysis. The proximate analysis evaluates the moisture, volatile matter, fixed carbon and ash content, whereas the ultimate analysis identifies the elemental composition [121].

Biomass is a renewable energy source and is formed from living organisms, primarily plants. In contrast to fossil fuels, which take millions of years to form, biomass renews in relatively short times, making it a sustainable alternative. Biomass resources that are sustainably available and suitable for direct combustion or conversion into alternative energy carriers are referred to as feedstocks. Common biomass feedstocks originate from botanical and biological sources, which are agriculture residues (e.g. straw, nutshells), forestry residues (e.g. trees, wood waste), municipal waste (e.g. food and paper waste) and dedicated energy crops (e.g. miscanthus, switchgrass). The majority of biomass originates from botanical sources. This plant-based biomass captures solar energy through photosynthesis and stores it in chemical bonds of C,H,O-containing compounds. The biomass composition varies significantly, depending on its source and processing steps, which highly influence the subsequent energy conversion process. Typical biomass contains more volatile matter, a higher mois-

ture content and a lower energy density than coal (upper right in Fig. 2.5). Structurally, biomass is composed primarily of three organic polymers, namely cellulose, hemicellulose and lignin. These components influence the thermal degradation behaviour, chemical reactivity and overall combustion characteristics of biomass. Similar to coal, biomass can also be characterised through proximate and ultimate analysis [122].

Proximate analysis

Proximate analysis is a measurement technique to determine the key chemical properties of volatile-containing solid fuels. The results provide information about the fuel composition and its quality. The analysis expresses the composition on a mass percent basis and categorises it into four main components: moisture, volatile matter, ash and fixed carbon. The measurement is standardised for coal in ISO 17246 and for biomass in ISO 18122, 18123 and 18134. The procedure to measure the four main components is briefly explained in the following:

- **Moisture** is determined by measuring the mass loss of a heated sample at $107 \pm 3\,^{\circ}\mathrm{C}$ for 1 hour until a constant weight is established. The calculation is as follows:

$$\text{Moisture in}\,\% = \frac{\text{weight loss}}{\text{weight of sample}} \cdot 100 \tag{2.27}$$

- **Volatile matter** is determined by measuring the mass loss of a heated sample (dry) at $950 \pm 20\,^{\circ}\mathrm{C}$ for 7 min in an inert atmosphere, such as nitrogen or argon. The calculation is as follows:

$$\text{Volatile matter in}\,\% = \frac{\text{weightloss due to volatile matter}}{\text{weight of dry sample}} \cdot 100 \tag{2.28}$$

- **Ash** is determined by measuring the residual mass of a heated sample (dry and without volatile matter) at $575 \pm 25\,^{\circ}\mathrm{C}$ for biomass and $750 \pm 15\,^{\circ}\mathrm{C}$ for coal in an oxidising gas, such as air. The temperature is held as long as all carbonaceous material is burnt. The calculation is as follows:

$$\text{Ash in}\,\% = \frac{\text{weight of residue}}{\text{weight of sample}} \cdot 100 \tag{2.29}$$

- **Fixed carbon** is a calculated value and is evaluated by the difference of 100 and the sum of the percentages of moisture, volatile matter and ash as

$$\text{Fixed carbon in}\,\% = 100 - (\text{Moisture} + \text{Volatile Matter} + \text{Ash}) \tag{2.30}$$

The yield of volatile gases is typically higher than the amount obtained by proximate analysis due to the faster heating conditions experienced in practical applications, which result in a higher initial amount of volatile matter (VM). To account for this difference, a Q-factor can be applied, defined as

$$Q = \frac{m_{p,\mathrm{VM},0}}{m_{p,\mathrm{VM,prox}}} \tag{2.31}$$

where $m_{p,\mathrm{VM},0}$ represents the available volatile matter at higher heating rates and $m_{p,\mathrm{VM,prox}}$ corresponds to the value obtained from proximate analysis.

Ultimate analysis

Ultimate analysis is another measurement method used to determine different key characteristics of solid fuels. The method identifies the elemental composition by measuring the amounts of carbon (C), hydrogen (H), nitrogen (N), sulphur (S) and oxygen (O). Compared to proximate analysis, ultimate analysis is more complex and costlier. The contents of C, H, and N are simultaneously measured by the combustion of the sample at elevated temperatures in an oxygen environment. From the corresponding gases of $CO_2, H_2O, N_2/NO_x$, the elemental composition is quantified with an elemental analyser. The standard procedures are outlined in ISO 29541 for coal and ISO 16948 for biomass. The elemental composition of sulphur can be determined using various methods. The most common methods are the Eschka method for coal (ISO 334) and high temperature method for biomass (ISO 15178). Finally, the oxygen content is calculated by the difference as

$$\mathrm{O\ in\,\%} = 100 - (\mathrm{C} + \mathrm{H} + \mathrm{N} + \mathrm{S} + \mathrm{Ash} + \mathrm{Moisture}). \tag{2.32}$$

The moisture and ash values are obtained from the proximate analysis. From the elementary composition, the calorific values of the solid fuels can be approximated.

Thermal conversion process

The thermal conversion process of volatile-containing solid fuel consists of several main stages, as schematically shown in Fig. 2.6. These stages are the (i) particle heating, (ii) particle drying, (iii) volatile gas release from the particle (devolatilisation or pyrolysis), (iv) homogeneous gas phase combustion and (v) heterogeneous particle surface reactions (char conversion). A brief overview of each stage is provided below with some parts following [123].

(i) **Particle heating**
In the initial stage, the fuel particle absorbs heat from the surrounding environment through convection and/or radiation, causing its temperature to rise. This temperature increase leads to moisture evaporation and initiates thermal decomposition, during

which chemical bonds are broken, forming lighter and heavier molecular fragments.

(ii) **Particle drying**
As the particle temperature approaches the boiling point of water ($\approx 373\,\mathrm{K}$), moisture starts to evaporate. Biomass typically contains a high moisture content, whereas coal contains significantly less due to its higher carbon content (see Fig. 2.5, lower left). Given the relatively low boiling point of water and the endothermic nature of evaporation, the drying process is mostly completed before subsequent thermal stages begin. The duration and effectiveness of drying are strongly influenced by the initial composition of the solid fuel, the particle size and ambient conditions.

(iii) **Particle devolatilisation**
The pyrolysis behaviour of the solid fuel is highly dependent on its initial molecular structure, which is composed of various monomers connected by chemical bonds. As the particle temperature rises, these chemical bonds undergo breaking and reformation. Variations in monomer composition and bonding (solid fuel structure) lead to significant differences in devolatilisation rates and product yields. Generally, the devolatilisation process can be divided into two distinct steps:

- **Primary devolatilisation** is mainly characterised by the breaking of labile chemical bonds and the formation of more stable bonds. Labile bonds are associated with releasing smaller molecular fragments, forming light gases and tar, while stable bonds contribute to char formation. During the thermochemical conversion of the solid particle, the rates of these competing reactions determine the relative release of gas, tar, and char. Some smaller fragments may remain within the particle and undergo crosslinking reactions.
- **Secondary devolatilisation** refers to subsequent gas-phase reactions of volatile species released during the primary devolatilisation process. During this stage, heavy tar compounds thermally crack into lighter molecules and potentially leading to pollutant formation. These reactions are strongly influenced by ambient conditions and typically occur in high-temperature regions.

(iv) **Homogeneous gas phase combustion**
The volatile gases are released into the gas phase and mixed with the surrounding oxidising atmosphere. Upon reaching a near-stoichiometric ratio, the mixture ignites, which is characteristic for non-premixed combustion. The resulting gas-phase combustion raises the temperature, which in turn heats the solid particle via convection and/or radiation. This accelerates the devolatilisation process, which continues until all embedded volatiles within the solid fuel particle have been released.

(v) **Heterogeneous surface reactions**

Char conversion mainly starts after devolatilisation but some overlap between the two processes may occur. As char conversion is significantly slower than devolatilisation, it plays an important role in determining the overall coal conversion time. The highly porous nature of the char, which is formed mainly during the devolatilisation phase, allows the progression of char conversion within three distinct reaction regimes:

- **Kinetically-controlled regime** occurs under low-temperature conditions, where char conversion only depends on the chemical reaction rates. In this regime, mass transport processes are faster than chemical reaction time scales and therefore do not limit the overall conversion rate.
- **Pore-diffusion-controlled regime** occurs under intermediate-temperature conditions. As the temperature increases, the reaction rates become faster, making pore diffusion processes more essential and partly the rate-limiting step.
- **Film-diffusion-controlled regimes** arise at very high-temperature conditions, where chemical reaction rates are significantly faster than mass transport processes. As a result, external diffusion becomes the dominant rate-limiting step in the overall char conversion process.

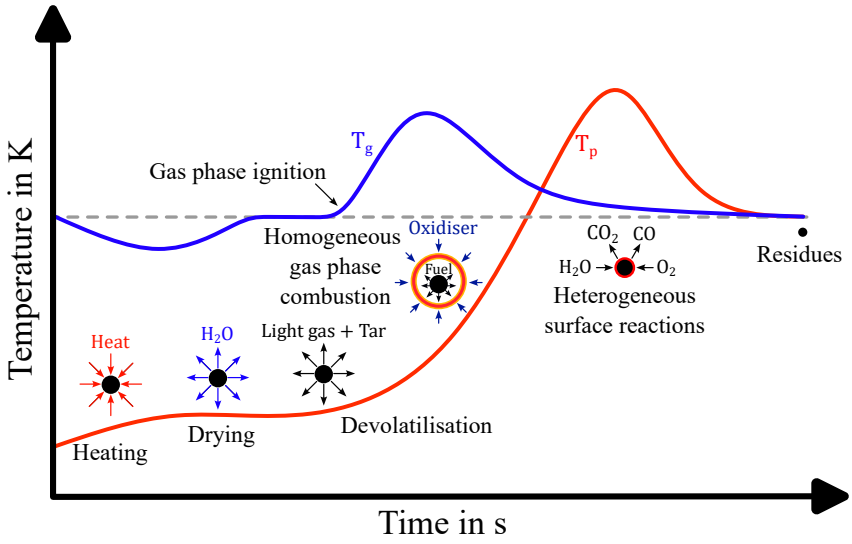

Figure 2.6: Schematic illustration of the overall volatile-containing solid fuel conversion process over time. Adapted from [124].

2.4.2 Non-volatile solid fuels

Fossil fuels remain the predominant energy source, but their adverse environmental impacts and finite availability have raised the urgent need for alternative energy sources. Renewable

energy sources such as wind and solar provide clean and carbon-free energy. However, their inconsistent supply and geographic limitations prevent reliable energy delivery to regions with high and continuous demands. A possible approach to address this limitation lies in implementing a carbon-free energy storage system. Yet, current storage technologies [125] are still underdeveloped or insufficiently explored. Among the emerging technologies with significant potential is the use of metals as emission-free energy carriers [15, 16] with the opportunity of using existing coal-fired power plant infrastructure [14]. Figure 2.7 compares the volumetric energy density and specific energy for various chemical energy carriers and different states. Metal fuels are relatively abundant and show high volumetric density with reasonable specific energy properties compared to conventional hydrocarbon fuels, making them attractive for energy storage systems. Iron is particularly well-suited for this role due to its natural abundance and favourable characteristics for transport and storage [15, 126]. Furthermore, coupling the iron oxidation with the reverse reduction of iron oxide, ideally

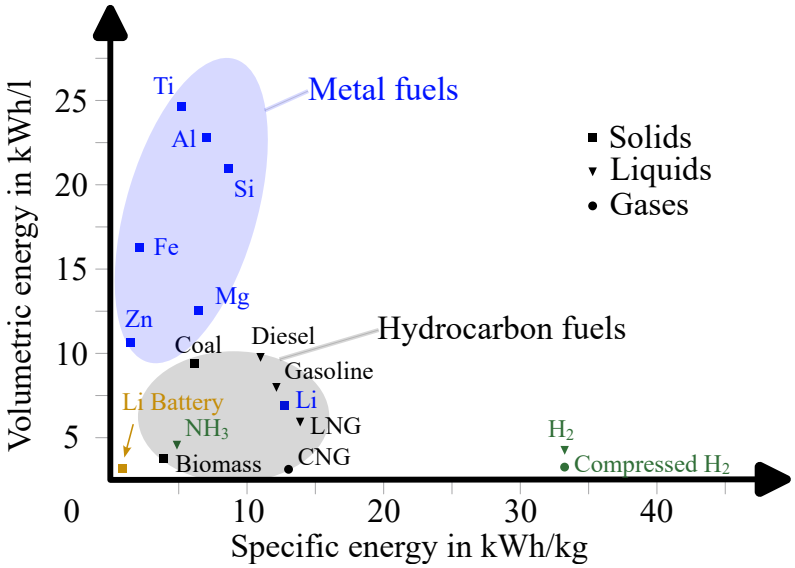

Figure 2.7: Volumetric energy density vs. specific energy for various chemical energy carriers. Adapted from [16].

based on renewable energy sources, enables the development of a sustainable circular zero-carbon energy economy. This possible sustainable circular energy economy is visualised in Fig. 2.8. Unlike conventional solid fuels such as coal or biomass, iron undergoes a non-volatile heterogeneous combustion such that modelling approaches for carbon-based solid fuels are not directly applicable to iron combustion. This has led to increased research efforts to understand the thermo-chemical processes of iron combustion.

Thermal conversion process

Similar to volatile solid fuels, non-volatile solid fuels (e.g. iron) undergo various stages of

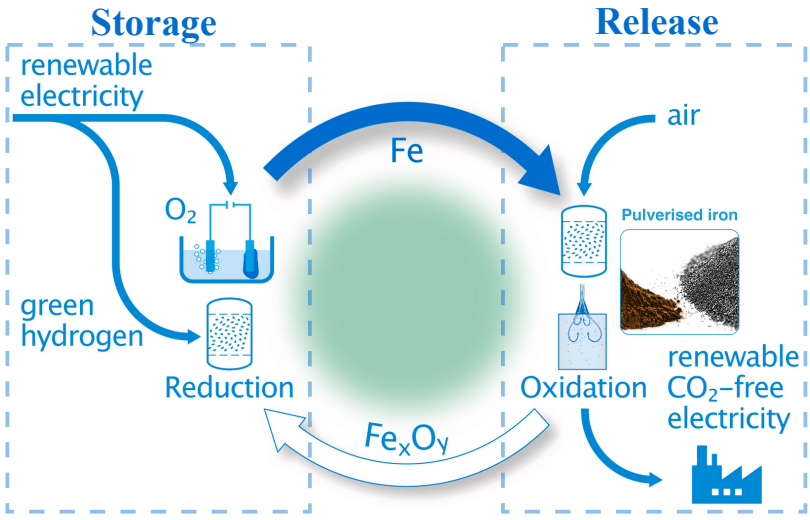

Figure 2.8: Schematic illustration of an iron reduction-oxidation (redox) circular zero-carbon energy economy. Adapted from [16].

thermal conversion as well. These stages are: (i) particle heating, (ii) heterogeneous particle surface reactions (iron ignition), (iii) particle melting, (iv) (possible) surface evaporation, (v) reactive cooling and (vi) particle solidification. The conversion stages are schematically shown in Fig. 2.9. The remainder of this section provides a brief discussion of each stage.

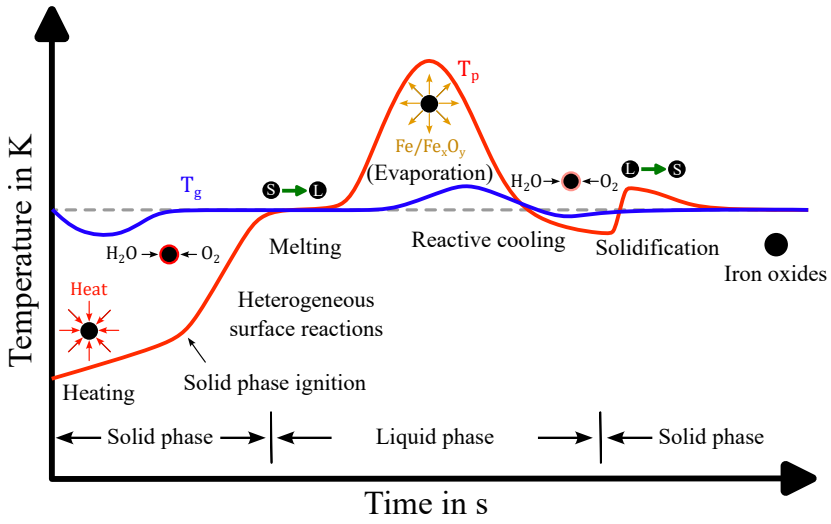

Figure 2.9: Schematic illustration of the overall non-volatile solid fuel conversion process over time. Adapted from [124].

(i) **Particle heating**

The iron particle absorbs heat through convection and/or radiation from the surroundings. This leads to a temperature increase of the iron particle and the initiation of the

oxidation process. Once the ignition temperature is reached, the particle will start its ignition process, which is also referred to as thermal runaway [127].

(ii) **Heterogeneous particle surface reactions (iron particle oxidation)**
At elevated temperatures, the iron particle interacts with the oxygen in the surrounding, and initiates the oxidation process. The oxidation process is either kinetically-controlled or diffusion-controlled:

- **Kinetically-controlled** regime appears at low particle temperatures, where the oxidation process solely depends on the chemical reaction rates. Here, diffusion transport processes to the particle are much faster and do not influence the overall oxidation process. Leading to the chemical reaction rates becoming the rate-limiting step.
- **Diffusion-controlled** regime occurs at very high temperatures. The time scale of the chemical reaction rates of the oxidation process is much faster compared to the mass diffusion time scale. The rate-limiting step is the external diffusion of oxygen from the environment to the particle surface, which controls the overall oxidation process.

Particle ignition leads to a rapid increase in particle temperature and subsequently heats up the surrounding environment through convection and/or radiation. Different from coal or biomass, no volatile gases are released into the gas phase, therefore, ignition does not take place in the gas phase, but on the particle surface. The increase of the gas phase temperature only depends on the heat transfer from the particle to the gas phase.

(iii) **Particle melting**
When the particle reaches its melting point, a phase transition occurs. The solid state transforms into a liquid state. This phase change process changes the thermophysical properties of the iron/iron oxide particle. The melting points of iron and iron oxides are summarised in Tab. 2.1.

Table 2.1: Melting and boiling points of iron and iron oxides. Fe_2O_3 does not melt at normal pressure because it dissociates before reaching a liquid state [128]

	T_{melt} in K	T_{boil} in K
Fe	1809 [129]	3134 [129]
FeO	1650 [129]	3396[a] [128]
Fe_3O_4	1869 [128]	2603[a] [128]
Fe_2O_3	-	-

[a] Dissociation point.

(iv) **Particle surface evaporation**
Oxidation processes can continue after transforming the particle from solid to liquid state, leading to a further increase in particle temperature. The boiling temperature (see Tab. 2.1) of the molten iron particle may be reached, leading to evaporation processes of iron and iron oxides. Released gaseous iron and iron oxide vapour can nucleate, coagulate and/or condense, which results in the formation of nanoparticles.

(v) **Reactive cooling**
After the primary oxidation process is completed, the particle starts to cool down. However, recent studies [130] have investigated the reactive cooling process during this period. During the reactive cooling process, the molten iron oxide continues to react. Although it releases heat, it is insufficient to counteract the external thermal losses, leading to a reduced cooling rate compared with non-reactive cooling.

(vi) **Particle solidification**
The particle continues to cool down until it reaches its melting point. At the melting point, a solidification process takes place, where the remaining molten iron oxide transforms into the solid phase.

Non-volatile solid fuels, e.g. iron, offer significant potential for the future energy transition. While their conversion processes indicate similarities with those of volatile-containing solid fuels, notable differences exist. The modelling approaches used to capture these differences will be discussed in detail in the following chapter.

3 Modelling of turbulent reactive multiphase flows (gas/solid)

This chapter presents the modelling approaches and strategies corresponding to the theoretical framework of turbulent reactive multiphase flows discussed in Chapter 2. It is structured into four main sections. The first Sec. 3.1 introduces the modelling of turbulent flows, including the relevant modifications to the governing equations. This is followed by an explanation of the modelling strategies for the solid phase (Sec. 3.2), addressing both volatile and non-volatile solid fuels, along with the coupling mechanisms between the gas and solid phases. The third Sec. 3.3 describes the approach used to model radiative heat transfer. Finally, the chapter concludes with the modelling of homogeneous gas-phase reactions, which is particularly relevant for volatile-containing solid fuels in Sec. 3.4.

3.1 Turbulence modelling

The set of governing equations to solve turbulent reactive multiphase flows has been already presented in Sec. 2.1.2. The governing equations cannot be solved analytically in most practical cases and, therefore, require the application of numerical methods. Several numerical approaches have been developed and established in the past. The three major approaches are the Finite Difference Method (FDM), Finite Element Method (FEM), and Finite Volume Method (FVM). Each of these methods offers advantages and limitations. In the context of this thesis, the FVM is used to solve the governing equations. This approach involves dividing the entire computational domain into a finite number of control volumes (*discretisation*) and solving the governing equations for each of these finite volumes. A more detailed explanation of the FVM is provided in Section 4.2. Based on the selected turbulence modelling approach, the discretisation grid is determined by the required cell size, denoted as Δ for each control volume (Δ^3). As already discussed in Sec. 2.3, turbulence is inherently a multiscale phenomenon, characterised by a wide range of eddy sizes. The Kolmogorov length scales η are particularly important, representing the smallest turbulent structures. To fully resolve all turbulent scales within a flow, the grid size has to be sufficiently small, which is characterised by the Kolmogorov length scale, i.e. $\Delta \leq 2.1\,\eta$ [131]. When this condition is satisfied, no additional turbulence modelling assumptions are necessary and the flow can

be computed using the DNS approach, which resolves all relevant turbulent length scales. However, in many practical applications, the Kolmogorov scales can become very small due to the high Reynolds numbers, resulting in very fine grids and, therefore, excessively high computational demands. As such, DNS is often not feasible for engineering-scale problems. This limitation has motivated the development of turbulence modelling strategies that use coarser grids while still capturing the effect of turbulence. Three principal approaches have been established, with each differing in the extent to which turbulent length scales, thus turbulent kinetic energy, are resolved or modelled. These are:

- Direct Numerical Simulation (DNS), which resolves all turbulent scales
- Large Eddy Simulation (LES), which resolves only the largest scales and
- Reynolds-Averaged Navier-Stokes (RANS), which models all turbulent fluctuations by solving only for time-averaged quantities.

A schematic overview of these modelling strategies and their treatment of the turbulent energy spectrum is presented in Figure 3.1.

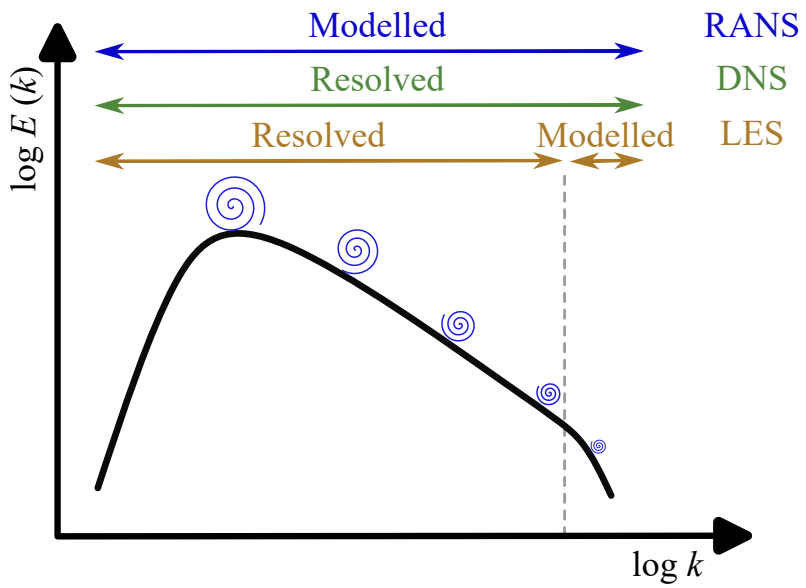

Figure 3.1: Schematic illustration of the modelling approaches of DNS, LES and RANS.

3.1.1 Direct numerical simulation (DNS)

DNS offers the most accurate approach by resolving all turbulent scales without relying on turbulence models. Consequently, the governing equations for mass, momentum, enthalpy and species are solved in their original form as given in Eqs. (2.6) – (2.9). The equations

are presented again here, for a clearer comparison with alternative turbulence modelling approaches:

$$\frac{\partial \rho}{\partial t} + \frac{\partial (\rho u_i)}{\partial x_i} = \dot{S}_{\rho,p}$$

$$\frac{\partial (\rho u_i)}{\partial t} + \frac{\partial (\rho u_i u_j)}{\partial x_j} = -\frac{\partial p}{\partial x_i} + \frac{\partial}{\partial x_j}\left[\mu\left(\frac{\partial u_j}{\partial x_i} + \frac{\partial u_i}{\partial x_j}\right) - \frac{2}{3}\mu\frac{\partial u_m}{\partial x_m}\delta_{ij}\right] + \rho g_i + \dot{S}_{u,p}$$

$$\frac{\partial (\rho h_s)}{\partial t} + \frac{\partial (\rho h_s u_j)}{\partial x_j} = \frac{\partial}{\partial x_j}\left(\frac{\mu}{\mathrm{Pr}}\frac{\partial h_s}{\partial x_j}\right) + \dot{S}_{\mathrm{rad}} + \dot{\omega}_{h_s} + \dot{S}_{h_s,p}$$

$$\frac{\partial (\rho Y_k)}{\partial t} + \frac{\partial (\rho Y_k u_j)}{\partial x_j} = \frac{\partial}{\partial x_j}\left(\frac{\mu}{\mathrm{Sc}}\frac{\partial Y_k}{\partial x_j}\right) + \dot{\omega}_k + \dot{S}_{Y_k,p}.$$

In this thesis, the Prandtl and Schmidt number are chosen to be $\mathrm{Pr} = \mathrm{Sc} = 0.7$. The source terms for interphase transfers between the gas and solid phases ($\dot{S}_{\rho,p}$, $\dot{S}_{u,p}$, $\dot{S}_{h_s,p}$, $\dot{S}_{Y_k,p}$) will be addressed in Sec. 3.2.1.2, radiation ($\dot{S}_{\mathrm{rad}}$) in Sec. 3.3 and chemical source terms ($\dot{\omega}_{h_s}$, $\dot{\omega}_k$) in Sec. 3.4. As already stated before, a DNS is only valid if the spatial and temporal resolution requirements of turbulence are satisfied. These are [113, 115, 131]

- the computational domain must be sufficiently large to capture the energy-containing scales (l_{int})
- the grid resolution must be fine enough to resolve the smallest scales (η) and
- the computational time step must be small enough to accurately represent the turbulent motion at the smallest scales (t_η).

If all conditions are simultaneously fulfilled, the computational cost for a DNS can be estimated with the Reynolds number based on the integral scale with $\mathrm{Re}_{\mathrm{int}} = (u_{\mathrm{int}} l_{\mathrm{int}})/\nu$ [131]. To ensure that the spatial resolution is of sufficient quality for a DNS, the domain with a typical size of L_Δ with N_Δ of cells of cell size Δ needs to be large enough to solve the energy-containing scales as $L_\Delta = N_\Delta \cdot \Delta \geq l_{\mathrm{int.}}$ in each direction. Assuming that the cell size is fine enough to resolve the Kolmogorov length scale ($\Delta \leq \eta$) it will result in the total number of required grid points for a three-dimensional case as

$$N_{\Delta^3} = \left(\frac{l_{\mathrm{int}}}{\eta}\right)^3 = \left(\frac{k^{3/2}}{\epsilon}\frac{\epsilon^{1/4}}{\nu^{3/4}}\right)^3 = \left(\frac{k^{1/2}k^{3/2}}{\nu\epsilon}\right)^{9/4} \sim \quad {\mathrm{Re}_{\mathrm{int}}}^{9/4} \tag{3.1}$$

To satisfy the temporal requirements, the computational time step Δt needs to correspond to the Kolmogorov time scale and the total simulation time $T_{\Delta t}$ needs to be long enough to capture the integral time scale or even multiples of it. Therefore the minimum number of

required time steps can be estimated as

$$N_{\Delta \mathrm{t}} \geq \frac{T_{\Delta t}}{\Delta t} = \frac{t_{\mathrm{int}}}{t_\eta} = \frac{k}{\epsilon}\frac{\epsilon^{1/2}}{\nu^{1/2}} = \left(\frac{k^{1/2}k^{3/2}}{\nu\epsilon}\right)^{1/2} \sim \quad {\mathrm{Re}_{\mathrm{int}}}^{1/2} \tag{3.2}$$

The minimum total computational effort can now be estimated as [131]

$$t_{\mathrm{total}} = N_{\Delta^3} \cdot N_{\Delta \mathrm{t}} = {\mathrm{Re}_{\mathrm{int}}}^{9/4} \cdot {\mathrm{Re}_{\mathrm{int}}}^{1/2} \sim \quad {\mathrm{Re}_{\mathrm{int}}}^{11/4} \tag{3.3}$$

The estimation reveals that DNS is not feasible for practical applications or engineering-scale problems which typically involve high Reynolds numbers ($\mathrm{Re}_{\mathrm{int}} \approx 10{,}000$ [131]). However, the strength of DNS lies in the representation of turbulent flows without using turbulence models. Therefore, it is an excellent tool for fundamental research. Consequently, it is an essential reference for validating and improving applied models in LES and RANS, which can be used to solve large-scale and practical applications. Despite the high computational cost, DNS provides reliable data and contributes to a better understanding of turbulent flows.

3.1.2 Large eddy simulation (LES)

Large Eddy Simulation (LES) resolves the larger turbulent length scales, while the smaller scales are modelled. This approach is based on the principle that most turbulent kinetic energy is contained in the large eddies, whereas the small eddies carry comparatively little energy, as illustrated in Fig. 2.4. Since large eddies are highly anisotropic and significantly influence the flow field, it is important to resolve them. In contrast, small eddies are nearly isotropic, have less impact on the overall flow and reveal universal characteristics, making them more suitable for modelling. Since LES models the small scales, the computational grid no longer needs to resolve the Kolmogorov scales. This allows for a coarser mesh with fewer grid cells, making LES significantly more efficient than DNS and better suited for practical applications and large-scale simulations. To separate turbulent structures into large and small scales, a filtering operation is applied. In the context of LES, any arbitrary quantity ϕ can be decomposed into a resolved component $\overline{\phi}$ and unresolved (sub-grid) component ϕ' as

$$\phi = \overline{\phi} + \phi'. \tag{3.4}$$

The general form of a filter operation is given as

$$\overline{\phi}(x_i, t) = \iiint G(x_i - x_i^*, \Delta_{\mathrm{filt}})\phi(x_i^*, t)dx_i^* \tag{3.5}$$

which involves the filter function G and the filter width Δ_{filt}. Filtering can be performed in either spectral or physical space [113, 115, 131], with physical-space filtering being more

relevant for CFD applications. It is commonly assumed that $\Delta_{\text{filt}} = \Delta$. Applying the filter operation from Eq. (3.4) to the governing equations introduces additional unclosed terms. As an example, this can be demonstrated by applying the filtering to the convective term in the momentum equation (Eq. (2.7), second term LHS) [115]

$$\overline{\rho u_i u_j} = \overline{\rho}\,\overline{u_i}\,\overline{u_j} + \overline{\rho}\overline{u_i' u_j'} + \overline{u_i}\overline{\rho' u_j'} + \overline{u_j}\overline{\rho' u_i'} + \overline{\rho' u_i' u_j'}. \tag{3.6}$$

To simplify the problem and reduce the number of unclosed terms, a density-weighted filtering method, also known as Favre filter, can be applied with

$$\widetilde{\phi} = \frac{\overline{\rho\phi}}{\overline{\rho}} \tag{3.7}$$

along with the corresponding Favre decomposition as

$$\phi = \widetilde{\phi} + \phi'' \tag{3.8}$$

where $< \widetilde{\ } >$ and $<''>$ indicate the resolved and unresolved (sub-grid) Favre components, respectively. When Favre-filtering is applied to the convective term in the momentum equation

$$\overline{\rho u_i u_j} = \overline{\rho} \widetilde{u_i} \widetilde{u_i} = \overline{\rho} \widetilde{u_i} \widetilde{u_j} + \overline{\rho u_i'' u_j''}, \tag{3.9}$$

it results in a formulation with fewer unclosed terms. Applying the Favre-filtering to, where applicable, the full set of governing equations in Eqs. (2.6) – (2.9) results in

$$\frac{\partial \overline{\rho}}{\partial t} + \frac{\partial (\overline{\rho} \widetilde{u_i})}{\partial x_i} = \overline{\dot{S}}_{\rho,p} \tag{3.10}$$

$$\frac{\partial (\overline{\rho} \widetilde{u_i})}{\partial t} + \frac{\partial (\overline{\rho} \widetilde{u_i} \widetilde{u_j})}{\partial x_j} = -\frac{\partial \overline{p}}{\partial x_i} + \frac{\partial}{\partial x_j}\left[\overline{\mu}\left(\frac{\partial \widetilde{u_j}}{\partial x_i} + \frac{\partial \widetilde{u_i}}{\partial x_j} - \frac{2}{3}\frac{\partial \widetilde{u_m}}{\partial x_m}\delta_{ij}\right) - \overline{\rho u_i'' u_j''}\right] + \overline{\rho} g_i + \overline{\dot{S}}_{u,p} \tag{3.11}$$

$$\frac{\partial (\overline{\rho} \widetilde{h_s})}{\partial t} + \frac{\partial (\overline{\rho} \widetilde{h_s} \widetilde{u_j})}{\partial x_j} = \frac{\partial}{\partial x_j}\left(\frac{\overline{\mu}}{\text{Pr}}\frac{\partial \widetilde{h_s}}{\partial x_j} - \overline{\rho h_s'' u_j''}\right) + \overline{\dot{S}}_{\text{rad.}} + \overline{\dot{\omega}}_{h_s} + \overline{\dot{S}}_{h_s,p} \tag{3.12}$$

$$\frac{\partial (\overline{\rho} \widetilde{Y_k})}{\partial t} + \frac{\partial (\overline{\rho} \widetilde{Y_k} \widetilde{u_j})}{\partial x_j} = \frac{\partial}{\partial x_j}\left(\frac{\overline{\mu}}{\text{Sc}}\frac{\partial \widetilde{Y_k}}{\partial x_j} - \overline{\rho Y_k'' u_j''}\right) + \overline{\dot{\omega}}_k + \overline{\dot{S}}_{Y_k,p}. \tag{3.13}$$

In the governing equations, it is assumed that the fluctuation terms in the diffusion/viscous terms after Favre-filtering can be neglected in the momentum equation

$$\overline{\mu\left(\frac{\partial u_j}{\partial x_i} + \frac{\partial u_i}{\partial x_j} - \frac{2}{3}\frac{\partial u_m}{\partial x_m}\delta_{ij}\right)} \approx \overline{\mu}\left(\frac{\partial \widetilde{u_j}}{\partial x_i} + \frac{\partial \widetilde{u_i}}{\partial x_j} - \frac{2}{3}\frac{\partial \widetilde{u_m}}{\partial x_m}\delta_{ij}\right) \tag{3.14}$$

with $\tau_{ij,1} \gg (\tau_{ij,2} + \tau_{ij,3})$ as

$$\underbrace{\overline{\mu}\left(\frac{\partial\widetilde{u_j}}{\partial x_i}+\frac{\partial\widetilde{u_i}}{\partial x_j}-\frac{2}{3}\frac{\partial\widetilde{u_m}}{\partial x_m}\delta_{ij}\right)}_{\tau_{ij,1}}+\underbrace{\overline{\mu}\left(\frac{\partial\overline{u_j''}}{\partial x_i}+\frac{\partial\overline{u_i''}}{\partial x_j}-\frac{2}{3}\frac{\partial\overline{u_m''}}{\partial x_m}\delta_{ij}\right)}_{\tau_{ij,2}}+\underbrace{\overline{\mu'\left(\frac{\partial u_j''}{\partial x_i}+\frac{\partial u_i''}{\partial x_j}-\frac{2}{3}\frac{\partial u_m''}{\partial x_m}\delta_{ij}\right)}}_{\tau_{ij,3}}, \tag{3.15}$$

in the sensible enthalpy equation

$$\overline{\frac{\mu}{\mathrm{Pr}}\frac{\partial h_s}{\partial x_j}} \approx \frac{\overline{\mu}}{\mathrm{Pr}}\frac{\partial\widetilde{h_s}}{\partial x_j} \qquad \text{with} \qquad \frac{\overline{\mu}}{\mathrm{Pr}}\frac{\partial\widetilde{h_s}}{\partial x_j} \gg \left(\frac{\overline{\mu}}{\mathrm{Pr}}\frac{\partial\overline{h_s''}}{\partial x_j}+\overline{\frac{\mu'}{\mathrm{Pr}}\frac{\partial h_s''}{\partial x_j}}\right) \tag{3.16}$$

and in the chemical species equation

$$\overline{\frac{\mu}{\mathrm{Sc}}\frac{\partial Y_k}{\partial x_j}} \approx \frac{\overline{\mu}}{\mathrm{Sc}}\frac{\partial\widetilde{Y_k}}{\partial x_j} \qquad \text{with} \qquad \frac{\overline{\mu}}{\mathrm{Sc}}\frac{\partial\widetilde{Y_k}}{\partial x_j} \gg \left(\frac{\overline{\mu}}{\mathrm{Sc}}\frac{\partial\overline{Y_k''}}{\partial x_j}+\overline{\frac{\mu'}{\mathrm{Sc}}\frac{\partial Y_k''}{\partial x_j}}\right). \tag{3.17}$$

The unclosed terms of $\overline{\rho u_i'' u_j''}$, $\overline{\rho h_s'' u_j''}$ and $\overline{\rho Y_k'' u_j''}$ in Eqs. (3.11) - (3.13) remain and must be modelled accordingly. The sub-grid scale (SGS) stress tensor ($\overline{\rho u_i'' u_j''}$) is typically described in analogy to the laminar stress tensor as

$$-\overline{\rho u_i'' u_j''} = \mu_t\left(\frac{\partial\widetilde{u_j}}{\partial x_i}+\frac{\partial\widetilde{u_i}}{\partial x_j}-\frac{2}{3}\frac{\partial\widetilde{u_m}}{\partial x_m}\delta_{ij}\right) \tag{3.18}$$

with μ_t the turbulent dynamic viscosity. A gradient-based approach [113] is typically applied to approximate the turbulent fluxes of energy and species

$$-\overline{\rho h_s'' u_j''} = \frac{\mu_t}{\mathrm{Pr}_t}\frac{\partial\widetilde{h_s}}{\partial x_j} \tag{3.19}$$

$$-\overline{\rho Y_k'' u_j''} = \frac{\mu_t}{\mathrm{Sc}_t}\frac{\partial\widetilde{Y_k}}{\partial x_j} \tag{3.20}$$

where Pr_t and Sc_t denote the turbulent Prandtl and Schmidt numbers, respectively. The final unclosed term associated with turbulent flow is the turbulent viscosity μ_t which is generally modelled using established turbulence modelling approaches. One of the most commonly used sub-grid scale turbulence models is the Smagorinsky model [132]. It is based on the Boussinesq approximation and considers an equilibrium between the production and dissipation of turbulent kinetic energy while also assuming the isotropic behaviour of the sub-grid scales. The Smagorinsky model employed in Sec. 5.2 adopts a slightly modified

formulation compared to the original version as

$$\mu_t = C_k \overline{\rho} \Delta \sqrt{k_t} \qquad \text{with} \qquad k_t = \frac{C_k \Delta^2 \sqrt{2\widetilde{S_{ij}}\widetilde{S_{ij}}}^2}{\mathrm{C_e}}. \tag{3.21}$$

Here, $C_k = 1.048$ and $C_e = 0.01$ are model constants, k_t the sub-grid turbulent kinetic energy and $\widetilde{S_{ij}}$ the Favre-filtered strain rate. The Favre-filtered strain rate is calculated as

$$\widetilde{S_{ij}} = \frac{1}{2}\left(\frac{\partial \widetilde{u_j}}{\partial x_i} + \frac{\partial \widetilde{u_i}}{\partial x_j}\right). \tag{3.22}$$

By combining Eq. (3.21) with (3.22), the following expression is obtained

$$\mu_t = C_k \sqrt{\frac{C_k}{C_e}} \overline{\rho} \Delta^2 \sqrt{2\widetilde{S_{ij}}\widetilde{S_{ij}}}. \tag{3.23}$$

This expression is similar to the original Smagorinsky formulation ($\mu_t = \overline{\rho}(C_T\Delta)^2\sqrt{2\widetilde{S_{ij}}\widetilde{S_{ij}}}$). The main advantages of the model lie in its simplicity, robustness, and widespread applicability. However, this simplicity comes at the cost that the model tends to overpredict turbulent viscosity in near-wall regions due to the strongly anisotropic behaviour [113, 115]. Furthermore, the model constants are strongly dependent on the specific flow configuration, but the default model constants mentioned above are used in Sec. 5.2.

3.1.3 Reynolds-Averaged-Navier-Stokes (RANS)

For completeness, the RANS approach is briefly explained in this section. RANS approaches aim to describe the statistical behaviour of turbulence by solving time-averaged forms of the governing equations. The advantage of RANS is its ability to operate with relatively coarse computational grids, resulting in significantly lower computational costs. However, because the approach depends on time-averaging, it only provides information on the mean, not the instantaneous flow field. Moreover, the accuracy of the simulation results highly depends on the applied turbulence models, as all turbulent scales are modelled rather than resolved, as illustrated in Fig. 3.1, and the governing equations contain no unsteady terms. A Reynolds decomposition is applied to derive the time-averaged form of the governing equations, which decomposes any arbitrary quantity ϕ into a time-mean $\overline{\phi}$ and fluctuating ϕ' component, as shown here

$$\phi = \overline{\phi} + \phi'. \tag{3.24}$$

Similar to LES, a Favre averaging process in Eq. (3.7) is applied to reduced the number of unclosed terms. The full set of governing equations with Favre(-RANS)-averaging is given

as

$$\frac{\partial \overline{\rho}}{\partial t} + \frac{\partial (\overline{\rho}\widetilde{u_i})}{\partial x_i} = \overline{\dot{S}}_{\rho,p} \tag{3.25}$$

$$\frac{\partial (\overline{\rho}\widetilde{u_i})}{\partial t} + \frac{\partial (\overline{\rho}\widetilde{u_i}\widetilde{u_j})}{\partial x_j} = -\frac{\partial \overline{p}}{\partial x_i} + \frac{\partial}{\partial x_j}\left[(\overline{\mu}+\mu_t)\left(\frac{\partial \widetilde{u_j}}{\partial x_i} + \frac{\partial \widetilde{u_i}}{\partial x_j} - \frac{2}{3}\frac{\partial \widetilde{u_m}}{\partial x_m}\delta_{ij}\right)\right] + \overline{\rho} g_i + \overline{\dot{S}}_{u,p} \tag{3.26}$$

$$\frac{\partial (\overline{\rho}\widetilde{h_s})}{\partial t} + \frac{\partial (\overline{\rho}\widetilde{h_s}\widetilde{u_j})}{\partial x_j} = \frac{\partial}{\partial x_j}\left[\left(\frac{\overline{\mu}}{\mathrm{Pr}} + \frac{\mu_t}{\mathrm{Pr}_t}\right)\frac{\partial \widetilde{h_s}}{\partial x_j}\right] + \overline{\dot{S}}_{\mathrm{rad.}} + \overline{\dot{\omega}}_{h_s} + \overline{\dot{S}}_{h_s,p} \tag{3.27}$$

$$\frac{\partial (\overline{\rho}\widetilde{Y_k})}{\partial t} + \frac{\partial (\overline{\rho}\widetilde{Y_k}\widetilde{u_j})}{\partial x_j} = \frac{\partial}{\partial x_j}\left[\left(\frac{\overline{\mu}}{\mathrm{Sc}} + \frac{\mu_t}{\mathrm{Sc}_t}\right)\frac{\partial \widetilde{Y_k}}{\partial x_j}\right] + \overline{\dot{\omega}}_k + \overline{\dot{S}}_{Y_k,p}. \tag{3.28}$$

It can be seen that the RANS equations share the same form as the LES equations, with the primary difference that $<\overline{\ }>$ and $<'>$ represent time averages in RANS, whereas they refer to filtered quantities in LES. In Eqs. (3.25) to (3.28) the unsteady terms are retained and can be used to capture low-frequency unsteady motions (URANS). However, in RANS, the turbulent viscosity μ_t needs to be modelled as well. The most common models in RANS are algebraic models (e.g. uniform-turbulent-viscosity model [131], mixing-length model [133]), one-equation models (e.g. k-model [134, 135], Spalart-Allmaras model [136]), two-equation models (e.g. k-ε model [137], k-ω model [138]) and Reynolds stress model (RSM) [139].

3.2 Solid phase modelling

This section provides a detailed discussion of the modelling approaches for the solid phase. Since the gas and solid phases are considered separate (albeit coupled) systems, it is necessary to solve a set of governing equations for mass, momentum and energy for the solid phase as well. These conservation equations are applied to each individual particle within the computational domain, and thus, increasing the particle number may significantly raise the computational cost. The governing equations for the solid phase can generally be formulated as follows

$$\frac{dm_p}{dt} = -\left(\frac{dm_{p,\mathrm{dry}}}{dt} + \frac{dm_{p,\mathrm{vol}}}{dt} + \frac{dm_{p,\mathrm{het}}}{dt}\right) \tag{3.29}$$

$$\frac{d\mathbf{u}_p}{dt} = \frac{\mathbf{u}_g - \mathbf{u}_p}{\tau_p} + \left(1.0 - \frac{\rho_g}{\rho_p}\right)\mathbf{g} \tag{3.30}$$

$$\frac{dT_p}{dt} = \frac{1}{\tau_{\mathrm{con}}}(T_g - T_p) + \frac{\varepsilon_p A_p \sigma}{m_p c_{\mathrm{p},p}}(\theta_r^4 - T_p^4) + \frac{\dot{Q}_{\mathrm{dry}}}{m_p c_{\mathrm{p},p}} + \frac{\dot{Q}_{\mathrm{vol}}}{m_p c_{\mathrm{p},p}} + \frac{\dot{Q}_{\mathrm{het}}}{m_p c_{\mathrm{p},p}} \tag{3.31}$$

with subscript $<g>$ and $<p>$ indicating gas and particle properties, respectively. Variables shown in bold correspond to vectors. The particle mass can change due to the drying process ($m_{p,\mathrm{dry}}$), release of volatile gases ($m_{p,\mathrm{vol}}$) and heterogeneous surface oxidation processes ($m_{p,\mathrm{het}}$). ε_p is the particle emissivity, $A_p = 0.25\pi d_p^2$ the particle projected area, d_p the particle

diameter, σ the Stefan-Boltzmann constant, θ_r the gas phase radiation temperature (see Sec. 3.3), $c_{\mathrm{p},p}$ the particle specific heat capacity and $\dot{Q}_{\mathrm{dry}}$, $\dot{Q}_{\mathrm{vol}}$ and $\dot{Q}_{\mathrm{het}}$ the heats of drying, devolatilisation and char conversion/heterogeneous reaction, respectively. τ_p is the particle relaxation time, which is calculated according to the Schiller-Naumann correlation [140] as

$$\tau_p = \frac{\rho_p d_p^2}{18\mu_f} \frac{1}{(1+0.15\mathrm{Re}_p^{2/3})} \qquad \text{with} \qquad \mathrm{Re}_p = \rho_g |\mathbf{u}_g - \mathbf{u}_p| \frac{d_p}{\mu_g}. \tag{3.32}$$

Here, Re_p the particle Reynolds number. Subscript $< f >$ denotes film properties and is explained in Sec. 4.4. The convective heat transfer time scale τ_{con} follows [141]

$$\tau_{\mathrm{con}} = \frac{1}{6}\frac{\mathrm{Pr}}{\mathrm{Nu}}\frac{c_{\mathrm{p},p}}{c_{\mathrm{p},f}}\frac{\rho_p d_p^2}{\mu_f} \qquad \text{with} \qquad \mathrm{Nu} = 2 + 0.552\mathrm{Re}_p^{1/2}\mathrm{Pr}^{1/3} \tag{3.33}$$

where Nu is the Nusselt number.

In CFD simulations of multiphase gas-solid systems, it is important to accurately describe the interactions between the gas and solid phase. Several coupling approaches are available, with the fully-resolved (FR) being the most detailed method that does not require explicit coupling, but it is associated with high computational demands, which limit its use to single particles or small particle groups. As an alternative, the two-way coupled Euler-Lagrange (EL) approach offers a balance between computational efficiency and accuracy for dispersed two-phase flows.

3.2.1 Modelling methods

3.2.1.1 Fully-resolved modelling (FR)

In FR simulations, all relevant gradients of the flow field including the particle boundary layers are resolved. The exchange of mass, momentum and energy between the gas phase and solid particles is realised through boundary conditions at the interface between both phases, therefore the interphase source terms in Eqs. (2.6)-(2.9) are set to zero

$$\dot{S}_{\rho,p} = \dot{S}_{u,p} = \dot{S}_{h_s,p} = \dot{S}_{Y_k,p} = 0. \tag{3.34}$$

Since the solution is entirely determined by the imposed boundary conditions, it is essential to define them accurately. The mass changed by drying, devolatilisation and char conversion or surface oxidation has been realised with a Robin boundary condition [142] as

$$\frac{dm_{p,k}}{dt} = \left(Y_{k,\mathrm{dry}}\frac{dm_{p,\mathrm{dry}}}{dt} + Y_{k,\mathrm{vol}}\frac{dm_{p,\mathrm{vol}}}{dt} + Y_{k,\mathrm{het}}\frac{dm_{p,\mathrm{het}}}{dt} \right) - \rho_{g,s} A_s D_{g,s}\frac{\partial Y_k}{\partial n}. \tag{3.35}$$

Here, the subscript $< k >$ and $< s >$ refers to the species associated with the particle process (dry, vol and het) and to the properties at particle surface, respectively. $A_s = \pi d_p^2$ is the particle surface area and $D_{g,s}$ the gas phase diffusivity at the particle surface. The heat transfer between gas and particle is described by a equal heat flux (gradient) approach

$$k_g \left.\frac{\partial T}{\partial r}\right|_{\text{gas phase}} = k_p \left.\frac{\partial T}{\partial r}\right|_{\text{solid phase}} \tag{3.36}$$

with k is the heat conductivity and r the radial coordinate. For further details on the FR simulation methodology, the reader is referred to Sec. 5.1.

3.2.1.2 Dispersed phase: Euler-Lagrange modelling (EL)

In this method, the gas phase surrounding the particles is treated as a continuum in the Eulerian framework, while the particles themselves are modelled as point-particles in the Lagrangian framework. The particle boundary layers are completely modelled in this approach. Interaction between the two phases is achieved through a two-way coupling, in which the particle obtains information from the gas phase (mass, momentum, energy and species composition), undergoes its conversion process and subsequently returns its influence (e.g. released mass or energy) to the gas phase. Due to the discretisation of the computational domain, the particle typically retrieves the gas phase information from the local Eulerian cell, in which it is located. Conversely, the influence of the particle on the gas phase is realised through source terms in the Eulerian governing equations, see Eqs. (2.6) – (2.9), applied within the same Eulerian cell. The source terms are calculated as

$$\dot{S}_{\rho,p} = -\frac{1}{\Delta^3} \sum_{p=1}^{N_p} \frac{dm_p}{dt} \tag{3.37}$$

$$\dot{S}_{u,p} = -\frac{1}{\Delta^3} \sum_{p=1}^{N_p} \frac{(dm_p \mathbf{u}_p)}{dt} \tag{3.38}$$

$$\dot{S}_{h_s,p} = -\frac{1}{\Delta^3} \sum_{p=1}^{N_p} \left[\frac{m_p c_{\mathrm{p},p}}{\tau_{\mathrm{con}}} (T_g - T_p) + \sum \left(Y_{k,\mathrm{dry}} \frac{dm_{p,\mathrm{dry}} h_{s,k,\mathrm{dry}}}{dt} \right) + \sum \left(Y_{k,\mathrm{vol}} \frac{dm_{p,\mathrm{vol}} h_{s,k,\mathrm{vol}}}{dt} \right) + \sum \left(Y_{k,\mathrm{het}} \frac{dm_{p,\mathrm{het}} h_{s,k,\mathrm{het}}}{dt} \right) \right] \tag{3.39}$$

$$\dot{S}_{Y_k,p} = -\frac{1}{\Delta^3} \sum_{p=1}^{N_p} \left(Y_{k,\mathrm{dry}} \frac{dm_{p,\mathrm{dry}}}{dt} + Y_{k,\mathrm{vol}} \frac{dm_{p,\mathrm{vol}}}{dt} + Y_{k,\mathrm{het}} \frac{dm_{p,\mathrm{het}}}{dt} \right) \tag{3.40}$$

with N_p the total number of particles in the Eulerian cell and Δ^3 the volume of the Eulerian cell.

For the EL approach to be reliable, the particle diameter must be significantly smaller than the Eulerian grid size, i.e. $d_p/\Delta \ll 1$. In practice, a minimum ratio of $\Delta/d_p \approx 5-10$ is recommended to keep the point-particle assumption valid [143, 144]. This condition is generally feasible in LES, but it may pose a fundamental issue in the context of DNS. When the EL approach is applied within the DNS context, it is commonly referred to as carrier-phase DNS (CP-DNS). In CP-DNS, the grid must be sufficiently fine to resolve all relevant turbulent scales, i.e. $\Delta \leq \eta$. At the same time, the point-particle assumption requires $d_p \ll \Delta$ to model the particle boundary layer. This leads to the following condition that defines the grid resolution of CP-DNS

$$d_p \ll \Delta < \eta. \tag{3.41}$$

This definition gives both, the lower and upper limits of the grid resolution. It ensures that turbulent structures are accurately resolved while preserving the validity of the point-particle assumption.

In some cases, the particle diameter d_p may be in a similar range as the Kolmogorov length scale η. This can be the case for pulverised biomass particles, which range from micrometres to millimetres in size. Under such conditions, Eq. (3.41) is no longer valid and can result in excessive coupling effects between the gas and solid phase, leading to unphysical results and numerical instabilities. To address this issue, coarse-graining (CG) methods have been developed. CG approaches mainly aim to mitigate localisation effects by distributing the particle source terms to multiple Eulerian cells and accounting for a fluid volume larger than the local cell.

Furthermore, in the EL approach, solid fuel particles are typically assumed to be thermally-thin, meaning that the temperature within the particle is uniform. This assumption can be related to the particle Biot number, which is defined as

$$\mathrm{Bi} = \frac{hL_p}{k_{p,\mathrm{cond}}} \qquad \text{with} \qquad L_p = \frac{\text{volume}}{\text{surface area}} = \frac{d_p}{6}. \tag{3.42}$$

Here, h is the convective heat transfer coefficient and L_p is the characteristic length of the particle, defined as the ratio of the particle volume to the particle surface area. The Biot number describes the ratio of internal thermal conduction resistance to external convective resistance at the particle surface. If $\mathrm{Bi} \leq 0.1$, the particle can be considered as thermally thin, which justifies the uniform internal temperature assumption. However, if $\mathrm{Bi} > 0.1$, a temperature gradient is present within the particle, relating it to the thermally-thick regime. Due to the relatively large particle diameters of pulverised biomass compared with coal, biomass is often classified in the thermally-thick regime, requiring the resolution of

intra-particle temperature gradients. To account for this, a thermally thick biomass particle sub-model is employed in Sec. 5.1, which solves a one-dimensional heat conduction equation within the particle. This model follows the interface-based approach, wherein the particle is discretised into multiple layers, each with its own temperature. Conversion processes are modelled to occur at the interface between two neighbouring layers. Additional details on the CG methods and thermally-thick particle modelling can be found in Sec. 5.1.

3.2.2 Volatile-containing solid fuels: Coal and Biomass

This section begins with an overview of the properties of coal and biomass, followed by the modelling of the conversion processes of volatile-containing fuels, as previously discussed in theory in Sec. 2.4.1.

3.2.2.1 Coal and Biomass properties

In this study, Rhenish lignite was selected as a representative coal, while torrefied wood was used to represent biomass. This selection aligns with experimental data used for validating the numerical setup. A brief discussion of their compositions and thermophysical properties is provided below:

Coal

The proximate, ultimate and corrected proximate (Q-factor) analysis of Rhenish lignite are given in Table. 3.1, which was given by the experiments in [145]. In the absence of an

Table 3.1: Proximate, ultimate and corrected proximate (Q-factor) analysis of coal (Rhenish lignite) in the experiment [145].

Proximate Analysis in wt. % - as received		Ultimate Analysis in wt. % - as received		Proximate Analysis after Q-factor correction in wt. % - dry	
Moisture	9.13	Carbon	58.21	Ash	5.52
Ash	5.52	Hydrogen	4.00	Volatile Matter	55.3
Volatile Matter	44.99	Nitrogen	0.83	Fixed Carbon	39.18
Fixed Carbon	40.36	Sulfur	0.37		
		Oxygen	21.94		

experimentally determined Q-factor, it has been estimated utilising the Pyrolysis Kinetics Pre-processor (PKP) [17]. PKP applies the experimentally or numerically extracted heating rates to the detailed CRECK-S-C model [146] to estimate the total volatile yield. This approach yields a Q-factor of $Q = 1.229$. The volatile composition is based on the data from [74], with the modification that the fractions of H_2S and NH_3 are added to the ash content. The assumed volatile composition is presented in Tab. 3.2. Furthermore an initial

Table 3.2: Assumed volatile composition for Rhenish lignite.

Species k	CH_4	C_2H_4	C_6H_6	CO	CO_2	H_2	H_2O
$Y_{p,k}$	0.086	0.039	0.152	0.252	0.282	0.010	0.179

coal density of $\rho_p = 1200\,\mathrm{kg/m^3}$ is assumed. The particle heat capacity is dynamically evaluated according to [147] [148] as

$$c_{\mathrm{p},p} = Y_{p,\mathrm{VM}} c_{\mathrm{p,VM}} + Y_{p,\mathrm{FC}} c_{\mathrm{p,FC}} + Y_{p,\mathrm{ash}} c_{\mathrm{p,ash}} \tag{3.43}$$

where $Y_{p,\mathrm{VM}}$, $Y_{p,\mathrm{FC}}$ and $Y_{p,\mathrm{ash}}$ are the particle mass fractions of volatile matter, fixed carbon (FC) and ash with their corresponding heat capacities $c_{\mathrm{p,VM}}$, $c_{\mathrm{p,FC}}$ and $c_{\mathrm{p,ash}}$, respectively. The heat capacities are calculated as

$$c_{\mathrm{p,VM}} = \frac{R_u}{6.83\,\frac{\mathrm{kg}}{\mathrm{kmol}}} \left[F_1\left(\frac{380}{T_p}\right) + 2F_1\left(\frac{1800}{T_p}\right) \right] \tag{3.44}$$

$$c_{\mathrm{p,FC}} = \frac{R_u}{12\,\frac{\mathrm{kg}}{\mathrm{kmol}}} \left[F_1\left(\frac{380}{T_p}\right) + 2F_1\left(\frac{1800}{T_p}\right) \right] \tag{3.45}$$

$$c_{\mathrm{p,ash}} = 539.9 + 0.596 T_p \tag{3.46}$$

with the function F_1 calculated as

$$F_1(x) = \frac{\mathrm{e}^x}{\left(\frac{\mathrm{e}^x - 1}{x}\right)^2}. \tag{3.47}$$

Biomass

The biomass used in this thesis is torrefied wood, as used in the experimental investigations

Table 3.3: Proximate and ultimate analysis of torrefied biomass based on the experiments [149, 150].

Proximate Analysis in wt. % - dry		Ultimate Analysis in wt. % - dry	
Moisture	< 0.1	Carbon	53.20
Ash	0.2	Hydrogen	6.00
Volatile Matter	81.9	Nitrogen	< 0.20
Fixed Carbon	19.9	Sulfur	< 0.02
		Oxygen	40.38

[149, 150]. The proximate and ultimate analyses are presented in Tab. 3.3. Following [107], the composition of the released light gases is assumed as shown in Tab. 3.4. Tar is represented by C_6H_8O, with thermophysical properties adopted from benzene [151]. The thermal properties of the biomass are listed in detail in Tab. 3.5.

Table 3.4: Assumed volatile composition for torrefied wood.

Species k	H_2	CO	CO_2	H_2O	CH_4
$Y_{p,k}$	0.100	0.363	0.192	0.228	0.117

Table 3.5: Thermophysical properties of torrefied wood: Initial density ρ, thermal conductivity k_{cond} and specific heat capacity c_p.

Biomass composition	Value	Ref.
Initial solid density in kg/m^3		
Wet wood	$\rho_{1,\text{init}} = 931.069$ (assume $Y_{\text{moist}} = 0.001$ with $c_{\text{p,moist}} = 1000\,\text{J/(kg K)}$)	
Dry wood	$\rho_{2,\text{init}} = 931$	[149]
Char	$\rho_{3,\text{init}} = 700$	[152]
Ash	$\rho_{4,\text{init}} = 2000$	[152]
Solid thermal conductivity in W/(m K)		
Wet wood	$k_{\text{cond},1} = \frac{\rho_2}{1000} \cdot (0.1941 + 0.4064 \cdot Y_{\text{moist}}) + 0.01864$	[153]
Dry wood	$k_{\text{cond},2} = 0.00249 + 0.000145 \cdot \rho_1 + 0.000184 \cdot (T_2 - 273.15)$	[154]
Char	$k_{\text{cond},3} = 1.47 + 0.0011 \cdot T_3$	[155]
Ash	$k_{\text{cond},4} = 1.03$	[152]
Solid specific heat capacity in J/(kg K)		
Wet wood	$c_{\text{p},1} = c_{\text{p},2} \cdot (1 - Y_{\text{moist}} \cdot 100) + 418550 \cdot Y_{\text{moist}} + \alpha$ $\alpha = 1000 \cdot (0.02355 \cdot T_1 - \frac{1.32 Y_{\text{moist}} \cdot 100}{1 - Y_{\text{moist}} \cdot 100} - 6.191) \cdot \frac{Y_{\text{moist}} \cdot 100}{1 - Y_{\text{moist}} \cdot 100}$	[153]
Dry wood	$c_{\text{p},2} = 2300 - 1150 \cdot \exp(-0.0055 \cdot (T_2 - 273.15))$	[156]
Char	$c_{\text{p},3} = 1430 + 0.355 \cdot T_3 - 7.3210 \cdot 10^7 \cdot T_3^2$	[157]
Ash	$c_{\text{p},4} = 754 + 0.586 \cdot (T_4 - 273.15)$	[152]

3.2.2.2 Drying process

As previously mentioned in Sec. 2.4.1, coal typically appears in the lower left region of the Van Krevelen diagram in Fig. 2.5, indicating its low H and O content and correspondingly high C content. This implies a low moisture content and combined with prior drying, makes it reasonable to neglect the drying process for coal. In contrast, biomass naturally contains a high initial moisture content (upper right region in the Van Krevelen diagram) and generally consists of larger particle sizes than coal. As a result, a drying model is typically employed when modelling biomass. In this work, a simplified drying model [158] is applied, which determines the drying rate based on the heat transferred to the particle as follows

$$\frac{dm_{p,\text{dry}}}{dt} = \frac{hA_s(T_g - T_p)}{\Delta H_{\text{vap}}} \cdot \frac{F(T_p)}{Y_{\text{moist}}} \qquad \text{with} \qquad F(T_p) = \frac{1}{760} \cdot 10^{\frac{8.07131 - 1730.63}{T_p - 39.724}} \tag{3.48}$$

where Y_{moist} is the mass fraction of moisture content (i.e. H_2O) within the particle, ΔH_{vap} the latent heat of water evaporation and $F(T_p)$ a function to capture mass transfer effects based on the Antoine expression for the vapour pressure of water.

3.2.2.3 Devolatilisation process

The devolatilisation process of solid fuel particles (see Sec. 2.4.1) is commonly described by a two-competing rates kinetic model [159] for coal and a two-stage parallel kinetic model [160] for biomass. During the devolatilisation process, it is assumed that the particle diameter remains constant, while the particle density varies in response to the changing particle mass as

$$\rho_p = 6\frac{m_p}{\pi d_{p,\text{const}}^3}. \tag{3.49}$$

Furthermore, a blowing correction [39,86,161] is applied to account for the effect of devolatilisation as

$$B_{\text{corr}} = \frac{\text{Pr}}{2\pi d_p \mu_g}\frac{dm_{p,\text{vol}}}{dt} \tag{3.50}$$

which modifies the particle relaxation time and Nusselt number as

$$\tau_p^* = \tau_p(1+B_{\text{corr}}) \qquad \text{and} \qquad \text{Nu}^* = \text{Nu}\cdot \text{e}^{0.6B_{\text{corr}}}. \tag{3.51}$$

Two-competing rates kinetic model

This kinetic model accounts for two reactions that compete at different temperature ranges, as shown in Fig. 3.2. It is designed to replicate the primary and secondary devolatilisation stages, as discussed in Sec. 2.4.1, with one reaction dominating at lower temperatures and the other at higher temperatures. Light volatile compounds are released at lower temperatures, while heavier volatiles are released at higher temperatures. A limitation of this model is that the total volatile content must be specified in advance and is not dynamically determined during the conversion process.

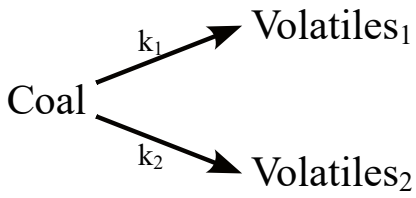

Figure 3.2: Schematic illustration of the two-competing rates kinetic model. Adapted from [159].

The instantaneous mass of released volatile gases is calculated as

$$\frac{dm_{p,\text{vol}}}{dt} = k_{\text{vol}}(m_{p,\text{VM},0} - m_{p,\text{VM}}) \tag{3.52}$$

where $m_{p,\text{VM},0}$ is the initially available volatile matter within the particle, $m_{p,\text{VM}}$ the current volatile mass and k_{vol} the devolatilisation rate. The latter is described by a two competing

rates Arrhenius-type expression as

$$k_{\mathrm{vol}} = \alpha_1 A_1 \mathrm{e}^{-\frac{E_1}{RuT_p}} + \alpha_2 A_2 \mathrm{e}^{-\frac{E_2}{RuT_p}}. \tag{3.53}$$

Here, the splitting constants are defined as $\alpha_1 = 1.5186$ and $\alpha_2 = 0.5608$, with the pre-exponential factors $A_1 = 2.5498 \cdot 10^{10}\,1/\mathrm{s}$ and $A_2 = 5.0 \cdot 10^{10}\,1/\mathrm{s}$ and the activation energies $E_1 = 1.3789 \cdot 10^8\,\mathrm{J/kmol}$ and $E_2 = 2.9627 \cdot 10^9\,\mathrm{J/kmol}$. These splitting constants and kinetic parameters were determined through a fitting procedure using PKP and the proximate and ultimate analysis data for Rhenish lignite, as listed in Tab. 3.1.

Two-stage parallel kinetic model

Unlike the two-competing rates kinetic model, the two-stage parallel kinetic model determines the release of volatile matter dynamically throughout the conversion process based on the heating rates experienced by the particle. This approach provides a more realistic representation of the physical processes involved, particularly for biomass, by accounting for the progressive degradation of the solid fuel. In the primary stage, the fuel particle decomposes into the three fractions of light gas, tar and char through three competing pathways. The tar further breaks down into light gas and char in the secondary stage. The concept of the two-stage parallel kinetic model is illustrated in Fig. 3.3.

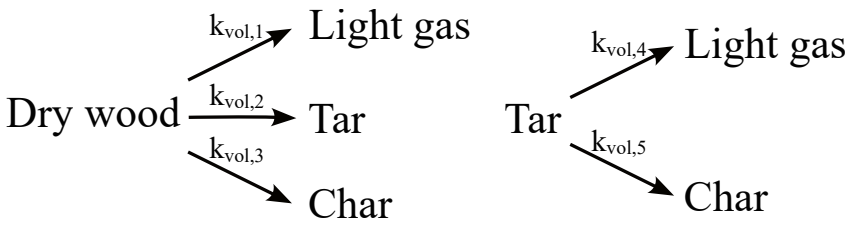

Figure 3.3: Schematic illustration of the two-stage parallel kinetic model. Adapted from [107].

Assuming that tar is a gaseous species, the total release rate of volatile matter can be expressed as

$$\frac{dm_{p,\mathrm{vol}}}{dt} = \frac{dm_{p,\mathrm{tar}}}{dt} + \frac{dm_{p,\mathrm{gas}}}{dt}. \tag{3.54}$$

The formation and consumption rates of tar and light gases are given by

$$\frac{dm_{p,\mathrm{tar}}}{dt} = k_{\mathrm{vol},2} m_p - (k_{\mathrm{vol},4} + k_{\mathrm{vol},5}) m_{p,\mathrm{tar}} \tag{3.55}$$

$$\frac{dm_{p,\mathrm{gas}}}{dt} = k_{\mathrm{vol},1} m_p + k_{\mathrm{vol},4} m_{p,\mathrm{tar}}. \tag{3.56}$$

The char formation rate is described as

$$\frac{dm_{p,\mathrm{char}}}{dt} = k_{\mathrm{vol},3} m_p + k_{\mathrm{vol},5} m_{p,\mathrm{tar}}. \tag{3.57}$$

During the devolatilisation process, the total particle mass decreases due to the release of gaseous species (i.e. light gas and tar) while char remains within or on the surface of the particle. Consequently, the overall change in particle mass is

$$\frac{dm_p}{dt} = -(k_{\mathrm{vol},1} + k_{\mathrm{vol},2} + k_{\mathrm{vol},3}) m_p + k_{\mathrm{vol},3} m_p + k_{\mathrm{vol},5} m_{p,\mathrm{tar}}. \tag{3.58}$$

3.2.2.4 Char burn-out process

After a certain amount of the volatile gases has been released, heterogeneous surface reactions, referred to as char conversion, begin to start. The remaining carbon within the particle reacts with the oxidiser, initiating surface reactions. As previously outlined in Sec. 2.4.1, char conversion can proceed under different limiting regimes: kinetically limited, pore-diffusion limited or external-diffusion limited. To capture the effects of all three regimes, an intrinsic reaction rate model is employed in this work, following the approach described in [162] and using the model variant proposed in [86]. The model assumes that char is composed entirely of carbon and only CO is formed during the char conversion process, described by the reaction

$$\mathrm{C_{(s)}} + \frac{1}{2}\mathrm{O_2} \longrightarrow \mathrm{CO}. \tag{3.59}$$

It is assumed that during the char conversion process, the particle density remains constant, whereas the particle diameter decreases due to the reduction in particle mass as

$$d_p = \left(\frac{m_p}{\rho_{p,\mathrm{const}}} \frac{6}{\pi} \right)^{1/3}. \tag{3.60}$$

The total rate of char conversion or the rate at which gaseous products are released from char (char off-gases) is expressed as

$$\frac{dm_{\mathrm{het}}}{dt} = X_{g,\mathrm{O_2}} p_g \pi d_p^2 \frac{R_{\mathrm{ox}} R_{\mathrm{char}}}{R_{\mathrm{ox}} + R_{\mathrm{char}}} \left[= A_s \rho_g R_u T_g \frac{Y_{g,\mathrm{O_2}}}{M_{\mathrm{O_2}}} \frac{R_{\mathrm{ox}} R_{\mathrm{char}}}{R_{\mathrm{ox}} + R_{\mathrm{char}}} \right] \tag{3.61}$$

with R_{ox} is the bulk molecular mass diffusion rate of oxygen, R_{char} the char reaction rate, $M_{\mathrm{O_2}}$ the molecular weight of oxygen and $X_{g,\mathrm{O_2}}$ and $Y_{g,\mathrm{O_2}}$ the molar and mass fraction of oxygen in the gas phase, respectively. The mass diffusion and reaction rate are given by

$$R_{\mathrm{ox}} = C_{\mathrm{diff}} \frac{T_m^{0.75}}{d_p} \qquad \text{and} \qquad R_{\mathrm{char}} = \eta_{\mathrm{eff}} \rho_p S_a \frac{d_p}{6} k_i. \tag{3.62}$$

Here, $C_{\text{diff}} = 5 \cdot 10^{-12}\,\text{s/K}^{0.75}$ is the mass diffusion limited rate constant and $T_m = (T_g + T_p)/2$ the mean temperature between gas phase and particle. The char reaction rate equation depends on the effectiveness factor η_{eff}, the specific internal surface area S_a and the intrinsic reactivity k_i. The effectiveness factor represents the pore diffusion resistance and is calculated as

$$\eta_{\text{eff}} = \frac{3}{\phi_T^2}(\phi_T \coth(\phi_T) - 1) \tag{3.63}$$

where the Thiele modulus ϕ_T describes the ratio of surface reaction rate to diffusion rate into the particles pores as

$$\phi_T = \frac{d_p}{2}\left(\frac{S_{\text{O}_2} S_a \rho_p k_i X_{g,\text{O}_2} p_g}{D_{\text{eff}} \rho_g Y_{\text{O}_2}}\right)^{1/2} \left[= \frac{d_p}{2}\left(\frac{S_{\text{O}_2} S_a \rho_p k_i p_{g,\text{O}_2}}{D_{\text{eff}} \rho_{g,\text{O}_2}}\right)^{1/2}\right] \tag{3.64}$$

with $S_{\text{O}_2} = 1.33$ representing the required stoichiometric mass of oxygen, D_{eff} the effective pore diffusion coefficient and p_{g,O_2} and ρ_{g,O_2} the gas partial pressure and gas density of oxygen. The effective pore diffusion coefficient is expressed by

$$D_{\text{eff}} = \frac{\theta}{\tau^2}\left(\frac{1}{D_{\text{Kn}}} + \frac{1}{D_{\text{ox}}}\right)^{-1} \tag{3.65}$$

and considers the Knudsen D_{Kn} and oxygen D_{ox} diffusion coefficients. $\theta = 0.7$ is the porosity of coal and $\tau = \sqrt{2}$ the tortuosity of the pores. The diffusion coefficients are estimated as

$$D_{\text{Kn}} = C_{\text{Kn}} \overline{r}_{\text{pore}} \sqrt{\frac{T_p}{M_{\text{O}_2}}} \qquad \text{with} \qquad \overline{r}_{\text{pore}} = 2\theta \frac{\sqrt{\tau}}{S_a \rho_p} \qquad \text{and} \qquad D_{\text{ox}} = D_0 \left(\frac{T_m}{T_0}\right)^{1.75} \tag{3.66}$$

where $C_{\text{Kn}} = 97\,\text{kg}^{0.5}\text{mK}^{-0.5}\text{kmol}^{-0.5}\text{s}^{-1}$ is a Knudsen diffusion constant, $\overline{r}_{\text{pore}}$ the mean pore radius, $D_0 = 3.13 \cdot 10^{-4}\,\text{m}^2/\text{s}$ a binary diffusion coefficient of oxygen with nitrogen and $T_0 = 1500\,\text{K}$ a reference temperature. The internal surface area S_a is calculated as a function of the char burnout b_{char} and the initial surface area $S_{a,0}$ by

$$S_a = (1 - b_{\text{char}})\sqrt{\frac{b_{\text{char}}}{\theta} + (1 - b_{\text{char}})} S_{a_0} \qquad \text{with} \qquad b_{\text{char}} = 1 - \frac{m_{p,\text{FC}}}{m_{p,\text{FC},0}} \tag{3.67}$$

and the initial surface area is given by

$$S_{a,0} = (1.5463 Y_{p,\text{FC}}^2 - 2.8349 Y_{p,\text{FC}} + 1.3017) \cdot 10^6 \tag{3.68}$$

with $Y_{p,\mathrm{FC}}$ being the fixed carbon mass fraction from the proximate analysis in Sec. 3.2.2.1. The intrinsic reactivity is obtained from

$$k_i = A_i \mathrm{e}^{-\frac{E_i}{R_u T_p}} \tag{3.69}$$

where the intrinsic pre-exponential factor is $A_i = 0.052\,\mathrm{kg/(m^2\ s\ Pa)}$ and the intrinsic activation energy is $E_i = 1.615 \cdot 10^8\,\mathrm{J/kmol}$.

3.2.3 Non-volatile containing solid fuel: Iron

This section outlines the modelling approach used for the conversion process of non-volatile solid fuels. As already outlined in Sec. 2.4.2, the conversion of non-volatile fuels differs fundamentally from that of volatile-containing fuels due to the absence of volatile matter release. In this work, the oxidation of Fe is limited to the formation of FeO. This simplification is justified as the FeO oxidation step releases the majority of heat [163] and recent iron combustion sub-models are based on the same assumption [23, 101, 164, 165], allowing for better comparability with these studies. Furthermore, the presented investigations in Secs. 5.3 and 5.4 focus on the ignition and initial oxidation behaviour, in which the FeO formation represents the primary reaction step. These established FeO sub-models effectively represent important oxidation physics (kinetically and/or diffusion-limited regimes) and have been reliably validated against experimental measurements. As a result, reactive cooling effects can be neglected since they are mainly associated with higher oxidation states. Furthermore, while peak temperatures during iron combustion can exceed the melting points of Fe and FeO, they typically remain below their respective boiling points and evaporation is therefore not considered in this study. The subsequent discussion focuses on iron oxidation, melting and solidification processes.

3.2.3.1 Oxidation process

The oxidation of iron to FeO is described by the following reaction equation

$$\mathrm{Fe} + 0.5\,\mathrm{O_2} \longrightarrow \mathrm{FeO} \tag{3.70}$$

with the total change of particle mass due to the oxidation process as

$$\frac{dm_p}{dt} = \frac{dm_{p,\mathrm{ox}}}{dt} = \frac{dm_{p,\mathrm{Fe}}}{dt} + \frac{dm_{p,\mathrm{FeO}}}{dt}. \tag{3.71}$$

The mass conversion rate of Fe and FeO is evaluated by using a first order single kinetic rate model [164–166] as

$$\frac{dm_{p,\mathrm{Fe}}}{dt} = -\frac{1}{s}\rho_f Y_{g,\mathrm{O_2}} A_d k_d \mathrm{Da}^* \tag{3.72}$$

$$\frac{dm_{p,\mathrm{Fe}}}{dt} = \frac{1+s}{s}\rho_f Y_{g,\mathrm{O_2}} A_d k_d \mathrm{Da}^* \tag{3.73}$$

with $s = 0.2865$ the stoichiometric ratio of the oxidation of iron to FeO, $A_r = A_d = \pi d_p^2$ the reactive and diffusive areas of the iron particle and Da^* the normalised Damköhler number. The latter is calculated by

$$\mathrm{Da}* = \frac{A_r k_r}{A_r k_r + A_d k_d}. \tag{3.74}$$

Here, k_r is the kinetic surface reaction rate and k_d the diffusive transfer rate. Both are given as

$$k_r = k_\infty \mathrm{e}^{-\frac{E_a}{R_u T_p}} \qquad \text{and} \qquad k_d = \mathrm{Sh}\frac{D_{f,\mathrm{O_2}}}{d_p}. \tag{3.75}$$

where $k_\infty = 75 \cdot 10^5\,\mathrm{m/s}$ is the pre-exponential factor, $E_a = 1.1973 \cdot 10^8\,\mathrm{J/kmol}$ the activation energy, $D_{f,\mathrm{O_2}}$ the film diffusion coefficient of oxygen and $\mathrm{Sh} = 2 + 0.552\mathrm{Re}_p^{1/2}\mathrm{Sc}^{1/3}$ the Sherwood number. Analogous to the blowing correction used in the devolatilisation process for volatile-containing solid fuels, a correction is also applied to account for oxygen consumption, commonly referred to as the Stefan flow effect. A Sherwood and Nusselt number correction [22, 167, 168] is applied

$$\mathrm{Sh}^* = \mathrm{Sh}\frac{\ln(1+B_M)}{B_M} \qquad \text{and} \qquad \mathrm{Nu}^* = \mathrm{Nu}\frac{\ln(1+B_T)}{B_T} \tag{3.76}$$

with the Spalding mass transfer number calculated as

$$B_M = \frac{Y_{g,\mathrm{O_2}} - Y_{p,\mathrm{O_2}}}{Y_{p,\mathrm{O_2}} - 1} \qquad \text{with} \qquad Y_{p,\mathrm{O_2}} = Y_{g,\mathrm{O_2}}\frac{A_d k_d}{A_r k_r + A_d k_d} \tag{3.77}$$

and the Spalding heat transfer number as

$$B_T = (1+B_M)^{\varphi} - 1 \qquad \text{with} \qquad \varphi = \frac{c_{\mathrm{p,O_2}}\big|_{T_p}}{c_{\mathrm{p},g}}\frac{\mathrm{Pr}}{\mathrm{Sc}} \tag{3.78}$$

with $c_{\mathrm{p,O_2}}\big|_{T_p}$ is the specific heat capacity of oxygen at particle temperature.

3.2.3.2 Melting and solidification

The melting and solidification of Fe and FeO are modelled using the apparent heat capacity method [169]. This approach implicitly captures the phase change interface by incorporating

the latent heat by modifying the heat capacity. The heat capacity is determined as follows

$$c_{\mathrm{p,eff}} = \frac{\partial h_t}{\partial T} \approx \frac{h_{t,T_p+\Delta T_2} - h_{t,T_p}}{\Delta T_2} \begin{cases} c_{\mathrm{p,solid}} & T_p < T_{m,s} \\ & T_{m,s} \le T_p < T_{m,s} + \Delta T_1 \\ c_{\mathrm{p,liquid}} & T_p \ge T_{m,s} + \Delta T_1 \end{cases} \tag{3.79}$$

with h_t the total specific enthalpy of the particle, $T_{m,s}$ the melting and solidification temperature, $\Delta T_1 = 3\,\mathrm{K}$ defines the temperature range over which the phase change occurs and $\Delta T_2 = 0.01\,\mathrm{K}$ is the temperature increment used to approximate the effective heat capacity during the transition.

3.3 Radiation modelling

The radiative enthalpy source term in Eq. (2.8) and the Eulerian gas phase radiation temperature in Eq. (3.31) can be calculated with several numerical methods. The aim of these methods is to solve the radiative transfer equation (RTE). The RTE for a grey, absorbing, emitting, anisotropically scattering continuous medium containing dispersed particles that absorb, emit and scatter radiation is defined as

$$\frac{dI(\mathbf{r},\mathbf{s})}{ds} = \underbrace{\kappa_g I_{b,g} + \kappa_p I_{b,p}}_{\text{gas + particle emission}} - \underbrace{(\kappa_g + \kappa_p + \sigma_{s,g} + \sigma_{s,p}) I(\mathbf{r},\mathbf{s})}_{\text{gas + particle absorption and scattering loss}} + \underbrace{\frac{\sigma_{s,g} + \sigma_{s,p}}{4\pi} \int_{4\pi} I(\mathbf{r},\hat{\mathbf{s}}) \beta(\mathbf{s},\hat{\mathbf{s}}) d\Omega}_{\text{gas + particle scattering addition}} \tag{3.80}$$

where $I(\mathbf{r},\mathbf{s})$ is the radiation intensity at a given location indicated by the position vector $\mathbf{r}$ in the direction $\mathbf{s}$, $I_{b,g} = \frac{\sigma T_g^4}{\pi}$ and $I_{b,p} = \frac{\sigma T_p^4}{\pi}$ the black-body intensity of gas and particle, κ the absorption/emission coefficient, σ_s the scattering coefficient, $\beta(\mathbf{s},\hat{\mathbf{s}}) = 1 + C\mathbf{s}\cdot\hat{\mathbf{s}}$ the scattering phase function from direction $\mathbf{s}$ to scattering direction $\hat{\mathbf{s}}$ with C the linear-anisotropic phase function coefficient and Ω the solid angle. The process of radiative heat transfer is illustrated in Fig. 3.4. More details about the modelling of radiation can be found in [170].

In this work, the discrete ordinate method (DOM) is used, which transforms the integral terms into a set of partial differential equations. A solution is found by solving a set of discrete directions spanning the total solid angle range of 4π. Therefore, DOM is simply a finite differencing of the directional dependence of the RTE. The integrals over the solid angle are approximated by numerical quadratures as

$$\int_{4\pi} I(\mathbf{r}) d\Omega \simeq \sum_{i=1}^{n} w_i I(\mathbf{s}_i) \tag{3.81}$$

w_i is the quadrature weight related to the directions of the angular ordinates $\mathbf{s}_i = \xi_i \mathbf{i} +$

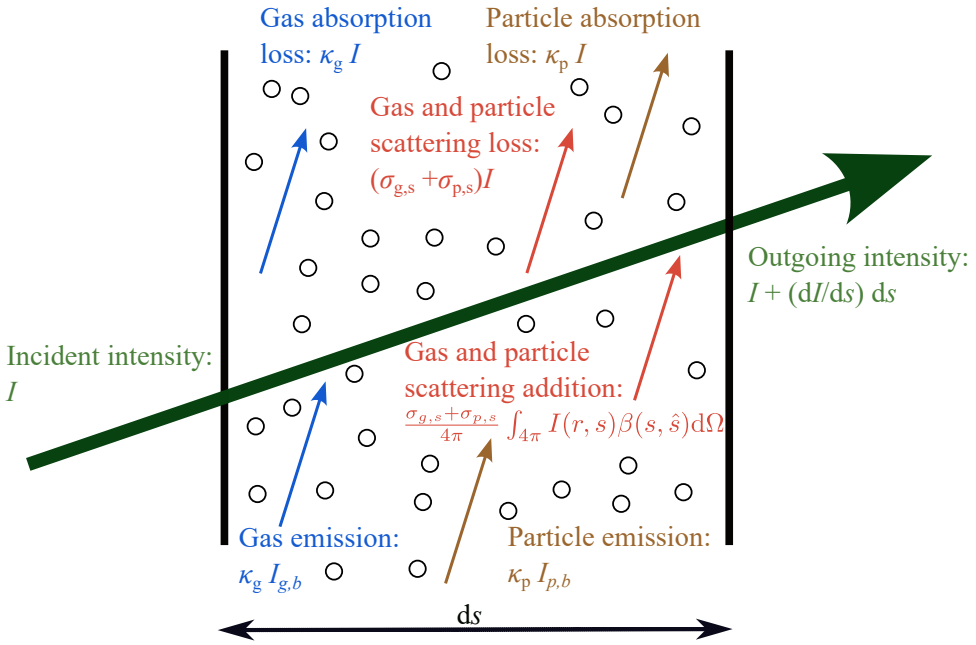

Figure 3.4: Schematic illustration of radiative heat transfer. Adapted from [171].

$\eta_i\mathbf{j}+\mu_i\mathbf{k}$ and n the total number of directions. A number of $n=80$ has been selected for this work. $\mathbf{i}$, $\mathbf{j}$ and $\mathbf{k}$ are unit vectors pointing into the x-, y- and z-directions. ξ_i, η_i and μ_i are the direction cosines. To achieve the number of sets of weights and corresponding angular ordinates, the solid angle needs to be discretised over a unit sphere. The discretised formulation of the RTE (Eq. (3.80)) is now given by a set of n equations as

$$\frac{dI(\mathbf{r},\mathbf{s})}{ds} = \underbrace{\kappa_g I_{b,g}+\kappa_p I_{b,p}}_{\text{gas + particle emission}} - \underbrace{(\kappa_g+\kappa_p+\sigma_{s,g}+\sigma_{s,p})I(\mathbf{r},\mathbf{s}_i)}_{\text{gas + particle absorption and scattering loss}} + \underbrace{\frac{\sigma_{s,g}+\sigma_{s,p}}{4\pi}\sum_{j=1}^{n} w_j I(\mathbf{r},\hat{\mathbf{s}}_j)\beta(\mathbf{s}_i,\hat{\mathbf{s}}_j)}_{\text{gas + particle scattering addition}} . \quad (3.82)$$

Once the intensities have been determined, the incident radiation can be calculated as

$$G=\int_{4\pi} I(\mathbf{r},\mathbf{s})\,d\Omega \simeq \sum_{i=1}^{n} w_i I(\mathbf{r},\mathbf{s}_i). \quad (3.83)$$

Now, the radiative source term in Eq. (2.8) can be calculated as

$$\dot{S}_{\mathrm{rad}} = \kappa_g G - 4\pi\kappa_g I_{b,g} \quad (3.84)$$

and the Eulerian gas phase radiation temperature in Eq. (3.31) as

$$\theta_r = \left(\frac{G}{4\sigma}\right)^{1/4}. \quad (3.85)$$

The individual particle emissivity ε_p needs to be defined as a constant for coal (unburnt particle e.g. $\varepsilon_{p,\text{coal}} = 0.9$) and ash (e.g. $\varepsilon_{p,\text{ash}} = 0.5$). The approach according to Stöllinger et al. [86] allows the particles to linearly vary their emissivity as a function of the char burnout b as

$$\varepsilon_p = \varepsilon_{p,\text{coal}} - (\varepsilon_{p,\text{coal}} - \varepsilon_{p,\text{ash}})b \tag{3.86}$$

with

$$b = \frac{(1 - Y_{\text{VM},0})m_{p,0} - m_p}{(1 - Y_{\text{VM},0})m_{p,0} - (1 - Y_{\text{VM},0} - Y_{\text{FC},0})m_{p,0}}. \tag{3.87}$$

The absorption/emission and scattering contribution of all N_p particles in an Eulerian cell are calculated as

$$\kappa_p = \sum_{i=1}^{N_p} \frac{1}{\Delta^3} A_{p,i}\varepsilon_{p,i}, \tag{3.88}$$

$$\sigma_{s,p} = \sum_{i=1}^{N_p} \frac{1}{\Delta^3} A_{p,i}(1 - \varepsilon_{p,i}) \tag{3.89}$$

The gas-phase absorption/emission coefficient κ_g in the equations are calculated by radiation sub-models. The most common sub-models are the constant, grey mean and weighted-sum-of-grey-gases (WSGGM). The WSGGM assumes a set of N_g grey gases, which are independent of the wave numbers. The temperature can vary, but the composition of the medium is (ideally) uniform. The total gas emissivity in the WSGGM is calculated as

$$\varepsilon_g = \sum_{i=0}^{N_g} d_i[1 - \exp(-k_i P_a L)]. \tag{3.90}$$

Here, d_i represents the temperature-dependent weighting factors for grey gas i, k_i the absorption coefficient of grey gas i, P_a the sum of partial pressures of absorbing gases, and L the path length. P_a can be expressed as $P_a = X_t P$, where $X_t = X_{\text{H}_2\text{O}} + X_{\text{CO}_2}$ is the total molar fraction of the absorbing gases. When normalising the temperature with a specific reference temperature T_{ref}, the relative error for the calculation of the WSGGM coefficients can be minimised. Therefore, the weighting factors are based on temperature-independent non-dimensional polynomial coefficients $c_{i,j}$ as

$$d_i = \sum_{j=1}^{N_c} c_{i,j} \left(\frac{T}{T_{ref}}\right)^{j-1} \quad , \quad i = 1, 2, ..., N_g. \tag{3.91}$$

Here, the subscript $< i >$ represents the index of the grey gas, whereas $< j >$ indicates the polynomial coefficients. The weighting factor coefficients $c_{i,j}$ and absorption coefficient k_i as

a function of the molar ratio MR of H_2O to CO_2 as

$$\mathrm{MR} = X_{\mathrm{H_2O}}/X_{\mathrm{CO_2}}. \tag{3.92}$$

are given by

$$c_{i,j} = C1_{i,j} + C2_{i,j}\mathrm{MR} + C3_{i,j}\mathrm{MR}^2, \tag{3.93}$$

$$k_i = CK1_i + CK2_i\mathrm{MR} + CK3_i\mathrm{MR}^2. \tag{3.94}$$

The coefficients $C1,\ldots,C3$ and $CK1,\ldots,CK3$ can be taken from [172]. The sum of the weighting factors must be one, therefore a transparent gas (indicated by $i=0$) with $k_0 = 0$ is calculated with

$$d_{i=0} = 1 - \sum_{i=1}^{N_g} d_i. \tag{3.95}$$

The total grey absorption/emission coefficient of the gas-phase for a single radiation transport equation is calculated as

$$\kappa_g = -\frac{\ln(1-\varepsilon_g)}{L}. \tag{3.96}$$

3.4 Combustion modelling

The following sections introduce two modelling approaches for solving homogeneous chemistry. First, the finite-rate chemistry approach is presented, which directly solves the homogeneous chemistry, followed by the simplified flamelet model.

3.4.1 Finite rate chemistry (FRC)

The finite rate chemistry (FRC) approach is a fundamental concept in the modelling of reacting flows, where the evolution of chemical species is governed by the local reaction rates for each species, considering the individual mixture composition, temperature and pressure. The FRC model typically solves the individual species transport equations, where the chemical source terms are evaluated using the finite rate kinetics. The overall reaction mechanism is represented as a set of elementary reactions in systems involving multiple chemical species and reactions, see Eq. (2.11). The production or consumption rates of a species are calculated as the sum of its contributions from all relevant reactions, accounting for both forward and backward reaction directions. This results in a set of coupled, non-linear ODEs. Due to the wide range of time scales in combustion systems where fast radical reactions occur alongside slower thermal decomposition steps, these ODEs are often stiff and require specific ODE solvers. This FRC modelling approach allows for the simulation of important non-equilibrium effects such as ignition delays, extinction, and pollutant formation, which are

not captured by equilibrium-based approaches. Therefore, FRC provides a more realistic and detailed representation of a reactive system. However, this approach can be very computationally expensive if hundreds of chemical species and thousands of chemical reactions are involved. In multiphase reactive DNS, the finite-rate chemistry approach is typically employed. However, the combination with the required high resolution makes it extremely computationally expensive and often impractical.

3.4.2 Flamelet/progress-variable (FPV)

The flamelet model is based on the fundamental assumption that chemical reactions and the turbulent flow field can be treated separately. This is often justified by the fact that chemical reactions are much faster than turbulent mixing times. As a result, a turbulent flame can be considered a collection of multiple small, laminar flamelets, as illustrated schematically in Fig. 3.5.

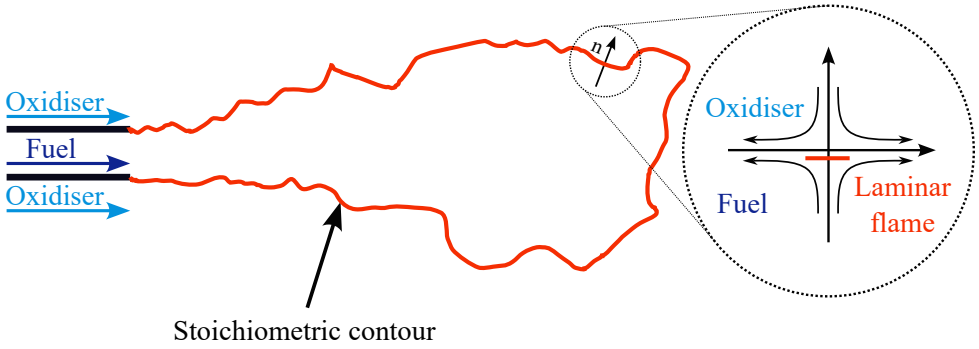

Figure 3.5: Schematic illustration of the fundamental assumption of the flamelet approach. Adapted from [112].

This separation allows the chemical processes to be calculated independently from the fluid dynamics. These laminar flamelets can be precomputed and stored in a table. Each thermochemical state within this flamelet table can be accessed via specific parameters. Commonly tabulated quantities include temperature and species mass fractions. During the actual numerical simulation, only the access parameters need to be solved. The corresponding values (e.g. species mass fractions and temperatures) are then retrieved from the flamelet table and can be used in the simulation. The advantage over the FRC approach lies in the reduced number of transport equations that need to be solved. Instead of solving for each individual chemical species, only a few transport quantities are needed, making the method computationally efficient even for larger and complex chemical mechanisms. Typical access parameters include the mean mixture fraction Z (characterises the mean composition of the mixture), the normalised progress variable C_{norm} (indicates the degree of chemical reaction) and the mixture fraction variance Z''^2 (captures the mixture fraction fluctuations). Z

and Z''^2 are statistical values of turbulence and therefore describe the effects of turbulence-chemistry interactions. The described approach is suitable for single-phase reactive systems with one fuel stream and one oxidiser stream. However, in configurations involving multiple fuel streams, such as volatile-containing solid fuels or additional fuel streams, modifications are necessary to accurately represent the flame dynamics. An example of such a system is shown in Fig. 3.6.

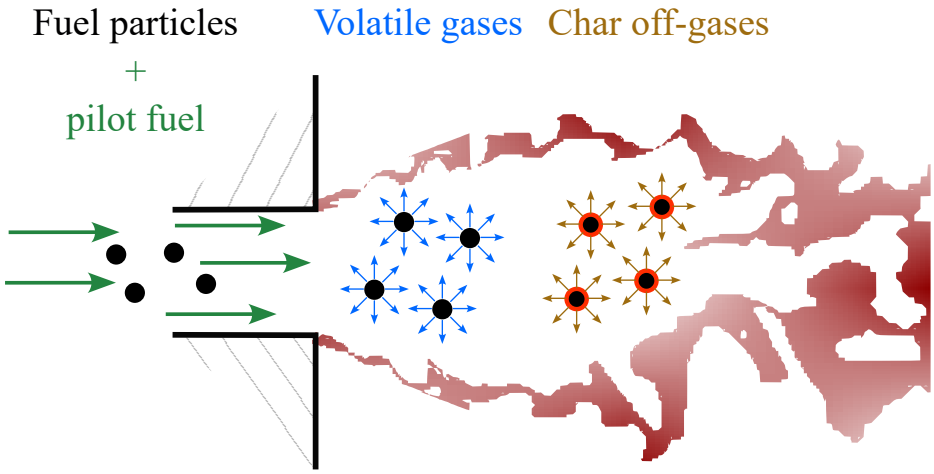

Figure 3.6: Configuration involving multiple fuel streams (volatile-containing particles + pilot fuel).

The various fuel streams include the pilot fuel, volatile gas release and char off-gas release. To address this issue, the literature [62, 74] recommends to introduce individual mixture fractions for each fuel stream, namely Z_{pil} for the pilot fuel, Z_{vol} for the volatile gases and Z_{cog} for the char off-gases. Additionally, the presence of multiple phases (i.e. gas and solid) requires consideration of heat exchange between the phases to account for differences in enthalpy level of the flamelet table. As a result, an additional transport equation for total enthalpy has to be included.

Flamelet generation

The flamelet tables used in this work are generated with *pyFLUT*, developed by STFS at TU Darmstadt which is coupled with *Cantera* [173], an open-source tool designed to solve problems related to chemical kinetics, thermodynamics and transport processes. *Cantera* is used to solve the one-dimensional governing equations for counterflow diffusion flames, including continuity, radial momentum, energy and species conservation. The 1D flamelet calculations do not account for radiation, which is, however, included in the CFD simulations. The application of one-dimensional flamelets in systems with multiple fuel streams is valid under the assumption that interactions between these streams are weak and therefore negligible. In this setup, the mixture fractions Z_{pil}, Z_{vol}, and Z_{cog} represent the contributions of the

pilot fuel, volatile gases and char off-gases, respectively. To efficiently tabulate the flamelet data in the presence of multiple fuel streams, the transformation method proposed by [174] is extended to three mixture fractions, following the approach of [70]. This transformation gives

$$Z = Z_{\mathrm{pil}} + Z_{\mathrm{vol}} + Z_{\mathrm{cog}} \tag{3.97}$$

with the following transport equations

$$\frac{\partial(\rho Z_{\mathrm{pil}})}{\partial t} + \frac{\partial(\rho Z_{\mathrm{pil}} u_j)}{\partial x_j} = \frac{\partial}{\partial x_j}\left(\frac{\mu}{\mathrm{Sc}}\frac{\partial Z_{\mathrm{pil}}}{\partial x_j}\right) \tag{3.98}$$

$$\frac{\partial(\rho Z_{\mathrm{vol}})}{\partial t} + \frac{\partial(\rho Z_{\mathrm{vol}} u_j)}{\partial x_j} = \frac{\partial}{\partial x_j}\left(\frac{\mu}{\mathrm{Sc}}\frac{\partial Z_{\mathrm{vol}}}{\partial x_j}\right) + \dot{S}_{Z_{\mathrm{vol}}} \quad \text{with} \quad \dot{S}_{Z_{\mathrm{vol}}} = -\frac{1}{\Delta^3}\sum_{p=1}^{N_p}\frac{dm_{p,\mathrm{vol}}}{dt} \tag{3.99}$$

$$\frac{\partial(\rho Z_{\mathrm{cog}})}{\partial t} + \frac{\partial(\rho Z_{\mathrm{cog}} u_j)}{\partial x_j} = \frac{\partial}{\partial x_j}\left(\frac{\mu}{\mathrm{Sc}}\frac{\partial Z_{\mathrm{cog}}}{\partial x_j}\right) + \dot{S}_{Z_{\mathrm{cog}}} \quad \text{with} \quad \dot{S}_{Z_{\mathrm{cog}}} = -\frac{1}{\Delta^3}\sum_{p=1}^{N_p}\frac{dm_{p,\mathrm{het}}}{dt} \tag{3.100}$$

and the two ratios

$$A = \frac{Z_{\mathrm{cog}}}{Z_{\mathrm{vol}} + Z_{\mathrm{cog}} + \epsilon} \quad \text{and} \quad B = \frac{Z_{\mathrm{vol}} + Z_{\mathrm{cog}}}{Z_{\mathrm{vol}} + Z_{\mathrm{cog}} + Z_{\mathrm{pil}} + \epsilon} \tag{3.101}$$

where ϵ is a small positive value to prevent division by zero. These transformed variables provide flexibility in representing different fuel combinations. Limiting cases for A, B, and Z are summarised in Table 3.6. To account for heat exchange between the solid and gas

Table 3.6: Limiting values of multiple fuel stream combination in the flamelet tabulation

Values	Fuel stream
$A = 0$	no char conversion
$A = 1$	no devolatilisation
$B = 0$	no devolatilisation and no char conversion
$B = 1$	no pilot stream
$Z = 0$	no fuel stream
$Z > 0$	fuel stream available

phases, flamelets at various total enthalpy levels must be generated. These levels are defined by using a normalised enthalpy

$$H_{\mathrm{norm}} = \frac{H_t(A,B,Z) - H_t(A,B,Z)^{\min}}{H_t(A,B,Z)^{\max} - H_t(A,B,Z)^{\min}}. \tag{3.102}$$

Similarly, the normalised progress variable is defined as

$$C_{\mathrm{norm}} = \frac{Y_c(A,B,Z) - Y_c(A,B,Z)^{\min}}{Y_c(A,B,Z)^{\max} - Y_c(A,B,Z)^{\min}}. \tag{3.103}$$

where Y_c is the progress variable. The definition of the progress variable, along with the corresponding reaction mechanism, is provided in Sec. 5.2. The one-dimensional governing equations are solved in physical space assuming a unity Lewis number and are subsequently mapped onto the A-B-Z-H_{norm}-C_{norm} space. Furthermore, a β-PDF integration is performed over the mixture fraction space to consider the turbulence-chemistry interaction. The final parameterisation of the flamelet table in the LES context is

$$\Phi = \Im(A, B, \widetilde{Z}, \widetilde{Z''^2}, \widetilde{H}_{norm}, \widetilde{C}_{norm}). \tag{3.104}$$

This results in a six-dimensional flamelet table with dimensions $6 \times 6 \times 101 \times 11 \times 11 \times 101$.

3.4.3 Combustion modelling for non-volatile solid fuels

The studies of non-volatile solid fuels in this thesis consider pure air as the gas phase and iron as the solid phase. As discussed in Sec. 2.4.2, iron primarily undergoes heterogeneous reactions. Since particle surface evaporation is neglected, there is no need to account for homogeneous gas phase chemistry, as outlined in Secs. 5.3 and 5.4.

4 Numerical methods in OpenFOAM

The theoretical background for reacting multiphase flow systems has been outlined in Chapter 2, and the corresponding modelling approaches have been described in Chapter 3. Due to the complexity, non-linearity and coupling of the governing equations and the corresponding sub-models, analytical solutions are not feasible, and an iterative numerical approach is required instead. This chapter describes the numerical methods employed to solve the equations introduced earlier and explains how they are implemented within the OpenFOAM framework. The chapter begins with a brief overview of OpenFOAM, followed by an introduction to the FVM, which is the basis of OpenFOAM. Subsequently, the solution algorithm used within OpenFOAM to manage reacting multiphase flows involving solid fuel particles is presented. Finally, the numerical treatment of Lagrangian point particles is briefly discussed.

4.1 OpenFOAM

OpenFOAM, which stands for Open source Field Operation And Manipulation, is a versatile toolbox written in the object-orientated programming language C++ and is developed for a broad range of CFD applications. OpenFOAM employs the FVM to solve particle differential equations on unstructured meshes composed of polyhedral cells. OpenFOAM offers a robust code framework that allows researchers to develop customised solvers by extending and integrating components based on the existing OpenFOAM suite.

The initial development of OpenFOAM began at Imperial College London in the late 1990s [175,176]. Since then, it has gained widespread adoption in both academia and industry due to the open-source possibilities. This broad user base has contributed significantly to developing and improving advanced numerical algorithms and libraries. Nowadays, OpenFOAM is released under the GNU General Public License and is maintained by the three independent operating organisations of OpenCFD Ltd. (*.com), CFD Direct Ltd. (*.org) and Wikki Ltd (foam-extend).

For the work presented in this thesis, the cases involving coal and iron were conducted using the OpenFOAM version by OpenCFD Ltd., a subsidiary of Keysight Technologies - ESI Group. The results related to biomass were obtained by the version of CFD Direct Ltd.

4.2 Finite volume method

The partial differential equations outlined in Sec. 2.1 cannot be solved directly by a computing system. Hence, numerical methods are required to convert these equations into discrete algebraic forms over finite volumes, where each volume corresponds to a computational cell. These algebraic equations can then be efficiently solved using numerical algorithms. Common discretisation techniques include the FDM, FEM and FVM. Among these, FVM has become widely adopted in CFD. An overview of the FVM solution procedure is provided in Tab. 4.1. To clarify the FVM, a one-dimensional general transport equation with a source

Table 4.1: Overview of the solution procedure in the FVM.

Step	Description
I	Discretise the geometric domain into non-overlapping control volumes
II	Transform partial differential equations into linear algebraic equations by integrating over each discrete control volume
III	Solve the system of algebraic equations to obtain values for each control volume

term for an arbitrary scalar variable ϕ is discretised below. The discretisation procedure follows the approach described in [115, 177] and starts with

$$\frac{\partial(\rho\phi)}{\partial t} + \frac{\partial(\rho\phi u_j)}{\partial x_j} = \frac{\partial}{\partial x_j}\left(\Gamma_\phi \frac{\partial \phi}{\partial x_j}\right) + \dot{S}_\phi \tag{4.1}$$

where Γ_ϕ is a diffusion coefficient. First, the domain is divided into discrete control volumes. In a one-dimensional grid system, specific nodal points are defined. The central node is labelled as $< C >$, with its nearest neighbours to the west and east denoted as $< W >$ and $< E >$, respectively. Nodes located further away are referred to as $< WW >$ and $< EE >$. The cell faces on the west and east sides of node C are labelled as $< w >$ and $< e >$. The distances between nodes W and C and between C and E are denoted as δx_w and δx_e, respectively. Figure 4.1, illustrates the grid layout and naming convention of the one-dimensional system.

Convection and diffusion term [115]

For a pure convection-diffusion problem without a source term, the discretisation of Eq. (4.1) starts with an integration over a one-dimensional control volume V_c, resulting in

$$\int_{V_c} \frac{\partial(\rho\phi u_j)}{\partial x_j} dV = \int_{V_c} \frac{\partial}{\partial x_j}\left(\Gamma_\phi \frac{\partial \phi}{\partial x_j}\right) dV. \tag{4.2}$$

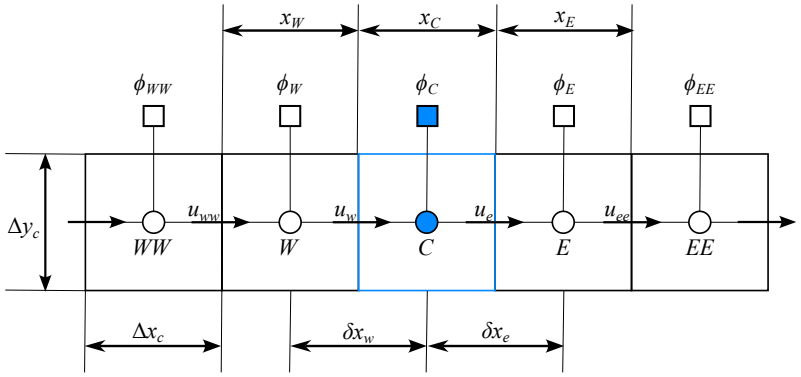

Figure 4.1: Illustration of a grid layout and notation used in a one-dimensional system. Adapted from [177].

The volume integrals are then converted into surface integrals using the divergence theorem, yielding

$$\int_A \mathbf{n} \cdot (\rho \phi u_j) dA = \int_A \mathbf{n} \left(\Gamma_\phi \frac{\partial \phi}{\partial x_j} \right) dA \tag{4.3}$$

where $\mathbf{n}$ is the outward-pointing unit normal vector to surface A. Subsequently, the surface integrals are replaced by a summation of the fluxes over the faces of the control volume

$$\sum_A \mathbf{n} \cdot (\rho \phi u_j) A_i = \sum_A \mathbf{n} \left(\Gamma_\phi \frac{\partial \phi}{\partial x_j} \right) A_i. \tag{4.4}$$

Considering the orientation of the surface vectors and assuming constant cross-sectional area across all control volumes, the equation simplifies to

$$(\rho \phi u_j)_e - (\rho \phi u_j)_w = \left(\Gamma_\phi \frac{\partial \phi}{\partial x_j} \right)_e - \left(\Gamma_\phi \frac{\partial \phi}{\partial x_j} \right)_w. \tag{4.5}$$

By defining the convective mass flux per unit area as $F = \rho u$, the diffusion conductance as $D = \Gamma / \delta x$ and applying a central differencing scheme for the linear approximation of $\partial \phi / \partial x$

$$\left(\Gamma_\phi \frac{\partial \phi}{\partial x_j} \right)_e = \Gamma_e \left(\frac{\phi_E - \phi_C}{\delta x_e} \right) \qquad \text{and} \qquad \left(\Gamma_\phi \frac{\partial \phi}{\partial x_j} \right)_w = \Gamma_w \left(\frac{\phi_C - \phi_W}{\delta x_w} \right) \tag{4.6}$$

the Eq. (4.5) leads to the following form

$$F_e \phi_e - F_w \phi_w = D_e (\phi_E - \phi_C) - D_w (\phi_C - \phi_W). \tag{4.7}$$

Similar to the diffusion term, a linear approximation can be applied for the cell face values as

$$\phi_e = \phi_C \frac{\phi_E - \phi_C}{(x_E - x_C)} \left(\frac{\delta x_e}{2} - x_C \right) \qquad \text{and} \qquad \phi_w = \phi_W \frac{\phi_C - \phi_W}{(x_C - x_W)} \left(x_C - \frac{\delta x_w}{2} \right). \tag{4.8}$$

However, for bounded scalar quantities (e.g. Y_k - between 0 and 1), linear interpolation may produce under- and/or overshoots, resulting in unphysical results and numerical instabilities. To prevent such issues, total variation diminishing (TVD) schemes are commonly employed, as they ensure an oscillation-free solution and keep the scalar within its physical bounds. For further details on TVD schemes, the reader is referred to [115, 177]. The discretisation procedure has to be applied for each control volume, which results in a system of algebraic equations. This system can then be solved by using a matrix solver to determine the distribution of the transported variable ϕ in the context of convection and diffusion.

Transient term [177]

To examine the time discretisation, Eq. (4.1) is simplified for clarity as

$$\frac{\partial(\rho\phi)}{\partial t} + F(\phi) = 0 \tag{4.9}$$

where $F(\phi)$ represents the collection of all non-transient terms. In the FVM, in order to evaluate the value at node C, all terms in the equation have to be integrated over the corresponding control volume as

$$\int_{V_c} \frac{\partial(\rho\phi)}{\partial t} dV + \int_{V_c} F(\phi) dV = 0. \tag{4.10}$$

Following the spatial discretisation step, the equation becomes

$$\frac{\partial(\rho_C \phi_C)}{\partial t} V_C + F(\phi_C^t) = 0. \tag{4.11}$$

where superscript $< t >$ indicates the term at a reference time. For temporal discretisation, the equation has to be integrated over a given time interval Δt

$$\int_{t-\Delta t/2}^{t+\Delta t/2} \frac{\partial(\rho_C \phi_C)}{\partial t} V_C dt + \int_{t-\Delta t/2}^{t+\Delta t/2} F(\phi_C^t) dt = 0. \tag{4.12}$$

By evaluating the integral, assuming that V_C remains constant and rearranging the terms, the expression yields

$$\frac{(\rho_C \phi_C)^{t+\Delta t/2} - (\rho_C \phi_C)^{t-\Delta t/2}}{\Delta t} V_C + F(\phi_C^t) = 0. \tag{4.13}$$

Common approaches for approximating the terms $(\rho_C \phi_C)^{t+\Delta t/2}$ and $(\rho_C \phi_C)^{t-\Delta t/2}$ are the implicit Euler method

$$(\rho_C \phi_C)^{t+\Delta t/2} = (\rho_C \phi_C)^t \qquad \text{and} \qquad (\rho_C \phi_C)^{t-\Delta t/2} = (\rho_C \phi_C)^{t-\Delta t} \tag{4.14}$$

and the explicit Euler method

$$(\rho_C \phi_C)^{t+\Delta t/2} = (\rho_C \phi_C)^{t+\Delta t} \qquad \text{and} \qquad (\rho_C \phi_C)^{t-\Delta t/2} = (\rho_C \phi_C)^{t}. \tag{4.15}$$

Source term [177]

The discretisation of the source term in Eq. (4.1) results in

$$\int_{V_c} S_\phi dV = \bar{S}_{\phi,C} V_C. \tag{4.16}$$

In this expression, $\bar{S}_{\phi,C}$ is the average value of the source term S_ϕ across the control volume V_C.

4.3 Solution algorithm in OpenFOAM

All the simulations in this thesis are performed with a transient low-Mach reactive multiphase solver based on OpenFOAM. The low-Mach approach assumes that the density can vary with temperature variations but remains independent of pressure. This assumption is valid when the flow within the computational domain is expected to be at low speeds (Ma $\ll$ 0.3), meaning pressure fluctuations are small and pressure can be considered approximately constant in the equation of state. As a result, density variations are attributed only to changes in temperature.

The transient solver used in OpenFOAM employs the PIMPLE pressure-velocity solution algorithm, which combines the SIMPLE (semi-implicit method for pressure-linked equations) and PISO (pressure implicit with splitting of operators) algorithm approaches. A detailed description of these algorithms can be found in [115]. The concept of the PIMPLE algorithm is to obtain a converged steady-state solution at each time step by performing iterative corrections using an inner loop (PISO) and an outer loop (SIMPLE) method.

The integrated solver, which combines the low-Mach assumption and the PIMPLE algorithm alongside Lagrangian solid fuel particle modelling, is described in Fig. 4.2.

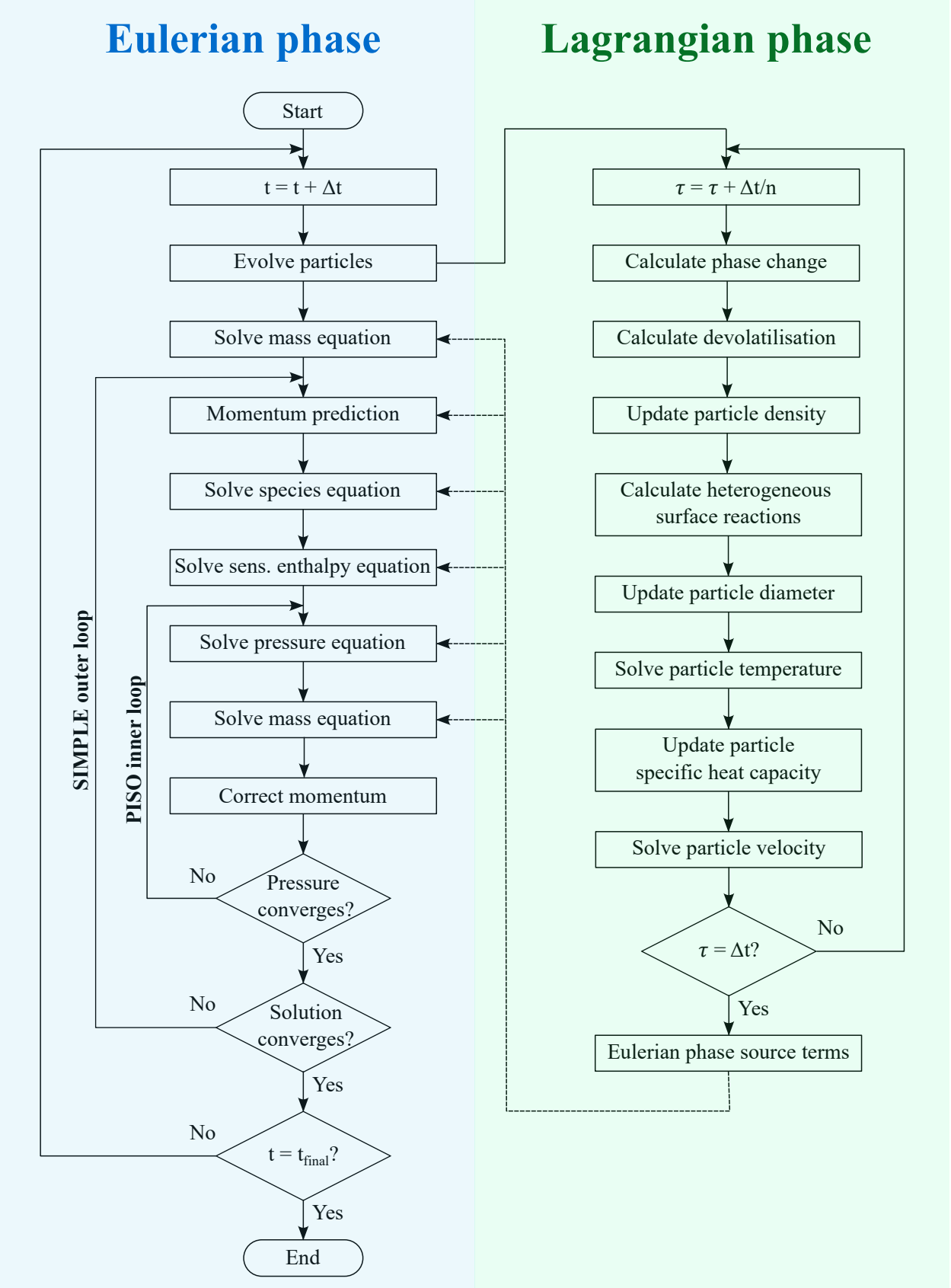

Figure 4.2: Flow chart of the low-Mach assumption and PIMPLE algorithm with Lagrangian solid fuel particle modelling in OpenFOAM.

4.4 Treatment of Lagrangian point-particles

Due to the assumption of Lagrangian point-particles, a specific treatment is required for their numerical handling. This includes retrieving reference data from the surrounding gas phase, estimating the properties of the gas film around the particles and implementing a numerical scheme to calculate the particle velocity and position, as well as their temperature.

Interpolation of reference data from the surrounding gas phase

The Lagrangian point-particles require information from the surrounding gas phase, such as temperature, velocity and density, to undergo conversion processes like devolatilisation and/or heterogeneous surface reactions. Typically, two common assumptions are made for retrieving this data, which are referred to as *cell* and *cellPoint* interpolation schemes (OpenFOAM interpolation routines).

- ***cell* interpolation scheme**
  In the *cell* interpolation scheme, the Lagrangian point-particle retrieves the necessary information from the cell in which it is located, assuming that the value at the cell centre is uniformly representative of the entire cell volume.

- ***cellPoint* interpolation scheme**
  The *cellPoint* interpolation scheme accounts for the point-particle position within a cell by applying an inverse distance-weighted interpolation. To begin with, the polyhedral cell in which the particle resides is subdivided into several tetrahedra. Each tetrahedron is constructed using the cell centre as one vertex, while the remaining three vertices correspond to the corresponding cell corners. The specific tetrahedron containing the particle is then identified. Then, the inverse distance between the particle position x_p and the vertices of the enclosing tetrahedron P_i are computed as

$$d_i = \frac{1}{|x_p - P_i|} \qquad \text{and} \qquad d_{\text{sum}} = \sum_{i=1}^{4} d_i \tag{4.17}$$

  with d_i being the inverse distance from the particle to each tetrahedral vertex. These distances are then used to calculate weight factors as

$$w_i = \frac{d_i}{d_{\text{sum}}}. \tag{4.18}$$

  The interpolated value of an arbitrary quantity ϕ at the particle location is then calculated as

$$\phi_{\text{ref}} = \sum_{i=1}^{4} w_i \phi_i \tag{4.19}$$

where ϕ_i represents the value of ϕ at the corresponding tetrahedral vertices. The *cellPoint* interpolation scheme is typically applied for the velocity field, where a continuous field is important. It is beneficial near boundaries, e.g. walls, where particles may interact with the wall with a high frequency.

Gas phase film properties

Due to the point-particle assumption, the particles lack a physical surface where gas phase properties (film properties) can be directly evaluated. Therefore, these film properties have to be approximated. A common approach is to estimate the film temperature T_f using a linear combination of the particle temperature T_p and the surrounding gas temperature T_g as given by the following equation

$$T_f = T_p + A_f(T_g - T_p). \tag{4.20}$$

where A_f is a weighting coefficient. A widely applied method is the one-third rule ($A_f = 1/3$), which is also used in this work. Once the film temperature has been determined, the remaining gas film properties can be calculated.

Calculation of particle velocity and temperature

The particle velocity and temperature are calculated using Eqs. (3.30) and (3.31), respectively. Both are first-order ODEs in time and can be expressed in the general form for an arbitrary quantity ϕ as

$$\frac{d\phi}{dt} = C_A - C_B \cdot \phi \tag{4.21}$$

with integration constants C_A and C_B. For the particle velocity ($\phi = \mathbf{u}_p$), the integration constants are

$$C_B = \frac{1}{\tau_p} \qquad \text{and} \qquad C_A = C_B \cdot \mathbf{u}_g + \left(1.0 - \frac{\rho_g}{\rho_p}\right)\mathbf{g} \tag{4.22}$$

and for the particle temperature ($\phi = T_p$)

$$C_B = \frac{1}{\tau_{\text{con}}} \qquad \text{and} \qquad C_A = C_B \cdot T_g + \frac{\varepsilon_p A_p \sigma}{m_p c_{\text{p},p}}(\theta_r^4 - T_p^4) + \frac{\dot{Q}_{\text{dry}}}{m_p c_{\text{p},p}} + \frac{\dot{Q}_{\text{vol}}}{m_p c_{\text{p},p}} + \frac{\dot{Q}_{\text{cog/ox}}}{m_p c_{\text{p},p}}. \tag{4.23}$$

This type of ODE can be solved either analytically or using numerical schemes such as the implicit Euler method:

- **Analytical method**
  The analytical solution to Eq. (4.21) is

$$\phi = \frac{C_1 \mathrm{e}^{-C_B \cdot (t + C_2)} - C_A}{-C_B} \tag{4.24}$$

with assuming the integration constants as $C_1 = C_2 = 1$. Approximating the change of $\Delta\phi$ over time step Δt is given by

$$\Delta\phi = \phi^{t+\Delta t} - \phi^t = (C_A - C_B \cdot \phi^t)\frac{1 - \mathrm{e}^{-C_B \cdot \Delta t}}{C_B} \tag{4.25}$$

- **Implicit Euler method**
  Using the implicit Euler integration scheme, Eq. (4.21) becomes

$$\frac{\phi^{t+\Delta t} - \phi^t}{\Delta t} = C_A - C_B \cdot \phi^{t+\Delta t}. \tag{4.26}$$

  Solving the change over the time step yields

$$\Delta\phi = \phi^{t+\Delta t} - \phi^t = (C_A - C_B \cdot \phi^t)\frac{\Delta t}{1 + C_B \cdot \Delta t}. \tag{4.27}$$

Both approaches can be used to compute the particle velocity and temperature, with the choice only based on the stability of the numerical solution. The studies in Chapter 5 apply the analytical method for particle temperature and the implicit Euler method for particle velocity.

The previous Chapters and Sections have provided the necessary background for understanding the solid fuel particle conversion processes. The following Chapter will build on this knowledge and apply the introduced concepts.

5 Analysis of solid fuel particle conversion

The theoretical background on multiphase reactive flows with solid fuels has been presented in Chapter 2, followed by the modelling details in Chapter 3 and its integration into the numerical framework of OpenFOAM in Chapter 4. With this background the required modelling tools are now available and can be applied to study the complex flow-chemistry-particle interaction problems between solid fuel particles and a surrounding oxidising gas atmosphere. Sections 2.4 and 3.2 have outlined the different classifications of solid particles and the physical processes that they can undergo. On the basis of this classification, a set of modelling approaches has been employed to address the research objectives stated at the beginning of this thesis, repeated here for completeness:

1. Determining the applicability range of Euler-Lagrange approaches for volatile-containing solid fuel particles in laminar flow.

2. Accurate LES modelling of the complex turbulence-chemistry-particle interaction phenomena occurring in the combustion of volatile-containing solid fuels.

3. Extending the modelling framework to study the ignition and combustion of innovative non-volatile solid fuels (metals) in the CP-DNS context.

These research objectives are addressed by four peer-reviewed research papers associated with this thesis as outlined below. The Euler-Lagrange approach is a robust and widely used method for numerical modelling of multiphase flows with dispersed particles. The fundamental assumption of the Euler-Lagrange method is that the particles are treated as point masses, which should be much smaller than the numerical grid size. The first objective of this work is addressed in the first paper, *Luu et al., Fuel 368:31600, 2024* [178], where the range of applicability of the standard Euler-Lagrange approach is investigated for a renewable solid fuel e.g. biomass. The study quantifies the validity of the standard Euler-Lagrange approach and explores coarse-graining methods by comparing single particle Euler-Lagrange data to corresponding simulations that fully resolve the particle boundary layer in a hot, quiescent, and inert gas environment. After taking into account the scope of validity of the standard Euler-Lagrange approach, a significantly more complex case with turbulence-chemistry-particle interactions is studied in *Luu et al., Proc. Combust. Inst. 39:3249-3258, 2023* [179] to fulfil the second objective. This second paper examines a laboratory-scale

gas-assisted turbulent swirling coal flame. The turbulence-chemistry-particle interactions are captured with a multiphase flamelet/progress variable approach in the context of LES. A pre-calculated six-dimensional flamelet table stores a wide range of chemical states and the values are retrieved during the simulation. The good qualitative and quantitative agreement between simulation results and experimental datasets confirms the accuracy of the modelling approach. Additionally, the work provides valuable insight into the contributions of various fuel streams and identifies the dominant regions where they occur within the burner. The third paper, *Luu et al., Flow Turb. Combust. 112:1083-1103, 2024* [180], extends the Euler-Lagrange approach for volatile-containing solid fuels to the oxidation of non-volatile iron particles and provides a first-of-its-kind study of monodisperse iron particle cloud ignition and combustion in shear-driven turbulence. The studies were carried out in the context of CP-DNS. While it resolves all turbulence and flame scales, it uses sub-models for momentum, heat, and mass transfer across the boundary layers between the bulk gas phase and the Lagrangian point particles. The study provides an initial understanding of the interaction between turbulence and the combustion of iron particle clouds. Particle behaviour throughout the entire process is observed, revealing several phenomena that differ from the general trends seen with volatile-containing solid fuels. The characterisation of the differences between the ignition and combustion of monodisperse and polydisperse iron particle clouds is presented in the fourth paper, *Luu et al., Proc. Combust. Inst. 40:105297, 2024* [181]. Here, a realistic experimental particle size distribution (PSD) is applied based on the monodisperse case from [180]. To gain a better understanding of the ignition behaviour for typical particle sizes, the particle ensemble in the PSD case is divided into several particle size classes. Further investigations indicate that the particle size has a crucial effect on the mixing process and ignition time.

The remainder of this chapter is structured chronologically such that the first publication addresses the first research objective, the second publication addresses the second objective and the third and fourth publications the third objective. Each publication is introduced with a brief summary.

5.1 Single particle conversion of woody biomass using fully-resolved and Euler–Lagrange coarse-graining approaches

Research highlights

The primary target of the first paper, *Luu et al., Fuel 368:31600, 2024* [178], is to address the first research objective. For this purpose, pulverised woody biomass was selected as the solid particle type, as it has a typical diameter in the micrometre to millimetre range after pulverisation and therefore might violate the fundamental point-particle assumption of the Euler-Lagrange (EL) method. A thermally thick layer-based sub-model proposed by Thunman et al. [151] and Ström et al. [158] has been integrated into a fully-resolved (FR) and EL simulation framework to model woody biomass conversion. The particles are divided into four layers, where the physical processes of drying, devolatilisation and char conversion occur. The FR simulation approach [19, 20, 24, 26] resolves the mass and heat transfer across the particle boundary layer, including all relevant gradients on the numerical grid. The FR approach is validated against experimental mass loss measurements at different temperatures from a drop tube reactor in an inert gas atmosphere conducted by Tolvanen et al. [149, 150]. The comparison is shown in Fig. 5.1 (left), where the temporal evolution and the final mass release from the FR simulation show a good agreement with the experimental data. The FR and EL simulation approaches are fundamentally different.

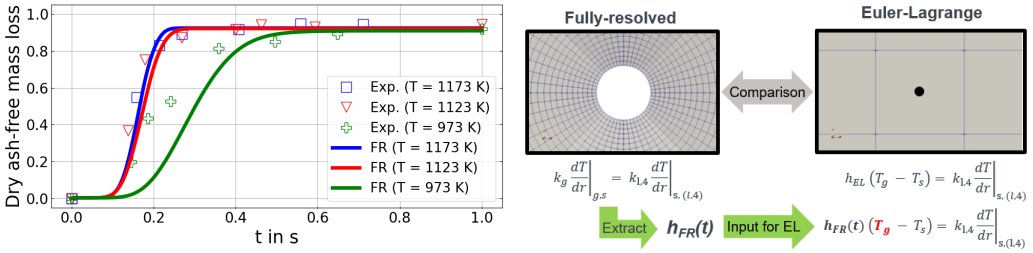

Figure 5.1: Left: Comparison of the dry/ash-free mass loss vs. time t from biomass particles at different temperatures between FR simulations (solid line) and experiments (square, triangle and plus) in a drop tube reactor. Right: Comparison methodology between FR and EL simulation approaches.

Thus, a detailed comparison methodology to compare both results is proposed and applied. The nominal heat transfer coefficient is evaluated from the FR simulation (h_{FR}) and replaces the modelled heat transfer coefficient (h_{EL}) in the EL boundary layer heat balance equation, as illustrated in Fig. 5.1 (right). With the heat flux provided by the FR simulation, the only remaining free parameter in the EL simulation is the local gas cell temperature, where the point-particle is located. The local gas cell temperature highly depends on the grid res-

olution, which quantifies grid dependence and determines the applicability range of the EL approach. The evaluation is conducted separately for pure heating and combined processes (i.e. heating, drying and devolatilisation) of a single biomass particle in a hot, quiescent, inert gas environment. Fig. 5.2 shows the time evolution of the particle surface temperature

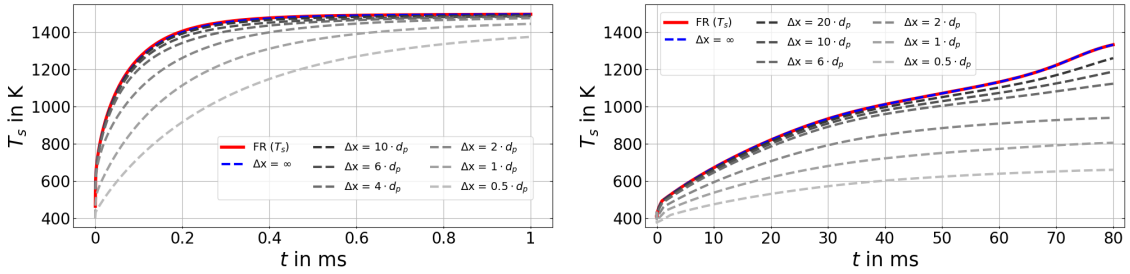

Figure 5.2: Comparison of particle surface temperature T_s over time from the FR (solid line) and standard EL, with varying numerical grid sizes, (dashed lines) simulation approaches. Right: Particle heating, drying and devolatilisation.

for the FR approach (red solid line). The dashed lines show the predicted particle surface temperature for the standard EL approach with varying numerical grid sizes. Decreasing the grid size results in increasingly larger deviations between the EL and FR temperature profiles. The cell volume intersects with the particle boundary layer for small grid sizes, causing the cell temperature to no longer represent the gas temperature at infinity, which is essential in the fundamental EL assumption. From the findings in Fig. 5.2, a numerical grid size to particle diameter ratio of $\Delta x/d_p \geq 10$ is acceptable, whereas coarse-graining (CG) methods should be applied for smaller ratios. Fig. 5.3 illustrates the CG methods, namely the moving average method (MAM) and the diffusion based method (DBM) in dashed lines applied to the standard EL approach with $\Delta x/d_p = 0.5$ (grey solid line). Using the two CG

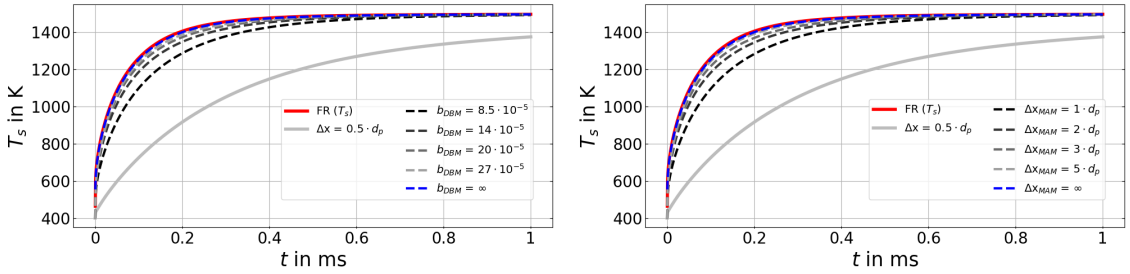

Figure 5.3: Pure particle heating: Comparison of particle surface temperature T_s vs. time from the FR (solid line), standard EL with $\Delta x/d_p = 0.5$ (grey solid line) and CG methods applied on standard EL with $\Delta x/d_p = 0.5$ (dashed lines). Left: Moving average method (MAM). Right: Diffusion based method (DBM).

methods allows for recovering the FR results, even when particle sizes are significantly larger than the grid size.

Paper 1:

Title: Single particle conversion of woody biomass using fully-resolved and Euler–Lagrange coarse-graining approaches

Authors:

Tien Duc Luu
Institute for Combustion Technology (ITV),
University of Stuttgart, Stuttgart, Germany

Jingyuan Zhang
Department of Energy and Process Engineering, Faculty of Engineering,
Norwegian University of Science and Technology, Trondheim, Norway

Jan W. Gärtner
Institute for Combustion Technology (ITV),
University of Stuttgart, Stuttgart, Germany

Shiqi Meng
Institute for Combustion Technology (ITV),
University of Stuttgart, Stuttgart, Germany

Andreas Kronenburg
Institute for Combustion Technology (ITV),
University of Stuttgart, Stuttgart, Germany

Tian Li
Department of Energy and Process Engineering, Faculty of Engineering,
Norwegian University of Science and Technology, Trondheim, Norway,
RISE Fire Research, Trondheim, Norway

Terese Løvås
Department of Energy and Process Engineering, Faculty of Engineering,
Norwegian University of Science and Technology, Trondheim, Norway

Oliver T. Stein
Institute for Combustion Technology (ITV),
University of Stuttgart, Stuttgart, Germany

Journal: Fuel

Year: 2024

Volume: 368

Article number: 131600

Contributions by the present author: Writing – original draft & editing, Visualisation, Validation, Software, Methodology, Formal analysis, Data curation.

Abstract

The conversion of woody biomass is studied by means of a layer-based model for thermally-thick biomass particles (Thunman et al. 2002, Ström et al. 2013). The model implementation is successfully validated against experiments that study particle conversion in a drop tube reactor. After this validation step, this work focuses on the well-known problem of grid dependence of two-phase numerical simulations using the standard Euler-Lagrange (EL) framework. This issue is addressed and quantified by comparing EL data that models the particle boundary layers to corresponding simulations which fully resolve these boundary layers (fully-resolved, FR, simulations). A comparison methodology for the conceptually different FR and EL approaches by extracting the heat transfer coefficient from the detailed FR simulations is proposed and confirms that the EL results are strongly grid-dependent. This issue is overcome by applying a set of coarse-graining methods for the EL framework. Two coarse-graining methods are evaluated, a previously suggested diffusion-based method (DBM) and a new approach based on moving averages referred to as MAM. It is shown that both DBM and MAM can successfully recover the detailed FR data for pure particle heating for a case where the grid size is half the particle diameter, i.e. when the standard EL method fails. Both coarse-graining methods also give improved results for an EL simulation that considers the more complex combined physics of particle heating, drying and devolatilisation, given that the CG model parameters that scale the corresponding CG interaction volumes are sufficiently large. Based on the available FR data, recommended model parameter ranges for DBM and MAM are provided as a function of normalised boundary layer thickness. The novel MAM approach is shown to be significantly more efficient than the DBM and therefore suitable for future EL simulations with multiple particles.

5.1.1 Introduction

The global energy demand is expected to increase in the next few decades as a result of the rising world population and economic growth. Fossil fuels are the most dominant global energy source, but the need for alternative sources increases due to the limited resources and negative environmental impact of fossil hydrocarbons, particularly coal. Solid biomass [182] is considered as a promising renewable alternative to coal due to the possibility of retrofitting existing coal-fired power plants. This offers the opportunity of making use of existing supply chains, infrastructure and proven power generation technology, while simultaneously reducing emissions by pure or co-firing of biomass [13, 183–185], in particular of torrefied biomass, due to similarities between the combustion of the latter and the one of coal [186]. However, transitioning from coal to biomass raises substantial challenges, such as fuel preparation, combustion stability and corrosive pollutants.

In the context of computational modelling, major challenges are the limited model fidelity of thermophysical sub-models specific to biomass and the relatively large diameter d_p of biomass particles in pulverised fuel applications, let alone fluidized or fixed beds. Sub-models for coal particle conversion have shown good results in predicting experimental evidence in the past [63, 66, 86, 179, 187–189] and can be considered as established for solid fuel particle conversion. A first attempt to develop thermophysical sub-models for biomass was to adapt reliable coal sub-models to biomass [40, 69, 190–194]. Typical predictions show reasonable results for small particle diameters but a mismatch between simulations and experiments occurs for larger particle diameters [195]. A major reason for these discrepancies is attributed to the fact that pulverised coal particle diameters are typically of (small) micrometre size, which satisfies the thermally-thin particle assumption, i.e. uniform intra-particle temperatures, that is invoked for most models. Conversely, typical pulverised biomass particle diameters are of (large) micrometre to millimetre size, which results in non-negligible intra-particle temperature gradients, i.e. thermally-thick particles, during the conversion process [196, 197]. To overcome this issue, several researchers have developed one-dimensional thermophysical sub-models specifically for thermally-thick biomass particles. Those sub-models can generally be classified into two types [198], namely interface-based models [151, 158, 199–204] and mesh-based models [205–208]. The mesh-based models solve the spatially discretised conservation equations on mesh points along the radius of the particle, which requires intra-particle discretisation that becomes costly for large particle ensembles. The underlying concept of interface-based models is to divide the particle into a set of layers, with different particle conversion processes like heating, drying, devolatilisation and char conversion occurring at the interface between two neighbouring layers. Since such interface-based sub-models are relatively easy to implement, have lower computational cost and ensure a higher model fidelity compared with simpler approaches, a layer-based particle conversion sub-model for woody biomass [151, 158] is used in the present work.

In the CFD modelling of multiphase gas-solid systems, the interaction between the gas phase and the solid particles needs to be specified as illustrated in Fig. 5.4. Various coupling

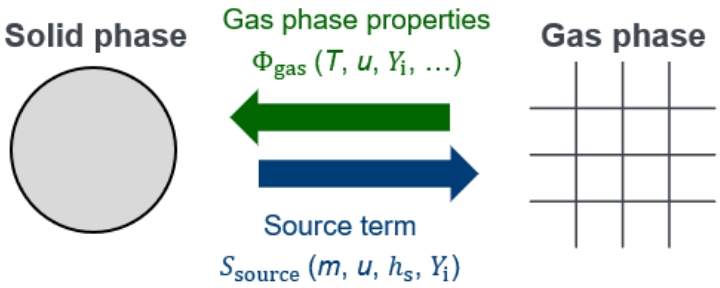

Figure 5.4: Coupling between gas and solid phase in two-phase (EL) simulations.

methods exist, but the most detailed approach to describe gas-solid interactions is the fully-resolved (FR) particle method [18–21]. In FR simulations, the governing equations (for total mass, momentum, energy and species) are solved in the Eulerian framework and all relevant gradients are resolved on the computational grid, including the particle boundary layers. In the FR approach the exchange of momentum, mass and heat between gas and solid is considered through a set of boundary conditions at the interface between both phases, while -different from Fig. 5.4- the governing equations do not contain any two-phase source terms. While this approach is highly accurate, it is associated with very high computational costs and therefore restricted to single particles and small particle groups [26–28]. Conversely, the two-way coupled Euler-Lagrange (EL) approach provides a good trade-off between accuracy and computational cost for dilute two-phase flows. In the EL approach, the bulk gas phase outside the particle boundary layers is treated as a continuum and solved analogously to the FR approach. However, the particle boundary layers are modelled and the solid particles are treated as dispersed point-particles in the Lagrangian framework. To model the crucial exchange processes across the particle boundary layers the point-particles need to retrieve information on the mass, momentum, energy and composition of the surrounding gas phase. This information is typically obtained from the local Eulerian cell (Δ) in which the particles reside. The reverse coupling from the particles to the gas phase is realised through a set of source terms in the Eulerian governing equations, cf. Fig. 5.4. However, for a reliable EL method contradictory requirements arise if small Eulerian cells are required to resolve the relevant gas phase physics (e.g. small turbulent vortices), while large Lagrangian particles are present. A typical assumption of the EL method is that the particle diameters are much smaller than the Eulerian grid size, i.e. $d_p/\Delta \ll 1$. For flows laden with small evaporating fuel droplets detailed indicators for the EL resolution requirements exist [144], but due to the larger size of biomass particles and the inherent differences between droplet evaporation and solid particle conversion these recommendations are not directly applicable to biomass. For biomass, the ratio d_p/Δ is typically of order one or even larger, which invalidates the standard EL approach. In this situation, exaggerated coupling effects between gas and solid phase can occur, leading to unphysical results and simulation instabilities [102,103]. To solve this issue, *coarse-graining* (CG) methods have been developed, see e.g. [37,104–110]. Sun et al. [105] briefly summarise the existing CG methods, referred to as particle centroid method, divided particle volume method, statistical kernel method and two-grid method. All these methods follow a different approach but have the same aim: The distribution of the particle source terms to more cells than just the local Eulerian cell and the consideration of a fluid volume larger than the local cell to obtain far-field gas phase information (e.g. temperature) to trigger the particle processes (e.g. pyrolysis). Zhang et al. [107] have demonstrated that the interplay between the Eulerian and the Langrangian framework strongly influences

the prediction of solid fuel particle conversion due to the non-linear coupling processes. However, studies of EL approaches coupled to CG methods (EL-CG) in the past have shown that dependencies of grid size vs. particle diameter are present, but in most CG methods an unknown free parameter is required, which needs further investigation and quantification.

In the present study, we consider the conversion of single woody biomass particles using a layer-based particle conversion sub-model with two complementary modelling approaches for gas-solid coupling. At first, a FR laminar flow simulation is validated against experimental data to obtain well-resolved comparison data for the evaluation of the EL framework. Subsequently, the FR data is compared to the results from the standard EL method and a set of EL-CG approaches. The objectives of the present study are to

- validate the thermally-thick layer-based biomass sub-model for particle conversion against recent experiments,
- propose a methodology to meaningfully compare FR and EL approaches,
- propose a simple and flexible CG method for enhanced EL-CG simulations,
- compare the high-fidelity FR data with data from the standard (grid dependent) and coarse-graining (grid independent) EL approaches.

The remainder of the paper first introduces the modelling approach in Sec. 5.1.2, followed by experimental validation in Sec. 5.1.3 and the description of the computational setup in Sec. 5.1.4. Results are shown and discussed in Sec. 5.1.5, and the major conclusions are drawn in Sec. 5.1.6.

5.1.2 Modelling

5.1.2.1 Gas phase

In the present section the governing equations of the gas phase are written in a general format including two-phase exchange terms. In the FR approach these source terms are set to zero and replaced by boundary conditions, while they are non-zero for EL simulations, as will be described later. The transport equations for total mass, momentum, sensible enthalpy and chemical species in the gas phase read

$$\frac{\partial \rho}{\partial t} + \frac{\partial}{\partial x_i}(\rho u_i) = \dot{S}_{\rho,p}, \tag{5.1}$$

$$\frac{\partial \rho u_i}{\partial t} + \frac{\partial}{\partial x_j}(\rho u_i u_j) = -\frac{\partial p}{\partial x_i} + \frac{\partial}{\partial x_j}\left(\mu\left[\frac{\partial u_j}{\partial x_i} + \frac{\partial u_i}{\partial x_j} - \frac{2}{3}\frac{\partial u_m}{\partial x_m}\delta_{ij}\right]\right) + \dot{S}_{u,p}, \tag{5.2}$$

$$\frac{\partial \rho h_s}{\partial t} + \frac{\partial}{\partial x_i}(\rho u_i h_s) = \frac{\partial}{\partial x_i}\left(\frac{\mu}{\mathrm{Pr}}\frac{\partial h_s}{\partial x_i}\right) + \dot{\omega}_{h_s} + \dot{S}_{h_s,p}, \tag{5.3}$$

$$\frac{\partial \rho Y_k}{\partial t} + \frac{\partial}{\partial x_i}(\rho u_i Y_k) = \frac{\partial}{\partial x_i}\left(\frac{\mu}{\mathrm{Sc}}\frac{\partial Y_k}{\partial x_i}\right) + \dot{\omega}_k + \dot{S}_{k,p}, \tag{5.4}$$

with subscripts $<i,j>$ indicating the coordinate directions, subscript $<p>$ particle properties, ρ is the density, u is the velocity, h_s is the sensible enthalpy, ω_{h_s} is the energy release from homogeneous chemical reactions, Y_k and ω_k are the mass fraction and homogeneous chemical reaction rates of chemical species k and t denotes time. The spatial coordinate is expressed by x, μ is the dynamic viscosity, δ is the Kronecker delta and $\mathrm{Pr} = \mathrm{Sc} = 0.7$ are the non-dimensional Prandtl and Schmidt numbers.

5.1.2.2 Solid phase

The thermally-thick spherical particles are described with the layer-based model originally proposed by Thunman et al. [151] and further developed by Ström et al. [158]. The particles are divided into four layers, namely moist/wet wood (1), dry wood (2), char (3) and ash (4), see Fig. 5.5. The intra-particle temperature gradient is estimated assuming that each inner

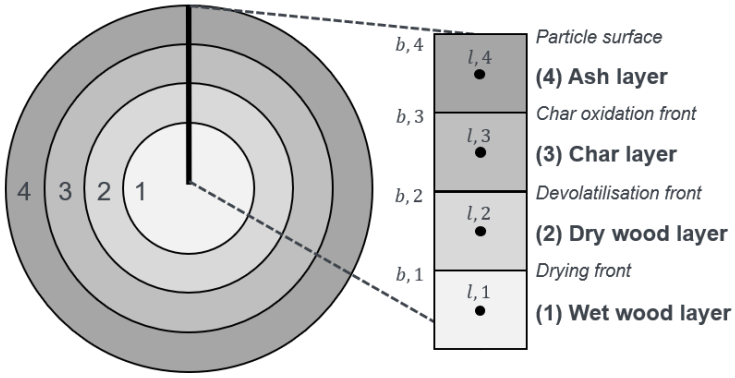

Figure 5.5: Schematic of layer-based woody biomass particle sub-model [151, 158].

layer (subscript $<l>$) has its own set of mass and temperature and each inner boundary (subscript $<b>$) has its own individual temperature. At these boundaries, the physical conversion processes of drying, devolatilisation and char conversion take place. The outer boundary represents the particle surface ($T_s = T_{b,4}$). All temperatures are calculated through a heat balance inside the particle, the outer surface temperature of which is additionally affected by the gas phase. The volume and surface areas for each layer are predicted from the mass balance, e.g. the progress of devolatilisation. The evaluation of the heat and mass balance can be simplified to a one-dimensional problem along the radial direction of the particle. The set of governing equations for all layers is given as

$$\frac{dm_p}{dt} = \sum_{i=1}^{N_l=4} \frac{dm_{l,i}}{dt} \tag{5.5}$$

$$\frac{dT_p}{dt} = \frac{1}{m_p c_{\mathrm{p},p}}(-\nabla \cdot q + S_l + \Delta Q) \tag{5.6}$$

where i is the i-th layer, $-\nabla \cdot q$ is the conductive heat transfer term, ΔQ is the heat of conversion on the boundaries and S_l is the heat source/sink term due to released gas within different layers (e.g. water vapor or volatiles). Equation (5.6) may take different forms depending on the location of its evaluation [107]. For layers, $-\nabla \cdot q$ is calculated as

$$-\nabla \cdot q = k_{l,i} A_{b,i} \left.\frac{dT}{dr}\right|_{(b,i),(l,i)} - k_{l,i} A_{b,i-1} \left.\frac{dT}{dr}\right|_{(b,i-1),(l,i)} \tag{5.7}$$

and for boundaries it is expressed as

$$-\nabla \cdot q = k_{l,i+1} A_{b,i} \left.\frac{dT}{dr}\right|_{(b,i),(l,i+1)} - k_{l,i} A_{b,i} \left.\frac{dT}{dr}\right|_{(b,i),(l,i)}. \tag{5.8}$$

Here, k_l is the layer heat conductivity, $A_b = 4\pi r_b^2$ is the boundary surface area with radius r. The temperature gradient along the radius is approximated for spherical particle as [158]

$$\left.\frac{dT}{dr}\right|_{m,n} \approx \frac{T_m - T_n}{r_m\left(\frac{r_m}{r_n} - 1\right)}. \tag{5.9}$$

Equations (5.7) and (5.8) describe the *intra-particle* heat balance between layers and boundaries. The *interphase* mass and heat balance between the solid phase and the gas are discussed later in Sec. 5.1.2.3.

A shrinkage model following [151] is applied to consider the volume change in each layer due to mass conversion as

$$\Delta V_{l,i} = \frac{\Delta m_{l,i-1}}{\rho_{i-1}} \eta_i - \frac{\Delta m_{l,i}}{\rho_i} \tag{5.10}$$

where $\Delta m_{l,i}$ is the change of mass in each layer and η_i is the shrinkage factor.

A drying model [209] is applied at boundary 1, between layers 1 and 2. The rate of drying is calculated from the heat flux to this boundary. The temperature of the drying front is limited by the boiling temperature of water at atmospheric pressure. A two-stage devolatilisation model is employed to model wood pyrolysis [160], which takes place at boundary 2 and is considered to be heat-neutral ($\Delta Q = 0$) [197]. One-step or two-step competing rates models commonly describe the devolatilisation process for solid fuels. The one-step model assumes a fixed char-to-volatile yield ratio, which only applies to systems with a single heating rate. The two-competing rates model overcomes this limitation and allows for varying char and volatile yields under different heating conditions. Both models neglect the details of the physical process of biomass degradation. However, as shown for example in [210], the leading order effects in the conversion of woody biomass can reliably be described by a two-stage model.

In the primary stage, dry wood is decomposed into the three fractions light gas, tar and char via three competing release steps. In the secondary stage, tar further decomposes into light gas and char. Tar is treated as a gaseous species. The Arrhenius reaction rate coefficients of the devolatilisation model are listed in Tab. 5.1. The selected rates are validated against experiments on woody biomass conversion in Sec. 5.1.3. Char burn-out is neglected in the present work.

Table 5.1: Arrhenius coefficients for the two-stage devolatilisation process.

No.	Reaction description	A in 1/s	E in kJ/mol	Ref.
1	Dry wood → Light gas	1.30×10^8	140	[211]
2	Dry wood → Tar	2.00×10^8	133	[211]
3	Dry wood → Char	7.40×10^5	106.5	[212]
4	Tar → Light gas	4.28×10^6	107.5	[213]
5	Tar → Char	1.00×10^5	107.5	[160]

5.1.2.3 Gas/solid interphase

The interphase mass and heat balance differ depending on whether the FR or EL framework is employed.

5.1.2.3.1 Gas/solid interphase for FR simulations

When employing the FR approach the particle conversion processes are treated as boundary conditions for the gas phase and, therefore the interphase source terms in Eqs. (5.1) - (5.4) are set to zero [19]:

$$\dot{S}_{\rho,p} = \dot{S}_{u,p} = \dot{S}_{h_s,p} = \dot{S}_{k,p} = 0. \tag{5.11}$$

At the particle surface (subscript $<s>$) two conditions need to be fulfilled for every surface cell layer in order to obtain consistent particle surface temperatures. These are for the temperature value itself

$$T_s = T_{g,s} = T_{b,4} \tag{5.12}$$

and for the temperature gradient

$$k_g \frac{T_g - T_s}{r_g\left(\frac{r_g}{r_s} - 1\right)} = k_{l,4} \frac{T_s - T_{l,4}}{r_s\left(\frac{r_s}{r_{l,4}} - 1\right)}. \tag{5.13}$$

Here, subscript $<g>$ denotes gas phase properties at particle position.

From Eqs. (5.12) and (5.13), the mean surface temperature ($\overline{T}_{b,4}$) averaged over the fully-resolved particle surface is calculated and serves as an input value for the intra-particle temperature change in Eqs. (5.7) and (5.8). The mass released by drying and devolatilisation

is imposed uniformly and normal to the particle surface direction with a Robin boundary condition [142] as

$$\frac{dm_{p,k}}{dt} = \sum_k \left(Y_k \frac{dm_{p,k}}{dt} \right) - \rho_{g,s} A_s D_{g,s} \frac{\partial Y_k}{\partial n} \tag{5.14}$$

where $A_s = A_{b,4}$ is the surface area of the particle and $D_{g,s}$ is the gas diffusivity at particle surface.

5.1.2.3.2 Gas/solid interphase for EL simulations

When conducting EL simulations, the particle boundary layers are not resolved, hence, correlation models for mass and heat transfer are required. The source terms $\dot{S}_{\rho,p}, \dot{S}_{u,p}, \dot{S}_{h_s,p}$ and $\dot{S}_{k,p}$ on the RHS of Eqs. (5.1)-(5.4) denote the gas/solid coupling terms and are calculated for a single particle as

$$\dot{S}_{\rho,p} = -\frac{1}{V_c} \frac{dm_p}{dt}, \tag{5.15}$$

$$\dot{S}_{u,p} = -\frac{1}{V_c} \frac{d(m_p \mathbf{u}_p)}{dt}, \tag{5.16}$$

$$\dot{S}_{h_s,p} = -\frac{1}{V_c} \left(\frac{m_p c_{\mathrm{p},p}}{\tau_{con}} (T_g - T_p) \right), \tag{5.17}$$

$$\dot{S}_{k,p} = Y_{\mathrm{moist}} \frac{1}{V_c} \frac{dm_{p,\mathrm{drying}}}{dt} + Y_{k,\mathrm{vol}} \frac{1}{V_c} \frac{dm_{p,\mathrm{devol}}}{dt} \tag{5.18}$$

where V_c is the volume of the local computational cell, m_p is the particle mass, $c_{\mathrm{p},p}$ is the particle specific heat capacity, T is the temperature and τ_{con} is the convective heat transfer time scale. Y_{moist} is the mass fraction of moisture (i.e. $= \mathrm{H_2O}$) content in the particle, $Y_{k,\mathrm{vol}}$ is the mass fraction of species k in the volatile composition, $m_{p,\mathrm{drying}}$ is the mass release of moisture and $m_{p,\mathrm{devol}}$ is the mass release of volatile content in the particle. The convective heat transfer time scale follows Ranz-Marshall [141]

$$\tau_{con} = \frac{1}{6} \frac{\mathrm{Pr}}{\mathrm{Nu}} \frac{c_{\mathrm{p},p}}{c_{\mathrm{p},f}} \frac{\rho_p d_p^2}{\mu_f} \tag{5.19}$$

with

$$\mathrm{Nu} = 2 + 0.6 \mathrm{Re}_p^{1/2} \mathrm{Pr}^{1/3} \tag{5.20}$$

Here, μ is the dynamic viscosity and Nu is the non-dimensional Nusselt number. Subscript $<f>$ denotes gas properties at film temperature evaluated with the 1/3-law as

$$T_f = T_s + \frac{1}{3}(T_g - T_s). \tag{5.21}$$

The boundary layer heat balance affecting the particle surface is given as

$$h_{EL}(T_g - T_s) = k_{l,4}\frac{T_s - T_{l,4}}{r_s\left(\frac{r_s}{r_{l,4}} - 1\right)} \tag{5.22}$$

with the Euler-Lagrange heat transfer coefficient defined as

$$h_{EL} = \mathrm{Nu}\frac{k_f}{d_p}. \tag{5.23}$$

5.1.2.4 Biomass properties

The biomass employed in this work is torrefied wood, used in the experimental investigations by Tolvanen et al. [149, 150]. The proximate and ultimate analyses are given in Tab. 5.2. Following [107], the released light gases have a presumed composition as listed in Tab. 5.3.

Table 5.2: Proximate and ultimate analyses for torrefied wood [149, 150].

Ultimate (dry wt %)		Proximate (dry wt %)	
S	< 0.02	Ash	0.2
C	53.2	Volatile matter	81.9
H	6	Fixed carbon	19.9
N	< 0.2	Moisture	< 0.1 wt %
O	40.38		
GHV	21.07 MJ/kg		
LHV	19.77 MJ/kg		

Tar is represented by C_6H_8O with thermophysical properties taken from benzene [151]. The thermal properties for each solid layer are shown in Tab. 5.4.

Table 5.3: Presumed light gas composition [107].

Species k	H_2	CO	CO_2	H_2O	CH_4
Y_k	0.100	0.363	0.192	0.228	0.117

5.1.2.5 Coarse-graining methods

As previously outlined in Sec. 5.1.1 EL methods, where the gas phase governing equations (5.1)-(5.4) contain interphase exchange terms, are in need of coarse-graining schemes for situations where the particle diameter is of the order of the Eulerian grid size or larger. For such cases, a CG method must be employed to distribute the particle source terms to more cells than the local Eulerian cell and to interrogate a fluid volume larger than the local cell for far-field gas data. The vast majority of CG approaches is based on four basic methods, namely the particle centroid method (PCM), divided particle method (DPM), two-grid method (TGM) and statistical kernel method (SKM). The original SKM is a method that applies statistical kernel/weight functions to map input data to an alternative space.

Table 5.4: Thermophysical properties of the solid layers: Initial density ρ, thermal conductivity k, specific heat capacity c_p and shrinkage factor η.

Layer	Value	Ref.
Initial solid density in kg/m^3		
Wet wood	$\rho_{1,init} = 931.069$ (assume $Y_{\text{moist}} = 0.001$ with $c_{\text{p,moist}} = 1000\,\text{J/(kg K)}$)	
Dry wood	$\rho_{2,init} = 931$	[149]
Char	$\rho_{3,init} = 700$	[152]
Ash	$\rho_{4,init} = 2000$	[152]
Solid thermal conductivity in W/(m K)		
Wet wood	$k_1 = \frac{\rho_2}{1000} \cdot (0.1941 + 0.4064 \cdot Y_{\text{moist}}) + 0.01864$	[153]
Dry wood	$k_2 = 0.00249 + 0.000145 \cdot \rho_1 + 0.000184 \cdot (T_{l,2} - 273.15)$	[154]
Char	$k_3 = 1.47 + 0.0011 \cdot T_{l,3}$	[155]
Ash	$k_4 = 1.03$	[152]
Solid specific heat capacity in J/(kg K)		
Wet wood	$c_{\text{p},1} = c_{\text{p},2} \cdot (1 - Y_{\text{moist}} \cdot 100) + 418550 \cdot Y_{\text{moist}} + \alpha$ $\alpha = 1000 \cdot (0.02355 \cdot T_{l,1} - \frac{1.32 Y_{\text{moist}} \cdot 100}{1 - Y_{\text{moist}} \cdot 100} - 6.191) \cdot \frac{Y_{\text{moist}} \cdot 100}{1 - Y_{\text{moist}} \cdot 100}$	[153]
Dry wood	$c_{\text{p},2} = 2300 - 1150 \cdot \exp(-0.0055 \cdot (T_{l,2} - 273.15))$	[156]
Char	$c_{\text{p},3} = 1430 + 0.355 \cdot T_{l,3} - 7.3210 \cdot 10^7 \cdot T_{l,3}^2$	[157]
Ash	$c_{\text{p},4} = 754 + 0.586 \cdot (T_{l,4} - 273.15)$	[152]
Shrinkage factor		
Wet wood	$\eta_1 = 0.1$	[151]
Dry wood	$\eta_2 = 0.39$	[151]
Char	$\eta_3 = 0.95$	[151]

Due to their flexibility and simplicity of implementation we only focus on the PCM and variants of the SKM in the present work, since these methods can be applied to the most general case of unstructured grids, moving particles and parallel computing with relative ease.

5.1.2.5.1 Particle centroid method (PCM, i.e. standard EL)

The most common and widely used method is the PCM, or standard EL approach. In the PCM, two-phase coupling is restricted to the grid cell, where the particle centroid is located, see Fig. 5.6 (left). All gas phase properties (Φ_{gas}) are retrieved from this local Eulerian

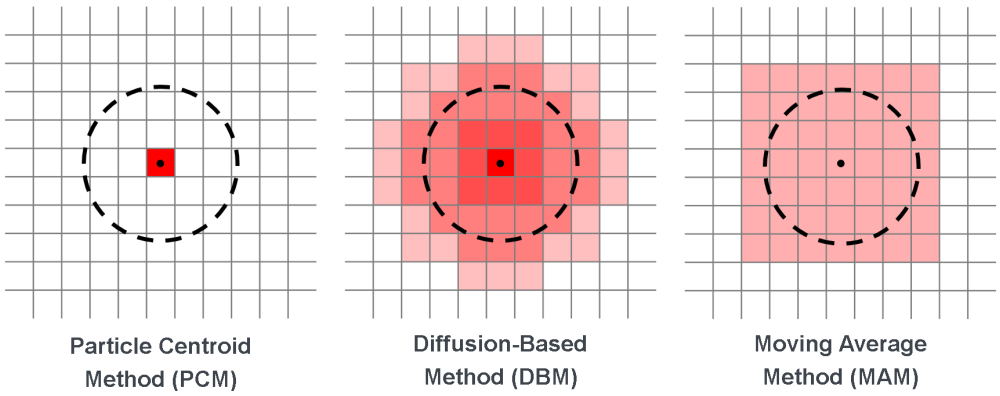

Figure 5.6: Visualisation of the CG methods employed in the present work, PCM (left), DBM (middle) and MAM (right).

cell and the source terms (S_{source}) are assigned to the same cell. For ratios of $d_p/\Delta \ll 1$,

when using reliable closures for the momentum, heat and mass transfer across the particle boundary layers, the PCM works well. However, for cases where the ratio d_p/Δ is close to unity or larger the error becomes unacceptable and causes unphysical behaviour, which may also lead to numerical instability.

5.1.2.5.2 Diffusion based method (DBM)

To overcome the limitations of the PCM, the diffusion based method (DBM) can be employed, see Fig. 5.6 (middle). The DBM belongs to the previously mentioned class of SKM, as it is based on the concept of a statistical kernel function to retrieve the reference gas field and to distribute the source terms. However, the DBM does not use an explicit kernel function, but solves a diffusion equation instead, which is equivalent to applying a kernel function [105]. Before the particle retrieves the far-field information from the gas phase, the unsteady diffusion equation

$$\frac{\partial \Phi_{\text{gas}}}{\partial \tau} = \nabla^2 \Phi_{\text{gas}} \tag{5.24}$$

is solved to obtain the reference gas phase properties Φ_{gas}. Conversely, to distribute the two-phase source terms to a larger volume, these source terms are first calculated and then diffused to the neighbouring cells according to the unsteady diffusion equation

$$\frac{\partial S_{\text{source}}}{\partial \tau} = \nabla^2 S_{\text{source}}. \tag{5.25}$$

The diffusion equation is solved for a time period $0 \leq \tau \leq \mathbf{T}$ which is equivalent to a Gaussian kernel function with bandwidth $b = \sqrt{4\mathbf{T}} = \sigma\sqrt{2}$.

5.1.2.5.3 Moving average method (MAM)

In the present work, we propose a simple and flexible alternative CG approach, referred to as moving average method (MAM). Similar to the DBM from Sec. 5.1.2.5.2, the MAM approach can be considered as a variant of the SKM, employing a uniform kernel function, which is equivalent to applying the number average method. The MAM uses an averaging operation for retrieving Φ_{gas} for the particle and for applying S_{source} to the gas phase, see Fig 5.6 (right). For the averaging operation, various geometrical shapes can be considered. In the present work, we choose a cubic distribution volume with edge length Δx_{MAM}. In the first step of MAM, the particle position is tracked and taken to be the centroid of the cubic distribution volume. Subsequently the gas phase properties are averaged according to

$$\Phi_{\text{gas}} = \frac{1}{N_{\text{cells}}} \sum_{n=1}^{N_{\text{cells}}} \Phi_n, \tag{5.26}$$

with the gas phase properties Φ_n of each Eulerian cell inside the cubic volume and the total number of cells within the cube N_{cells}. Conversely, the source terms from the underlying Eulerian grid are first summed up to a total source term for the entire cube S_{source} and then equally distributed to all cells within the cube

$$S_n = \frac{S_{\text{source}}}{N_{\text{cells}}}, \tag{5.27}$$

where S_n is the source term for each Eulerian cell within the cube. In a general EL-CG framework where particles are transported by a carrier flow, the location of the each moving particle (i.e. the centroid of the averaging volume) can be updated at every time step such that the averaging volume moves along with the particle, hence the term moving average method. Finally, we remark that the functionality and performance of MAM is independent of any given mesh structure. The novel MAM approach constructs a look-up table of each cell's neighbours at the start of the simulation that remains unchanged and is efficiently read over the course of the simulation, to define the averaging volumes for MAM.

5.1.3 Validation

As a crucial validation of our numerical methodology, we compare our most accurate -and computationally expensive- modelling approach for conversion of the woody biomass considered in this work to experimental data. The modelling approach with the highest fidelity (and cost) is achieved by combining the layer-based biomass model for intra-particle conversion from Sec. 5.1.2.2 with the FR closures to accurately describe the boundary layer and far-field gas phase processes outlined in Sec. 5.1.2.3.1. The experimental data used for validation are the measurements conducted by Tolvanen et al. using a drop tube reactor (DTR) at different temperatures with solid fuel particles in an inert atmosphere (N_2) [149, 150]. The experimental campaign aimed to investigate the pyrolysis behaviour of coal, peat and various types of woody biomass, while we focus on the woody biomass data only. The experimental configuration comprises of a particle-feeding silo, a water-cooled movable injector, a steel tube with heating elements and a particle-collecting system. From the experiments it is known that the biomass particles are non-spherical and highly elongated. However, the experimentalists also showed that a simplified model, based on a spherical equivalent diameter, is able to capture the rate of mass loss [150]. Therefore, the experimentally determined spherical equivalent diameter is used in this work to set up a fully spherical FR case for comparison with the experiments (see Fig. 5.8 in Sec. 5.1.4 for more details on the computational configuration).

Figure 5.7 shows the dry/ash-free mass loss of a torrefied biomass particle with $d_p = 160\,\mu\text{m}$ over time at different gas temperatures inside the DTF. The initial and boundary conditions

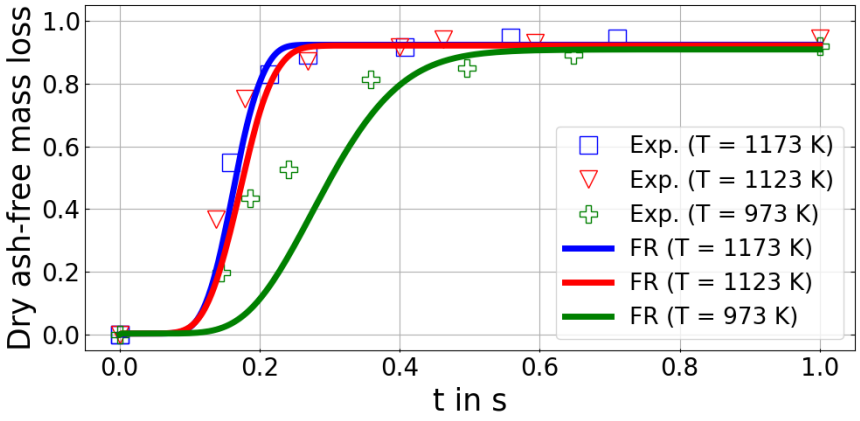

Figure 5.7: Comparison of the dry/ash-free mass loss vs. time t from biomass particles with an equivalent diameter $d_p = 160\,\mu\text{m}$ at different temperatures between FR simulations (solid line) and experiments [149, 150] (square, triangle and plus) in a drop tube reactor.

have been extracted from previous experiments [149, 150, 214]. The biomass particle needs $t \approx 0.1\,\text{s}$ to heat up for the two high gas temperature cases ($T_g = 1123/1173\,\text{K}$) before starting its pyrolysis process. The conversion process takes $\approx 0.15\,\text{s}$ until reaching the final state with only char and ash remaining in the particle. Due to the inert gas atmosphere, char conversion processes are suppressed, which explains that the mass loss does not reach a final value of one. However, a higher final volatile yield than the proximate analysis is due to the low heating rates in the chemical kinetic studies [149]. The comparison of the FR predictions with the experimental data shows an excellent agreement both of the temporal evolution and the final mass release for the two high temperature cases. At lower gas temperatures ($T_g = 973\,\text{K}$), the FR simulation predicts the conversion process to start slightly later and the whole process takes around 0.5 s, which is two times longer than with higher gas temperatures. A comparison with the experimental evidence shows differences in the time range $0.1 < t < 0.3\,\text{s}$, where the numerical model predicts a slightly later start of the conversion process. At late times the experimental data and FR predictions agree again very well. The differences between the numerical and experimental data at early times for $T_g = 937\,\text{K}$ may be attributed to the simplification of the particle shape (spherical) in the simulation, whereas elongated particles are present in the experiments. Moreover, there is some uncertainty in the activation energies reported in Tab. 5.1 (particularly No. 1 and 2) that govern the mass loss profiles show in Fig. 5.7, where the fits seem to work well for higher temperatures/heating rates, but are not ideal for the lower temperature/heating rate case $T_g = 937\,\text{K}$. However, further experimental and numerical analyses are required to come to a definitive conclusion on these remaining deviations.

Overall, the predictions from the FR simulation approach using the layer-based biomass sub-model for intra-particle conversion show a good agreement with the experimental evidence. The FR approach correctly predicts the dependence of the mass loss rate and final

particle conversion ratio on the ambient gas temperature in the DTF. Therefore, the detailed FR data is taken as a reference for the subsequent evaluation of the EL approach and EL-CG methods.

5.1.4 Computational configuration

5.1.4.1 Computational setup

With our main focus on comparing detailed FR simulation data to results from the standard EL method and EL-CG methods for large particles, two basic computational setups for FR and EL simulations are considered. The three-dimensional computational domains and grid designs for both approaches are shown in Fig. 5.8. To obtain a well-defined setup for the FR

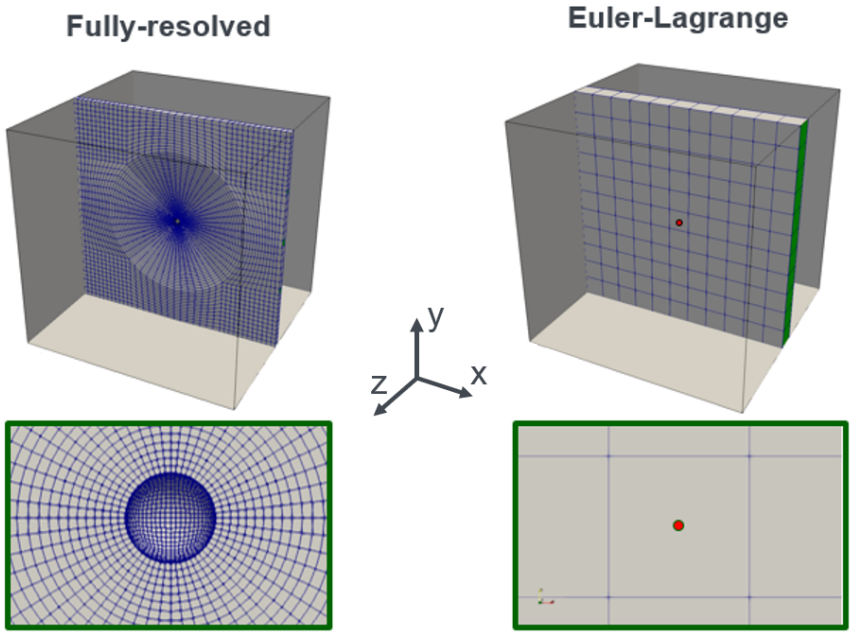

Figure 5.8: Computational setup for single biomass particle conversion in the context of FR (left) and EL (right) simulations.

vs. EL comparison the gas phase is initialised as a quiescent medium with $T_{g,\mathrm{init}} = 1500\,\mathrm{K}$ and $Y_{\mathrm{N_2},\mathrm{init}} = 1$. Due to the inert gas environment, no homogeneous reactions occur such that $\dot{\omega}_{h_s} = \dot{\omega}_k$ in Eqs. (5.3) and (5.4) are zero. A single biomass particle is located in the centre of the domain with $d_{p,\mathrm{init}} = 118\,\mu\mathrm{m}$ and $T_{p,\mathrm{init}} = 350\,\mathrm{K}$.

The computational domain for the FR setup has a size of $L_x = L_y = L_z = 40 \cdot d_p$ and consists of 113,280 cells, the size of which varies from $6.5 \leq \Delta x_{FR} \leq 113\,\mu\mathrm{m}$, with the smallest cells located at the particle surface and increasing cell sizes with increasing distance from the particle to fully resolve the particle boundary layer. The mesh is considered fixed and does not change during the simulations.

For the EL simulations, the domain has either 1,331 (standard EL approach) or 274,625 (EL-CG methods) cells which are uniform and cubic. The domain size varies for the various investigated cases as $L_x = L_y = L_z = \mathbf{j} \cdot d_p \cdot \mathbf{n}$ with $j = \{0.5, 1, 2, 4, 6, 8, 10, 20\}$ and the domain is discretised in x-, y-, z-direction with $\mathbf{n}$ grid cells, which corresponds to $\Delta x_{\mathrm{EL}} = \mathbf{j} \cdot d_p$ µm. For the standard EL approach $\mathbf{n} = 11$, whereas $\mathbf{n} = 65$ for the EL-CG methods. It is noted that, for increased computational efficiency, the domain size of the EL domain with the finest resolution is smaller than the size of the FR reference domain. However, the relevant physics are captured within the bounds of the smallest EL domain already, such that the boundary conditions do not unduly affect the predictions.

All the simulations are performed with a low-Mach second-order finite volume multiphase solver based on the OpenFOAM library. The transport equations of the gas phase are solved with a constant time-step of $\Delta t_g = 5 \cdot 10^{-7}$ s, while the biomass particle sub-model considers sub-steps of size $\Delta t_p = 1 \cdot 10^{-7}$ s.

5.1.4.2 Comparison methodology to study grid independence - FR/EL

Since the FR and EL modelling frameworks are fundamentally different, a detailed comparison methodology to compare results from the two approaches is required. This comparison methodology also serves to demonstrate the grid dependence of the standard EL and EL-CG methods. The steps of the comparison methodology are given as follows:

1. A FR reference case is solved for a specific time interval.

2. As reflected by Eq. (5.13) in FR simulations the gas-solid coupling directly occurs at the (resolved) particle surface, from which a nominal heat transfer coefficient can be calculated.

3. Detailed information on the gas phase thermophysical properties (i.e. k_g), particle surface temperature (T_s), temperature of the first cell layer around the particle (T_c), initial gas temperature ($T_{g,\mathrm{init}}$), surface area of the particle (A_s) and the distance between the particle surface and the centroid of the first gas cell layer are retrieved from the FR simulation.

4. The nominal FR heat transfer coefficient h_{FR} is evaluated at every time-step as

$$h_{\mathrm{FR}} = \frac{Q}{A_s \cdot (T_{g,\mathrm{init}} - T_s)} \qquad \text{with} \qquad Q = k_g A_s \frac{dT}{dn} \tag{5.28}$$

   and stored in a table.

5. The boundary layer heat balance in the EL approach is given in Eq. (5.22), where (the

modelled) h_{EL} is now replaced by the nominal value from the FR simulation h_{FR}:

$$h_{FR}(t)(T_g - T_s) = k_{l,4} \frac{T_s - T_{l,4}}{r_s \left(\frac{r_s}{r_{l,4}} - 1 \right)} \tag{5.29}$$

6. At every time-step, h_{FR} is retrieved from the previously generated table and used for Eq. (5.29).

7. With the heat flux provided by the FR simulation, the only remaining unknown parameter is T_g, which is the local gas cell temperature where the particle centroid resides.

The local gas cell temperature highly depends on the grid resolution, which allows for the evaluation of grid (in-)dependence of the EL approach. A schematic representation of the comparison methodology is shown in Fig. 5.9.

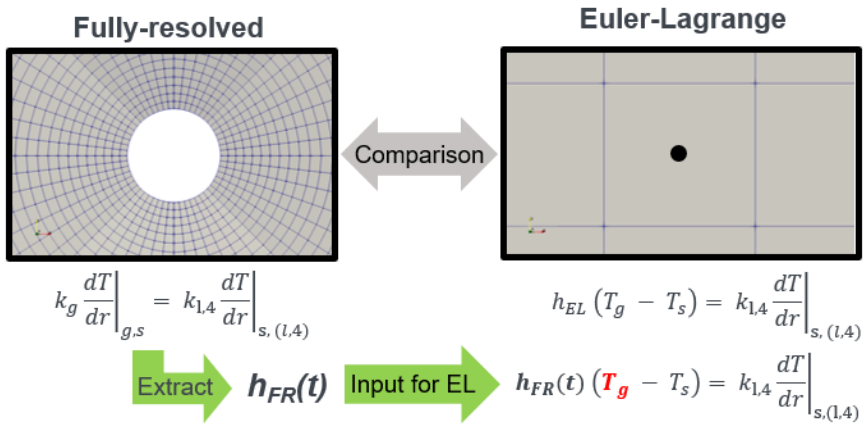

Figure 5.9: Schematic representation of the comparison method between the FR and EL simulation approaches.

5.1.5 Results and discussion

After validating the layer-based sub-model for woody biomass conversion within the detailed FR simulation framework against the experimental evidence in Sec. 5.1.3 and providing a detailed comparison strategy between FR and EL data in Sec. 5.1.4.2 we can now evaluate the performance and grid (in-)dependence of the standard EL approach (EL-PCM) and the two alternative EL-CG approaches (namely EL-DBM and EL-MAM, see Secs 5.1.2.5.2 and 5.1.2.5.3). The evaluation is carried out separately for pure heating of the biomass particle in Sec. 5.1.5.1 and for combined heating, drying and devolatilisation in Sec. 5.1.5.2.

5.1.5.1 Pure heating

Figure 5.10 shows the time evolution of the particle surface temperature over time for the FR setup, as indicated by the red solid line. The dashed lines show the predicted particle surface temperature over time for the standard EL approach (EL-PCM) with varying grid sizes.

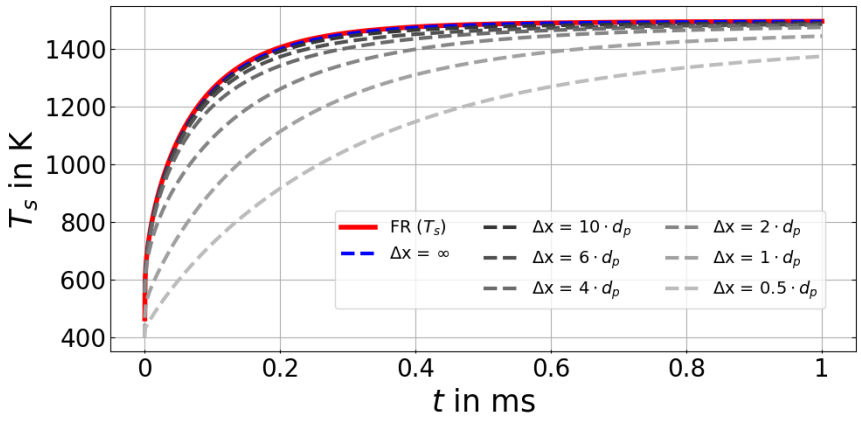

Figure 5.10: Pure particle heating: Comparison of particle surface temperature T_s vs. time from the FR (solid line) and standard EL (dashed lines) simulation approaches, where the EL grid size has been varied.

Considering the FR data, the particle surface temperature strongly increases from the beginning of the simulation until $t = 0.2\,\text{ms}$ due to the injection of the initially cold particle ($T_p = 350\,\text{K}$) into the high temperature environment ($T_g = 1500\,\text{K}$). At the end of the simulation, the particle surface temperature approaches the gas phase temperature which has not decreased significantly due to the limited effect of the small particle cooling the comparatively large gas volume.

The heat transfer coefficient h_{FR} extracted from the FR case is now used as an input for the (standard) EL cases shown in Fig. 5.10, with the EL heat transfer governed by Eq. (5.29). The EL cases have been set up to fully reflect the physics of the FR case. As a validation benchmark a reference EL case with $\Delta x = \infty$ is shown by the blue solid line. This case reflects that the EL approach works for an infinitely large cell where the FR and EL results fully match. Furthermore, it also indicates that the methodology described in Sec. 5.1.4.2 is correct. The reference EL case $\Delta x = \infty$ is approximated by reducing the two-way coupled EL approach to one-way coupling, which results in an unaffected gas phase ($T_g = \text{const.}$).

Reducing the grid size leads to increasingly larger deviations of the EL temperature profile from the FR temperature. This is due to the fact that for small grid sizes the cell volume intersects with the particle boundary layer, such that the cell temperature does no longer reflect the (undisturbed) gas temperature at infinity that is required for heat transfer in the EL framework. For a large grid size, the effect of the particle heating up the local

cell is comparatively small such that $T_g = 1500\,\mathrm{K} \approx \text{const.}$, whereas with smaller grid size $T_g < 1500\,\mathrm{K}$ directly affects the particle surface heat flux. The most extreme case studied here $\Delta x = 0.5 \cdot d_p$ (i.e. a particle spans across two cells) has -within the considered simulation time- a final relative temperature error of $\approx 8\,\%$ for a simple heating problem. This raises the need of using coarse-graining methods for large particles.

In Fig. 5.11, the temperature profile of the standard EL case with $\Delta x = 0.5 \cdot d_p$ is used as the base setup to apply the diffusion-based CG method (CG-DBM). The bandwidth

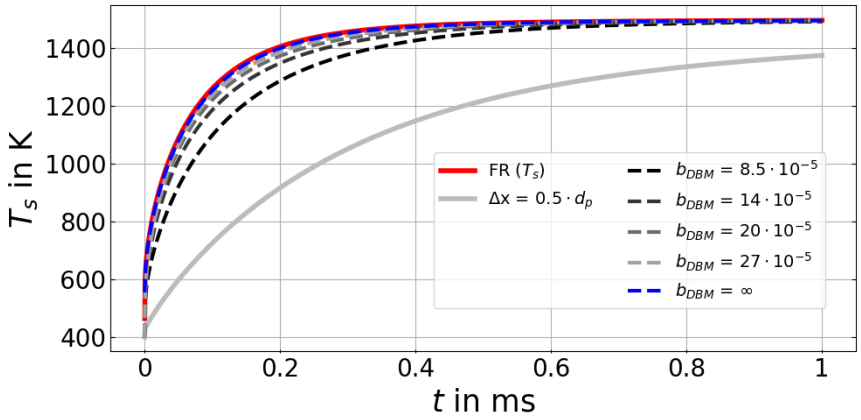

Figure 5.11: Pure particle heating: Comparison of particle surface temperature T_s vs. time from the FR (red solid line), standard EL (blue solid line) and EL-DBM (dashed lines) simulation approaches. The EL grid size is kept constant, while the bandwidth b_{DBM} used for DBM has been varied.

b_{DBM} used for the DBM has been varied across the range shown in the legend of Fig. 5.11, with increasing bandwidth widths leading to longer diffusion times and, hence, gas-solid interaction volumes that are considerably larger than the local Eulerian cell. Using the relation $b = \sigma\sqrt{2}$, the DBM considers Eulerian cells within the range $3 \cdot d_p\,(b = 8.5 \cdot 10^{-5})$ to $10 \cdot d_p\,(b = 27 \cdot 10^{-5})$, while $b = \infty$ is equivalent to the one-way coupling approach.

A similar behaviour can be found for the moving average CG method in Fig. 5.12. For the MAM different cube sizes have been set, i.e. $\Delta x_{\mathrm{MAM}} = \mathbf{i} \cdot d_p$ with $\mathbf{i} = 1, 2, 3, 5$. From Fig. 5.12 it is observed that $\Delta x_{\mathrm{MAM}} = 1 \cdot d_p$ (i.e. increasing the gas-solid interaction volume to have the width of the particle diameter, while the grid size is smaller than the latter) already shows a significant improvement compared to the non-CG EL data $\Delta x = 0.5 \cdot d_p$. Here, $\Delta x = \infty$ is equivalent to one-way coupling. Increasing the cube size for the MAM leads to further improvements of the EL-MAM predictions, where for $\Delta x_{\mathrm{MAM}} = 5 \cdot d_p$ the FR reference result is (almost) recovered. Overall, the application of the two coarse-graining methods EL-DBM and EL-MAM allows for recovering the detailed FR reference data, despite considering particle sizes considerably larger than the grid size.

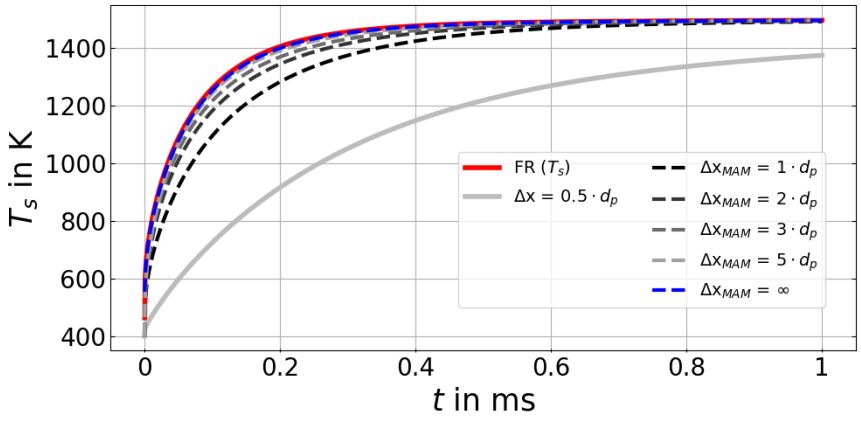

Figure 5.12: Pure particle heating: Comparison of particle surface temperature T_s vs. time from the FR (red solid line), standard EL (blue solid line) and EL-MAM (dashed lines) simulation approaches. The EL grid size is kept constant, while the cube size Δx_{MAM} used for MAM has been varied.

5.1.5.2 Heating, drying and devolatilisation

After demonstrating that the CG-DBM and CG-MAM EL approaches are capable of recovering the detailed FR data for pure particle heating, we turn our attention to the more general case of heating, drying and devolatilisation of a biomass particle. Figure 5.13 presents particle surface temperatures vs. time in a similar format as in the previous Sec. 5.1.5.1. The

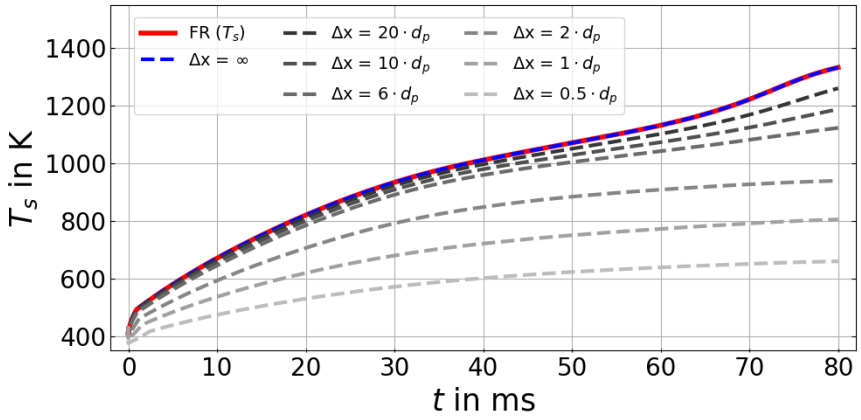

Figure 5.13: Particle heating, drying and devolatilisation: Comparison of particle surface temperature T_s vs. time from the FR (solid line) and standard EL (dashed lines) simulation approaches, where the EL grid size has been varied.

surface temperature profile of the FR case differs from the pure heating case because of the additional heat exchange due to the release of water vapour and volatile gases from the particle. The gases are released at particle surface temperature in the direction normal to the particle surface. Furthermore, the absorbed energy is used for the evaporation of moisture in the inner-most particle layer, that is included in the gases released from the particle surface and it also heats up the growing char layer.

The profiles predicted by the FR and (standard) EL approaches are identical for the benchmark case with $\Delta x = \infty$, again validating the comparison approach. Similar to the previous case of pure heating, refining the EL grid by decreasing the grid size also leads to increasingly larger deviations from the FR result for the present case of heating, drying and pyrolysis. Comparing the surface temperature at $t = 80\,\mathrm{ms}$ between the cases $\Delta x = \infty$ and $\Delta x = 0.5 \cdot d_p$ results in $\approx 50.5\,\%$ relative error.

In analogy to Sec. 5.1.5.1 the standard EL case with $\Delta x = 0.5 \cdot d_p$ is now taken as a reference and compared with results from the EL-DBM (Fig. 5.14) and EL-MAM (Fig. 5.15) approaches. As can be observed, both CG methods lead to significant improvements of the

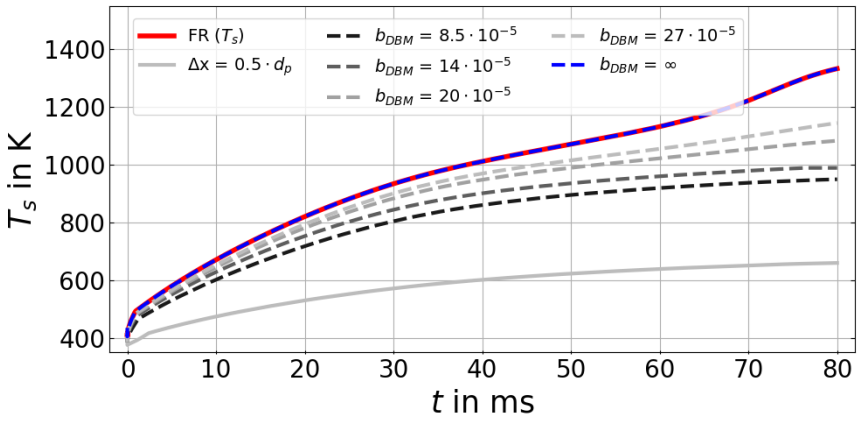

Figure 5.14: Particle heating, drying and devolatilisation: Comparison of particle surface temperature T_s vs. time from the FR (red solid line), standard EL (blue solid line) and EL-DBM (dashed lines) simulation approaches. The EL grid size is kept constant, while the bandwidth b_{DBM} used for DBM has been varied.

EL surface temperature predictions. This is achieved by either increasing the bandwidth of the DBM or increasing the edge length of the cube in MAM, both of which have a similar effect of considering a larger gas-solid interaction volume for CG.

With very large Δx_{MAM} or b_{DBM}, the FR data can faithfully be reproduced due to $T_g \rightarrow$ const., which is equivalent to the $\Delta x = \infty$ case in Fig. 5.13. Since it can be hypothesised that the required size of the CG interaction volume may be correlated with the thickness of the thermal boundary layer δ_t around the particle, next Sec. 5.1.5.3 studies the relationship between δ_t and suitable interaction volume sizes.

5.1.5.3 Boundary layer thickness and its relation to CG interaction volume

To establish correlations of boundary layer thickness δ_t and CG interaction volume, we extract δ_t from the FR data as the distance from the particle surface where $T_g = 0.99 T_\infty$ for pure particle heating and $T_g = 0.99 T_{g,\max}$ for particle heating, drying and devolatilisation. Correspondingly, the times when the (absolute) differences between the particle surface

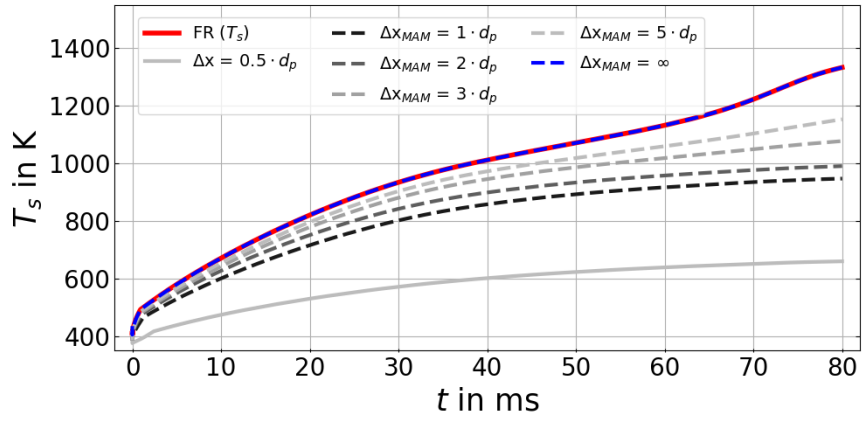

Figure 5.15: Particle heating, drying and devolatilisation: Comparison of particle surface temperature T_s vs. time from the FR (red solid line), standard EL (blue solid line) and EL-MAM (dashed lines) simulation approaches. The EL grid size is kept constant, while the cube size Δx_{MAM} used for MAM has been varied.

temperatures from FR and CG deviate by a threshold of 50 K are recorded for given values of the model parameters Δx_{MAM} and b_{DBM} from the cases shown in Figs 5.11, 5.12, 5.14 and 5.15. Using this data, time ranges of validity of the tested parameter values can be evaluated. For example in Fig. 5.15 $\Delta x_{\mathrm{MAM}} > 5 \cdot d_p$ is only valid for $0 \leq t < 48.6$ ms, before a deviation greater than 50 K from the FR data occurs. Making use of the FR data on boundary layer thickness as a function of time ($\delta_t = f(t)$), these validated CG model parameters can be mapped to given intervals of boundary layer thickness. Finally, the following general expressions for Δx_{MAM} and b_{DBM} as functions of normalised boundary layer thickness δ_t/d_p can be found using regression

$$b_{\mathrm{DBM}} \approx 18.679 \cdot 10^{-5} (\delta_t/d_p)^{0.113} \tag{5.30}$$

$$\Delta x_{\mathrm{MAM}}/d_p \approx 2.802 (\delta_t/d_p)^{0.146}. \tag{5.31}$$

Equivalently, for the combined physics of particle heating, drying and devolatilisation, the recommended CG parameter values can be reduced to

$$b_{\mathrm{DBM}} \approx 8.472 \cdot 10^{-5} \cdot 1.083^{(\delta_t/d_p)} \tag{5.32}$$

$$\Delta x_{\mathrm{MAM}}/d_p \approx 0.992 \cdot 1.117^{(\delta_t/d_p)}. \tag{5.33}$$

In the above expressions, the thickness of the thermal boundary layer was extracted from the FR data, which is generally not available in (inherently under-resolved) EL simulations. Therefore, in practical EL-CG simulations the boundary layer thickness must first be estimated, either based on the heat flux for quiescent environments or with the aid of the

Nusselt number for convective cases [215]

$$q_s = \frac{(d_p + 2\delta_t)k(T_s - T_g)}{\delta_t d_p} \quad \text{or} \quad \mathrm{Nu} = \frac{d_p + 2\delta_t}{\delta_t}, \tag{5.34}$$

before the above-derived expressions for the CG model parameters can be employed.

5.1.5.4 Computational time using EL-CG methods

Apart from accuracy, an important aspect of employing EL-CG methods is the increased computational time associated with employing the coarse-graining approach. Using the CPU time for the general case of particle heating, drying and devolatilisation in the standard EL framework (EL-PCM) as a reference, the normalised CPU time for the CG methods is PCM = 1.0, DBM = 58.62 and MAM = 1.1514. These numbers reveal that the MAM is slightly more expensive than the PCM, whereas DBM is almost 60 times more costly. This is due to the fact that the solid-gas interaction volume in MAM is limited to the MAM cube (or alternative shape), whereas for the DBM, by default, diffusion is applied to the entire computational domain. At the beginning of the simulation, the MAM identifies the cell neighbourhood relations, finds the neighbouring cells of each control volume inside Δx_{MAM} and stores them in a table. During the simulation, these neighbours are simply retrieved from the table without further search steps for increased efficiency. Moreover, MAM is computed in the two principal steps of averaging and redistributing the average to the underlying grid cells only, whereas the DBM may involve the computation of a large number of diffusion time steps for large bandwidths. While the efficiency of the DBM could also be increased by choosing an appropriate diffusion range, such improvements have not been attempted here and solely the CPU time for the standard DBM is reported.

5.1.6 Conclusions

In the present work, a layer-based sub-model for woody biomass conversion [151, 158] is coupled to both FR and EL simulation frameworks for solid particle conversion studies. A single cold biomass particle is located in a hot, quiescent, inert gas environment. The inert gas consists of nitrogen to suppress volatile combustion and char oxidation, and the heating, drying and devolatilisation of the particle is studied. The detailed FR setup is successfully validated against experimental data on torrefied woody biomass conversion in a drop tube reactor. Subsequently the layer-based sub-model is solved in the standard EL framework, showing that the EL approach is capable of reproducing the FR data for infinitely large grid sizes, while the standard EL method fails for highly refined computational grids where the grid size is close to or smaller than the particle size. To resolve this issue, a

previously suggested diffusion based method is employed for coarse-graining. Moreover, a new simple and efficient CG approach based on moving averages referred to as CG-MAM is proposed. The two CG methods recover the detailed FR data for both pure particle heating and heating, drying and devolatilisation if the CG model parameters that scale the CG interaction volumes are sufficiently large. Using the available FR data, recommended model parameter ranges are provided as a function of normalised boundary layer thickness. CG-MAM is shown to give similar results as CG-DBM, but at a much reduced computational cost, which makes it suitable for future simulations with multiple Lagrangian particles. We note that the cases investigated in the present work do not include chemical reactions or particle-particle interaction effects that occur in reacting dense particle clouds. Including chemical reactions and particle-particle effects requires detailed analyses of computationally-expensive FR simulations of particle groups in chemically reacting flow for a relevant range of conditions. Such FR simulations, see e.g. [27,28], and their intricate relationship with CG methods for EL approaches (that would need to account for a range of thermal boundary layer thicknesses, and relative flame-particle and particle-particle distances to only name some principal parameters) are beyond the scope of the present study, but should be considered by the research community in future work.

5.1.7 Acknowledgements

The authors acknowledge the financial support by the Deutsche Forschungsgemeinschaft for project number 450158108 and the Chinese Scholarship Council (no. 201906420087, S. Meng). The authors gratefully acknowledge the financial support by the Helmholtz Association of German Research Centres (HGF), within the research field Energy, program Materials and Technologies for the Energy Transition (MTET), topic Resource and Energy Efficiency.

5.2 Flame characterisation of gas-assisted pulverised coal combustion using FPV-LES

Research highlights

The second paper, *Luu et al., Proc. Combust. Inst. 39:3249-3258, 2023* [179] investigates the turbulence-chemistry-particle interaction by applying a FPV-LES modelling approach [62, 98, 216] to study a swirl-stabilised turbulent piloted coal flame in a laboratory-scale combustion chamber [145, 217, 218]. The combustion chamber consists of three inlet streams, namely the primary, secondary and tertiary flow. A rich mixture of methane-air and coal is injected through the primary flow. Additional air is provided via the secondary and tertiary flow for complete combustion. Products and burnt-out coal particles can leave the combustion chamber at the bottom through an annular orifice. The experimental geometry is illustrated in Fig. 5.16 (left). Small solid coal particles have been used as tracers

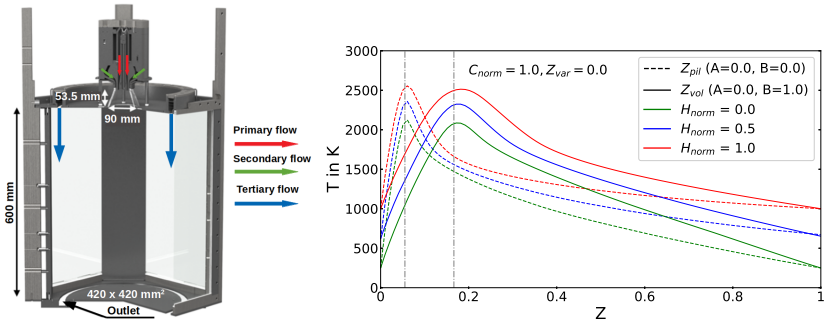

Figure 5.16: Left: Experimental geometry and inlet/outlet streams of the burner and combustion chamber. Right: Selected data from the six-dimensional flamelet table with temperature vs. Z for various enthalpy levels H_{norm}.

by PIV to determine the gas velocity [145]. The gas temperature is measured by vibrational O_2-CARS and tomographic absorption spectroscopy (TAS) [218]. The coal particles are described within the standard Euler-Lagrange approach. During the simulation, the filtered transport equations of mass, momentum and FPV control variables are solved, and the values of species mass fraction, enthalpy and progress variable source term are retrieved from the pre-calculated six-dimensional flamelet look-up table. A six-dimensional flamelet table is required to accurately model the complex turbulence-chemistry-particle interactions in the present gas-assisted coal flame within the multiphase FPV-LES framework. This table stores the various possible chemical states for retrieval during the simulation. The six dimensions of the table are a result of the occurrence of various fuel streams, which originate from coal volatiles, char off-gases and methane (three dimensions), the turbulence-chemistry interaction of the mixture (one dimension), the heat exchange between gas and solid phase

(one dimension) and the reaction progress variable (one dimension). A selected section of the flamelet table is shown in Fig. 5.16 (right) for different input parameters. At first, the simulation results are validated against experimental data of mean and RMS gas velocities, see Fig. 5.17 (top row), and mean gas temperature, see Fig. 5.17 (bottom row) at different downstream positions. From Fig. 5.17, a good agreement of the predicted mean and RMS

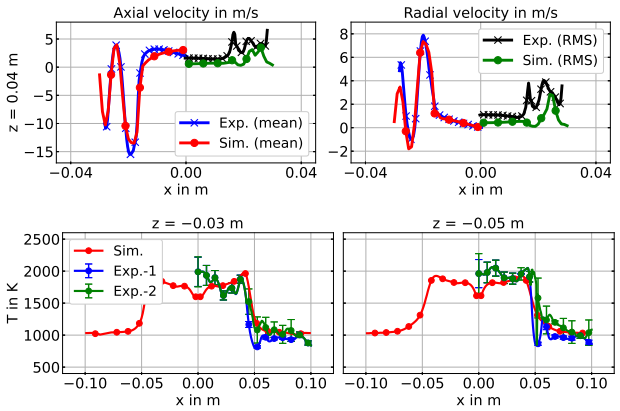

Figure 5.17: Top row: Comparison of the mean (left-half) and RMS (right-half) axial and radial gas velocity profiles between experiment and simulation. Bottom row: Comparison of the mean gas phase temperature profiles between experiment and simulation.

velocities and the mean gas temperature between experiments and simulations is obtained. After successfully validating the complex FPV-LES modelling approach, the combustion

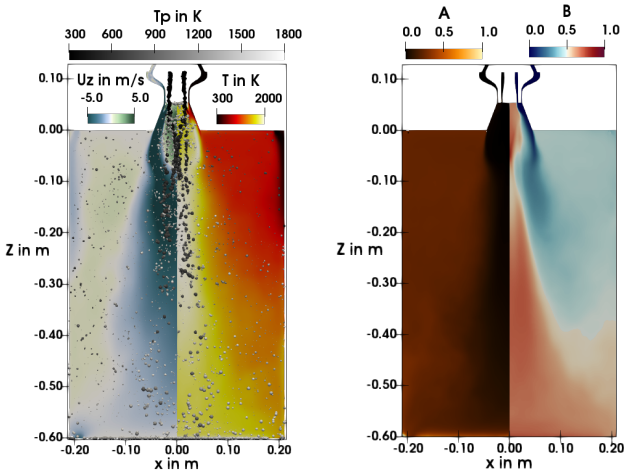

Figure 5.18: Time-averaged contours in the central x-z plane of the combustion chamber. Left: Axial gas velocity u_z and gas temperature T. Right: Flamelet input parameters A and B.

dynamics within the chamber are analysed in terms of axial gas velocity, gas and particle temperature and particle size distribution in Fig. 5.18 (left), providing valuable insights into the phenomena occurring inside the combustion chamber. Furthermore, the contributions of the distinct fuel streams are identified through the flamelet input parameters in Fig. 5.18 (right), allowing for the characterisation of regions where the different fuel streams dominate.

Paper 2:

Title:	Flame characterisation of gas-assisted pulverised coal combustion using FPV-LES
Authors:	Tien Duc Luu Institute for Combustion Technology (ITV), University of Stuttgart, Stuttgart, Germany Ali Shamooni Institute for Combustion Technology (ITV), University of Stuttgart, Stuttgart, Germany Oliver T. Stein Institute for Combustion Technology (ITV), University of Stuttgart, Stuttgart, Germany Andreas Kronenburg Institute for Combustion Technology (ITV), University of Stuttgart, Stuttgart, Germany Sebastian Popp Simulation of reactive Thermo-Fluid Systems (STFS), Technical University of Darmstadt, Darmstadt, Germany Hendrik Nicolai Simulation of reactive Thermo-Fluid Systems (STFS), Technical University of Darmstadt, Darmstadt, Germany Henrik Schneider Reactive Flows and Diagnostics (STFS), Technical University of Darmstadt, Darmstadt, Germany Xu Wen Simulation of reactive Thermo-Fluid Systems (STFS), Technical University of Darmstadt, Darmstadt, Germany Christian Hasse Simulation of reactive Thermo-Fluid Systems (STFS), Technical University of Darmstadt, Darmstadt, Germany
Journal:	Proceedings of the Combustion Institute
Year:	2023
Volume:	39
Pages:	3249-3258
Contributions by the present author:	Writing – original draft & editing, Methodology, Software, Validation, Formal analysis, Investigation, Data curation, Visualisation

Abstract

A multiphase flamelet/progress variable (FPV) model for the large eddy simulation (LES) of gas-assisted pulverised coal combustion (PCC) is developed. The target of the simulation is the Darmstadt turbulent gas-assisted swirling solid fuel combustion chamber. The coal particles are treated as Lagrangian point particles, the position, momentum and energy of which are tracked. The gas phase is described by the low-Mach Navier-Stokes equations alongside the Eulerian transport equations of the governing variables for the FPV model. The set of chemical states of the PCC flame is pre-tabulated in a six-dimensional flamelet table and determined by the mixing of the primary fuel stream, volatiles and char off-gases with the oxidising air, the progress of chemical reactions, the interphase heat transfer, as well as sub-grid scale variations. A presumed β-PDF approach for the total mixture fraction is applied to capture sub-grid scale effects. The discrete ordinate method (DOM) with the weighted sum of grey gases model (WSGGM) is employed to model radiation. The FPV-LES results are validated against the experimental evidence and a good agreement of the predicted mean and RMS velocities, as well as the mean gas temperature between experiments and simulations is obtained. The contributions of the pilot, volatile and char off-gas fuel streams to the coal flame are analysed. It is found that most regions of the furnace are dominated by either pilot or volatile combustion, while char conversion only occurs in the far downstream and outer furnace regions. The pilot gas dominates the near-wall region inside the quarl, whereas the volatile gas mainly released from small particles dominates a first volatile combustion zone in the interior of the internal recirculation zone. Larger particles heat up more slowly and release their volatile content further downstream, leading to a secondary volatile combustion zone.

5.2.1 Introduction

Pulverised coal combustion (PCC) is still a major source of primary energy and among the most widespread technologies for generating electrical baseload power. Therefore, the emission of pollutants and greenhouse gases from PCC continues to drive major research efforts to gain deeper insight in its underlying chemical and physical processes with the aim of mitigating pollution and climate change. The four major thermo-physical stages of PCC are heat-up and drying of the particles in a hot environment by convection and radiation, devolatilisation of the light gases initially embedded inside the particles, homogeneous gas combustion and heterogeneous char conversion. These processes primarily occur in consecutive order, but overlaps may exist and require appropriate modelling.

Direct numerical simulation (DNS) studies have been conducted for fully-resolved single particles [20, 27] and small particle clusters [26, 27]. Two recent examples extended the stud-

ies to large particle clouds by means of carrier-phase DNS [39, 42]. Nevertheless, the DNS of industrially-relevant applications remains unfeasible at present, due to the large-scale geometries, the wide range of turbulent scales, the enormous number of solid fuel particles, complex interphase coupling processes and the costly homogeneous and heterogeneous chemistry in PCC. A reasonable trade-off between computational cost and accuracy is the large eddy simulation (LES) approach for the gas phase coupled with Lagrangian tracking of the fuel particles, which has been applied in several recent studies on laboratory-scale and semi-industrial coal burners [66, 68, 72, 73]. An established combustion modelling approach with limited cost is the tabulated flamelet model that has been widely employed for single phase combustion in the past. An improvement of the flamelet model is provided by the flamelet/progress variable (FPV) approach [98], which is advantageous for capturing the flame dynamics. Watanabe et al. [62] devised FPV for solid fuel combustion with the introduction of two mixture fractions for the mixing of the volatiles and char off-gases with air, with later applications by Rieth et al. [100] and Wen et al. [216] to solid fuel flames in a turbulent mixing layer. The applicability of FPV-LES to laboratory and semi-industrial scale PCC burners has been demonstrated e.g. by Watanabe et al. [99] and Rieth et al. [66]. For gas-assisted PCC, as considered in the present study, Wen et al. [70] reported that a third mixture fraction is needed to characterise the gaseous pilot fuel. Knappstein et al. [68] and Nicolai et al. [72] avoided the third mixture fraction by assuming the volatile composition to correspond to the one of the pilot fuel. However, to consider a more typical volatile composition, a third mixture fraction is inevitable. Wen et al. [74] demonstrated first reasonable FPV-LES results for gas-assisted coal combustion using three mixture fractions.

The gas-assisted coal flame considered in the present study is the turbulent swirl flame experimentally studied at TU Darmstadt. Previous numerical predictions of this combustion chamber were reported in [68, 72, 74] and based on the earlier operating conditions of Becker et al. [219]. Recently, updated operating conditions and new measurements have been reported by Schneider et al. [145], Meißner et al. [217] and Emmert et al. [218], providing an extensive experimental database for the simulations in this work. The objectives of the present study are

- To accurately model the combustion in swirling gas-assisted coal flames
- To validate the predictions against state-of-the-art measurements
- To characterise the contributions of the pilot, volatile and char off-gas streams to the flame

and our progress towards these aims is discussed in the following sections.

5.2.2 Modelling approach

5.2.2.1 Gas phase

The gas phase is described by the filtered transport equations of total mass, momentum and the FPV control variables. The control variables are the reaction progress variable Y_{C}, total enthalpy H (sens. + chem.) and three mixture fractions Z_α, where α denotes the fuel streams originating from the coal volatiles ($\alpha = \mathrm{vol}$) and char off-gases ($\alpha = \mathrm{cog}$). Moreover, in the context of gas-assisted coal flames, a third mixture fraction ($\alpha = \mathrm{pil}$) is required to describe the mixing of the pilot fuel with air. The sub-grid viscosity is closed by the Smagorinsky approach [132]. The assumption $Le = 1$ is invoked and the turbulent mass/heat diffusivities are obtained from turbulent Schmidt/Prandtl numbers set to 0.7 [72]. The reaction progress variable is defined as $Y_{\mathrm{C}} = Y_{\mathrm{CO}} + Y_{\mathrm{CO_2}} + Y_{\mathrm{H_2O}} + Y_{\mathrm{H_2}}$ [220–222] The progress variable source term is retrieved from the flamelet look-up table. Thermal radiation is considered as a source term in the enthalpy transport equation. Radiative heat transfer is modelled by the discrete ordinate method (DOM) using 80 directions, where the absorption/emission coefficients are calculated with the weighted-sum-of-grey-gases model (WSGGM) and the coefficients from [223]. Isotropic scattering by the particles is considered to be dominant, while gas phase scattering is neglected. The gas phase is coupled to the Lagrangian particles via interphase transfer terms [39].

5.2.2.2 Solid phase

The solid particles are described within the Lagrangian framework. Their interaction with the gas phase is characterised by the transfer of mass from devolatilisation and char conversion, momentum from drag, gravity and sub-grid dispersion, and energy through convective and radiative heat transfer, as well as the heats of devolatilisation and char conversion. The solid phase governing equations read

$$\frac{dm_p}{dt} = -(\dot{m}_{p,\mathrm{devol}} + \dot{m}_{p,\mathrm{char}}) \tag{5.35}$$

$$\frac{d\mathbf{u}_p}{dt} = \frac{\widetilde{\mathbf{u}} - \mathbf{u}_p}{\tau_p} + \left(1.0 - \frac{\bar{\rho}}{\rho_p}\right)\mathbf{g} + \frac{d\mathbf{u}_{p,\mathrm{sgs}}}{dt} \tag{5.36}$$

$$\frac{dT_p}{dt} = \frac{6\mathrm{Nu}\cdot c_p\bar{\mu}}{\mathrm{Pr}\cdot c_{p,p}\rho_p d_p^2}(T - T_p) + \frac{\varepsilon_p A_p \sigma}{m_p c_{p,p}}(\Theta_r^4 - T_p^4) + \frac{\dot{Q}_{\mathrm{devol}}}{m_p c_{p,p}} + \frac{\dot{Q}_{\mathrm{char}}}{m_p c_{p,p}}, \tag{5.37}$$

where ρ_p, d_p, $c_{p,p}$, A_p are the density, diameter, heat capacity, and projected area of the particle, with otherwise standard nomenclature. The particle response time is calculated as $\tau_p = \frac{\rho_p d_p^2}{18\bar{\mu}}(1 + 0.15 Re_p^{2/3})^{-1}$. The particle Reynolds number is calculated as $\mathrm{Re}_p = \bar{\rho}|\widetilde{\mathbf{u}} - \mathbf{u}_p|\frac{d_p}{\bar{\mu}}$ and the Nusselt number as $\mathrm{Nu} = 2 + 0.552\mathrm{Re}_p^{1/2}\mathrm{Pr}^{1/3}$. The term $\frac{d\mathbf{u}_{p,\mathrm{sgs}}}{dt}$ refers to sub-grid

particle dispersion according to the model by Bini and Jones [224]. The particle emissivity ε_p linearly reduces from 0.9 to 0.5 during char burnout [39]. The Eulerian radiation temperature Θ_r is retrieved from the DOM [86, 189]. Devolatilisation is described by a competing two-step model with coefficients fitted to the Rhenish lignite coal [145] from the experiments. Darmstadt's Pyrolysis Kinetics Preprocessor (PKP) is employed for fitting, with a multi-step heterogeneous mechanism of PoliMi [146] for a range of heating rates extracted from the simulations of Nicolai et al. [72]. It is assumed that char entirely consists of carbon such that the char off-gases are solely composed of CO and N_2. During devolatilisation, the particle diameter is assumed to remain constant and the density of the particle reduces, whereas constant density and shrinking particle diameter are assumed during char conversion. To consider the effect of devolatilisation in the momentum and energy equations of the particle, a blowing correction is applied. The particle heat capacity, two-step devolatilisation model, char conversion and blowing correction model are similar to [39].

5.2.2.3 Combustion modelling

The chemistry tables are generated with the flamelet solver *pyFLUT* coupled with *Cantera* [173] to solve the 1D governing equations of continuity, radial momentum, energy, and species for counterflow diffusion flames. Similar to Wen et al. [70] we employ a three mixture fraction system based on the total mixture fraction Z

$$Z = Z_{\mathrm{pil}} + Z_{\mathrm{vol}} + Z_{\mathrm{cog}} \tag{5.38}$$

and two mixing ratios [225]

$$A = \frac{Z_{\mathrm{cog}}}{Z_{\mathrm{vol}} + Z_{\mathrm{cog}} + \epsilon}, \quad B = \frac{Z_{\mathrm{vol}} + Z_{\mathrm{cog}}}{Z_{\mathrm{vol}} + Z_{\mathrm{cog}} + Z_{\mathrm{pil}} + \epsilon} \tag{5.39}$$

where ϵ represents a small positive number. To consider heat exchange between the gas and solid phase, flamelet tables with various enthalpy levels are generated, accounting for the minimum and maximum enthalpy of the fuel and oxidiser. A normalisation method is employed to the total enthalpy and reaction progress variable to simplify flamelet tabulation [226], leading to normalised quantities H_{norm} and C_{norm} ranging from zero to one. Turbulence-chemistry interactions are considered via integration of a β-PDF for the filtered total mixture fraction $\widetilde{Z}$ and its subgrid variance $\widetilde{Z''^2}$, with the latter obtained algebraically [227]. Homogeneous chemistry is described by the CRECK52 mechanism consisting of 52 species and 452 reactions [27]. The flamelet table is parameterised via $\Phi = \Im(A, B, \widetilde{Z}, \widetilde{Z''^2}, \widetilde{H}_{\mathrm{norm}}, \widetilde{C}_{\mathrm{norm}})$ with dimensions $6 \times 6 \times 101 \times 11 \times 11 \times 101$, resulting in a total size of 25 GB. For efficient parallel computing, a memory abstraction layer (MAL) [228] is employed.

A selected section of the flamelet table is visualised in Fig. 5.19. The input parameters have been selected to refer to the (pure) pilot and volatile fuel streams as an example. The stoichiometric mixture fractions of the fuels in air are shown as $Z_{\mathrm{pil,st}} = 0.055$ and $Z_{\mathrm{vol,st}} = 0.167$. For the selected values of $C_{\mathrm{norm}} = 1$ and $Z_{\mathrm{var}} = 0$ Fig. 5.19 shows pure pilot and volatile fuel combustion for three levels of normalised enthalpy H_{norm}, with the latter controlling the flamelet boundary temperature.

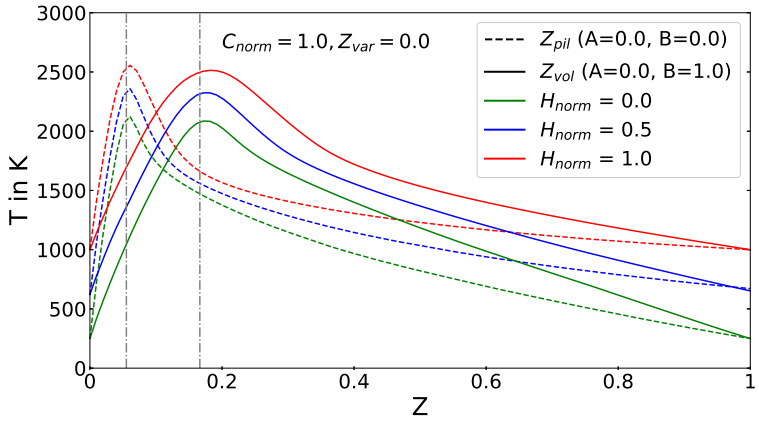

Figure 5.19: Selected data from the six-dimensional flamelet table with temperature vs. Z for various enthalpy levels. The input parameters have been selected to refer to either pure pilot or volatile fuel. The vertical dashed-dotted lines indicate the corresponding stoichiometric mixture fractions.

5.2.3 Experimental and numerical setup

The experimental configuration is the swirling gas-assisted solid fuel combustion chamber of TU Darmstadt [68, 74, 219]. The experimental geometry and computational domain are shown in Fig. 5.20. The combustion chamber has a cross-section of 420×420 mm^2 and a height of 600 mm. Various fuels and oxidisers may enter the chamber via three inlet streams, namely the primary (I), secondary (II) and tertiary flow (III), where a split into straight and inclined inlet channels allows for a variation of swirl in the secondary flow. Here, we consider coal combustion with air using the injection rates given in Tab. 5.5, which follows the experiments [145, 217, 218]. Coal particles are injected in a rich mixture of methane and air, which serves as a pilot stream to ignite the particles. The secondary flow provides swirling

Table 5.5: Volume flows and particle load of the investigated operating condition. Primary (I), secondary (II) and tertiary inlet flow (III). Units [m^3/h] for gas and [kg/h] for particles.

I Methane	2.01	II Straight Oxid.	0
I Particles	3.36	II Inclined Oxid.	11.09
I Oxidiser	12.1	III Oxidiser	24.02

air as oxidiser, while additional air is injected via the tertiary flow to support complete

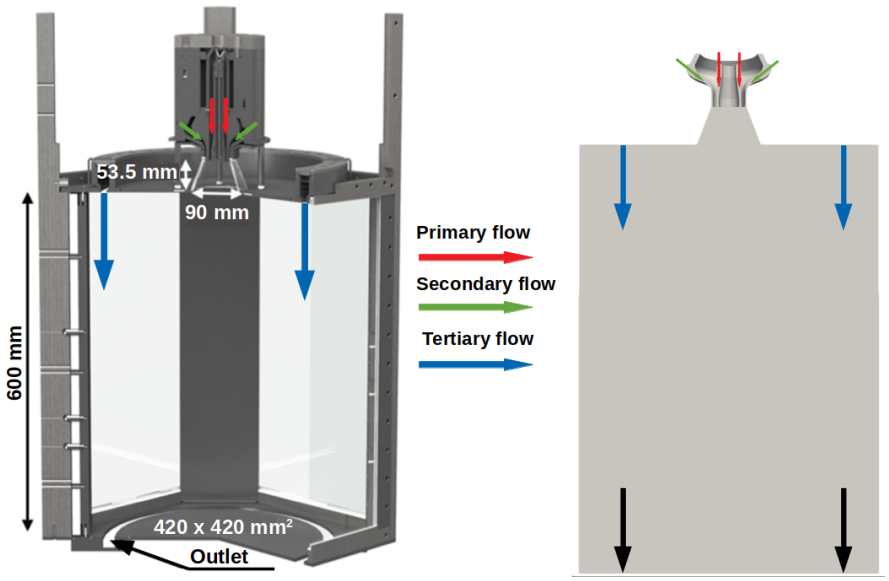

Figure 5.20: Geometry and inlet/outlet streams of the TUD burner. Left: Experiment [145], right: Computational domain.

combustion. The contribution of coal and methane to the total thermal input is 50% each, with the stability limit lying at 40-45% methane. Products leave the chamber through an annular orifice at the bottom of the chamber. The surrounding walls of the burner quarl and combustion chamber consist of quartz glass for optical access. Small solid coal particles are used as tracers to determine the gas velocity by PIV [145]. The gas temperature is measured by vibrational O_2-CARS and tomographic absorption spectroscopy (TAS) [218].

The computational mesh is generated with *snappyHexMesh* and contains a total of 3,843,172 hexahedral and split-hexahedral cells, ranging from $\Delta_{x_i} \approx 1$ mm (within the quarl) to 4 mm (downstream). Two thin layers of cells increase the near-wall resolution. A uniform velocity profile is assumed for the inlet patches, matching the experimental mass flow rates from Tab. 5.5. The inlet boundary conditions for the flamelet control variables are $Z_{\mathrm{pil}} = 0.08456$, $Z_{\mathrm{vol}} = Z_{\mathrm{cog}} = Y_C = 0.0$ and $H = -376{,}008\,\mathrm{J/kg}$ ($T = 314\,\mathrm{K}$) for the primary stream. The (cold) pilot mixture is ignited by temporarily adding an artificial source term for the reaction progress variable in the quarl region, which is removed after 250 ms. At the remaining inlet patches all Z_α and Y_C are zero, and the enthalpy is set to reflect air at 314 K. An a priori calculation of the two-phase flow and heat transfer upstream of the inlet patches of the simulation domain has been conducted to determine the inlet gas temperature $T_g = 314\,\mathrm{K}$ and particle conditions for the computational domain. A no-slip wall boundary condition is employed at the lateral boundaries and wall temperatures correspond to the experiments [217]. The radiative emissivity of the quartz walls is set to $\varepsilon_w = 0.7$. Rhenish lignite is considered, with its proximate and ultimate analysis given in [145]. After Q-factor adjustment the initial coal composition becomes $Y_{\mathrm{ash}} = 0.0552$, $Y_{\mathrm{VM}} = 0.553$ and $Y_{\mathrm{FC}} = 0.3918$. The volatile com-

position corresponds to the one of Wen et al. [74], apart from removing H_2S and NH_3 from the volatiles and adding their mass to the ash. The volatile composition is $Y_{CH_4} = 0.086$, $Y_{C_2H_4} = 0.039$, $Y_{C_6H_6} = 0.152$, $Y_{CO} = 0.252$, $Y_{CO_2} = 0.282$, $Y_{H_2} = 0.01$ and $Y_{H_2O} = 0.179$. The size distribution of the injected coal particles follows ref. [68].

The simulations are performed with a low-Mach reactive multiphase solver based on OpenFOAM-v2006. Second-order central differencing is used for spatial discretisation, while a total variation diminishing (TVD) limiter (denoted as *limitedLinear* in OpenFOAM) is employed for convection. Limiters were adopted to obtain bounded scalars and for enhanced simulation stability. Time integration is performed with a backward differencing scheme. A variable time-step of $\Delta t \approx 5e^{-6}$s is chosen, corresponding to CFL ≈ 0.3. The simulations are first run for single-phase reacting conditions, i.e. without coal particles. Subsequently particles are injected and temporal statistics are started when the particle ensemble in the upstream furnace reaches a steady state (after 2 s). Computations are run for a total physical time of 3.5 s, resulting in 265K statistical samples. A typical FPV-LES run requires ≈150,000 CPUh using 512 AMD-7742 cores on HLRS *Hawk*.

5.2.4 Results and discussion

5.2.4.1 Numerical validation

A first validation of the simulation results can be obtained by comparing the predicted mean and RMS gas velocities to the experimental data in Figs. 5.21 and 5.22. At $z = 0.04$ m in Fig. 5.21, i.e. just downstream of the primary and secondary inlets to the burner quarl, the two inlet streams can clearly be identified by the negative peaks of axial velocity (which is defined negatively in the positive downstream direction [219]). Conversely, the positive axial velocities observed in the centre of the domain and between the two inlets indicate the inner recirculation zone, as well as a small annular recirculation zone that leads to the formation of the side flame (discussed later in Fig. 5.24 (a)). At $z = 0.04$ m the agreement of the mean velocity predictions and experiments is good, with a slight under-prediction of the velocity peaks in the simulation. The quality of agreement between the simulations and the experiments remains good when moving to the downstream measurement locations $z = 0.03 ... -0.09$ m, with somewhat narrower profiles of the predicted mean velocity at intermediate positions $z = 0.02$ and -0.01 m, and a better correspondence again further downstream. Similarly, the predictions of the mean radial velocity profiles are very good throughout, with mild under-predictions of the peak values at $z = 0.03 ... 0.02$ m. The comparison of the RMS profiles of the axial and radial gas velocities shows that the level of turbulent fluctuations is generally captured well by the simulations, with minor discrepancies for larger values of $|x|$. The predicted RMS is somewhat lower than the measured one,

which is partially attributed to the fact that only the resolved part of the velocity RMS from the LES is compared to the measurements. Larger discrepancies can be observed for the

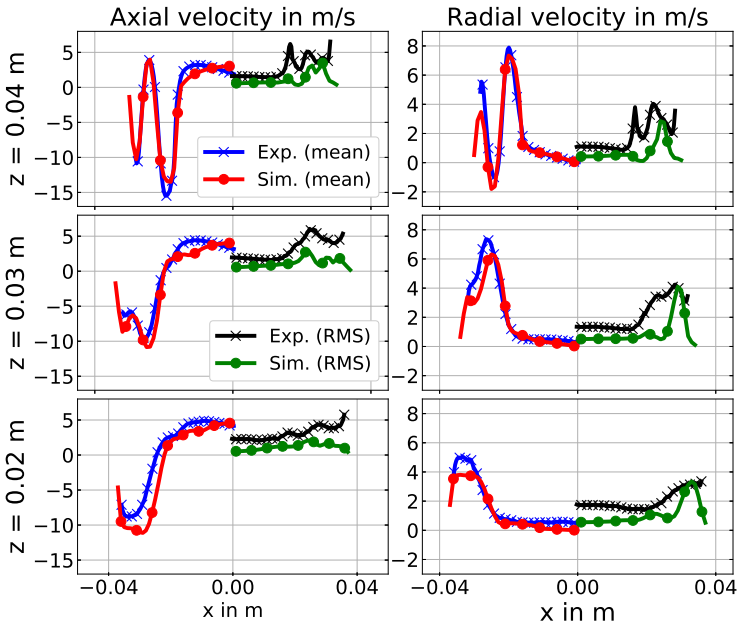

Figure 5.21: Comparison of the mean (left-half) and RMS (right-half) axial and radial gas velocity profiles between experiment and simulation inside the quarl.

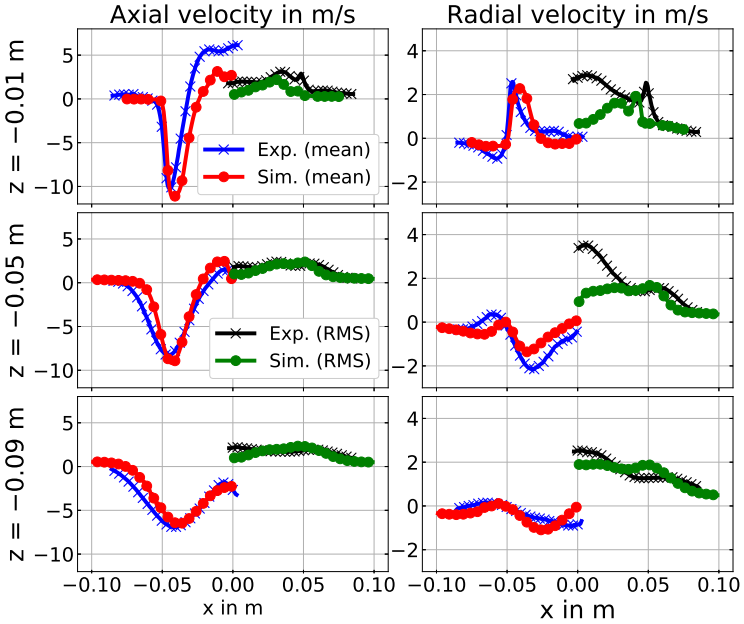

Figure 5.22: Comparison of the mean (left-half) and RMS (right-half) axial and radial gas velocity profiles between experiment and simulation downstream of the quarl.

RMS of the radial gas velocity at $z = -0.01$ and $-0.05\,\mathrm{m}$ for $|x| < 0.05\,\mathrm{m}$. In these regions volatile gases are released from small particles and a strong momentum exchange with large particles occurs, see Fig. 5.24 (b) later, which dampens the turbulent fluctuations in the gas

phase. The discrepancy may be explained by the fact that the comparison shows predicted gas phase velocities vs. measured velocities obtained from using the coal particles as flow tracers and by minor asymmetries in the PIV measurements. However, given the complexity of the considered multiphase reacting flow, the overall agreement shown in Figs. 5.21 and 5.22 is good.

This finding is confirmed by the comparison of the mean gas temperatures from simulations and experiments along the radial coordinate shown at different downstream positions in Fig. 5.23. The overall agreement between the FPV-LES predictions and the experimental

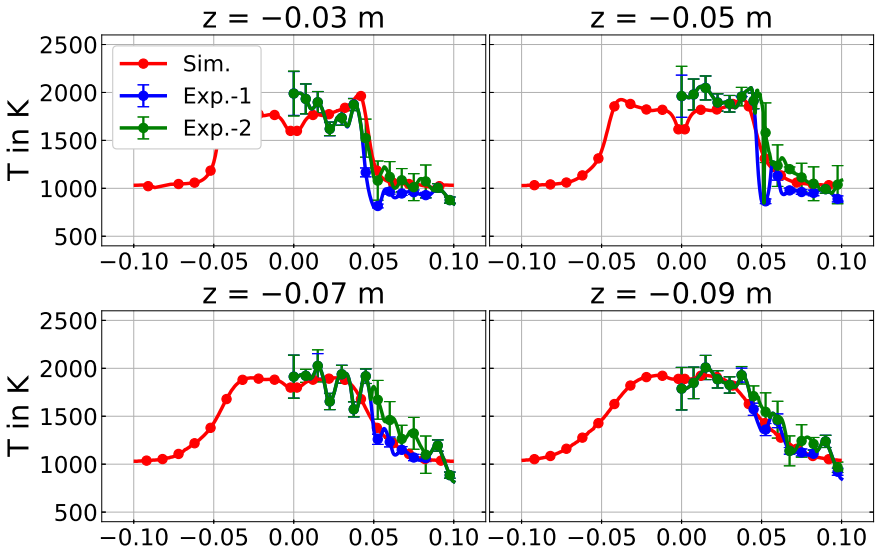

Figure 5.23: Comparison of the mean gas phase temperature profiles between experiment and simulation at selected downstream positions. Regular TAS (Exp-1, blue) and TAS overlaid with fluctuation model (Exp-2, green) [218].

evidence is good, with the predicted temperature mostly lying well inside the experimental scatter. The only exception is the under-prediction of the gas temperature near the centreline at $z = -0.03$ and $-0.05\,\mathrm{m}$. A fuel composition of $\approx 80\%$ volatiles and $\approx 20\%$ pilot fuel can be found at these axial locations on the centreline. As the peak temperature of the pilot flame is slightly higher than the one of the volatile flame, see Fig. 5.19, we attribute the under-prediction of the mean temperature to a slight underestimation of the mixing between pilot and volatiles. As the pilot fuel becomes more dominant at larger radii, the temperature increases and matches the experiment very well, Fig. 5.23. However, considering the uncertainties of both the simulation approach and the experiments for this complex multi-physics problem, the joint agreement demonstrated in Figs. 5.21, 5.22 and 5.23 is overall satisfactory and the FPV-LES methodology captures both the flow field and flame position accurately.

5.2.4.2 Flame analysis

After validating the modelling approach, a first impression of the coal conversion process inside the combustor can be obtained from Fig. 5.24 which shows time-averaged contours of

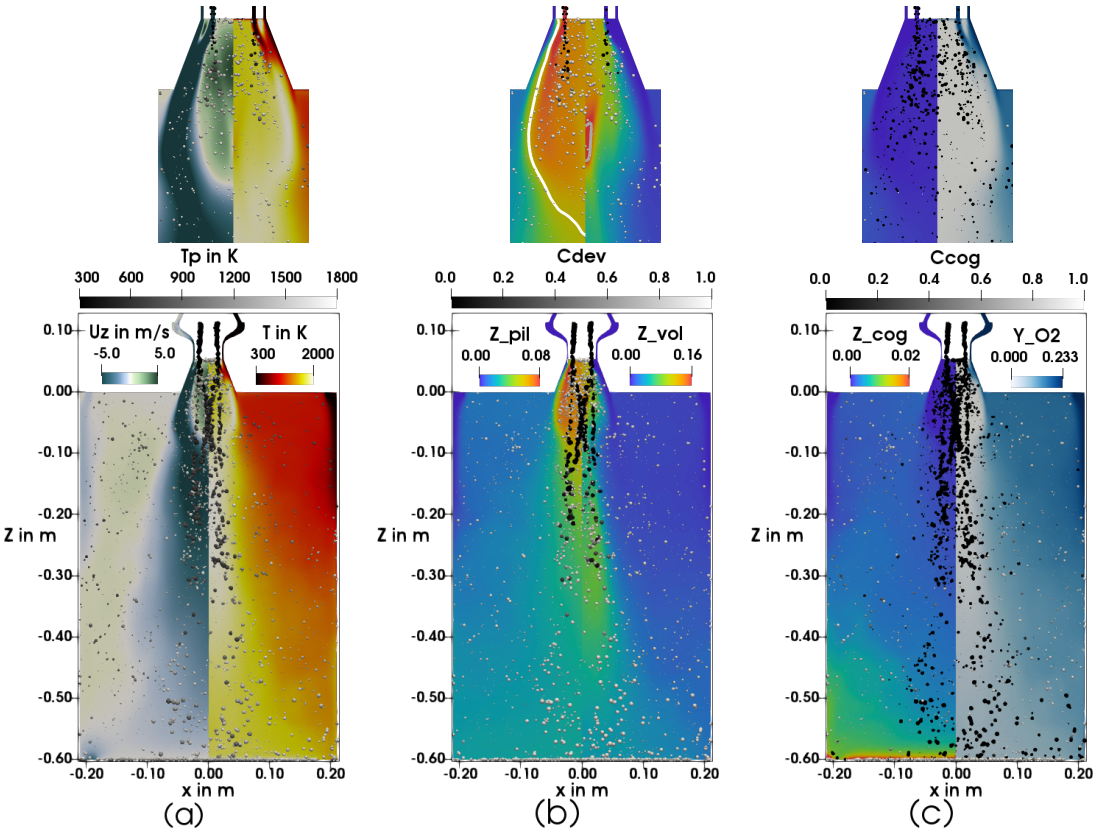

Figure 5.24: Time-averaged contours in the central x-z plane of the combustion chamber with a zoom into the quarl region (with only small particles for clarity) in the top row. (a) axial velocity and temperature of the gas, (b) pilot and volatile mixture fraction with isolines $Z_{\mathrm{pil,st}}$ (white) and $Z_{\mathrm{vol,st}}$ (grey), (c) char off-gas mixture fraction and mass fraction of O_2. An instantaneous snapshot of the coal particles is overlaid, where particles are scaled by diameter and coloured according to (a) temperature T_p, (b) devolatilisation progress C_{dev} and (c) char conversion progress C_{cog}.

the principal flame quantities that characterise the multiphase fuel conversion process. The mean gas phase contours are overlaid by instantaneous snapshots of the Lagrangian particles coloured by their temperature T_p, devolatilisation C_{dev} and char conversion C_{cog} progress in Fig. 5.24 (a), (b) and (c) respectively. C_{dev} and C_{cog} are defined to be 0/1 at the beginning/end of the devolatilisation/char conversion process. In Fig. 5.24 (a), it can be observed that in the quarl region the (unswirled) primary and (swirled) secondary flow streams merge rapidly and form a bell-shaped inner recirculation zone mainly composed of hot combustion products. From its injection location at $z = 0$, $x = \pm 0.195\,\mathrm{m}$ the (unswirled) tertiary flow stream initially stays close to the lateral walls of the combustion chamber, developing a large external recirculation zone (green colours on the left half of Fig. 5.24 (a)). The right frame

of Fig. 5.24 (a) shows that the highest gas temperatures are located inside the burner quarl and along the centreline of the combustion chamber, with increasingly wider profiles of high temperature with increasing downstream distance. Directly at the entrance of the quarl, between the primary and secondary streams, a side flame is established, as was also discussed in an earlier study of the same combustor [68]. While larger particles ($d_p > 100\,\mu m$) leave the burner quarl towards the downstream region, most of the smaller particles are entrained in the inner recirculation zone where they heat up quickly and proceed with their conversion process. Conversely, the large particles heat up more slowly and are mainly converted in the middle and downstream furnace. A comparison of gas temperature from Fig. 5.24 (a) with the pilot and volatile mass fractions in Fig. 5.24 (b) shows that the flame is located in regions of large gradients of Z_{pil} in the upstream and of Z_{vol} in the middle and downstream regions. The pilot flame dominates the inner recirculation zone, the outside of which features stoichiometric regions of Z_{pil} (white line). The small coal particles are heated up by the pilot flame and hot combustion products, releasing their volatiles as indicated by their high values of C_{dev}. However, only a limited mass of volatiles is released in the quarl, as indicated by the small region of $Z_{\mathrm{vol,st}}$ (grey line), due to the large particles mainly escaping the inner recirculation zone without significant levels of devolatilisation progress. The higher thermal inertia of the large particles leads to a slower increase of C_{dev} and, therefore, a later release of volatile matter, indicated by the regions with increased values of Z_{vol} in the main furnace from $z = -0.15 \ldots -0.4$ m. However, in regions where large particles start their conversion process the mean values of Z_{vol} show that the stoichiometric value is not reached, while instantaneous snapshots of Z_{vol} (not shown for brevity) reveal that locally around individual coal particles, although values of $Z_{\mathrm{vol}} > Z_{\mathrm{vol,st}}$ are reached, only small local volatile flames are stabilised. The left side of Fig. 5.24 (c) shows the mixture fraction of the char off-gases. No char conversion can be observed in the quarl region and regions near the centreline, as indicated by both Z_{cog} and C_{cog}. This can be explained by the absence of oxygen in these regions, which has been fully consumed by the combustion of the pilot fuel and coal volatiles, see right side of Fig. 5.24 (c). However, significant levels of char conversion can be observed at the bottom of the combustion chamber. Here, particles are clustered and due to the sufficient amount of oxygen, provided from the tertiary stream, char conversion proceeds.

The flame is now analysed in terms of the contributions of the various fuel streams to combustion. As was observed in Fig. 5.24 (c) char conversion only occurs in the downstream and outer regions of the furnace, whereas the inner and upstream zones are dominated by the pilot and volatile streams. Therefore, the present paragraph focuses on the characteristics of the pilot and volatile flame. Figure 5.25 (a) compares the mean gas temperature from the coal flame (multiphase, right half) to an auxiliary simulation of a pilot-only flame without coal particles (single phase, left half). Lower temperatures can be observed in the

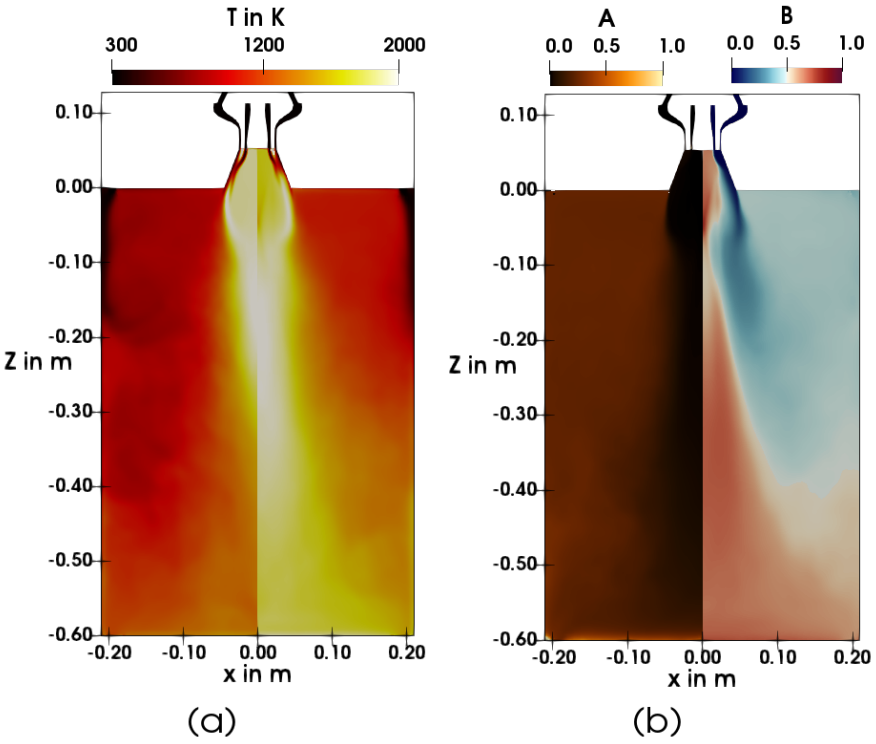

Figure 5.25: Time-averaged gas quantities in the central x-z plane. a) Temperature contours of the pilot-only flame (single phase, left half) and piloted coal flame (multiphase, right half), (b) flamelet input parameters A and B (multiphase).

internal recirculation zone of the coal flame when compared to the pilot-only flame, which is attributed to the coal particles and volatile gases absorbing heat from the surrounding gas phase. Different visual flame lengths can be seen in Fig. 5.25 (a), where the pilot-only flame reaches $z = -0.25\,\mathrm{m}$ and the coal flame $z = -0.4\,\mathrm{m}$. The peak temperature for both flames is similar, which is reasonable due to the tabulated temperatures shown in Fig. 5.19. A clear differentiation of the contributions of the pilot and volatile fuel to the coal flame can be obtained from the flamelet input parameters A and B, the temporal means of which are shown in Fig. 5.25 (b). In the absence of char conversion in the upper furnace A and B from Eq. (5.39) can be used to uniquely identify a pilot-only flame by $A = B = 0$, whereas $A = 0$, $B = 1$ indicates are pure volatile flame. A flame from mixed pilot and volatile fuel is obtained for $A = 0$ and $0 < B < 1$. In Fig. 5.25 (b), the mixing ratio A attains values of zero in the upstream and central part of the furnace, confirming the presence of pilot and/or volatile fuel and the absence of char conversion in these regions. The mixing ratio B illustrates two major flame zones where A is zero, with the blue regions for B indicating the pilot as the main fuel source, whereas red colours for B refer to volatile fuel. The pilot fuel dominates the outside of the internal swirl-stabilised recirculation zone and the external recirculation zone. The volatile fuel dominates the interior of the internal recirculation zone up to $z = -0.05\,\mathrm{m}$ and a secondary downstream volatile combustion zone spanning from $z = -0.1 \ldots -0.6\,\mathrm{m}$ with in-

creasingly wider profiles with increasing downstream distance. Hence, in the mean, volatile combustion proceeds in a small upstream region inside the quarl where mainly fuel from the smallest particles is consumed, and in a secondary volatile combustion zone in the centre of the downstream furnace, where the volatile fuel from the larger particles is burnt. This is confirmed in Fig. 5.26 which shows a scatter plot of the particle devolatilisation progress C_{dev} vs. the downstream z-coordinate coloured by the particle diameter. It can be observed

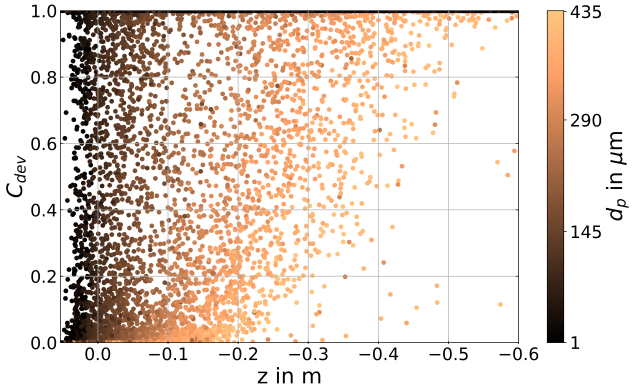

Figure 5.26: Scatterplot of particle devolatilisation progress C_{dev} vs. z-coordinate coloured by the particle diameter.

that the majority of small particles completes its devolatilisation progress in the upstream recirculation region, whereas most large particles only reach $C_{\mathrm{dev}} = 1$ in the downstream furnace, resulting in the two separated zones of volatile combustion.

5.2.5 Conclusions

In the present work a comprehensive model for the turbulent combustion of piloted pulverised solid fuels, namely a six-dimensional multiphase FPV-LES approach, is proposed and validated. The modelling approach is applied to predict a swirl-stabilised piloted coal flame in the TU Darmstadt solid fuel combustion chamber. The simulation results are validated against the experimental evidence and radial profiles of the mean and RMS gas velocities, as well as the mean gas temperature show a good accordance between experiments and simulations. When analysing the contributions of the pilot, volatile and char off-gas fuel streams to the coal flame, it is found that the pilot gas mainly dominates the area near the wall inside the quarl and the external recirculation zone. Two separate zones of volatile combustion are identified. A small upstream region in the interior of the inner recirculation zone that is mainly fuelled by recirculating small particles and a secondary volatile flame region in the centre of the downstream furnace that is dominated by the larger coal particles. Char conversion is negligible where pilot and volatile fuel dominates, but char combustion occurs near the bottom of the combustion chamber and at larger radii.

5.2.6 Acknowledgments

The authors acknowledge the financial support by the Deutsche Forschungsgemeinschaft for project numbers 238057103, 450158108 and 215035359. We are grateful for HPC time on HLRS Hawk and bwHPC.

5.3 Carrier-Phase DNS of Ignition and Combustion of Iron Particles in a Turbulent Mixing Layer

Research highlights

The Euler-Lagrange approach has been successfully validated and applied for volatile-containing solid fuel particles (i.e. coal and biomass) in the first and second research paper associated with the present research objectives. In the third paper, *Luu et al., Flow Turb. Combst. 112:1083-1103, 2024* [180], the third research objective is addressed. Here, the Euler-Lagrange framework is extended from volatile-containing solid fuels to the oxidation of non-volatile metal particle clouds. In this context, an iron oxidation sub-model [164, 165] has been implemented in the Euler-Lagrange framework of OpenFOAM and CP-DNS of monodisperse reacting iron particle clouds in a turbulent mixing layer has been studied. The study provides a first-of-its-kind study of iron particles in shear-driven turbulence. At first,

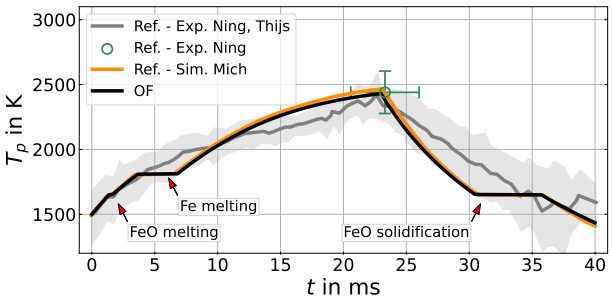

Figure 5.27: Comparison of particle temperature T_p vs. time t for laser-ignited single iron particles. Present work (OF), ref. [165] (Ref.–Sim.) and refs [23, 229] (Ref.–Exp.).

the implementation of the iron oxidation sub-model has been successfully validated against experimental data from a laser-ignited reactive single iron particle [23, 229] in Fig. 5.27. The comparison in Fig. 5.27 shows good alignment between the reference simulation and experimental measurements. Additionally, various particle diameters and environmental conditions were tested, demonstrating the robustness and reliability of the results. After the validation, the interaction between turbulence, ignition and combustion of iron particle clouds in the CP-DNS framework is investigated. A first visual impression of the temporal evolution of the mixing layer can be seen in Fig. 5.28. The initially separate streams develop and create a mixing region between them. This mixing process carries particles from the cooler upper stream to the hotter lower stream. As these particles interact with the hot stream, they heat up and oxidise once they reach the critical ignition temperature. A significant increase in gas temperature is observed only in areas with a high concentration of iron particles. The particle behaviour throughout the entire process is observed and visualised in scatterplots. The

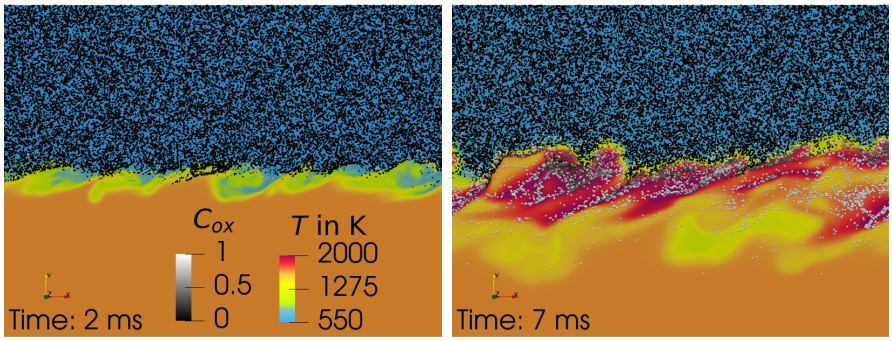

Figure 5.28: Snapshots of gas temperature T in the x-y plane at $L_z/2$. The particles are coloured by their oxidation progress C_{ox}.

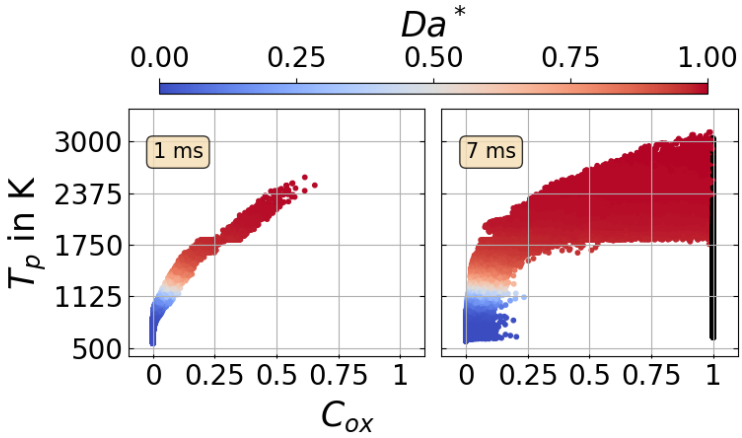

Figure 5.29: Scatterplots of particle temperature T_p vs. oxidation progress C_{ox} coloured by the normalised Damköhler number Da^*.

scatterplots in Fig. 5.29 indicate that the particles experience different combustion regimes. By analysing the particle colour, which represents the normalised Damköhler number, it is shown that for temperatures $T_p < 1125\,\mathrm{K}$ and oxygen concentrations $C_{\mathrm{ox}} < 0.2$, all particles are in the kinetically limited regime ($\mathrm{Da}^* \to 0$). In the intermediate temperature range of $1125 < T_p < 1500\,\mathrm{K}$, a transition from kinetic to diffusion-limited ($\mathrm{Da}^* \to 1$) can be observed.

Paper 3:

Title: Carrier-Phase DNS of Ignition and Combustion of Iron Particles in a Turbulent Mixing Layer

Authors:

Tien Duc Luu
Institute for Combustion Technology (ITV),
University of Stuttgart, Stuttgart, Germany,
Engler-Bunte-Intsitute, Simulation of Reacting Thermo-Fluid Systems (TFS),
Karlsruhe Institute of Technology, Karlsruhe, Germany

Ali Shamooni
Institute for Combustion Technology (ITV),
University of Stuttgart, Stuttgart, Germany

Andreas Kronenburg
Institute for Combustion Technology (ITV),
University of Stuttgart, Stuttgart, Germany

Braig Daniel
Simulation of reactive Thermo-Fluid Systems (STFS),
Technical University of Darmstadt, Darmstadt, Germany

Johannes Mich
Simulation of reactive Thermo-Fluid Systems (STFS),
Technical University of Darmstadt, Darmstadt, Germany

Bich-Diep Nguyen
Simulation of reactive Thermo-Fluid Systems (STFS),
Technical University of Darmstadt, Darmstadt, Germany

Arne Scholtissek
Simulation of reactive Thermo-Fluid Systems (STFS),
Technical University of Darmstadt, Darmstadt, Germany

Christian Hasse
Simulation of reactive Thermo-Fluid Systems (STFS),
Technical University of Darmstadt, Darmstadt, Germany

Gabriel Thäter
Institute of Fluid Mechanics (ISTM),
Karlsruhe Institute of Technology, Karlsruhe, Germany

Maurizio Carbone
Theoretical Physics I,
University of Bayreuth, Bayreuth, Germany,
Max Planck Institute for Dynamics and Self-Organisation, Göttingen

Bettina Frohnapfel
Institute of Fluid Mechanics (ISTM),
Karlsruhe Institute of Technology, Karlsruhe, Germany

Oliver T. Stein
Institute for Combustion Technology (ITV),
University of Stuttgart, Stuttgart, Germany,
Engler-Bunte-Intsitute, Simulation of Reacting Thermo-Fluid Systems (TFS),
Karlsruhe Institute of Technology, Karlsruhe, Germany

Journal: Flow, Turbulence and Combustion

Year: 2024

Volume: 112

Pages: 1083-1103

Contributions by the present author: Writing – original draft & editing, Visualisation, Validation, Software, Methodology, Formal analysis, Data curation.

Abstract

Three-dimensional carrier-phase direct numerical simulations (CP-DNS) of reacting iron particle dust clouds in a turbulent mixing layer are conducted. The simulation approach considers the Eulerian transport equations for the reacting gas phase and resolves all scales of turbulence, whereas the particle boundary layers are modelled employing the Lagrangian point-particle framework for the dispersed phase. The CP-DNS employs an existing sub-model for iron particle combustion that considers the oxidation of iron to FeO and that accounts for both diffusion- and kinetically-limited combustion. At first, the particle sub-model is validated against experimental results for single iron particle combustion considering various particle diameters and ambient oxygen concentrations. Subsequently, the CP-DNS approach is employed to predict iron particle cloud ignition and combustion in a turbulent mixing layer. The upper stream of the mixing layer is initialised with cold particles in air, while the lower stream consists of hot air flowing in the opposite direction. Simulation results show that turbulent mixing induces heating, ignition and combustion of the iron particles. Significant increases in gas temperature and oxygen consumption occur mainly in regions where clusters of iron particles are formed. Over the course of the oxidation, the particles are subjected to different rate-limiting processes. While initially particle oxidation is kinetically-limited it becomes diffusion-limited for higher particle temperatures and peak particle temperatures are observed near the fully-oxidised particle state. Comparing the present non-volatile iron dust flames to general trends in volatile-containing solid fuel flames, non-vanishing particles at late simulation times and a stronger limiting effect of the local oxygen concentration on particle conversion is found for the present iron dust flames in shear-driven turbulence.

5.3.1 Introduction

Due to industrial growth in both developing and developed countries, as well as the increasing world population, the global energy demand is expected to rise over the next few decades. Energy from fossil fuels is still dominant, but their negative environmental impact and limited resources have raised the need for alternative energy sources. Renewable energy sources from wind and solar are clean (carbon-free) but due to the geographical locations of wind farms and volatility from solar plants, regions with high energy demand cannot be supplied continuously. A possible approach to solve this issue is the use of carbon-free energy storage systems. Nowadays, energy storage technologies are still underdeveloped and partially unexplored. A promising emission-free technology for future energy systems is the oxidation of iron [15, 16] and the potential of using existing coal power plant infrastructures [14]. Iron has a high potential for serving as a carbon-free energy carrier due to its high

energy density and abundance combined with its excellent transport and storage properties [15, 126]. When combining iron oxidation with the reverse iron oxide reduction process, based on renewable energy sources, a sustainable circular zero-carbon energy economy can be developed [126, 230]. Due to its non-volatile heterogeneous combustion property [231] iron combustion differs significantly from coal and biomass conversion such that existing modelling strategies for carbon-based solid fuels cannot directly be used. This lack of reliable modelling approaches drives significant research efforts to examine the underlying chemical and physical processes, and to develop new models.

Goroshin et al. [232] developed a simple analytical model for single metal particles to capture heating, ignition and diffusive burnout in both the fuel-lean and fuel-rich limits. Extension of the analytical model for binary mixtures of reacting fuels has been conducted by Goroshin et al. [233] and Palecka et al. [234]. Independently, Sidorov and Shevchuk [235] developed a similar analytical model. Goroshin et al. [236], Tang et al. [237] and Lam et al. [238] developed numerical models to investigate the discrete combustion regime that may occur for solid metal fuels. Soo et al. [166] proposed a kinetically- and diffusion-limited model for iron that was later extended by Hazenberg and van Oijen [164], considering the major oxidation step of Fe to FeO. Recently, Thijs et al. [22] and Mich et al. [165] extended this model by deriving improved heat and mass transfer correlations from fully-resolved particle simulations [22] and studying polydispersity effects on single particle combustion in the Euler-Lagrange framework [165]. Mi et al. [127] proposed an alternative iron combustion model that describes the growth of iron oxide layers consisting of FeO and Fe_3O_4 by a parabolic rate law. Over the last couple of years, the step from single particle investigations [128, 229, 239–244] to the study of metal particle clouds in laminar flows has received a substantial boost both numerically and experimentally. The experimental investigations mainly focus on the stabilisation and quantification of laminar burning velocities and on identifying different combustion regimes [245–253]. Numerical studies are based on single particle model developments and examine various physical aspects such as discreteness [236–238, 254], flame structure and laminar burning velocities [101, 164, 233, 234, 255].

The transition from laminar to turbulent iron cloud combustion introduces additional challenges. From previous research on solid fuel combustion with volatiles, it is known that a strong coupling between turbulent mixing, homogeneous chemistry and solid fuel kinetics exists. However, the non-volatile nature of iron requires us to re-examine this interplay for iron cloud flames. Direct numerical simulations (DNS) are essential to investigate these processes in detail. While fully-resolved DNS, that resolves all particle boundary layers, is only possible for single particles [22] and small particle groups, the carrier-phase direct numerical simulation (CP-DNS) approach provides a good trade-off between accuracy and efficiency for particle cloud combustion. CP-DNS resolves all scales of turbulence and the flame, but

employs sub-models for the momentum, heat and mass transfer across the boundary layers between the bulk gas phase and the Lagrangian point particles. Recent CP-DNS of solid fuel particle cloud combustion with volatile gases from coal or biomass were conducted by several researchers [34–36, 39, 41–45]. Hemamalini et al. [256] considered reacting iron particle clouds in a double shear layer configuration by CP-DNS and provided a qualitative impression of early-time iron cloud combustion. Here, we conduct CP-DNS of a reacting iron particle cloud in a turbulent mixing layer by using the First Order Surface Kinetics (FOSK) iron combustion sub-model proposed by Mich et al. [165]. Our objectives are to

- provide a first-of-its-kind study of iron particle cloud ignition and combustion in shear-driven turbulence using existing iron combustion sub-models,
- investigate the non-volatile combustion behaviour of iron particle clouds and qualitatively compare it to volatile-containing solid fuel flames,
- provide a CP-DNS database for further model development of iron particle cloud flames.

The remainder of the paper describes the modelling approach in Sec. 5.3.2, shows validation results for the iron combustion sub-model in Sec. 5.3.3 and introduces the computational configuration in Sec. 5.3.4. The CP-DNS results are presented and discussed in Sec. 5.3.5, followed by conclusions in Sec. 5.3.6.

5.3.2 Modelling

5.3.2.1 Gas phase

In the context of CP-DNS, the gas phase is described by the governing equations of mass (Eq. 5.40), momentum (Eq. 5.41), energy (Eq. 5.42) and chemical species (Eq. 5.43) [39]

$$\frac{\partial \rho}{\partial t} + \frac{\partial}{\partial x_i}(\rho u_i) = \dot{S}_{\rho,p}, \tag{5.40}$$

$$\frac{\partial \rho u_i}{\partial t} + \frac{\partial}{\partial x_j}(\rho u_i u_j) = -\frac{\partial p}{\partial x_i} + \frac{\partial}{\partial x_j}\left(\mu\left[\frac{\partial u_j}{\partial x_i} + \frac{\partial u_i}{\partial x_j} - \frac{2}{3}\frac{\partial u_m}{\partial x_m}\delta_{ij}\right]\right) + \dot{S}_{u,p}, \tag{5.41}$$

$$\frac{\partial \rho h_s}{\partial t} + \frac{\partial}{\partial x_i}(\rho u_i h_s) = \frac{\partial}{\partial x_i}\left(\frac{\mu}{\mathrm{Pr}}\frac{\partial h_s}{\partial x_i}\right) + \dot{S}_{h_s,p} + \dot{S}_{\mathrm{rad}}, \tag{5.42}$$

$$\frac{\partial \rho Y_k}{\partial t} + \frac{\partial}{\partial x_i}(\rho u_i Y_k) = \frac{\partial}{\partial x_i}\left(\frac{\mu}{\mathrm{Sc}}\frac{\partial Y_k}{\partial x_i}\right) + \dot{\omega}_k + \dot{S}_{k,p} \tag{5.43}$$

with density ρ, time t, spatial coordinate x, coordinate directions i,j, velocity u, Kronecker delta δ_{ij} and pressure p. The symbol μ denotes dynamic viscosity, h_s sensible enthalpy, Y_k

mass fraction of species k and $\mathrm{Pr} = \mathrm{Sc} = 0.7$ are the non-dimensional Prandtl and Schmidt numbers. $\dot{S}_{\mathrm{rad}}$ denotes the radiative source term. Radiative heat transfer is modelled by the discrete ordinate method (DOM) using 80 directions. However, assuming a mixture of O_2 and N_2 (pure air) the gas is nearly transparent in the infrared wavelength and does not absorb or emit major parts of the radiation ($\varepsilon_{\mathrm{gas}} \approx 0.001$). The further RHS source terms $\dot{S}_{\rho,p}$, $\dot{S}_{u,p}$, $\dot{S}_{h_s,p}$ and $\dot{S}_{k,p}$ denote the exchange of mass, momentum and energy between the gas phase and the iron particles, and $\dot{\omega}_k$ is the homogeneous chemical reaction rate of species k. Assuming purely non-volatile iron conversion, the iron oxide formed during oxidation entirely remains on the particle in solid form and no homogeneous reactions occur such that $\dot{\omega}_k = 0$. However, the mass transfer terms $\dot{S}_{\rho,p}$ and $\dot{S}_{k,p}$ for $k = \mathrm{O_2}$ are non-zero, since oxygen is consumed from the gas phase. The non-zero source terms are calculated as

$$\dot{S}_{\rho,p} = \dot{S}_{\mathrm{O_2},p} = -\frac{1}{\Delta^3} \sum_{p=1}^{N_p} \frac{dm_p}{dt}, \tag{5.44}$$

$$\dot{S}_{u,p} = -\frac{1}{\Delta^3} \sum_{p=1}^{N_p} \frac{d(m_p \mathbf{u}_p)}{dt}, \tag{5.45}$$

$$\dot{S}_{h_s,p} = -\frac{1}{\Delta^3} \sum_{p=1}^{N_p} \left(\frac{m_p c_{\mathrm{p},p}}{\tau_{con}} (T_g - T_p) + \frac{dm_p}{dt} h_{s,\mathrm{O_2}}|_{T_p} \right) \tag{5.46}$$

with the particle mass m_p, particle temperature T_p, gas phase temperature T_g at the particle position, convective heat transfer time scale τ_{con}, particle specific heat capacity $c_{\mathrm{p},p}$ and the sensible enthalpy of consumed oxygen during the oxidation process at particle temperature $h_{s,\mathrm{O_2}}|_{T_p}$. Equations (5.44)-(5.46) specify the semi-discretised source terms from N_p iron particles within every gas phase cell with edge length Δ and Eq. (5.45) excludes external forces, e.g. gravity.

5.3.2.2 Solid phase

The particles are described in the Lagrangian framework and their interaction with the carrier-phase is defined by the transfer of momentum, energy and oxygen mass. The particles are initialised as pure iron. During the oxidation process FeO is produced according to

$$\mathrm{Fe} + 0.5\mathrm{O_2} \rightarrow \mathrm{FeO}. \tag{5.47}$$

Although higher oxidation states of iron (Fe_3O_4 and Fe_2O_3) exist, we limit ourselves to the sole production of FeO. This is because a recent set of iron combustion sub-models is based on the same assumption [23, 101, 164, 165] such that limiting ourselves to FeO results in a better comparability of our data to these recent references. These existing FeO sub-models

represent the most important oxidation physics (kinetic and/or diffusion limitation) and have been successfully validated against experimental data. Despite the proven existence of higher oxidation states, there are currently no reliable sub-models that can represent the entire physics of their production for the present conditions. Moreover, with our current focus on ignition, particle residence times in the mixing layer remain short, such that substantial iron oxidation to the final state Fe_2O_3 does not occur. During the simultaneous presence of both Fe and FeO, their thermophysical properties (ρ, c_p and h_s) need to be defined. In this work, the densities are calculated in analogy to [165]. The remaining thermophysical properties are taken from the NIST database [129] and described by the Shomate equations. The particle specific heat capacity is expressed as $c_{\mathrm{p},p} = Y_{\mathrm{Fe}} c_{\mathrm{p,Fe}} + Y_{\mathrm{FeO}} c_{\mathrm{p,FeO}}$. Melting and solidification of both iron and iron oxide are considered by the apparent heat capacity method [23]. The mass conversion rate of Fe to FeO is predicted using the FOSK model by Mich et al. [165]

$$\frac{dm_{p,\mathrm{Fe}}}{dt} = -\frac{1}{s}\rho_f Y_{\mathrm{O_2}} A_d k_d \mathrm{Da}^*, \tag{5.48}$$

$$\frac{dm_{p,\mathrm{FeO}}}{dt} = \frac{1+s}{s}\rho_f Y_{\mathrm{O_2}} A_d k_d \mathrm{Da}^*. \tag{5.49}$$

Here,

$$\mathrm{Da}^* = \frac{A_r k_r}{A_r k_r + A_d k_d} \tag{5.50}$$

is the normalised Damköhler number, $A_r = A_d = \pi d_p^2$ the reactive and diffusive areas of the particle, $k_r = k_\infty \mathrm{e}^{-E_a/R_u T_p}$ the kinetic surface reaction rate and $k_d = \mathrm{Sh}\frac{D_{\mathrm{O_2},f}}{d_p}$ the diffusive transfer rate. $\mathrm{Sh} = 2 + 0.552\mathrm{Re}_p^{1/2}\mathrm{Sc}^{1/3}$ denotes the Sherwood number, $\mathrm{Re}_p = \rho_f |\mathbf{u}_g - \mathbf{u}_p| \frac{d_p}{\mu_f}$ the particle Reynolds number and s the stoichiometric ratio of the oxidation of iron to iron oxide. Subscript f denotes film properties evaluated using the 1/3-law $T_f = T_p + \frac{1}{3}(T_g - T_p)$. The remaining coefficients in the model are based on [165] and further model details can be found therein.

Only drag force is considered to act on the particles. While it has been found that gravity may have an impact on laboratory scale iron particle flames [253], it is neglected for the present canonical mixing layer configuration. Uniform temperature is assumed within the particles ($\mathrm{Bi} \approx 0.001 - 0.01$ [127]) which is governed by convective heat transfer with the gas phase, radiation, heat of oxidation and the consumption of oxygen from the gas phase. With these assumptions, the solid phase governing equations read

$$\frac{dm_p}{dt} = \frac{dm_{p,\mathrm{Fe}}}{dt} + \frac{dm_{p,\mathrm{FeO}}}{dt}, \tag{5.51}$$

$$\frac{d\mathbf{u}_p}{dt} = \frac{\mathbf{u}_g - \mathbf{u}_p}{\tau_p}, \tag{5.52}$$

$$\frac{dT_p}{dt} = \frac{1}{\tau_{con}}(T_g - T_p) + \frac{\varepsilon_p A_p \sigma}{m_p c_{p,p}}(\Theta_r^4 - T_p^4) + \frac{\dot{Q}_{\mathrm{FeO}}}{m_p c_{p,p}} + \frac{\dot{Q}_{\mathrm{O_2}}}{m_p c_{p,p}} \tag{5.53}$$

where $\mathbf{u}_g$ is the gas velocity at the particle position, $\mathbf{u}_p$ the particle velocity and τ_p the particle relaxation time that reads

$$\tau_p = \frac{\rho_p d_p^2}{18\mu_f} \frac{1}{(1 + 0.15\mathrm{Re}_p^{2/3})}. \tag{5.54}$$

$\varepsilon_p = 0.9$ [257] is the particle emissivity, σ the Stefan-Boltzmann constant, Θ_r the gas phase radiation temperature computed by DOM, $\dot{Q}_{\mathrm{FeO}} = \frac{dm_{p,\mathrm{FeO}}}{dt}\Delta h_{c,\mathrm{FeO}}$ the heat release due to Fe oxidation, $\Delta h_{c,\mathrm{FeO}}$ the formation enthalpy of FeO based on Eq. (5.47), and $\dot{Q}_{\mathrm{O_2}}$ the energy transfer due to oxygen consumption at particle temperature. The convective heat transfer time scale follows Ranz-Marshall [141]

$$\tau_{con} = \frac{1}{6}\frac{\mathrm{Pr}}{\mathrm{Nu}}\frac{c_{\mathrm{p},p}}{c_{\mathrm{p},f}}\frac{\rho_p d_p^2}{\mu_f} \tag{5.55}$$

with

$$\mathrm{Nu} = 2 + 0.552\mathrm{Re}_p^{1/2}\mathrm{Pr}^{1/3} \tag{5.56}$$

A Sherwood and Nusselt number correction is applied to account for Stefan flow [22,167,168]

$$\mathrm{Sh}^* = \mathrm{Sh}\frac{\ln(1+B_M)}{B_M}, \tag{5.57}$$

$$\mathrm{Nu}^* = \mathrm{Nu}\frac{\ln(1+B_T)}{B_T} \tag{5.58}$$

such that Sh^* replaces Sh in the expression for k_d and Nu^* is used instead of Nu in Eq. (5.55). The Spalding mass transfer number B_M is calculated as

$$B_M = \frac{Y_{\mathrm{O_2},g} - Y_{\mathrm{O_2},p}}{Y_{\mathrm{O_2},p} - 1} \quad \text{with} \quad Y_{\mathrm{O_2},p} = Y_{\mathrm{O_2},g}\frac{A_d k_d}{A_r k_r + A_d k_d} \tag{5.59}$$

and the Spalding heat transfer number B_T as

$$B_T = (1 + B_M)^{\varphi} - 1 \quad \text{with} \quad \varphi = \frac{c_{\mathrm{p,O_2}}|_{T_p}}{c_{\mathrm{p},g}}\frac{\mathrm{Pr}}{\mathrm{Sc}} \tag{5.60}$$

where $c_{\mathrm{p,O_2}}|_{T_p}$ is the specific heat capacity of oxygen at particle temperature and $c_{\mathrm{p},g}$ the specific heat capacity of the gas phase.

5.3.3 Validation

The sub-model for iron combustion is validated by comparing results from it for a laser-heated iron particle configuration to numerical predictions from [165] and experimental data published in [23, 229]. The configuration is the laser-heated reactive single iron particle for various oxygen environmental conditions and varying particle diameters by Ning et al. [229]. Figure 5.30 shows the time evolution of particle temperature for a laser-ignited iron particle with $d_p \approx 54\,\mu\text{m}$ in air at $T_{\text{air}} = 300\,\text{K}$. The initial particle temperature is $T_p = 1500\,\text{K}$ due

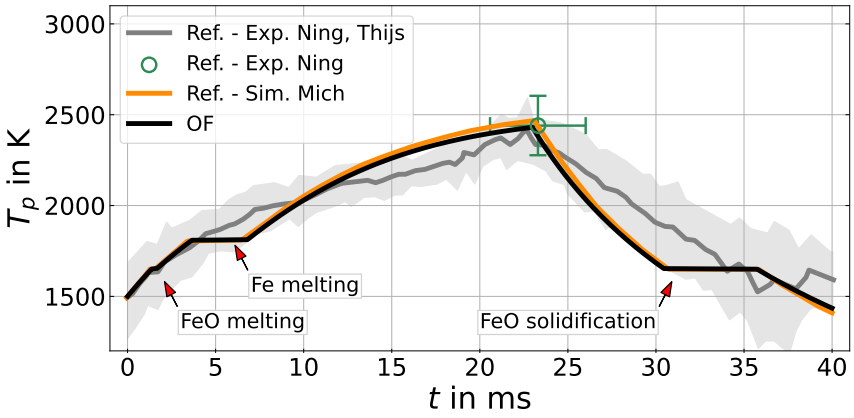

Figure 5.30: Comparison of particle temperature T_p vs. time t for laser-ignited single iron particles with $d_p = 54\,\mu\text{m}$ in air at $T_{\text{air}} = 300\,\text{K}$. Present work (OF), ref. [165] (Ref.–Sim.) and refs [23, 229] (Ref.–Exp.) with mean (dark grey line) and standard deviation (gray shading) from the measurements.

to heating by the laser. The laser initiates the heterogeneous reaction, which leads to a steady increase of the particle temperature until $t = 23\,\text{ms}$. The particle reaches a peak temperature of $\approx 2400\,\text{K}$ that levels off to $\approx 1400\,\text{K}$ at $t = 40\,\text{ms}$ due to the full consumption of Fe. The time evolution profile exhibits three plateaus of constant particle temperature which are induced by the melting and solidification phenomena inside the iron particle. The first ($1.2 < t < 1.6\,\text{ms}$) and third plateau ($30.5 < t < 36\,\text{ms}$) at $T_p = 1650\,\text{K}$ correspond to the melting and solidification temperature of FeO, while the second plateau ($3.5 < t < 6.8\,\text{ms}$) at $T_p = 1810\,\text{K}$ represents the melting temperature of Fe. The first plateau (melting of FeO) is comparatively short, as only a small fraction of FeO has formed during the initial stages of the oxidation process. After the peak particle temperature has been reached at 23 ms the particle only consists of FeO and hence, there is no solidification plateau for Fe at 1810 K, but only the one for FeO at 1650 K during the time period $30.5 < t < 36\,\text{ms}$. Comparing the results between the two different codes [165] and the experimental data from [23, 229] in Fig. 5.30, consistent numerical predictions are observed which both lie within the experimental scatter.

Figure 5.31 shows a comparison of times to peak particle temperature t_{peak} (e.g. 23 ms in Fig. 5.30) as a function of particle diameter and gas oxygen concentration for single laser-heated iron particles. Increasing the particle diameter leads to extended time periods to

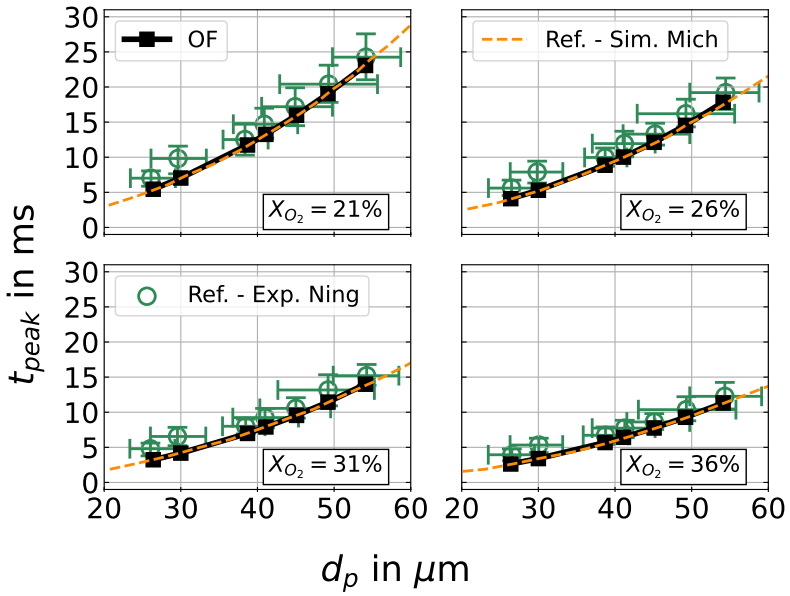

Figure 5.31: Comparison of times to peak particle temperature t_{peak} vs. particle diameter d_p for various gas oxygen concentrations for laser-ignited single iron particles at $T_{\text{gas}} = 300\,\text{K}$. Present work (OF), [165] (Ref.–Sim.) and [229] (Ref.–Exp.) with mean and standard deviation from the measurements.

reach the peak particle temperature as expected. Also in line with expectations, increasing the gas oxygen concentrations yields a reduction of t_{peak}, e.g. by a factor of around two when increasing X_{O_2} from 21% to 36%. This reflects the (oxygen) diffusion-limited character of the heterogeneous reaction process of iron that is attained for the high particle temperatures of the laser-ignited particle experiments. The predictions by the present particle model implementation are fully aligned with the reference implementation from [165] and both simulations agree very well with the measurements from [229]. As illustrated in Figs. 5.30 and 5.31 the present implementation of the FOSK iron combustion sub-model is valid for a wide range of particle and environmental conditions and can therefore be used as a reliable sub-model for individual particles in the Lagrangian particle cloud within the subsequent CP-DNS of the mixing layer.

5.3.4 Computational configuration

A turbulent reacting mixing layer is studied, similar to the work by Rieth et al. [39] on coal particle cloud combustion. However, different from the setup in [39] and following the work by O'Brien et al. [258] the present configuration is based on the initial definition and time evolution of the momentum thickness δ_θ, which allows for the evaluation of a self-similar region of the shear-induced turbulence. The setup consists of two opposed streams, initialised as air at elevated temperature ($Y_{\text{O}_2} = 0.233$, $Y_{\text{N}_2} = 0.767$ and $T = 550\,\text{K}$) and iron particles in the upper stream (US), and hot air at $T = 1650\,\text{K}$ in the lower stream (LS). The

velocity of the two streams is chosen to be equal, but directed in the opposite x-direction with $\Delta u_x = 30\,\mathrm{m/s}$, see Fig. 5.32. Following [258], a hyperbolic tangent profile is used to

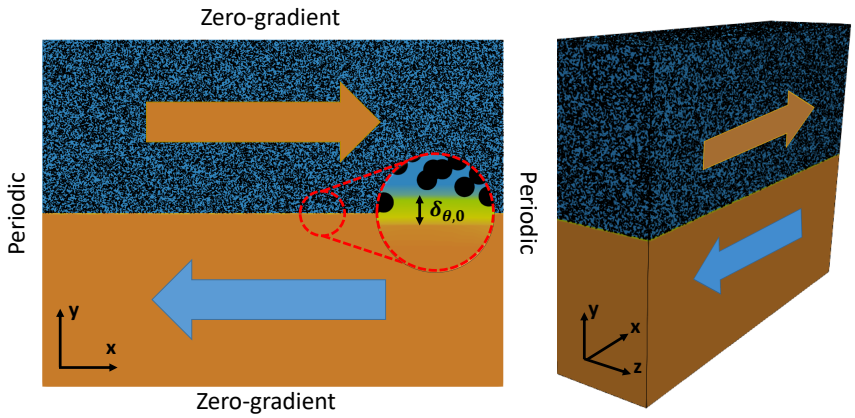

Figure 5.32: Initial and boundary conditions of the reacting mixing layer with iron particles.

initialise the streamwise velocity field

$$u_x = \frac{\Delta u_x}{2} \tanh\left(\frac{y - L_y/2}{2\delta_{\theta,0}}\right) \tag{5.61}$$

(while $u_y = u_z = 0$), where $\delta_{\theta,0}$ is the initial momentum thickness corresponding to Reynolds number

$$\mathrm{Re}_{\theta,0} = \frac{\Delta u_x \delta_{\theta,0}}{(\nu_{\mathrm{US}} + \nu_{\mathrm{LS}})/2} = 44.018 \tag{5.62}$$

where ν_{US} and ν_{LS} are the initial viscosities of the upper and lower stream, respectively. The three-dimensional computational domain has geometrical dimensions $L_x = 320 \times \delta_{\theta,0}$, $L_y = 240 \times \delta_{\theta,0}$ and $L_z = 80 \times \delta_{\theta,0}$. The setup consists of a total of 84,934,656 cubic Eulerian cells with a constant size of $\Delta = 100\,\mu\mathrm{m}$. A total of 4,900,000 spherical iron particles with an initial diameter of $d_{p,\mathrm{init}} = 10\,\mu\mathrm{m}$, $T_{p,\mathrm{init}} = 550\,\mathrm{K}$ and $Y_{\mathrm{Fe,init}} = 1$ are randomly distributed in the upper stream. The particle diameter chosen for the simulations is close to the nominal surface mean size (12.7 µm) of the experimental PSD from [253]. Note that these iron particles are produced via atomisation and the particle size is adjustable. In the context of the considered power plant oxidation-reduction process typical iron particle sizes are in the range 10-20 µm and therefore comparable to (the low end) of PSDs for pulverised volatile-containing solid fuels [14], while their size is expected not to change significantly after multiple oxidation-reduction cycles [259]. Future simulations will use the full PSD from [253] to explore the effects of particle size on ignition and combustion. The number of particles has been set to obtain $\phi = 1$ in the upper stream, based on the oxidation of Fe to FeO i.e. Eq. (5.47). Particle velocities are initialised with the bulk gas velocity of the upper stream.

To speed up the growth of the mixing layer, isotropic velocity perturbations of $u'u' = v'v' = w'w' = 0.01\,(\Delta u_x)^2$ with a length scale of $0.01 \cdot L_x$ are generated with the methods by Klein et al. [260] and Kempf et al. [261]. These instabilities are initially superimposed on the bulk velocity field at $y/L_y = 0.5$ with a height of $4 \cdot \delta_{\theta_0}$ and exponentially decrease to zero along the y-axis. The boundary conditions (BC) for pressure and momentum are periodic in x- and z-direction, whereas a zero-gradient BC for momentum and ambient pressure is assumed in y-direction. To ensure sufficient resolution of the CP-DNS, the Kolmogorov length scale is estimated. Following Rieth et al. [39] we define spatial averages for an arbitrary quantity Φ by averaging across the homogeneous x- and z-directions, i.e.

$$\langle \Phi \rangle (y,t) = \frac{1}{L_x L_z} \int_0^{L_x} \int_0^{L_z} \Phi(x,y,z,t) dx dz. \tag{5.63}$$

Then, the local velocity fluctuation can be obtained as $\mathbf{u}' = \mathbf{u} - \langle \mathbf{u} \rangle$. The average dissipation is given as $\langle \epsilon \rangle = \langle \tau_{ij} \frac{\partial u_i'}{\partial x_j} \rangle$, with the viscous stress tensor τ_{ij}. Using the average dissipation rate and spatially-averaged kinematic fluid viscosity, the Kolmogorov length scale can be calculated as

$$\langle \eta \rangle = \left(\frac{\langle \nu \rangle^3}{\langle \epsilon \rangle} \right)^{1/4}. \tag{5.64}$$

After the initial time steps of the simulation the minimum Kolmogorov length scale that can be estimated from Eq. (5.64) is always larger than the computational grid size ($\eta > \Delta = 100\,\mu m$) such that all turbulent scales are resolved, as detailed further below.

Following the evaluation in [258], Fig. 5.33 shows the time evolution of the momentum thickness δ_θ in the present mixing layer. The momentum thickness grows with time with

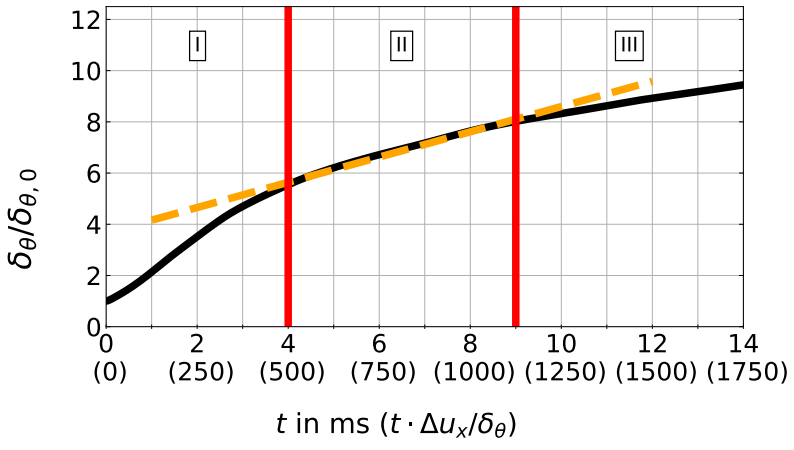

Figure 5.33: Time evolution of momentum thickness δ_θ of the mixing layer. Vertical red lines delineate the time period of self-similarity.

different ascending slopes which divide it into three different regions. The first region (I) represents the initialisation period where the initial perturbations are replaced by the de-

velopment of the shear-driven turbulence. In the second region (II) a quasi-linear growth of δ_θ is observed, which indicates fully-developed self-similar turbulence. The final region (III) shows a reduction of the slope which implies external processes increasingly acting on the flow field, i.e. boundary effects. Using Eq. (5.64) a minimum Kolmogorov length scale of 213 µm is found during the self-similar period. For the applied CP-DNS approach to be valid, the ideal grid size Δ_{ideal} should follow $d_p \ll \Delta_{ideal} < \eta$, such that all turbulent scales are resolved, while the Lagrangian particles can still be considered as point-particles. With $d_p = 10\,\mu m$, $\Delta = 100\,\mu m$ and $\eta_{min} = 213\,\mu m$ the present configuration achieves a reasonable trade-off during the self-similar period. The subsequent analysis will mainly focus on the self-similar region ($4 < t < 9\,ms$) where no boundary effects have yet affected the development of the inner shear layer. However, results from earlier and later times are also presented for a more complete documentation of the overall particle oxidation process.

The simulations are conducted using a finite volume solver based on OpenFOAM-v2012, with a typical computational cost of ≈165,225 CPUh on 1024 × Intel Xeon Platinum 8358 cores. Within the framework of the International Conference on Numerical Combustion ICNC (see Abdelsamie et al. [262]) Zirwes et al. have shown that -despite OpenFOAM's second order numerical accuracy- detailed simulations of highly-transient chemically reacting flows can be achieved that demonstrate very good HPC scaling capabilities and provide results in excellent agreement with high-order combustion codes [263]. A necessary requirement for excellent results from OpenFOAM is typically the use of a higher grid resolution than the corresponding high-order code for the same case, since the latter code will converge faster. Under this condition, depending on the mesh type, OpenFOAM has been demonstrated to provide "quasi-DNS" data for both chemically non-reacting [264] and reacting single phase flows [265]. Here we use an in-house reacting multiphase solver extension of OpenFOAM that has previously been employed for detailed CP-DNS analyses of volatile-containing solid fuel combustion [42–44]. With CP-DNS, a considerable level of additional models and numerical methods are added to the classical DNS framework, which are -among others- models for the heat, mass and momentum transfer across the particle boundary layers, particle tracking techniques, particle-source in cell methods etc. To still achieve reliable CP-DNS predictions, great care has to be taken with respect to the relative size of the Lagrangian particle diameter d_p, Eulerian grid resolution Δ and turbulent Kolmogorov scale η, leading to the criterion $d_p \ll \Delta_{ideal} < \eta$ given above.

5.3.5 Results and discussion

After validating the iron combustion sub-model, the CP-DNS framework is used to predict the mixing layer with reacting iron particles. A visual impression of its temporal evolution can be obtained from Fig. 5.34 which shows snapshots of the gas temperature (top row) and

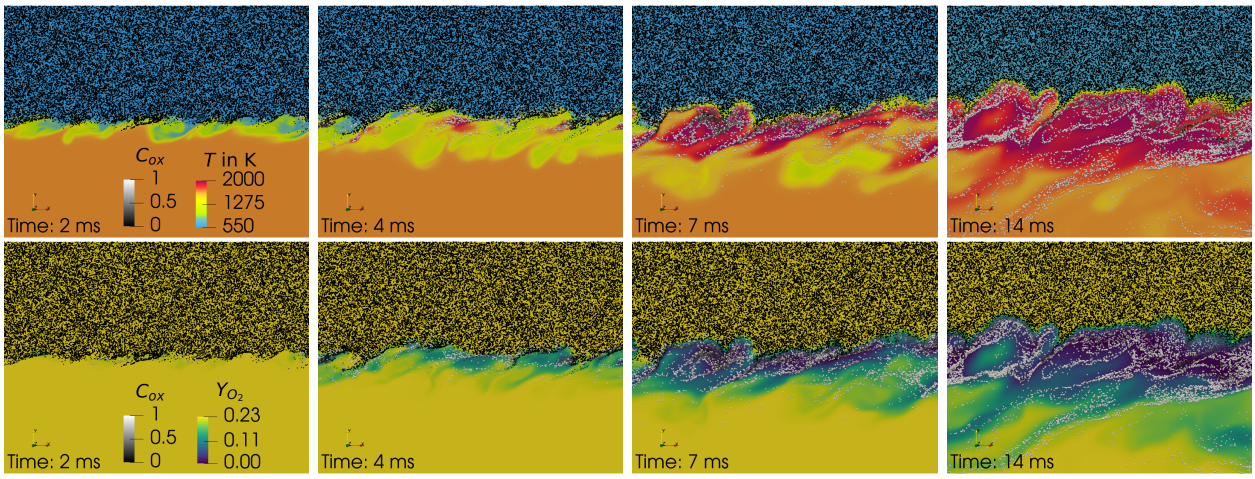

Figure 5.34: Snapshots of gas temperature (top row) and mass fraction of O_2 (bottom row) in the x-y plane at $L_z/2$. The particles are coloured by their oxidation progress C_{ox}.

oxygen mass fraction in the gas phase (bottom row) at selected times in the x-y plane at $L_z/2$. The particles are coloured by their oxidation progress C_{ox} defined as the extent of iron consumption $C_{\mathrm{ox}} = \frac{m_{\mathrm{Fe},0} - m_{\mathrm{Fe}}}{m_{\mathrm{Fe},0}}$ with $m_{\mathrm{Fe},0}$ and m_{Fe} denoting the initial and current iron mass inside the particle at time t. Inspecting Fig. 5.34, it can be seen that the initially separate streams develop and generate a mixing region between them. Due to this mixing process the particles are entrained from the upper to the lower stream, as indicated at $t = 2\,\mathrm{ms}$. When these particles interact with the lower stream they heat up. During this initial stage of heat-up the particles are still in the kinetically-limited regime and their oxidation progress is close to zero.

At $t = 4\,\mathrm{ms}$ the turbulent mixing process has progressed and significantly more particles have been entrained into the lower stream for oxidation. Particles with longer residence times in the lower stream have reached the critical ignition temperature and ignite, as can be observed from the formation of localised hot pockets, while the local oxygen concentration reduces simultaneously. The regions of local hot pockets show the development of individual distinctive high temperature zones with highly reactive particles residing inside. However, an interesting observation is that larger pockets of substantial gas temperature increase are mostly limited to regions where particle clusters are located.

At $t = 7\,\mathrm{ms}$ a large number of iron particles has been entrained into the lower stream, which has led to the formation of a continuous flame zone with high temperatures and full oxygen depletion. This flame zone is aligned with particle clusters in which particles typically have a similar state of oxidation. The majority of particles in the lower stream is now fully oxidised (indicated by white colour), showing that their oxidation process from Fe to FeO is fully completed. However, in the centre of the mixing layer filament-like, black-coloured particle streaks can be observed, the oxidation state of which is still zero ($C_{\mathrm{ox}} = 0$). Here,

particle clusters have been entrained into regions with locally zero oxygen concentration, such that these particles cannot oxidise immediately. These observations differ from the well-known phenomena in volatile-containing solid fuel flames, from e.g. coal [39] (Fig. 3) and biomass [40] (Fig. 3). In high-temperature regions devoid of oxygen, volatile-containing solid fuels still continue their devolatilisation process, whereas (non-volatile) iron particles only heat up without any further material release or oxidation progress.

For the last reported time step $t = 14\,\text{ms}$, more particles are clustered, hence, more simultaneous particle oxidation occurs and therefore, a strong increase of gas phase temperature and oxygen consumption can be observed. A continuous flame front has been established and is constantly fed by fresh particles entering from the upper stream. Nevertheless, this time step is located outside of the self-similar region, see Fig. 5.33, and boundary effects may have begun to influence the results. Further snapshots at later times (omitted for brevity) show that the entrainment and oxidation progress continues until the end of the simulation.

Figure 5.35 (top row) shows the total mass of FeO produced and O_2 consumed by iron oxidation in the entire computational domain vs. time. A significant increase of the mass of

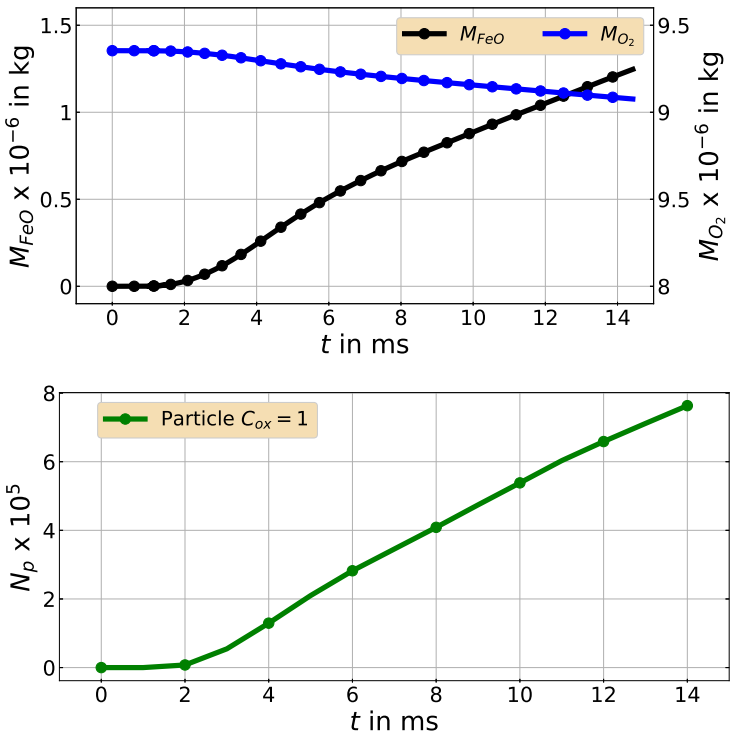

Figure 5.35: Total mass of produced FeO and consumed O_2 in the entire domain (top row) and total number of fully oxidised particles N_p (bottom row) vs. time.

produced iron oxide can be observed from $t = 2\,\text{ms}$ onwards, after which there is a near-linear mass increase of FeO up to around 1.25 x 10^{-6} kg at $t = 14\,\text{ms}$. The mass of oxygen in the gas phase decreases simultaneously, reaching its lowest value at the end of the simulation. Figure 5.35 (bottom row) shows the total number of particles that is fully oxidised ($C_{\text{ox}} = 1$)

as a function of time. It can be observed that N_p increases simultaneously as the mass of FeO, subsequently reaches a near-linear profile and at $t = 14\,\text{ms}$ around 763,000 ($\approx 15.6\,\%$) particles have been fully oxidised within the bounds of the CP-DNS simulation time.

Figure 5.36 shows scatterplots of the particle oxidation progress C_{ox} vs. the normalised y/L_y coordinate for all particles at different times. The particles are coloured by the gas temperature surrounding them. At $t = 1\,\text{ms}$, a small set of particles at positions close to

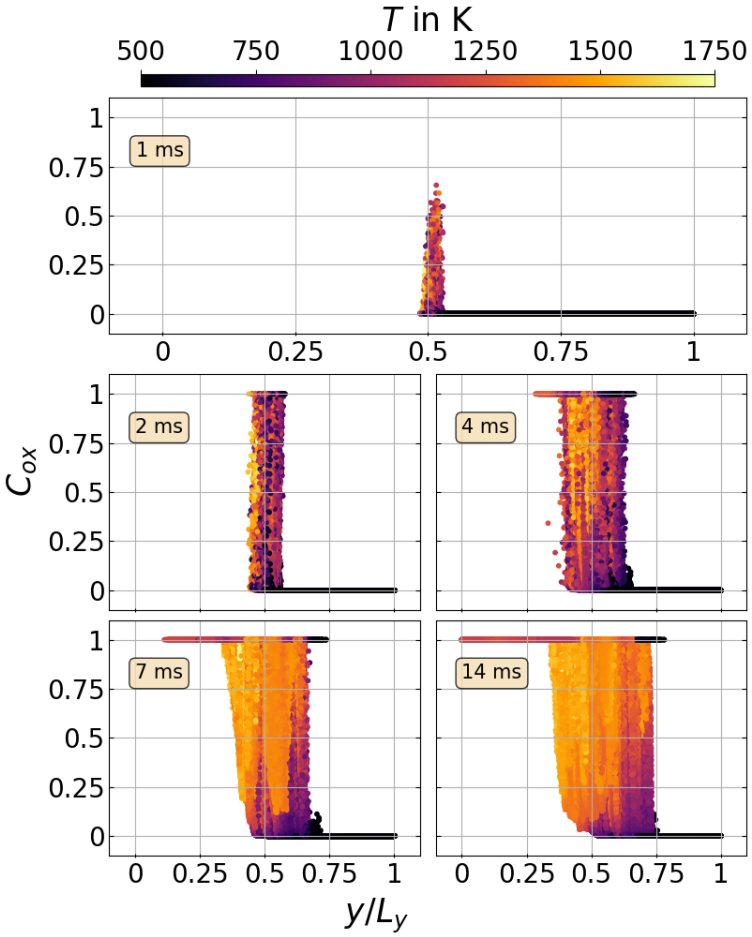

Figure 5.36: Scatterplot of particle oxidation progress C_{ox} vs. normalised cross-stream coordinate y coloured by the gas temperature surrounding the particle at different times.

$y/L_y = 0.5$ has been heated up by the lower stream and begins to oxidise. As time progresses to $t = 2\,\text{ms}$, more particles are entrained into the lower stream, heat up and oxidise, such that a significant number of them has already reached the state of full oxidation $C_{\text{ox}} = 1$. This process continues up to the end of the simulation, with further broadening of the oxidation region across the y-axis and an increasing number of particles reaching full oxidation. At 4 ms it can be observed that particles in the lower half of the domain are surrounded by higher gas temperatures, whereas their surrounding gas is significantly colder in the upper half. At $y/L_y \approx 0.6$ a set of particles has already reached full oxidation, despite being surrounded by relatively cold gas (black particles with $C_{\text{ox}} \to 1$). This corresponds to rare

events where particles have already experienced a hot gas environment for oxidation in the lower stream and have subsequently be re-entrained upwards into to cold gas of the upper stream, see Fig. 5.34 at early times. For the time range $7 \leq t \leq 14\,\mathrm{ms}$ it can be observed that particles with a small oxidation progress are surrounded by cold gas, while the intermediate range of oxidation progress $0 < C_{\mathrm{ox}} < 1$ is mostly correlated with high values of surrounding gas temperature (yellow) and only a small fraction of particles is subjected to intermediate temperatures (purple). Particles that are fully oxidised ($C_{\mathrm{ox}} = 1$) can be observed across the entire range of y/L_y of the lower stream and up to about half of the upper stream at $t = 14\,\mathrm{ms}$. These particles are either surrounded by the background gas temperature of the lower stream (orange), are subjected to the hot gases of the main oxidation region (yellow) for intermediate values of y/L_y, or surrounded by the low gas temperatures of the upper stream (purple-black), where -again- the latter correspond to rare re-entrainment events of oxidised particles into the upper stream. The fraction of fully reacted particles re-entrained into the cold gas is less than 5% for the inspected time range. These particles transfer heat to the cold gas, but due to their small fraction, no significant effect on the gas phase can be observed, see gas temperature in Fig. 5. We note that for volatile-containing solid fuels that undergo char conversion (small) particles would be fully consumed at (very) late times of the simulation, whereas this cannot happen for iron particle combustion where, apart from few particles having left the computational domain through the y-boundaries, no significant particle loss has occurred at the end of the simulation.

Figure 5.37 presents scatterplots of particle temperature vs. oxidation progress C_{ox} over the course of the simulation, where particles are coloured according to their normalised Damköhler number Da^* (Eq. 5.50). Fully oxidised particles are coloured in black since their mass conversion rate of Fe to FeO is zero and the evaluation of Da^* becomes obsolete. In line with Fig. 5.36 at $t = 1\,\mathrm{ms}$ a first set of particles has started to partially oxidise. Corresponding to the second plateau in Fig. 5.30, a constant maximum particle temperature across the range $0.2 \leq C_{ox} \leq 0.25$ delineates the melting process of Fe at $T_p = 1810\,\mathrm{K}$. At $t = 2\,\mathrm{ms}$ some particles have already reached $C_{\mathrm{ox}} = 1$, where the highest particle temperatures are attained. Considering the reactants solid iron at the initial temperature of the upper stream ($T = 550\,\mathrm{K}$) and gaseous air at the temperature of the lower stream ($T = 1650\,\mathrm{K}$), while assuming the products of iron oxidation to be liquid FeO and gaseous nitrogen only, an adiabatic flame temperature of more than 3100 K is obtained, in line with the peak temperatures observed in Fig. 5.37. At $C_{\mathrm{ox}} = 1$ (black particles) particle oxidation has completely finished such that particles cool down again to a level determined by their local gas environment. For the time range $4 \leq t \leq 7\,\mathrm{ms}$ the particle scatter becomes substantially thicker due to many particles attaining a broad range of oxidation states and temperatures. These particles are mainly located in the main flame region in the centre of the mixing layer,

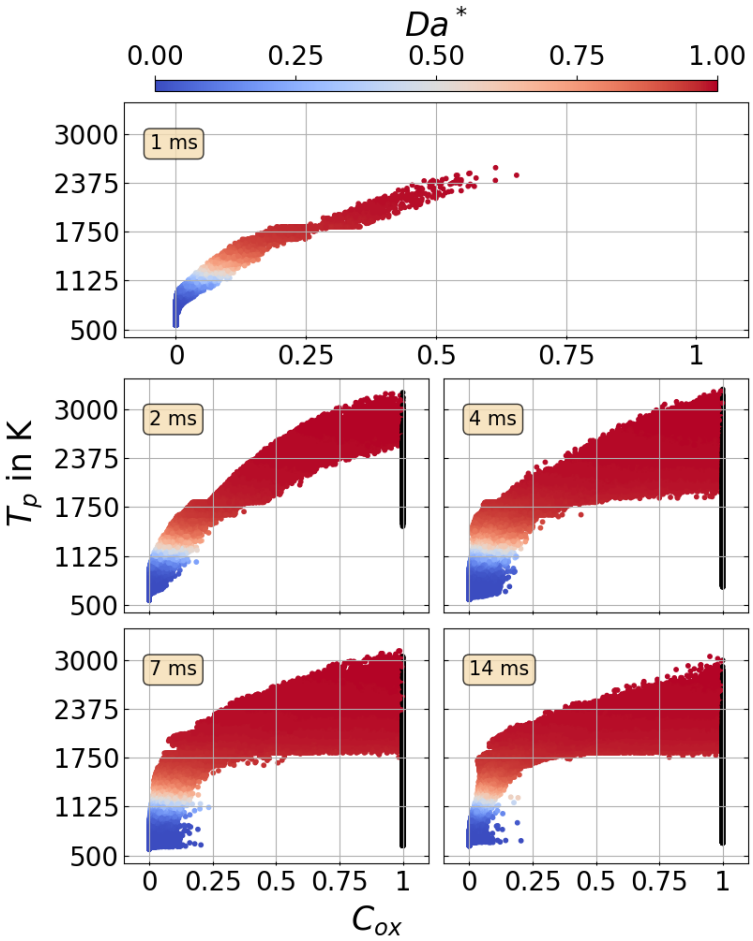

Figure 5.37: Scatterplot of particle temperature T_p vs. oxidation progress C_{ox} coloured by the normalised Damköhler number Da^* at different times. Black colour indicates a fully oxidised state.

see Fig. 5.36. At $t = 14\,\mathrm{ms}$, the temperature range for particles with elevated oxidation progress ($C_{\mathrm{ox}} > 0.3$) is $1750 \leq T_p \leq 2900\,\mathrm{K}$, which corresponds to the set of particles in the main reaction zone in Fig. 5.34. Focusing on the colour of the particles, i.e. the normalised Damköhler number, it can be observed that for $T_p < 1125\,\mathrm{K}$ and $C_{\mathrm{ox}} < 0.2$, all particles are in the kinetically-limited regime ($\mathrm{Da}^* \to 0$) as expected. For $1125 < T_p < 1500\,\mathrm{K}$, the transition from kinetic to diffusion limitation ($\mathrm{Da}^* \to 1$) occurs. This is because particle temperatures are so high such that the conversion rate is now solely limited by the availability of oxygen.

In the previous figures the (strong) impact of turbulence on iron particle ignition and combustion in the mixing layer has been demonstrated. For a quantitative evaluation of turbulence effects on the transition from kinetic to diffusion limitation of particle conversion Fig. 5.38 shows the time to reach this transition ($\mathrm{Da}^* = 0.5$) for different particle Nusselt numbers in varying oxygen environments. The data shown in Fig. 5.38 are generated by conducting separate simulations of single iron particle conversion in various oxygen environments using the same models and implementation from Sec. 5.3.2. The conditions are chosen to mimic entrainment events from the mixing layer with initially cold particles at

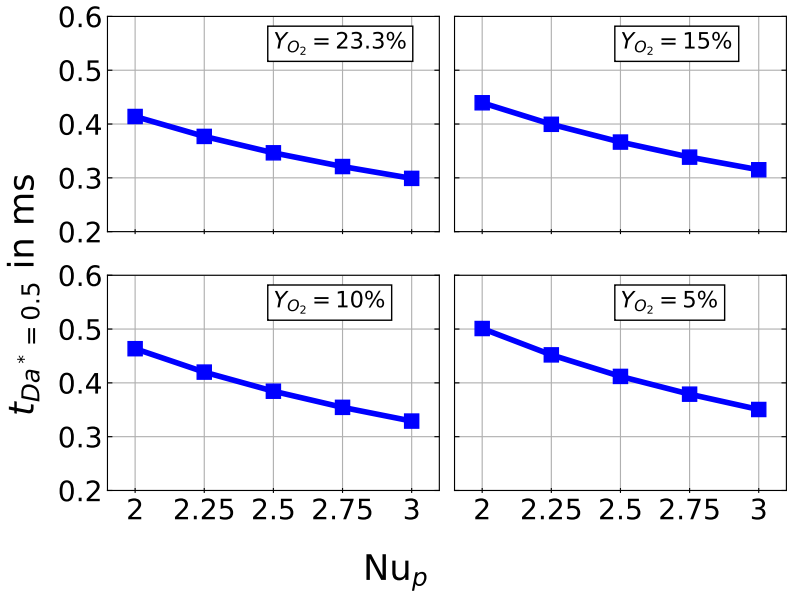

Figure 5.38: Time to normalised Damköhler at transition point $t_{\mathrm{Da}^*=0.5}$ vs. particle Nusselt number Nu_p for various gas oxygen environments for a single iron particle at $T_p = 550\,\mathrm{K}$ in $T_{\mathrm{gas}} = 1650\,\mathrm{K}$.

$T_p = 550\,\mathrm{K}$ entering the lower stream at $T_{\mathrm{gas}} = 1650\,\mathrm{K}$. The range of particle Nusselt numbers has been extracted from the mixing layer during the self-similar period ($t = 4 - 9\,\mathrm{ms}$). Here, $\mathrm{Nu}_p = 2$ indicates a particle that perfectly follows the flow field (zero slip velocity), see Eq. (5.56), whereas for $\mathrm{Nu}_p = 3$, a slip velocity between the particle and gas is present that is enhanced by turbulent mixing. In Fig. 5.38 a decrease of oxygen in the environment leads to an increase of transition time because of the direct dependence of the FeO formation rate on oxygen concentration, see Eq. (5.49). Increasing the particle Nusselt number, equivalent to increasing the degree of turbulence, leads to a $\approx 25 - 30\,\%$ faster process of oxidation.

In summary, our results show some similarities, but also distinct differences between non-volatile iron and volatile-containing solid fuel flames in the present shear-driven turbulence, namely remaining oxide particles at late times and a stronger dependence of particle conversion on the local availability of oxygen for iron combustion.

5.3.6 Conclusions

CP-DNS of iron particle cloud ignition and combustion in a turbulent mixing layer is conducted using existing sub-models for iron particle combustion [165]. The iron combustion sub-model is successfully validated against single-particle reference data and capable of recovering measured particle temperatures, melting and solidification phenomena. Subsequently, the model is used for CP-DNS of iron particle cloud ignition and combustion in shear-driven turbulence. Simulation results show that particles are entrained into the hot lower stream, where ignition occurs and the heat release from particle oxidation increases the gas tempera-

ture far above the background temperature. While the local oxidation of individual particles has a limited effect on gas temperature, the major heat transfer to the gas phase originates from particle clusters. The global analysis of FeO mass production and O_2 consumption from oxidation across the entire domain shows that FeO is continuously produced, while molecular oxygen is consumed, leading to localised regions fully depleted of oxygen at late times. The analysis of the normalised Damköhler number, describing the transition from kinetically-limited to diffusion-limited iron combustion, shows that kinetic limitation applies for particle temperatures and particle oxidation progress of less than 1125K and 20 %, respectively. For higher particle temperatures the oxidation rate is diffusion-limited and peak particle temperatures are observed near the fully-oxidised particle state. The major differences between the present non-volatile iron flames and volatile-containing solid fuel flames are non-vanishing particles at late simulation times and a stronger limiting effect of the local oxygen concentration on the overall conversion process in iron dust flames. Future work will remove the present assumption of mono-sized iron particles and explore the effects of polydispersity on iron particle cloud ignition and combustion.

5.3.7 Acknowledgements

This work is conducted within the *Clean Circles* research initiative financially supported by KIT Strategiefonds and the Hessian Ministry of Higher Eduction, Research, Science and the Arts. O.T. Stein gratefully acknowledges support by the Helmholtz Association of German Research Centres (HGF), within the research field *Energy*, program *Materials and Technologies for the Energy Transition (MTET)*. The authors acknowledge support by the state of Baden-Württemberg through bwHPC and are grateful for HPC time on HLRS Hawk.

5.4 Carrier-phase DNS study of particle size distribution effects on iron particle ignition in a turbulent mixing layer

Research highlights

The fourth paper, *Luu et al., Proc. Combust. Inst. 40:105297, 2024* [181], builds on the third paper by applying a realistic experimental particle size distribution to the previous monodisperse case from *Luu et al., Flow Turb. Combst. 112:1083-1103, 2024* [180]. It continues the investigation of the third research objective. This study highlights distinct differences in the ignition behaviour of the monodisperse (MD) and polydisperse (PD) iron particle clouds under turbulent conditions. A first observation is presented in Fig. 5.39, where a snapshot for the MD case (left) and PD case (right) is shown at the same physical time (4 ms). It is clear that a significant increase in gas temperature can be observed in the MD case, whereas no such increase is seen in the PD case. To investigate the reason for this

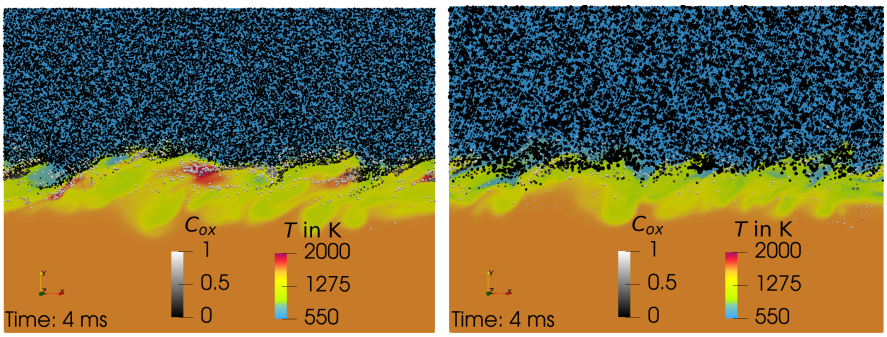

Figure 5.39: Time evolution of gas temperature and particles coloured by their oxidation progress C_{ox} in the x-y plane at $L_z/2$. Left: Monodisperse. Right: Polydisperse.

behaviour, the entire particle ensemble is divided into three particle size classes according to Tab. 5.6 and the characteristics of each class are analysed individually. The particle

Table 5.6: Definition of the introduced particle size classes.

Name	Definition in μm
Class1	$5 < d_p \leq 10$
Class2	$10 < d_p \leq 15$
Class3	$15 < d_p \leq 35$

classes are examined according to their local position, oxidation progress C_{ox}, surrounding gas oxygen mass fraction Y_{O_2}, local solid-gas equivalence ratio Φ and normalised Voronoi volume $\mathrm{v}/\mathrm{v}_{\mathrm{mean}}$ (a measure of particle clustering). A major result of this study is shown in

Fig. 5.40. A comparison of oxidation state (particle colour) and equivalence ratio (ordinate)

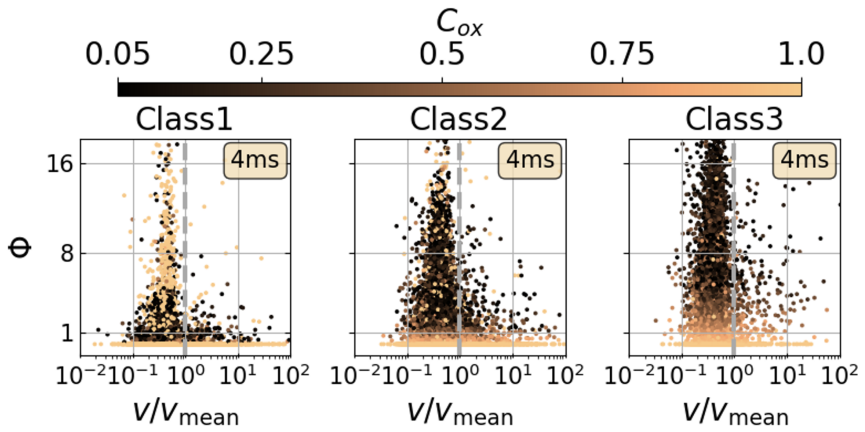

Figure 5.40: Scatterplot of the equivalence ratio surrounding the particles Φ vs. normalised Voronoi volume v/v_{mean} at different times.

across particle size classes shows that large *Class3* particles indicate a trend of $C_{ox} \rightarrow 1$ with $\Phi \rightarrow 0$, while small *Class1* particles display no clear trend, with many fully-oxidised particles even at high equivalence ratios. This is due to quick entrainment and early ignition of small particles, which consume oxygen before being entrained into regions with unreacted particles. In contrast, larger particles ignite much later due to delayed entrainment, higher thermal inertia and the prior oxygen consumption by the smaller particles but release the majority of heat. As a result, bulk ignition in the PD case occurs more unevenly. It is delayed compared to the MD case due to the wide range of individual particle ignition times and weak clustering effects.

Paper 4:

Title: Carrier-phase DNS study of particle size distribution effects on iron particle ignition in a turbulent mixing layer

Authors:

Tien Duc Luu
Engler-Bunte-Intsitute, Simulation of Reacting Thermo-Fluid Systems (TFS),
Karlsruhe Institute of Technology, Karlsruhe, Germany

Ali Shamooni
Institute for Combustion Technology (ITV),
University of Stuttgart, Stuttgart, Germany

Andreas Kronenburg
Institute for Combustion Technology (ITV),
University of Stuttgart, Stuttgart, Germany

Braig Daniel
Simulation of reactive Thermo-Fluid Systems (STFS),
Technical University of Darmstadt, Darmstadt, Germany

Johannes Mich
Simulation of reactive Thermo-Fluid Systems (STFS),
Technical University of Darmstadt, Darmstadt, Germany

Bich-Diep Nguyen
Simulation of reactive Thermo-Fluid Systems (STFS),
Technical University of Darmstadt, Darmstadt, Germany

Arne Scholtissek
Simulation of reactive Thermo-Fluid Systems (STFS),
Technical University of Darmstadt, Darmstadt, Germany

Christian Hasse
Simulation of reactive Thermo-Fluid Systems (STFS),
Technical University of Darmstadt, Darmstadt, Germany

Gabriel Thäter
Institute of Fluid Mechanics (ISTM),
Karlsruhe Institute of Technology, Karlsruhe, Germany

Maurizio Carbone
Theoretical Physics I,
University of Bayreuth, Bayreuth, Germany,
Max Planck Institute for Dynamics and Self-Organisation, Göttingen

Bettina Frohnapfel
Institute of Fluid Mechanics (ISTM),
Karlsruhe Institute of Technology, Karlsruhe, Germany

Oliver T. Stein
Engler-Bunte-Intsitute, Simulation of Reacting Thermo-Fluid Systems (TFS),
Karlsruhe Institute of Technology, Karlsruhe, Germany

Journal: Proceedings of the Combustion Institute

Year: 2024

Volume: 40

Article number: 105297

Contributions by the present author: Methodology, Software, Validation, Formal analysis, Investigation, Data curation, Visualisation, Writing – original draft & editing

Abstract

The ignition and combustion of iron particles in a turbulent mixing layer is studied by means of three-dimensional carrier-phase direct numerical simulations (CP-DNS). A particular focus is set on particle size distribution (PSD) effects on the ignition behaviour by comparing CP-DNS results from using a realistic experimental PSD to DNS data based on a monodisperse (MD) particle cloud with the same equivalence ratio. The CP-DNS solves the Eulerian transport equations of the reacting gas phase and resolves all turbulent scales, while the particle boundary layers are modelled in the Lagrangian point-particle framework. A previously validated sub-model for the oxidation of iron to Wüstite (FeO) that accounts for both diffusion- and kinetically-limited combustion is employed. The mixing layer is initialised with an upper stream of air carrying cold iron particles and an opposed lower stream of hot air. Simulation results show distinct differences in the ignition behaviour between the MD and PSD cases. The ignition of the PSD case is delayed compared to the MD case and does not show any significant particle clustering prior to ignition. Further investigations indicate that the particle size has a crucial effect on the mixing process and ignition time. Small particles start their oxidation process early and already consume some of the available oxygen, while not crucially affecting the gas temperature due to their limited iron mass contribution. Conversely, a slower entrainment into the lower stream combined with higher thermal inertia and the prior oxygen depletion by the small particles leads to a delayed oxidation of the larger particles. As a net result, the PSD case shows a wide spread of individual particle ignition delay times and overall delayed bulk ignition compared to the MD case, where the majority of the particles ignites over a shorter period of time.

5.4.1 Introduction

In the next few decades, the global energy demand is expected to rise due to the global industrial growth and increasing world population. Fossil fuels still dominate the energy supply, but their non-renewable nature and negative environmental effects raise the need for alternative sources. Wind and solar energy are renewable and carbon-free, but their limited geographical distribution and high volatility make it difficult to supply regions with high energy demand continuously. A possible solution is the development of new emission-free energy storage technologies. A promising approach is the metal oxidation/reduction cycle based on iron [16, 126]. The potential of iron as a carbon-free energy carrier is due to its high energy density and abundance combined with its excellent transport and storage properties [15]. When suitably combining iron oxidation and oxide reduction a sustainable circular zero-carbon energy economy can be achieved [126]. The most significant difference between iron oxidation and classical solid fuel conversion (e.g. coal) is the non-volatile

heterogeneous combustion behaviour of iron [231], such that existing modelling strategies for carbon-based solid fuels cannot be used without modification. The current lack of a deeper understanding and reliable models for the relevant physics drive major research efforts to improve our fundamental knowledge on iron flames.

Goroshin et al. [232] proposed a simple analytical model for the heating, ignition and diffusive burnout of single metal particles. Soo et al. [166] developed a kinetically- and diffusion-limited iron combustion model with the major oxidation step of Fe to FeO that was later extended by Hazenberg and van Oijen [164], Thijs et al. [22] and Mich et al. [165]. In [22], improved heat and mass transfer correlations from fully-resolved particle simulations were derived and in [165] polydispersity effects on Euler-Lagrange simulations were studied. Mi et al. [127] proposed an alternative sub-model that describes the growth of FeO and Fe_3O_4 layers by a parabolic rate law. In the past few years, experimental studies on single iron particles [229, 243, 244] and iron particle clouds [245, 250, 253] in laminar flows have been conducted. Concurrent numerical modelling research has examined various physical aspects such as discreteness [29, 237, 238], flame structure and laminar burning velocities [101, 164, 255].

The transition from laminar to turbulent iron dust flames introduces further challenges. It is known from previous research on volatile-driven solid fuel combustion that turbulent mixing, homogeneous chemistry and solid fuel kinetics are strongly coupled. However, the corresponding coupling processes for non-volatile iron dust flames will likely be different. To investigate these processes in detail, direct numerical simulations (DNS) are essential. Fully-resolved DNS directly simulates the full turbulence spectrum and resolves all particle boundary layers, but due to its high computational cost, it is restricted to single particles [22] and small particle groups [29]. For particle clouds, the carrier-phase DNS (CP-DNS) approach provides a good balance between accuracy and efficiency. CP-DNS resolves all turbulent scales and the flame front, but uses sub-models for the transfer of momentum, heat and mass across the particle boundary layers. CP-DNS of volatile-driven solid fuel combustion from coal or biomass have been conducted by several researchers [34, 39, 42, 45]. A first impression of early-time iron cloud combustion in a double mixing layer examined by CP-DNS has been given by Hemamalini et al. [256]. In our previous work [180] we studied the ignition and combustion of a monodisperse iron particle cloud in a turbulent shear layer by means of CP-DNS using the (FOSK) iron sub-model proposed by Mich et al. [165]. Here, we extend our previous work by considering a realistic particle size distribution (PSD) to re-examine the underlying ignition mechanism. The objectives of this paper are to

- examine iron particle cloud ignition in shear-driven turbulence using an experimentally determined PSD,
- characterise the differences between the ignition of simplified monodisperse particle

clouds and clouds with a realistic PSD.

5.4.2 Modelling approach

5.4.2.1 Gas phase

The gas phase is governed by the conservation equations for mass, momentum, enthalpy and chemical species. The $\mathrm{Le} = 1$ assumption is invoked and the mass/heat diffusivities are obtained from $\mathrm{Sc} = \mathrm{Pr} = 0.7$. Radiative heat transfer is described by the discrete ordinates method (DOM). Isotropic particle scattering is considered, while the pure air carrier gas does not absorb or emit radiation ($\varepsilon_{\mathrm{gas}} \approx 0.001$). Strictly assuming non-volatile iron conversion, the oxides formed by combustion remain on the particles and homogeneous chemistry is ignored. Gas-solid coupling is achieved via interphase source terms

$$\dot{S}_{\rho,p} = \dot{S}_{\mathrm{O}_2,p} = -\frac{1}{\Delta^3} \sum_{p=1}^{N_p} \frac{dm_p}{dt}, \tag{5.65}$$

$$\dot{S}_{u,p} = -\frac{1}{\Delta^3} \sum_{p=1}^{N_p} \frac{d(m_p \mathbf{u}_p)}{dt}, \tag{5.66}$$

$$\dot{S}_{h_s,p} = -\frac{1}{\Delta^3} \sum_{p=1}^{N_p} \left(\frac{m_p c_{\mathrm{p},p}}{\tau_{con}} (T_g - T_p) + \frac{dm_p}{dt} h_{s,\mathrm{O}_2}|_{T_p} \right) \tag{5.67}$$

with the particle mass m_p, particle (gas) temperature T_p (T_g), convective heat transfer time scale τ_{con}, particle specific heat capacity $c_{\mathrm{p},p}$, sensible enthalpy of consumed oxygen during oxidation at particle temperature $h_{s,\mathrm{O}_2}|_{T_p}$, and the number of particles per cell N_p with edge length Δ.

5.4.2.2 Solid phase

The Lagrangian particles are initialised as pure iron. During the oxidation FeO is produced via $\mathrm{Fe} + 0.5\mathrm{O}_2 \rightarrow \mathrm{FeO}$ and the thermophysical properties (ρ, c_p and h_s) of Fe and FeO are required. The densities are calculated analogously to [165] and the further thermophysical properties are retrieved from [129] using the Shomate equations. The particle specific heats are obtained from $c_{\mathrm{p},p} = Y_{\mathrm{Fe}} c_{\mathrm{p,Fe}} + Y_{\mathrm{FeO}} c_{\mathrm{p,FeO}}$, with melting and solidification modelled by the apparent heat capacity method [23]. The iron mass conversion rate is determined from the FOSK model by Mich et al. [165]

$$\frac{dm_{p,\mathrm{Fe}}}{dt} = -\frac{1}{s} \rho_f Y_{\mathrm{O}_2} A_d k_d \mathrm{Da}^*, \tag{5.68}$$

$$\frac{dm_{p,\mathrm{FeO}}}{dt} = \frac{1+s}{s}\rho_f Y_{\mathrm{O}_2} A_d k_d \mathrm{Da}^*, \tag{5.69}$$

where,

$$\mathrm{Da}^* = \frac{A_r k_r}{A_r k_r + A_d k_d} \tag{5.70}$$

is the normalised Damköhler number, $A_r = A_d = \pi d_p^2$ the reactive and diffusive areas of the particle (assumed identical), $k_r = k_\infty \mathrm{e}^{-E_a/R_u T_p}$ the rate of kinetic surface reactions and $k_d = \mathrm{Sh}\frac{D_{\mathrm{O}_2,f}}{d_p}$ the diffusive transfer rate. $\mathrm{Sh} = 2 + 0.552\mathrm{Re}_p^{1/2}\mathrm{Sc}^{1/3}$ is the Sherwood number, $\mathrm{Re}_p = \rho_f |\mathbf{u}_g - \mathbf{u}_p| \frac{d_p}{\mu_f}$ the particle Reynolds number and s the mass stoichiometric ratio of the oxidation to iron oxide. Subscript $< f >$ refers to properties at film temperature. Further model coefficients are based on [165], with corresponding model details reported therein.

Only drag force is assumed to act on the particles. Given that the Biot number $\mathrm{Bi} \approx 0.001 - 0.01$ [127], uniform particle temperatures are assumed and governed by convective heat exchange, radiation, heat of combustion and oxygen consumption from the gas phase. Hence, the solid phase governing equations are

$$\frac{dm_p}{dt} = \frac{dm_{p,\mathrm{Fe}}}{dt} + \frac{dm_{p,\mathrm{FeO}}}{dt}, \tag{5.71}$$

$$\frac{d\mathbf{u}_p}{dt} = \frac{\mathbf{u}_g - \mathbf{u}_p}{\tau_p}, \tag{5.72}$$

$$\frac{dT_p}{dt} = \frac{1}{\tau_{con}}(T_g - T_p) + \frac{\varepsilon_p A_p \sigma}{m_p c_{p,p}}(\Theta_r^4 - T_p^4) + \frac{\dot{Q}_{\mathrm{FeO}}}{m_p c_{p,p}} + \frac{\dot{Q}_{\mathrm{O}_2}}{m_p c_{p,p}} \tag{5.73}$$

with the gas velocity at particle position $\mathbf{u}_g$, the particle velocity $\mathbf{u}_p$ and the particle relaxation time $\tau_p = \frac{\rho_p d_p^2}{18\mu_f}(1 + 0.15\mathrm{Re}_p^{2/3})^{-1}$. $A_p = \frac{1}{4}\pi d_p^2$ is the projected area of the particle, $\varepsilon_p = 0.9$ [257] the particle emissivity, σ the Stefan-Boltzmann constant, Θ_r the gas phase radiation temperature from DOM, $\dot{Q}_{\mathrm{FeO}} = \frac{dm_{p,\mathrm{FeO}}}{dt}\Delta h_{c,\mathrm{FeO}}$ the heat released by Fe oxidation, $\Delta h_{c,\mathrm{FeO}}$ the formation enthalpy of FeO, and $\dot{Q}_{\mathrm{O}_2}$ the energy transfer due to oxygen consumption at T_p. Convective heat transfer follows Ranz-Marshall [141]

$$\tau_{con} = \frac{1}{6}\frac{\mathrm{Pr}}{\mathrm{Nu}}\frac{c_{\mathrm{p},p}}{c_{\mathrm{p},f}}\frac{\rho_p d_p^2}{\mu_f} \tag{5.74}$$

with $\mathrm{Nu} = 2 + 0.552\mathrm{Re}_p^{1/2}\mathrm{Pr}^{1/3}$. Sherwood and Nusselt numbers corrected for Stefan flow [167] are considered

$$\mathrm{Sh}^* = \mathrm{Sh}\frac{\ln(1+B_M)}{B_M}, \quad \mathrm{Nu}^* = \mathrm{Nu}\frac{\ln(1+B_T)}{B_T} \tag{5.75}$$

such that Sh^* and Nu^* replace Sh and Nu in the previous equations. B_M is calculated as

$$B_M = \frac{Y_{\mathrm{O}_2,g} - Y_{\mathrm{O}_2,p}}{Y_{\mathrm{O}_2,p} - 1}, \tag{5.76}$$

$$Y_{\mathrm{O}_2,p} = Y_{\mathrm{O}_2,g} \frac{A_d k_d}{A_r k_r + A_d k_d} \tag{5.77}$$

and B_T via

$$B_T = (1 + B_M)^{\varphi}, \quad \varphi = \frac{c_{\mathrm{p,O}_2}|_{T_p}}{c_{\mathrm{p},g}} \frac{\mathrm{Pr}}{\mathrm{Sc}} \tag{5.78}$$

where $c_{\mathrm{p,O}_2}|_{T_p}$ is the specific heat of oxygen at particle temperature and $c_{\mathrm{p},g}$ the gas specific heat. The iron sub-model considers melting and solidification of Fe and FeO. Therefore, the peak temperature can be higher than the melting point of Fe and FeO, but is typically far below boiling point. Under these conditions the vapour pressure of iron is low and the non-volatile assumption for iron particle combustion remains valid. This also implies negligible nanoparticle formation and deposition effects which do not affect the PSD. As a result of considering melting and solidification, the different densities of Fe (solid or liquid) and FeO (solid or liquid) are all considered in the model, in proportion to the instantaneous mass fractions of Fe and FeO within the particle [165]. Accordingly, the instantaneous properties of each particle reflect the relative contributions of Fe and FeO and their effect on the PSD. The present sub-model for iron particle oxidation has been validated against laser-heated particle combustion experiments published in [23, 229] and predictions from [165] in our previous work [180].

5.4.3 Computational configuration

A turbulent reacting mixing layer similar to Rieth et al. [39], but based on the evolution of the momentum thickness δ_θ to determine the self-similar regime of the shear-induced turbulence [258] is studied. The upper stream (US) of mixing layer is initialised as air at $T = 550\,\mathrm{K}$ carrying iron particles, while the lower stream (LS) is hot air at $T = 1650\,\mathrm{K}$. The velocity of the two streams is equal but they flow in the opposite x-direction with $\Delta u_x = 30\,\mathrm{m/s}$, see Fig. 5.41. A hyperbolic tangent profile is used to initialise u_x

$$u_x = \frac{\Delta u_x}{2} \tanh\left(\frac{y - L_y/2}{2\delta_{\theta,0}}\right), \tag{5.79}$$

with the initial momentum thickness $\delta_{\theta,0}$ corresponding to Reynolds number

$$\mathrm{Re}_{\theta,0} = \frac{\Delta u_x \delta_{\theta,0}}{(\nu_{\mathrm{US}} + \nu_{\mathrm{LS}})/2} = 44.018 \tag{5.80}$$

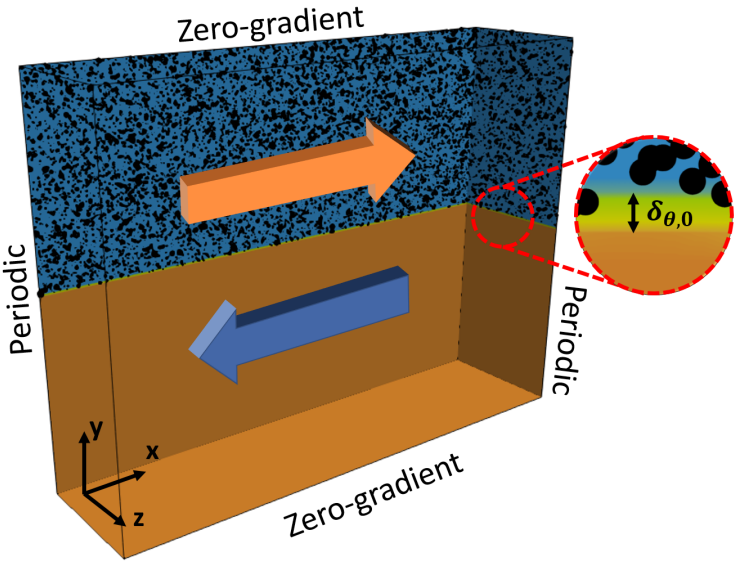

Figure 5.41: Initial and boundary conditions of the mixing layer.

with ν_{US} (ν_{LS}) the initial viscosities of the upper (lower) stream. The computational domain has dimensions $L_x = 320 \times \delta_{\theta,0}$, $L_y = 240 \times \delta_{\theta,0}$ and $L_z = 80 \times \delta_{\theta,0}$ and consists of a total of 85M cubic cells with a constant size of $\Delta = 100\,\mu\mathrm{m}$. Spherical iron particles are initialised with the velocity and temperature of their carrying (upper) stream and their number is chosen to initially have $\phi = 1$ in this stream. To evaluate the effect of the PSD on particle ignition, DNS data from the previously studied monodispersed case with a uniform initial $d_p = 10\ \mu\mathrm{m}$ [180] is compared to the present case with 2,175,000 particles initialised with the experimental PSD of Fedoryk et al. [253] ($5\,\mu\mathrm{m} < d_p < 35\,\mu\mathrm{m}$). The size of every Lagrangian particle is tracked individually and dynamically adapts to the considered physics, e.g. increasing particle size due to oxide deposition. To speed up the computations, isotropic velocity perturbations $u'u' = v'v' = w'w' = 0.01\,(\Delta u_x)^2$ with a size of $0.01 \cdot L_x$ generated according to Klein and Kempf et al. [260, 261] are initially superimposed on the bulk velocity in the main shear region. The pressure and momentum boundary conditions are periodic in x- and z-direction, while a zero-gradient momentum boundary and ambient pressure is assumed in y-direction.

Following [39], the Kolmogorov length scale is estimated by computing spatial averages $<.>$ across the homogeneous x/z-directions. Then, local velocity fluctuations can be calculated as $\mathbf{u}' = \mathbf{u} - \langle \mathbf{u} \rangle$ and the average dissipation becomes $\langle \epsilon \rangle = \langle \tau_{ij} \frac{\partial u_i'}{\partial x_j} \rangle$, with the viscous stress tensor τ_{ij}. Finally, the Kolmogorov length scale is estimated as $\langle \eta \rangle = \left(\frac{\langle \nu \rangle^3}{\langle \epsilon \rangle} \right)^{1/4}$. Following [258], Fig. 5.42 shows the time evolution of the momentum thickness δ_θ in the present mixing layer, which grows in time with changing slopes that delineate three distinct regions [180]. While region I (initialisation period) and III (boundary effects) are of little interest here, the quasi-linear growth of δ_θ in region II implies a time period of self-similar turbu-

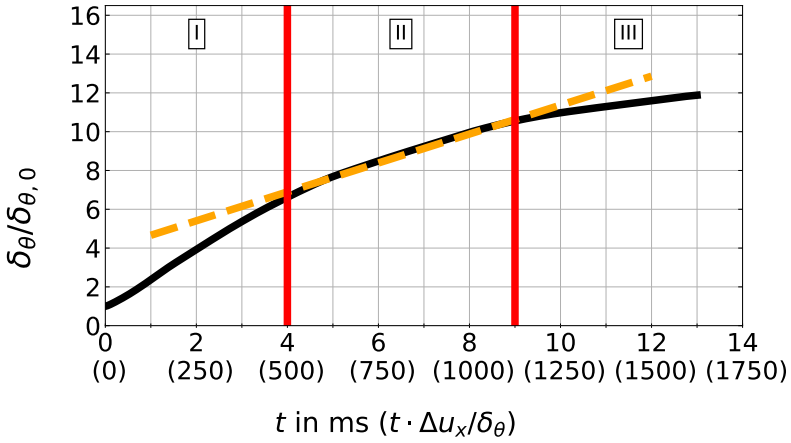

Figure 5.42: Time evolution of momentum thickness δ_θ. Vertical red lines delineate the period of self-similarity.

lence for $4 < t < 9$ ms. A minimum Kolmogorov length scale of 123 µm is estimated for region II. For a valid CP-DNS, the ideal grid size Δ_{ideal} should follow $d_p \ll \Delta_{ideal} < 2.1\eta$ [131] during the evaluation period, such that all turbulent scales are resolved, while the particles can still be considered as Lagrangian point-particles. With $d_{p,\text{mean}} = 12.7$ µm, $d_{p,\text{max}} = 35$ µm, $\Delta = 100$ µm and $\eta_{min} = 123$ µm the present configuration achieves a reasonable trade-off between all relevant scales.

The simulations are conducted with a low-Mach second order finite volume multiphase solver based on OpenFOAM that has previously been employed for detailed CP-DNS analyses of volatile-driven solid fuel combustion [42–44]. A typical CP-DNS simulation costs ≈ 360,000 CPUh on 8192 × AMD-7742 cores.

5.4.4 Results and discussion

Figure 5.43 gives a visual impression of the temporal evolution of the mixing layer. It shows the gas temperature and particle ensemble in the x-y plane at $L_z/2$, comparing the monodisperse (MD) particle cloud with $d_p = 10$ µm from [180] to the present CP-DNS data based on the experimental PSD from [253] with $d_{p,\text{mean}} = 12.7$ µm (bottom row). The particles are coloured by their oxidation progress defined as the extent of Fe consumption $C_{\text{ox}} = \frac{m_{\text{Fe},0} - m_{\text{Fe}}}{m_{\text{Fe},0}}$ with $m_{\text{Fe},0}$ and m_{Fe} denoting the initial and instantaneous iron mass inside the particle.

After $t = 4$ ms the initially separated streams (Fig. 5.41) have developed into a turbulent mixing layer, which leads to the entrainment of cold particles from the upper stream into the hot lower stream, where they heat up and begin their oxidation to FeO, see Fig. 5.43 (left). A noteable difference between the MD and PSD cases can be observed, where the MD case already shows regions with significantly elevated gas temperatures indicating heat transfer from ignited particles to the gas at $t = 4$ ms, whereas no such increase of T_g can be

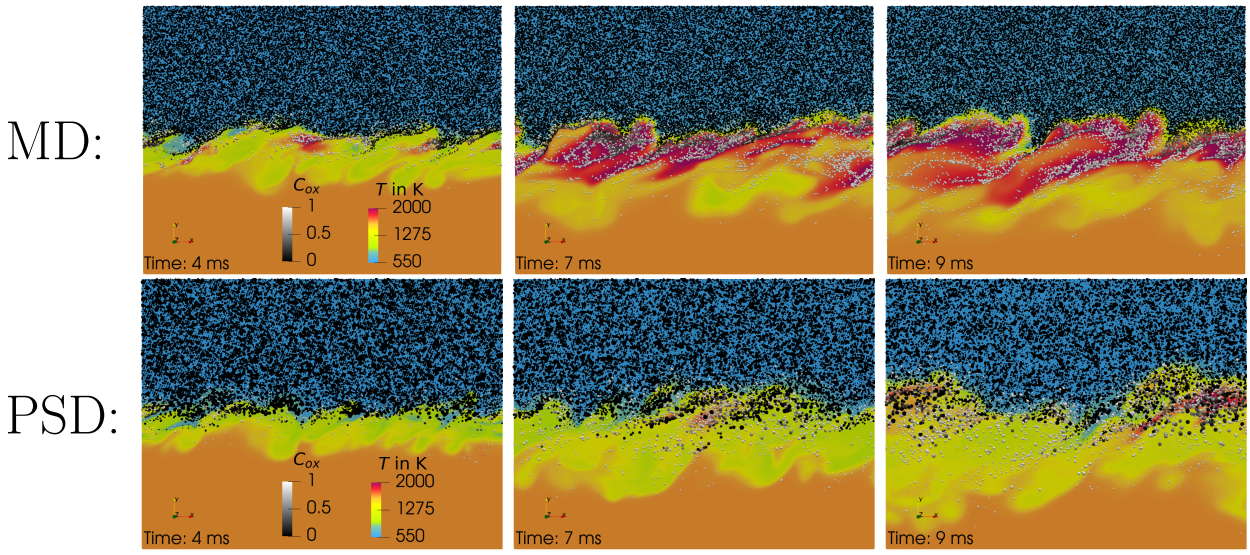

Figure 5.43: Time evolution of gas temperature and particles coloured by their oxidation progress C_{ox} in the x-y plane at $L_z/2$. Top: Monodisperse (MD) particle cloud with $d_p = 10\,\mu\mathrm{m}$ [180]. Bottom: Particle size distribution (PSD) from experiments [253]. For the PSD case particles are sized proportionally to their instantaneous diameter (but not to scale).

seen for the PSD case. Both cases already feature partially- (grey) and fully-oxidised (white) particles at this stage, however, the number of fully-oxidised particles is higher for the MD case.

At $t = 7\,\mathrm{ms}$ the MD case shows a large number of particles with significant oxidation progress in the lower stream, which has led to the formation of a continuous flame region (red). This flame region is associated with particle streaks that imply considerable particle clustering. However, there are also clusters with black-coloured particles indicating that at this stage some particles are hampered from their further oxidation by a localised lack of -previously consumed- oxygen (not shown for brevity). In contrast, the PSD case at $t = 7\,\mathrm{ms}$ shows only a small number of fully-oxidised (white) particles and considerably less regions of elevated gas temperatures compared to MD. In these regions, predominantly small particles have $C_{\mathrm{ox}} = 1$ (white), while larger particles show less oxidation progress (black...grey). The PSD case also features localised areas of elevated particle number densities, but no strong clustering effects as for the MD case can be observed. At $t = 9\,\mathrm{ms}$, the continuous flame region of the MD case has grown further and is constantly fed by fresh particles from the upper stream, while the majority of particles in the lower stream is now fully oxidised. The PSD case shows that the local regions of elevated gas temperature have grown and more particles feature $C_{\mathrm{ox}} = 1$, but at this stage there is no continuous flame region comparable to the MD case. Summarising Fig. 5.43, there are strong differences in the ignition behaviour between the MD and the PSD case, with the MD case showing considerable particle clustering and earlier ignition, while particles are more uniformly distributed and ignition occurs

later for the PSD case. These findings are corroborated by Fig. 5.44, which shows the spatially-averaged gas temperature (top) and O_2 mass fraction (bottom) vs. the normalised y-coordinate as a function of time. Comparing the MD (dashed lines) and PSD (continuous

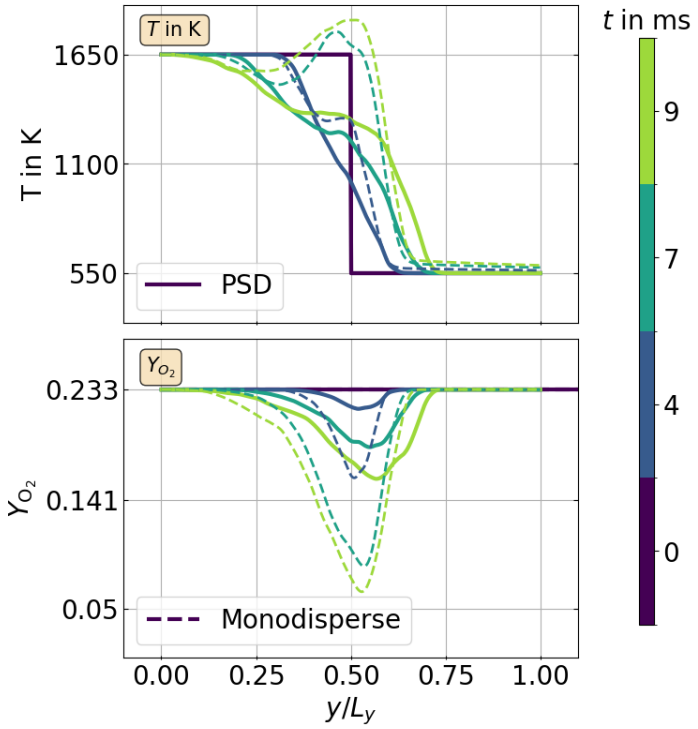

Figure 5.44: Spatially-averaged gas temperature (top) and O_2 mass fraction (bottom) as a function of y/L_y and time. MD (dashed lines) and PSD (continuous lines).

lines) cases, it is observed that at $t = 4\,\text{ms}$ (blue) the spatial average of gas temperature shows a localised peak at $y/L_y = 0.5$ for MD, while the corresponding PSD curve has no such peak, implying mostly non-reactive mixing between the two streams. At $t = 7\,\text{ms}$ (green) a local peak also appears for the PSD case, however, the corresponding MD peak is already much higher and even exceeds the lower stream temperature (1650K). The spatially-averaged profiles of Y_{O_2} in Fig. 5.44 (bottom) characterise the mean O_2 consumption and confirm the previous impression of earlier ignition and combustion for the MD case, as the MD profiles always indicate more O_2 depletion than for the PSD case at corresponding times.

Figure 5.45 shows number- and mass-based averages of particle oxidation progress vs. time, where only particles that have at least 5% oxidation progress are considered, to exclude the majority of fully unreacted particles far in the upper stream at early times, see e.g. Fig. 5.43 at $t = 4\,\text{ms}$. It can be seen that the number-based average oxidation progress (black) of the PSD case is always higher than for MD, implying that at any given time a larger fraction of particles has ignited when considering the PSD. This initially also holds for the mass-averages (blue), but this trend is inverted at $t = 5\,\text{ms}$, when the mass-averaged C_{ox} of the MD case exceeds the one of the PSD case. However, irrespective of the averaging method, at early

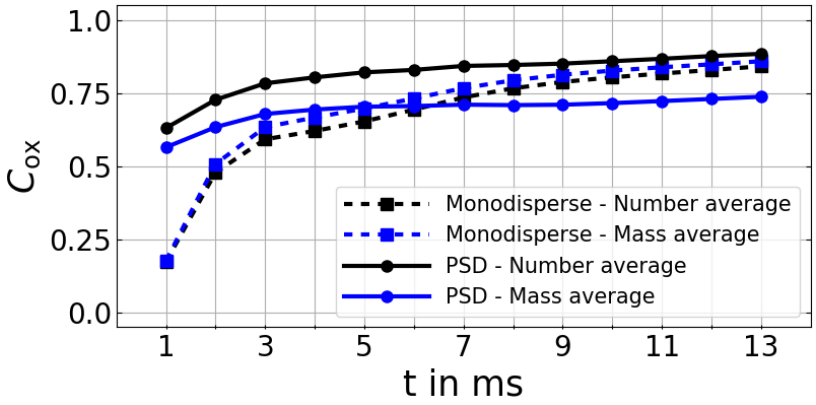

Figure 5.45: Number- and mass-based average of oxidation progress C_{ox} vs. time

times the PSD case shows a larger average particle oxidation state than the MD case, which seems in apparent contrast to the earlier ignition for MD found in Figs 5.43 and 5.44. To further investigate the ignition behaviour of typical particle sizes, the particle ensemble of the PSD case is subdivided into a set of particle size classes for data analysis. Different variants of particle size classes have been applied in post-processing, but only a limited influence of these variants has been found. As a result, the particles are grouped in accordance with their most characteristic trends, where every particle is allowed to adhere to the physics related to its individual temporal evolution and all particles follow the same assumptions. The final sub-division splits the entire particle ensemble into three particle size classes, according to Tab. 5.7 and the (mass-)averaged oxidation progress of each class is shown in Fig. 5.46.

Table 5.7: Definition of the particle size classes.

Name	Definition in μm
Class1	$5 < d_p \leq 10$
Class2	$10 < d_p \leq 15$
Class3	$15 < d_p \leq 35$

It can be seen that the high average particle conversion progress of the PSD case at early times in Fig. 5.45 is attributed to the small particle sizes only. In particular, the smallest size *Class1* is subject to the combined effect of strong entrainment into the lower stream (lowest Stokes number) and comparatively fast heat-up (largest surface-area-to-volume ratio for small particles) leading to a faster oxidation process, whereas larger particles have a slow entrainment and heat-up, and therefore lower average C_{ox} throughout the simulation. However, despite the earlier conversion of the smallest particles for the PSD case, the mass of iron fuel m_{Fe} and associated heat release is rather limited for *Class1*, such that their impact on the gas temperature remains low. Moreover, the larger surface-to-volume ratio and ability to follow turbulent fluctuations promptly also leads to a faster dissipation of the heat released by the oxidation of the small particles. In contrast, the larger particles require

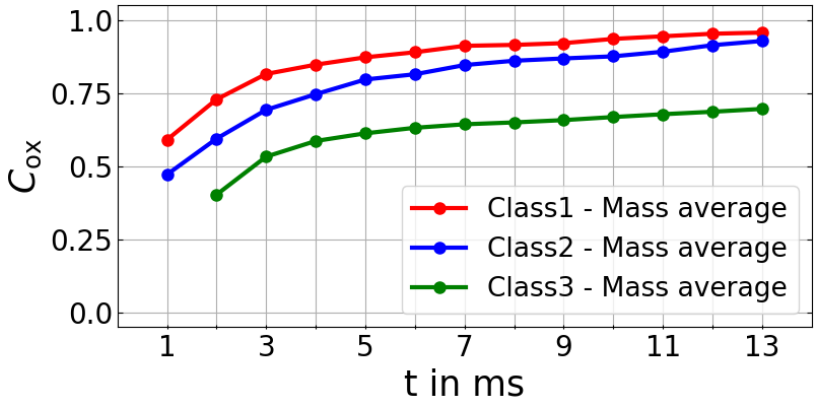

Figure 5.46: Mass-averaged oxidation progress for different size classes of the PSD case (particles with $C_{ox} > 0.05$ only).

significantly more time to heat up and ignite, such that their slow conversion and delayed heat release postpones bulk ignition. As a net consequence, the uniform particle size of the MD case leads to a more simultaneous heat-up, ignition and solid-to-gas heat transfer, and therefore earlier bulk ignition compared to the investigated PSD case. The latter case shows earlier ignition of individual small particles with little specific heat release, but a much delayed conversion of the larger particles and therefore a globally delayed bulk ignition, as found in Figs 5.43 and 5.44.

Figure 5.47 shows scatterplots of particle oxidation progress C_{ox} vs. the normalised y/L_y coordinate for particles in the PSD with $C_{ox} > 0.05$ at different times. Particles are coloured by their surrounding gas oxygen mass fraction Y_{O_2}. It is observed that the smallest *Class1* particles undergo oxidation without any major limitations due the initial abundance of available oxygen (mostly red...yellow scatter), whereas the largest *Class3* particles see increasingly lacking oxygen at late simulation times. This is particularly true for the central region of the mixing layer where the smallest particles lead to early oxygen depletion, while all particle sizes can still find enough oxygen when entrained into the upper and particularly the far lower stream (yellow particles for $y/L_y \to 0$).

Figure 5.48 shows scatterplots of the (oxygen-based) equivalence ratio Φ [165] vs. normalised Voronoi volume coloured by particle oxidation progress C_{ox} for the PSD case. The Voronoi volume is a commonly used indicator for particle clustering, with small Voronoi volumes indicating small particle distances, i.e. strong particle clustering. Voronoi volumes of all particles are computed [266] and normalised by the mean Voronoi volume in the entire domain. At all times shown in Fig. 5.48, all particle size classes exhibit a fraction of particles with $\Phi \to 0$ and $C_{ox} \to 1$, i.e. fully oxidised particles in a very lean oxygen environment. This would not occur in gas combustion, where very lean mixtures cannot ignite, while heterogeneous iron combustion allows for locally stoichiometric conditions (prior to the shown state of these particles) that lead to full particle conversion. Comparing the oxidation state

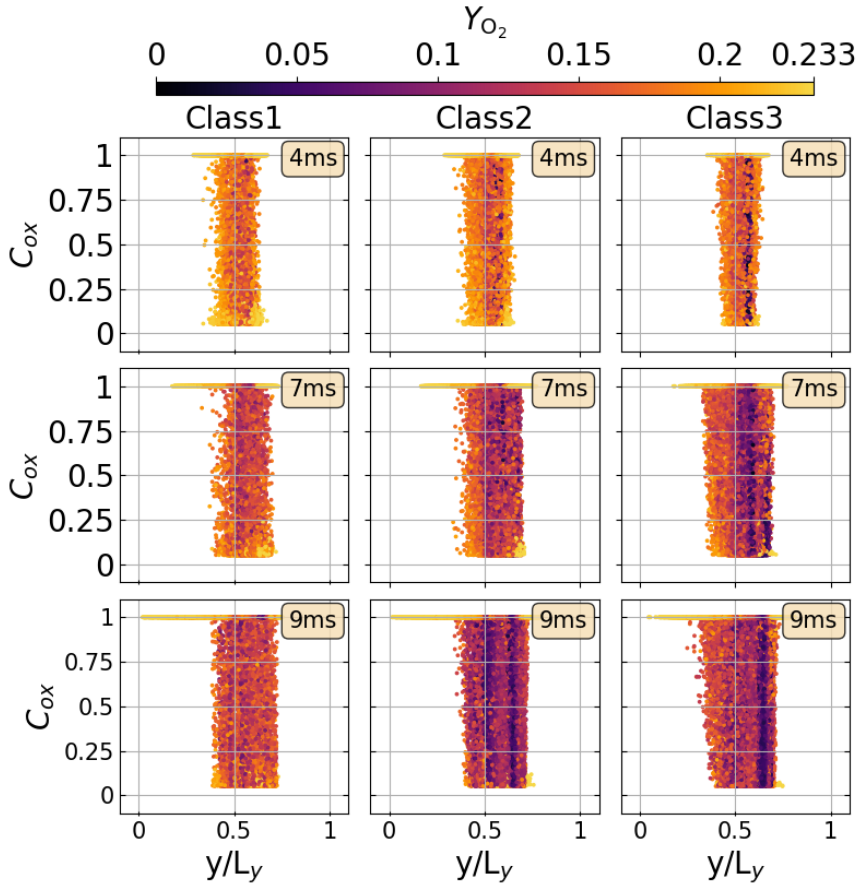

Figure 5.47: PSD case, scatterplot of C_{ox} vs. y/L_y coloured by the gas oxygen mass fraction $Y_{\mathrm{O_2}}$ surrounding the particles at different times (particles with $C_{\mathrm{ox}} > 0.05$ only).

(particle colour) and equivalence ratio (ordinate) for various size classes and times in Fig. 5.48, it is observed that the largest *Class3* particles show increasingly higher C_{ox} with $\Phi \to 0$, whereas the smallest *Class1* particles do not show a similarly clear trend, with a considerable number of fully oxidised small particles at high equivalence ratios. This is because small particles may have already consumed enough oxygen for full particle conversion, before being entrained into regions with many unreacted (larger) particles such that the local equivalence ratio is very high. In contrast, larger particles contain more mass and therefore contribute more strongly to locally large equivalence ratios, in particular when they form clusters. Since particle conversion of the large particles is generally delayed, Fig. 5.46, large particles are mostly exposed to rich conditions in regions where small particles have previously consumed O_2, which slows down their oxidation progress even further. As a result, the conversion of large *Class3* particles strongly correlates with decreasing equivalence ratio, indicating a reduced availability of oxygen. Considering the normalised Voronoi volume as an indicator for particle clustering, it can be seen that small *Class1* particles tend to have smaller than average Voronoi volumes, whereas the largest *Class3* particles show a wide distribution of Voronoi volumes around the mean. Overall, only a weak dependence of the particle oxida-

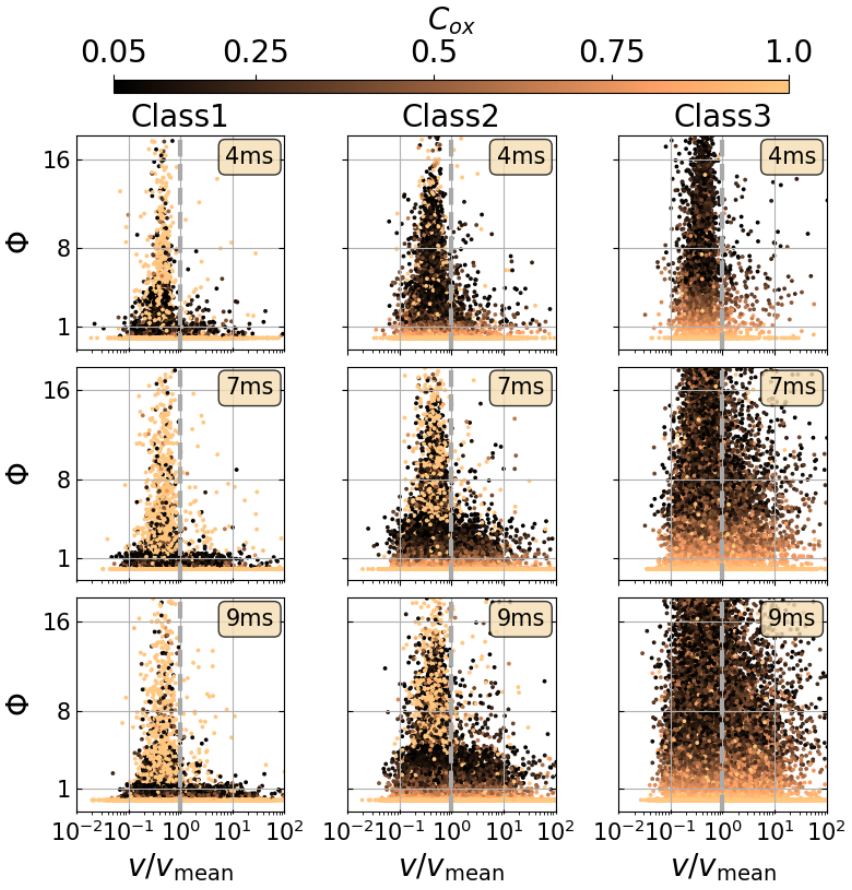

Figure 5.48: PSD case, scatterplot of the equivalence ratio surrounding the particles Φ vs. normalised Voronoi volume v/v_{mean} at different times (particles with $C_{ox} > 0.05$ only)

tion progress on particle clustering can be observed in Fig. 5.48, in line with the qualitatively weaker clustering behaviour of the PSD case already seen in Fig. 5.43.

5.4.5 Conclusion

The ignition and combustion of iron particles in a turbulent mixing layer is studied by means of CP-DNS and the results from a monodispersed particle cloud are compared to equivalent data that assumes an experimental PSD [253]. The MD and PSD cases show different bulk ignition characteristics, which is attributed to the different behaviour of individual particle sizes for the PSD case. While small particles are quickly entrained into the lower stream, where they ignite early and partially consume the available oxygen, large particles ignite significantly later due delayed entrainment, higher thermal inertia, and previous oxygen depletion by the small particles. As a net effect, bulk ignition in the MD case occurs more uniformly and globally earlier, whereas the wide distribution of individual particle ignition times leads to later global ignition for the PSD. The PSD case shows less clustering effects compared to the MD case and only a weak effect of clustering on ignition. The present

work extends our previous CP-DNS study on monodisperse iron particle combustion in shear-driven turbulence [180] to polydisperse conditions based on a realistic experimental PSD. Based on this, a myriad of further physical effects that may affect iron particle cloud ignition and combustion can be explored. Such possibly interesting effects include ballistic particle motion vs. turbophoresis, Stokes number effects on particle spatial distributions and clustering, radiation sub-models, cooling due to thermal inertia, turbulence modulation due to reacting particles, just to name a few. These remaining questions are beyond the scope of the present study, but leave an extremely rich field of exploration for the metal combustion research community in future work.

5.4.6 Acknowledgments

This work is conducted within the *Clean Circles* research initiative financially supported by KIT Strategiefonds and the Hessian Ministry of Higher Eduction, Research, Science and the Arts. The authors gratefully acknowledge the financial support by the Helmholtz Association of German Research Centres (HGF), within the research field *Energy*, program *Materials and Technologies for the Energy Transition (MTET)*. We acknowledge support by the state of Baden-Württemberg through bwHPC and are grateful for HPC time on HLRS Hawk.

6 Conclusions and Outlook

6.1 Summary and conclusions

In this work, a comprehensive study of laminar and turbulent, as well as non-reacting and reacting multiphase flows has been conducted using the Euler-Lagrange approach for gas-solid systems involving various types of solid fuel particles. Solid fuels are generally classified as either volatile-containing (e.g. coal and biomass) or non-volatile (e.g. iron), with each class undergoing different physical conversion processes. Accordingly, specific modelling strategies were developed for each category and integrated into the open-source CFD framework OpenFOAM.

This work addresses three main research objectives of (1) assessing the applicability range of EL approaches, (2) modelling the complex turbulence-chemistry-particle interaction and (3) extending the methodology to non-volatile solid fuels. These objectives have been explored through four key studies.

The first study, *Luu et al., Fuel 368:31600, 2024* [178] presented in Sec. 5.1, investigates the conversion of woody biomass using a layer-based model for thermally thick particles. Woody biomass was chosen due to its typical particle diameter, ranging from micrometres to millimetres, which may violate the standard assumptions of the EL approach. The conversion model was implemented and successfully validated against experimental data from single-particle conversion in a drop tube reactor. After the validation, the grid dependence of the EL framework has been investigated. To ensure reliable reference data for comparison, the same conversion model was also applied in FR simulations. The grid dependence studies were conducted for a single cold biomass particle in a hot, quiescent and inert nitrogen environment, designed to suppress volatile combustion and char oxidation. The focus of the study was limited to heating, drying, and devolatilisation processes. The EL framework revealed that this method can reproduce the FR data for infinitely large grid sizes. However, the approach fails for refined computational grids, particularly when the cell size approaches the particle diameter. An acceptable grid resolution has been found at approximately $\Delta \approx 10 d_p$. When such coarse grids are not feasible, e.g. due to the limitations of DNS by the need to resolve the Kolmogorov scales, CG methods are suggested. These methods retrieve gas-phase information from a volume larger than the individual cell and distribute the particle source term over a correspondingly larger volume. The two investigated CG strategies were

able to reproduce the detailed FR results with the condition that the CG interaction volumes were sufficiently large. Based on the FR data, suitable parameter ranges for the CG model were recommended as a function of the normalised boundary layer thickness.

In the second study, *Luu et al., Proc. Combust. Inst. 39:3249-3258, 2022* [179] in Sec. 5.2, a comprehensive model has been developed to simulate the complex interaction between turbulence, chemistry and particles. This study focused on the turbulent swirl combustion of coal with a methane pilot within a combustion chamber at the Technical University of Darmstadt. To address the multi-physics challenges, a six-dimensional multiphase flamelet/progress variable approach was developed and applied. The model consists of six input parameters, namely the total mixture fraction, its variance, two ratios, the normalised enthalpy and the normalised progress variable. The simulation results were validated against experimental data, showing good agreement for radial profiles of mean and RMS gas velocities, as well as mean gas temperature. An analysis of the fuel contributions revealed that the pilot gas predominantly influenced regions near the wall and the external recirculation zone. Two distinct zones of volatile combustion were identified. A small upstream region within the inner recirculation zone is caused by small recirculated particles and while larger coal particles dominate the downstream region. Char conversion was negligible in regions dominated by pilot and volatile gases but occurred closer to the bottom of the chamber and at larger radii.

The third study (*Luu et al., Flow Turb. Combst. 112:1083-1103, 2024* [180] in Sec. 5.3) extended the Euler–Lagrange approach, previously used for volatile-containing solid fuels, to the oxidation of non-volatile iron particles. It presents the first detailed investigation of monodisperse iron particle cloud combustion in shear-driven turbulence using a CP-DNS framework. Existing iron combustion sub-models were implemented, which have been validated against experimental data, including particle temperatures and phase-change behaviour (melting and solidification). The simulation results showed that particles were entrained into the hot lower stream, where they heated up, initiated ignition and significantly increased the local gas temperature. While individual iron particle oxidation had a limited impact, iron particle clusters were the primary source of heat transfer to the gas phase. These clusters also led to local oxygen depletion. Kinetic limitations apply for particles with temperatures below 1125 K and oxidation progress of below 20 %, whereas higher temperatures and higher conversion progress indicated diffusion-limited behaviour. Notably, in contrast to volatile fuels, iron particles did not completely vanish at late times, and oxygen availability played a stronger limiting role in the overall combustion process.

The fourth study (*Luu et al., Proc. Combust. Inst. 40:105297, 2024* [181] in Sec. 5.4) builds upon the previous investigation by removing the assumption of monodispersity and considering a realistic polydisperse particle size distribution based on experimental data. The

polydisperse results were then compared to the monodisperse case. It was found that the bulk ignition characteristics differed due to variations in particle size. Smaller particles were entrained and ignited earlier, consuming oxygen and delaying ignition for larger particles, which required more time due to higher thermal inertia and delayed entrainment. As a result, global ignition occurred earlier and more uniformly in the monodisperse case, whereas the polydisperse case showed a wider ignition time distribution and, therefore, delayed overall ignition. Additionally, clustering effects were less pronounced in the polydisperse case and only a weak influence of clustering on ignition was observed.

6.2 Outlook

The studies and findings presented in this thesis demonstrate that the Euler-Lagrange approach is a highly adaptable, practical and powerful framework for modelling reactive gas-solid multiphase systems, highlighting its strong potential for future research and development in the field of solid fuel combustion. At the same time, the four fundamental studies conducted also revealed specific limitations, providing multiple opportunities for future research projects:

- **Evaluate the applicability limits of the Euler–Lagrange method for reactive systems, including particle–particle interactions**
  The grid dependence study presented in this work in Sec. 5.1 was conducted for a single cold particle in a hot, quiescent and inert environment. However, practical applications typically involve reactive conditions and particle clouds. It would be of interest to investigate how the conclusions drawn here might be affected by the presence of a developing flame front around individual particles, as well as by particle-particle interactions. Additionally, it remains to be explored whether the CG methods applied here can be extended to account for these effects and whether a functional relationship for the CG parameters based on the normalised boundary layer thickness can still be established.

- **Examine the generality and scalability of the FPV–LES modelling framework**
  An FPV-LES modelling framework coupled with the EL approach has been successfully applied to coal combustion in this work. However, questions remain regarding the generality of the approach, specifically whether it can be reliably extended to different burner configurations, conditions and other types of solid fuel particles, such as iron. A particularly relevant and practical interest for future research is the scalability of the method as outlined in the introduction (Chapter 1). Different geometric scales

have been investigated in the literature. It would be valuable to explore whether the FPV-LES approach maintains its robustness across all scales. Additionally, ongoing improvements in computational efficiency are making its application at industrial scales increasingly practical and appealing for industry use.

- **Perform a comparative analysis of various iron oxidation sub-models in sheared turbulence**
  The implementation of the iron oxidation sub-model in this work is restricted to the formation of FeO. However, alternative models have been proposed in the literature (e.g. [127]) that account for higher oxidation states, such as Fe_2O_3 and Fe_3O_4. Studies such as [165, 267, 268] have demonstrated that these sub-models can show significantly different results under laminar and single particle conditions. It remains an open question whether similar discrepancies exist under turbulent conditions, where the interplay between the turbulent time scale, oxygen concentration and temperature may significantly influence iron conversion. Moreover, in systems of particle clouds, the formation of clusters leads to local oxygen depletion, potentially changing the oxidation dynamics. Investigating these phenomena under turbulent and multi-particle conditions would provide valuable insights into the robustness and accuracy of different iron oxidation models. Finally, applying the oxidation model to a practical burner configuration, e.g. the one discussed in Sec. 5.2, would lead to longer residence times and likely enable the formation of higher oxidation states.

- **Integrate additional physical phenomena into the modelling of iron oxidation**
  The inclusion of additional iron oxidation states introduces various melting and boiling points (see Tab. 2.1). The results presented in Secs. 5.3 and 5.4 show that particle temperatures can become very high to approach or exceed the boiling points of certain iron oxides, indicating that evaporation of these phases may become significant. As such, future work should consider evaporation mechanisms in the modelling framework. Moreover, the presence of iron(-oxide) vapours raises the possibility of condensation, nucleation, nanoparticle formation and subsequent deposition processes that need to be considered. Given the high computational cost associated with tracking individual nanoparticles, it is advisable to couple a population balance model with the Euler–Lagrange framework to represent these phenomena efficiently.

Bibliography

[1] IPCC, Intergovernmental Panel on Climate Change: Sixth Assessment Report - Climate Change 2022: Impacts, Adaptation and Vulnerability (2022).

[2] M. W. Jones, G. P. Peters, T. Gasser, R. M. Andrew, C. Schwingshackl, J. Gütschow, R. A. Houghton, P. Friedlingstein, J. Pongratz, C. Le Quéré, National contributions to climate change due to historical emissions of carbon dioxide, methane, and nitrous oxide since 1850 – with major processing by Our World in Data 2024, Sci. Data 10 (2023) 155.

[3] WMO, World Meteorological Organization: Annual Report - State of the Climate 2024 (2024).

[4] WMO, World Meteorological Organization: Annual Report - State of the Climate 2023 (2023).

[5] IPCC, Intergovernmental Panel on Climate Change: Special Report - Global Warming of 1.5°C (2022).

[6] WRI, World Resources Institute: Climate Watch Historical Country Greenhouse Gas Emissions Data 1990-2022 (2023).

[7] V. Smil, Energy Transitions: Global and National Perspectives - with major processing by Our World in Data, 2nd Edition, 2016.

[8] EI, Energy Institute: Report - Statistical Review of World Energy - with major processing by Our World in Data 1800-2023 (2024).

[9] IEA, International Energy Agency: Report - World Energy Outlook 2024 (2024).

[10] H. Ritchie, What are the safest and cleanest sources of energy?, Our World in Data (2020).

[11] M. E. Munawer, Human health and environmental impacts of coal combustion and post-combustion wastes, J. Sustain Min. 17 (2) (2018) 87–96.

[12] J. Gasparotto, K. Da Boit Martinello, Coal as an energy source and its impacts on human health, Energy Geosci. 2 (2) (2021) 113–120.

[13] I. Andrić, N. Jamali-Zghal, M. Santarelli, B. Lacarrière, O. Le Corre, Environmental performance assessment of retrofitting existing coal fired power plants to co-firing with biomass: carbon footprint and emergy approach, J. Cleaner Product. 103 (2015) 13–27.

[14] J. Janicka, P. Debiagi, A. Scholtissek, A. Dreizler, B. Epple, R. Pawellek, A. Maltsev,

C. Hasse, The potential of retrofitting existing coal power plants: A case study for operation with green iron, Appl. Energy 339 (2023) 120950.

[15] J. M. Bergthorson, S. Goroshin, M. J. Soo, P. Julien, J. Palecka, D. L. Frost, D. J. Jarvis, Direct combustion of recyclable metal fuels for zero-carbon heat and power, Appl. Energy 160 (2015) 368–382.

[16] P. Debiagi, R. C. Rocha, A. Scholtissek, J. Janicka, C. Hasse, Iron as a sustainable chemical carrier of renewable energy: Analysis of opportunities and challenges for retrofitting coal-fired power plants, Renew. Sustain. Energy Rev. 165 (2022) 112579.

[17] M. Vascellari, H. Xu, C. Hasse, Flamelet modeling of coal particle ignition, Proc. Combust. Inst. 34 (2013) 2445–2452.

[18] D. Safronov, M. Kestel, P. Nikrityuk, B. Meyer, Particle resolved simulations of carbon oxidation in a laminar flow, Can. J. Chem. Eng. 92 (2014) 1669–1686.

[19] G. L. Tufano, O. T. Stein, A. Kronenburg, A. Frassoldati, T. Faravelli, A. M. Kempf, M. Vascellari, C. Hasse, Resolved flow simulation of pulverized coal particle devolatilization and ignition in air- and O_2/CO_2-atmospheres, Fuel 186 (2016) 285–292.

[20] S. Farazi, M. Sadr, S. Kang, M. Schiemann, N. Vorobiev, V. Scherer, H. Pitsch, Resolved simulations of single char particle combustion in a laminar flow field, Fuel 201 (2017) 15–28.

[21] G. L. Tufano, O. T. Stein, A. Kronenburg, G. Gentile, A. Stagni, A. Frassoldati, T. Faravelli, A. M. Kempf, M. Vascellari, C. Hasse, Fully-resolved simulations of coal particle combustion using a detailed multi-step approach for heterogeneous kinetics, Fuel 240 (2019) 75–83.

[22] L. C. Thijs, C. E. A. G. van Gool, W. J. S. Ramaekers, J. G. M. Kuerten, J. A. van Oijen, L. P. H. de Goey, Improvement of heat- and mass transfer modeling for single iron particles combustion using resolved simulations, Combust. Sci. Technol. 1 (2022) 1–17.

[23] L. C. Thijs, C. E. A. G. van Gool, W. J. S. Ramaekers, J. A. van Oijen, L. P. H. de Goey, Resolved simulations of single iron particle combustion and the release of nano-particles, Proc. Combust. Inst. 39 (2023) 3551–3559.

[24] A. Shamooni, O. T. Stein, A. Kronenburg, A. M. Kempf, P. Debiagi, T. Li, A. Dreizler, B. Böhm, C. Hasse, Fully-resolved simulations of volatile combustion and NOx formation from single coal particles in recycled flue gas environments, Proc. Combust. Ins. 39 (2023) 4529–4539.

[25] L. C. Thijs, M.-A. Van Ende, J. A. van Oijen, P. de Goey, X. Mi, A numerical study of internal transport in oxidizing liquid core–shell iron particles, Combust. Flame 271 (2025) 113826.

[26] T. Sayadi, S. Farazi, S. Kang, H. Pitsch, Transient multiple particle simulations of

char particle combustion, Fuel 199 (2017) 289–298.

[27] G. L. Tufano, O. T. Stein, B. Wang, A. Kronenburg, M. Rieth, A. M. Kempf, Coal particle volatile combustion and flame interaction. Part I: Characterization of transient and group effects, Fuel 229 (2018) 262–269.

[28] G. L. Tufano, O. T. Stein, B. Wang, A. Kronenburg, M. Rieth, A. M. Kempf, Coal particle volatile combustion and flame interaction. Part II: Effects of particle Reynolds number and turbulence, Fuel 234 (2018) 723–731.

[29] F. H. Vance, A. Scholtissek, H. Nicolai, C. Hasse, Flame propagation modes for iron particle clusters in air, Part II: Transition from continuous to discrete propagation mode under strong convection effects, Combust. Flame (2024) 113199

[30] F. H. Vance, A. Scholtissek, H. Nicolai, C. Hasse, Flame propagation modes for iron particle clusters in air– Part I: transition from continuous to discretepropagation mode under weak convection effects, Combust. Flame 260 (2024) 113265.

[31] F. H. Vance, A. Scholtissek, H. Nicolai, C. Hasse, A numerical analysis of multi-dimensional iron flame propagation using boundary-layer resolved simulations, Fuel 369 (2024) 131793.

[32] F. H. Vance, A. Scholtissek, H. Nicolai, C. Hasse, Effect of oxidizer composition on flame propagation modes in iron particle clusters, Fuel 381 (2025) 133505.

[33] K. Luo, H. Wang, J. Fan, F. Yi, Direct Numerical Simulation of Pulverized Coal Combustion in a Hot Vitiated Co-flow, Energy Fuels 26 (10) (2012) 6128–6136.

[34] T. Hara, M. Muto, T. Kitano, R. Kurose, S. Komori, Direct numerical simulation of a pulverized coal jet flame employing a global volatile matter reaction scheme based on detailed reaction mechanism, Combust. Flame 162 (2015) 4391–4407.

[35] T. Brosh, D. Patel, D. Wacks, N. Chakraborty, Numerical investigation of localised forced ignition of pulverised coal particle-laden mixtures: A Direct Numerical Simulation (DNS) analysis, Fuel 145 (2015) 50–62.

[36] Y. Bai, K. Luo, K. Qiu, J. Fan, Numerical investigation of two-phase flame structures in a simplified coal jet flame, Fuel 182 (2016) 944–957.

[37] J. Krüger, N. E. L. Haugen, T. Løvås, Correlation effects between turbulence and the conversion rate of pulverized char particles, Combust. Flame 185 (2017) 160–172.

[38] M. Muto, K. Yuasa, R. Kurose, Numerical simulation of ignition in pulverized coal combustion with detailed chemical reaction mechanism, Fuel 190 (2017) 136–144.

[39] M. Rieth, A. M. Kempf, A. Kronenburg, O. T. Stein, Carrier-phase DNS of pulverized coal particle ignition and volatile burning in a turbulent mixing layer, Fuel 212 (2018) 364–374.

[40] M. Rieth, M. Rabaçal, A. M. Kempf, A. Kronenburg, O. T. Stein, Carrier-Phase DNS of Biomass Particle Ignition and Volatile Burning in a Turbulent Mixing Layer, Chem.

Eng. Trans. 65 (2018) 37–42.

[41] K. Wan, L. Vervisch, J. Xia, P. Domingo, Z. Wang, Y. Liu, K. Cen, Alkali metal emissions in an early-stage pulverized-coal flame: DNS analysis of reacting layers and chemistry tabulation, Proc. Combust. Inst. 37 (2019) 2791–2799.

[42] A. Shamooni, P. Debiagi, B. Wang, T. D. Luu, O. T. Stein, A. Kronenburg, G. Bagheri, A. Stagni, A. Frassoldati, T. Faravelli, A. M. Kempf, X. Wen, C. Hasse, Carrier-phase DNS of detailed NO_x formation in early-stage pulverized coal combustion with fuel-bound nitrogen, Fuel 291 (2021) 119998.

[43] X. Wen, A. Shamooni, O. T. Stein, L. Cai, A. Kronenburg, H. Pitsch, A. M. Kempf, C. Hasse, Detailed analysis of early-stage NO formation in turbulent pulverized coal combustion with fuel-bound nitrogen, Proc. Combust. Inst. 38 (2021) 4111–4119.

[44] B. Wang, A. Shamooni, O. T. Stein, A. Kronenburg, A. M. Kempf, P. Debiagi, C. Hasse, Investigation of Turbulent Pulverized Solid Fuel Combustion with Detailed Homogeneous and Heterogeneous Kinetics, Energy Fuels 35 (2021) 7077–7091.

[45] G. Chen, H. Wang, K. Luo, J. Fan, A DNS study of pulverized coal combustion in a hot turbulent environment: Effects of particle size, mass loading and preferential concentration, Combust. Flame 254 (2023) 112839.

[46] G. Thäter, M. Carbone, T. D. Luu, O. T. Stein, B. Frohnapfel, The influence of clustering in homogeneous isotropic turbulence on the ignition behavior of iron particles, Proc. Combust. Inst. 40 (2024) 105348.

[47] S. Hemamalini, B. Cuenot, J. van Oijen, X. Mi, Numerical study probing the effects of preferential concentration on the combustion of iron particles in a mixing layer, Proc. Combust. Inst. 40 (2024) 105617.

[48] R. Kurose, H. Makino, Large eddy simulation of a solid-fuel jet flame, Combust. Flame 135 (1–2) (2003) 1–16.

[49] H. Watanabe, R. Kurose, S. Komori, Large-Eddy Simulation of Swirling Flows in a Pulverized Coal Combustion Furnace with a Complex Burner, J. Environ. Eng. 4 (2009) 1–11.

[50] P. Edge, S. R. Gubba, L. Ma, R. Porter, M. Pourkashanian, A. Williams, LES modelling of air and oxy-fuel pulverised coal combustion-impact on flame properties, Proc. Combust. Inst. 33 (2011) 2709–2716.

[51] K. Yamamoto, T. Murota, T. Okazaki, M. Taniguchi, Large eddy simulation of a pulverized coal jet flame ignited by a preheated gas flow, Proc. Combust. Inst. 33 (2011) 1771–1778.

[52] M. Gharebaghi, R. Irons, L. Ma, M. Pourkashanian, A. Pranzitelli, Large eddy simulation of oxy-coal combustion in an industrial combustion test facility, Int. J. Greenhouse Gas Control 5 (2011) 100–110.

[53] J. Pedel, J. N. Thornock, P. J. Smith, Large Eddy Simulation of Pulverized Coal Jet Flame Ignition Using the Direct Quadrature Method of Moments, Energy Fuels 26 (2012) 6686–6694.

[54] L. Chen, A. F. Ghoniem, Simulation of Oxy-Coal Combustion in a 100 kWth Test Facility Using RANS and LES: A Validation Study, Energy Fuels 26 (2012) 4783–4798.

[55] B. Franchetti, F. Cavallo Marincola, S. Navarro-Martinez, A. Kempf, Large Eddy simulation of a pulverised coal jet flame, Proc. Combust. Inst. 34 (2013) 2419–2426.

[56] O. T. Stein, G. Olenik, A. Kronenburg, F. Cavallo Marincola, B. M. Franchetti, A. M. Kempf, M. Ghiani, M. Vascellari, C. Hasse, Towards Comprehensive Coal Combustion Modelling for LES, Flow, Turbul. Combust. 90 (2013) 859–884.

[57] P. Warzecha, A. Boguslawski, LES and RANS modeling of pulverized coal combustion in swirl burner for air and oxy-combustion technologies, Energy 66 (2014) 732–743.

[58] X. Wen, H. Jin, O. T. Stein, J. Fan, K. Luo, Large Eddy Simulation of piloted pulverized coal combustion using the velocity-scalar joint filtered density function model, Fuel 158 (2015) 494–502.

[59] M. Muto, H. Watanabe, R. Kurose, S. Komori, S. Balusamy, S. Hochgreb, Large-eddy simulation of pulverized coal jet flame – Effect of oxygen concentration on NO formation, Fuel 142 (2015) 152–163.

[60] A. G. Clements, S. Black, J. Szuhánszki, K. Stęchły, A. Pranzitelli, W. Nimmo, M. Pourkashanian, LES and RANS of air and oxy-coal combustion in a pilot-scale facility: Predictions of radiative heat transfer, Fuel 151 (2015) 146–155.

[61] M. Rabaçal, B. M. Franchetti, F. C. Marincola, F. Proch, M. Costa, C. Hasse, A. M. Kempf, Large Eddy Simulation of coal combustion in a large-scale laboratory furnace, Proc. Combust. Inst. 35 (2015) 3609–3617.

[62] J. Watanabe, K. Yamamoto, Flamelet model for pulverized coal combustion, Proc. Combust. Inst. 35 (2015) 2315–2322.

[63] G. Olenik, O. T. Stein, A. Kronenburg, LES of swirl-stabilised pulverised coal combustion in IFRF furnace No. 1, Proc. Combust. Inst. 35 (2015) 2819–2828.

[64] M. Rieth, F. Proch, M. Rabaçal, B. M. Franchetti, F. C. Marincola, A. M. Kempf, Flamelet LES of a semi-industrial pulverized coal furnace, Combust. Flame 173 (2016) 39–56.

[65] X. Wen, K. Luo, Y. Luo, H. I. Kassem, H. Jin, J. Fan, Large eddy simulation of a semi-industrial scale coal furnace using non-adiabatic three-stream flamelet/progress variable model, Appl. Energy 183 (2016) 1086–1097.

[66] M. Rieth, F. Proch, A. G. Clements, M. Rabaçal, A. M. Kempf, Highly resolved flamelet LES of a semi-industrial scale coal furnace, Proc. Combust. Inst. 36 (2017)

3371–3379.

[67] M. Rieth, A. G. Clements, M. Rabaçal, F. Proch, O. T. Stein, A. M. Kempf, Flamelet LES modeling of coal combustion with detailed devolatilization by directly coupled CPD, Proc. Combust. Inst. 36 (2017) 2181–21–89.

[68] R. Knappstein, G. Kuenne, L. G. Becker, F. di Mare, A. Sadiki, A. Dreizler, J. Janicka, Large Eddy Simulation of a Novel Gas-Assisted Coal Combustion Chamber, Flow Turbul. Combust. 101 (2018) 895–926.

[69] M. Rabaçal, M. Costa, V. Vascellari, C. Hasse, M. Rieth, A. M. Kempf, A Large Eddy Simulation Study on the Effect of Devolatilization Modelling and Char Combustion Mode Modelling on the Structure of a Large-Scale, Biomass and Coal Co-Fired Flame, J. Combust. 2018 (2018) 1–15.

[70] X. Wen, Y. Luo, H. Wang, K. Luo, H. Jin, J. Fan, A three mixture fraction flamelet model for multi-stream laminar pulverized coal combustion, Proc. Combust. Inst. 37 (2019) 2901–2910.

[71] H. Shen, Y. Wu, M. Zhou, H. Zhang, G. Yue, J. Lyu, Large eddy simulation of a 660 MW utility boiler under variable load conditions, Frontiers Energy 15 (2020) 124–131.

[72] H. Nicolai, G. Kuenne, R. Knappstein, H. Schneider, L. G. Becker, C. Hasse, F. di Mare, A. Dreizler, J. Janicka, Large Eddy Simulation of a laboratory-scale gas-assisted pulverized coal combustion chamber under oxy-fuel atmospheres using tabulated chemistry, Fuel 272 (2020) 1–16.

[73] Y. Chen, O. T. Stein, A. Kronenburg, J. Xing, K. Luo, K. H. Luo, C. Hasse, Analysis of Gas-Assisted Pulverized Coal Combustion in Cambridge Coal Burner CCB1 Using FPV-LES, Energy Fuels 34 (2020) 7477–7489.

[74] X. Wen, H. Nicolai, H. Schneider, L. Cai, J. Janicka, H. Pitsch, C. Hasse, Flamelet LES of a swirl-stabilized multi-stream pulverized coal burner in air and oxy-fuel atmospheres with pollutant formation, Proc. Combust. Inst. 38 (2021) 4141–4149.

[75] D. Meller, T. Lipkowicz, M. Rieth, O. T. Stein, A. Kronenburg, C. Hasse, A. M. Kempf, Numerical Analysis of a Turbulent Pulverized Coal Flame Using a Flamelet/Progress Variable Approach and Modeling Experimental Artifacts, Energy Fuels 35 (2021) 7133–7143.

[76] X. Wen, H. Nicolai, P. Debiagi, D. Zabrodiec, A. Maßmeyer, R. Kneer, C. Hasse, Flamelet LES of a 40 kWth pulverized torrefied biomass furnace in air and oxy-fuel atmospheres, Proc. Combust. Inst. 39 (2023) 4563–4572.

[77] P. Steffens, L. Berkel, S. Gierth, P. Debiagi, B. Özer, A. Maßmeyer, H. Nicolai, C. Hasse, LES of a swirl-stabilized 40 kWth biomass flame and comparison to a coal flame, Fuel 372 (2024) 132098.

[78] L. L. Berkel, P. Steffens, H. Nicolai, S. Gierth, P. Debiagi, H. Schneider, A. Dreizler,

C. Hasse, Comprehensive analysis of the effect of oxyfuel atmospheres on solid fuel combustion using Large Eddy Simulations, Fuel 380 (2025) 133449.

[79] A. Sadiki, S. Agrebi, M. Chrigui, A. Doost, R. Knappstein, F. Di Mare, J. Janicka, A. Massmeyer, D. Zabrodiec, J. Hees, R. Kneer, Analyzing the effects of turbulence and multiphase treatments on oxy-coal combustion process predictions using LES and RANS, Chem. Eng. Sci. 166 (2017) 283–302.

[80] L. Zhao, M. J. Cleary, O. T. Stein, A. Kronenburg, A two-phase MMC-LES model for pyrolysing solid particles in a turbulent flame, Combust. Flame 209 (2019) 322–336.

[81] W. P. Adamczyk, B. Isaac, J. Parra-Alvarez, S. T. Smith, D. Harris, J. N. Thornock, M. Zhou, P. J. Smith, R. Żmuda, Application of LES-CFD for predicting pulverized-coal working conditions after installation of NOx control system, Energy 160 (2018) 693–709.

[82] R. Weber, J. Dugué, A. Sayre, B. M. Visser, Quarl zone flow field and chemistry of swirling pulverized coal flames: Measurements and computation, Symp. (Int.) Combust. 24 (1992) 1373–1380.

[83] J. Fan, X. Zha, P. Sun, K. Cen, Simulation of ash deposit in a pulverized coal-fired boiler, Fuel 80 (5) (2001) 645–654.

[84] T. Asotani, T. Yamashita, H. Tominaga, Y. Uesugi, Y. Itaya, S. Mori, Prediction of ignition behavior in a tangentially fired pulverized coal boiler using CFD, Fuel 87 (2008) 482–490.

[85] N. Hashimoto, R. Kurose, H. Shirai, Numerical simulation of pulverized coal jet flame employing the TDP model, Fuel 97 (2012) 277–287.

[86] M. Stöllinger, B. Naud, D. Roekaerts, N. Beishuizen, S. Heinz, PDF modeling and simulations of pulverized coal combustion – Part 2: Application, Combust. Flame 160 (2013) 396–410.

[87] N. Hashimoto, H. Watanabe, Numerical analysis on effect of furnace scale on heat transfer mechanism of coal particles in pulverized coal combustion field, Fuel Process. Technol. 145 (2016) 20–30.

[88] R. Laubscher, P. Rousseau, Numerical investigation into the effect of burner swirl direction on furnace and superheater heat absorption for a 620 MWe opposing wall-fired pulverized coal boiler, Int. J. Heat Mass Transf. 137 (2019) 506–522.

[89] R. Kurose, H. Watanabe, H. Makino, Numerical Simulations of Pulverized Coal Combustion, KONA Powder Part. J. 27 (2009) 144–156.

[90] A. C. Benim, C. Deniz Canal, Y. E. Boke, A Validation Study for RANS Based Modelling of Swirling Pulverized Fuel Flames, Energies 14 (2021) 7323.

[91] D. Spalding, Mixing and chemical reaction in steady confined turbulent flames, Symp. (Int.) Combust. 13 (1971) 649–657.

[92] B. Magnussen, B. Hjertager, On mathematical modeling of turbulent combustion with special emphasis on soot formation and combustion, Symp. (Int.) Combust. 16 (1977) 719–729.

[93] B. Magnussen, On the structure of turbulence and a generalized eddy dissipation concept for chemical reaction in turbulent flow, in: 19th Aerospace Sciences Meeting, 1981.

[94] S. Pope, PDF methods for turbulent reactive flows, Prog. Energy Combust. Sci. 11 (1985) 119–192.

[95] A. Klimenko, R. Bilger, Conditional moment closure for turbulent combustion, Prog. Energy Combust. Sci. 25 (1999) 595–687.

[96] A. Y. Klimenko, S. B. Pope, The modeling of turbulent reactive flows based on multiple mapping conditioning, Physics Fluids 15 (2003) 1907–1925.

[97] N. Peters, Laminar Diffusion Flamelet Models in Non-Premixed Turbulent Combustion, Prog. Energy Combust. Sci. 10 (1984) 319–339.

[98] C. D. Pierce, P. Moin, Progress-variable approach for large-eddy simulation of non-premixed turbulent combustion, J. Fluid. Mech. 504 (2004) 73–97.

[99] J. Watanabe, T. Okazaki, K. Yamamoto, K. Kuramashi, A. Baba, Large-eddy simulation of pulverized coal combustion using flamelet model, Proc. Combust. Inst. 36 (2017) 2155–2163.

[100] M. Rieth, A. M. Kempf, O. T. Stein, A. Kronenburg, C. Hasse, M. Vascellari, Evaluation of a flamelet/progress variable approach for pulverized coal combustion in a turbulent mixing layer, Proc. Combust. Inst. 37 (2019) 2927–2934.

[101] X. Wen, A. Scholtissek, J. van Oijen, J. Bergthorson, C. Hasse, Numerical modeling of pulverized iron flames in a multidimensional hot counterflow burner, Combust. Flame 248 (2023) 112572.

[102] C. Lian, G. Xia, C. L. Merkle, Impact of source terms on reliability of CFD algorithms, Comput. Fluids 39 (10) (2010) 1909–1922.

[103] S. Wang, Y. Shen, Coarse-grained CFD-DEM modelling of dense gas-solid reacting flow, Int. J. Heat Mass Transf. 184 (2022) 122302.

[104] J. M. Link, L. A. Cuypers, N. G. Deen, J. A. M. Kuipers, Flow regimes in a spout–fluid bed: A combined experimental and simulation study, Chem. Eng. Sci. 60 (2005) 3425–3442.

[105] R. Sun, H. Xiao, Diffusion-based coarse graining in hybrid continuum–discrete solvers: Theoretical formulation and a priori tests, Int. J. Multiphase Flow 77 (2015) 142–157.

[106] S. Farazi, A. Attili, S. Kang, H. Pitsch, Numerical study of coal particle ignition in air and oxy-atmosphere, Proc. Combust. Inst. 37 (2019) 2867–2874.

[107] J. Zhang, T. Li, H. Ström, T. Løvås, Grid-independent Eulerian-Lagrangian approaches

for simulations of solid fuel particle combustion, Chem. Eng. J. 387 (2020) 123964.

[108] J. Zhang, T. Li, H. Ström, T. Løvås, Computationally efficient coarse-graining XDEM/CFD modeling of fixed-bed combustion of biomass, Combust. Flame 238 (2022) 111876.

[109] M. Yang, J. Zhang, S. Zhong, T. Li, T. Løvås, H. Fatehi, X. S. Bai, CFD modeling of biomass combustion and gasification in fluidized bed reactors using a distribution kernel method, Combust. Flame 236 (2022) 111744.

[110] M. Yang, S. M. Mousavi, H. Fatehi, X.-S. Bai, Numerical simulation of biomass gasification in fluidized bed gasifiers, Fuel 337 (2023) 127104.

[111] S. R. Turns, An Introduction to Combustion: Concept and Applications, 1st Edition, The McGraw-Hill Companies, 2000.

[112] N. Peters, Turbulent Combustion, 1st Edition, Cambridge University Press, 2004.

[113] T. Poinsot, D. Veynante, Theoretical and Numerical Combustion, 2nd Edition, R.T. Edwards, Inc., 2005.

[114] J. Warnatz, U. Maas, R. W. Dibble, Combustion - Physical and Chemical Fundamentals, Modeling and Simulation, Experiments, Pollutant Formation, 4th Edition, Springer-Verlag Berlin Heidelberg, 2006.

[115] H. K. Versteeg, W. Malalasekera, An Introduction to Computational Fluid Dynamics, 2nd Edition, Pearson Education Limited, 2007.

[116] I. Glassman, Y. R. A., Combustion, 4th Edition, Elsevier Inc., 2008.

[117] M. Sommerfeld, Numerical Methods for Dispersed Multiphase Flows, Springer International Publishing, 2017.

[118] R. W. Bilger, The structure of turbulent nonpremixed flames, Symp. (Int.) Combust. 22 (1989) 475–488.

[119] L. F. Richardson, P. Lynch, Weather Prediction by Numerical Process, 2007.

[120] D. W. van Krevelen, Coal - Typology, Physics, Chemistry, Constitution, 3rd Edition, Elsevier, 1993.

[121] Methods of Classification and Characterization of Coal, in: T. Kabe, A. Ishihara, E. W. Qian, I. P. Sutrisna, Y. Kabe (Eds.), Coal and Coal-Related Compounds, Vol. 150 of Studies in Surface Science and Catalysis, 2004, pp. 1–79.

[122] P. Basu, Biomass Gasificationand Pyrolysis - Practical Design and Theory, 2010.

[123] C. Hasse, P. Debiagi, X. Wen, K. Hildebrandt, M. Vascellari, T. Faravelli, Advanced modeling approaches for CFD simulations of coal combustion and gasification, Prog. Eng. Combust. Sci. 86 (2021) 100938.

[124] T. Li, C. Geschwindner, A. Dreizler, B. Böhm, Particle-resolved optical diagnostics of solid fuel combustion for clean power generation: a review, Meas. Sci. Technol. 34 (2023) 122001.

[125] D. A. Elalfy, E. Gouda, M. F. Kotb, V. Bureš, B. E. Sedhom, Comprehensive review of energy storage systems technologies, objectives, challenges, and future trends, Energy Strat. Rev. 54 (2024) 101482.

[126] J. M. Bergthorson, Recyclable metal fuels for clean and compact zero-carbon power, Prog. Energy Combust. Sci. 68 (2018) 169–196.

[127] X. Mi, A. Fujinawa, J. M. Bergthorson, A quantitative analysis of the ignition characteristics of fine iron particles, Combust. Flame 240 (2022) 112011.

[128] D. Ning, Y. Shoshin, M. van Stiphout, J. van Oijen, G. Finotello, P. de Goey, Temperature and phase transitions of laser-ignited single iron particle, Combust. Flame 236 (2022) 111801.

[129] M. W. Chase, NIST-JANAF Thermochemical Tables, 4th Edition, Vol. 9, Am. Inst. Phys., Gaithersburg, 1998.

[130] J. Mich, A. K. da Silva, D. Ning, T. Li, D. Raabe, B. Böhm, A. Dreizler, C. Hasse, A. Scholtissek, Modeling the oxidation of iron microparticles during the reactive cooling phase, Proc. Combust. Inst. 40 (2024) 105538.

[131] S. B. Pope, Turbulent Flows, Cambridge: Cambridge University Press, 2000.

[132] J. Smagorinsky, General Circulation Experiments with the Primitive Equations. I. The Basic Experiment, Monthly Weather Review 91 (1963) 99–164.

[133] L. Prandtl, 7. Bericht über Untersuchungen zur ausgebildeten Turbulenz, ZAMM - Journal of Applied Mathematics and Mechanics / Zeitschrift für Angewandte Mathematik und Mechanik 5 (1925) 136–139.

[134] A. N. Kolmogorov, Equations of turbulent motion in an incompressible fluid, Dokl. Akad. Nauk SSSR 30 (1941) 299–303.

[135] L. Prandtl, Über ein neues Formelsystem für die ausgebildete Turbulenz, Nachrichten der Akademie der Wissenschaften in Göttingen, Mathematisch-Physikalische Klasse, Vandenhoeck and Ruprecht, 1945, 6-19.

[136] P. Spalart, S. Allmaras, A one-equation turbulence model for aerodynamic flows (1992).

[137] W. Jones, B. Launder, The prediction of laminarization with a two-equation model of turbulence, Int. J. Heat Mass Transfer 15 (1972) 301–314.

[138] D. C. Wilcox, Turbulence Modeling for CFD, 3rd Edition, DCW Industries, Inc., La Canada Ca, 2006.

[139] G. J. R. Launder, W. Rodi, Progress in the Development of a Reynolds-Stress Turbulent Closure, J. Fluid Mechanics 68 (1975) 537–566.

[140] L. Schiller, A. Naumann, A Drag Coefficient Correlation, Zeitschrift des Vereins Deutscher Ingenieure 77 (1935) 318–320.

[141] W. E. Ranz, J. Marshall, Evaporation from drops - Part 1, Chem. Eng. Progr. 48

(1952) 141–146.

[142] K. Gustafson, Domain decomposition, operator trigonometry, Robin condition, Contemporary Mathematics 218 (1998).

[143] F. Evrard, F. Denner, B. van Wachem, Quantifying the errors of the particle-source-in-cell Euler-Lagrange method, Int. J. Multiph. Flow 135 (2021) 103535.

[144] M. Sontheimer, A. Kronenburg, O. T. Stein, Grid dependence of evaporation rates in Euler-Lagrange simulations of dilute sprays, Combust. Flame 232 (2021) 111515.

[145] H. Schneider, S. Valentiner, N. Vorobiev, B. Böhm, M. Schiemann, V. Scherer, R. Kneer, A. Dreizler, Investigation on flow dynamics and temperatures of solid fuel particles in a gas-assisted oxy-fuel combustion chamber, Fuel 286 (2021) 119424.

[146] S. Sommariva, T. Maffei, G. Migliavacca, T. Faravelli, E. Ranz, A predictive multi-step kinetic model of coal devolatilization, Fuel 89 (2010) 318–328.

[147] D. Merrick, Mathematical models of the thermal decomposition of coal: 2. Specific heats and heats of reaction, Fuel 62 (1983) 540–546.

[148] B. S. Brewster, L. L. Baxter, L. D. Smoot, Treatment of coal devolatilization in comprehensive combustion modeling, Energy Fuels 2 (1988) 362–370.

[149] H. Tolvanen, L. Kokko, R. Raiko, Fast pyrolysis of coal, peat, and torrefied wood: Mass loss study with a drop-tube reactor, particle geometry analysis, and kinetics modeling, Fuel 111 (2013) 148–156.

[150] H. Tolvanen, T. Keipi, R. Raiko, A study on raw, torrefied, and steam-exploded wood: Fine grinding, drop-tube reactor combustion tests in N_2/O_2 and CO_2/O_2 atmospheres, particle geometry analysis, and numerical kinetics modeling, Fuel 176 (2016) 153–164.

[151] H. Thunman, B. Leckner, F. Niklasson, F. Johnsson, Combustion of wood particles—a particle model for Eulerian calculations, Combust. Flame 129 (2002) 30–46.

[152] S. Hermansson, H. Thunman, CFD modelling of bed shrinkage and channelling in fixed-bed combustion, Combust. Flame 158 (2011) 988–999.

[153] A. TenWolde, J. D. McNatt, L. Krahn, Thermal properties of wood and wood panel products for use in buildings, Tech. rep., USDA Forest Service, Forest Products Laboratory (1988).

[154] T. Harada, T. Hata, S. Ishihara, Thermal constants of wood during the heating process measured with the laser flash method, J. Wood Sci. 44 (1998) 425–431.

[155] H. Thunman, B. Leckner, Thermal conductivity of wood - models for different stages of combustion, Biomass Bioenergy 23 (2002) 47–54.

[156] J. Blondeau, H. Jeanmart, Biomass pyrolysis at high temperatures: Prediction of gaseous species yields from an anisotropic particle, Biomass Bioenergy 41 (2012) 107–121.

[157] J. Larfeldt, B. Leckner, M. C. Melaaen, Modelling and measurements of heat transfer

in charcoal from pyrolysis of large wood particles, Biomass Bioenergy 18 (2000) 507–514.

[158] H. Ström, H. Thunman, CFD simulations of biofuel bed conversion: A submodel for the drying and devolatilization of thermally thick wood particle, Combust. Flame 160 (2013) 417–431.

[159] H. Kobayashi, J. B. Howard, A. F. Sarofim, Coal devolatilization at high temperatures, Symp. (Int.) Combust. 16 (1977) 411–425.

[160] C. Di Blasi, Analysis of Convection and Secondary Reaction Effects Within Porous Solid Fuels Undergoing Pyrolysis, Combust. Sci. Technol. 90 (1992) 315–340.

[161] L. Smoot, Pulverized-Coal Combustion and Gasification, 1st Edition, Springer US, 1979.

[162] I. W. Smith, The combustion rates of coal chars: A review, Symp. (Int.) Combust. 19 (1982) 1045–1065.

[163] C. van Gool, L. Thijs, W. Ramaekers, J. van Oijen, L. de Goey, Particle Equilibrium Composition model for iron dust combustion, Appl. Energy Combust. Sci. 13 (2023) 100115.

[164] T. Hazenberg, J. A. van Oijen, Structures and burning velocities of flames in iron aerosols, Proc. Combust. Inst. 38 (2021) 4383–4390.

[165] J. Mich, D. Braig, T. Gustmann, C. Hasse, A. Scholtissek, A comparison of mechanistic models for the combustion of iron microparticles and their application to polydisperse iron-air suspensions, Combust. Flame 256 (2023) 112949.

[166] M. Soo, S. Goroshin, J. M. Bergthorson, D. L. Frost, Reaction of a Particle Suspension in a Rapidly-Heated Oxidizing Gas, Prop. Expl. Pyrotechn. 40 (2015) 604–612.

[167] D. B. Spalding, Combustion and mass transfer, 1st Edition, Pergamon Press, London, 1979, p. 51-81.

[168] R. B. Bird, W. E. Steward, E. N. Lightfoot, Transport Phenomena, 2nd Edition, John Wiley and Sons, New York, 2002, p. 703-716.

[169] COMSOL, COMSOL Multiphysics® v. 6.3.: Heat Transfer Module User's Guide. COMSOL AB, Stockholm, Sweden. (2024).

[170] M. F. Modest, Radiative Heat Transfer, 3rd Edition, Academic Press, 2013.

[171] Ansys, ANSYS® Fluent v. 12: Modeling Radiation Theory Guide. ANSYS, Inc. (2009).

[172] T. Kangwanpongpan, F. H. R. França, R. Corrêa da Silva, P. S. Schneider, H. J. Krautz, New correlations for the weighted-sum-of-gray-gases model in oxy-fuel conditions based on HITEMP 2010 database, Int. J. Heat Mass Transfer 55 (2012) 7419–7433.

[173] D. G. Goodwin, H. K. Moffat, R. L. Speth, Cantera: An Object-oriented Soft-

ware Toolkit for Chemical Kinetics, Thermodynamics, and Transport Processes, https://www.cantera.org/, version 2.4.0 (2018).

[174] C. Hasse, N. Peters, A two mixture fraction flamelet model applied to split injections in a DI Diesel engine, Proc. Combust. Inst. 30 (2005) 2755–2762.

[175] H. Jasak, Error Analysis and Estimation for the Finite Volume Method with Applications to Fluid Flows, Ph.D. thesis, Imperial College London, London (1996).

[176] H. G. Weller, G. Tabor, H. Jasak, C. Fureby, A tensorial approach to computational continuum mechanics using object-oriented techniques, Computers in Physics 12 (1998) 620–631.

[177] F. Moukalled, L. Mangani, M. Darwish, The finite volume method in computational fluid dynamics, Vol. 113, Springer, 2016.

[178] T. D. Luu, J. Zhang, J. W. Gärtner, S. Meng, A. Kronenburg, T. Li, T. Løvås, O. T. Stein, Single particle conversion of woody biomass using fully-resolved and Euler–Lagrange coarse-graining approaches, Fuel 368 (2024) 131600.

[179] T. D. Luu, A. Shamooni, O. T. Stein, A. Kronenburg, S. Popp, H. Nicolai, H. Schneider, X. Wen, C. Hasse, Flame characterisation of gas-assisted pulverised coal combustion using FPV-LES, Proc. Combust. Inst. 39 (2023) 3249–3258.

[180] T. D. Luu, A. Shamooni, A. Kronenburg, D. Braig, J. Mich, B.-D. Nguyen, A. Scholtissek, C. Hasse, G. Thäter, M. Carbone, B. Frohnapfel, O. T. Stein, Carrier-Phase DNS of Ignition and Combustion of Iron Particles in a Turbulent Mixing Layer, Flow Turb. Combust. 112 (2024) 1083–1103.

[181] T. D. Luu, A. Shamooni, A. Kronenburg, D. Braig, J. Mich, B.-D. Nguyen, A. Scholtissek, C. Hasse, G. Thäter, M. Carbone, B. Frohnapfel, O. Stein, Carrier-phase DNS study of particle size distribution effects on iron particle ignition in a turbulent mixing layer, Proc. Combust. Inst. 40 (2024) 105297.

[182] A. V. Bridgwater, Renewable fuels and chemicals by thermal processing of biomass, Chem. Eng. J. 91 (2003) 87–102.

[183] D. A. Tillman, Biomass cofiring: the technology, the experience, the combustion consequences, Biomass Bioenergy 19 (2000) 365–384.

[184] J. Riaza, M. V. Gil, L. Álvarez, C. Pevida, J. J. Pis, F. Rubiera, Oxy-fuel combustion of coal and biomass blends, Energy 41 (2012) 429–435.

[185] V. Keller, B. Lyseng, J. English, T. Niet, K. Palmer-Wilson, I. Moazzen, B. Robertson, P. Wild, A. Rowe, Coal-to-biomass retrofit in Alberta –value of forest residue bioenergy in the electricity system, Renew. Energy 125 (2018) 373–383.

[186] C. Ndibe, S. Grathwohl, M. Paneru, J. Maier, G. Scheffknecht, Emissions reduction and deposits characteristics during cofiring of high shares of torrefied biomass in a 500 kW pulverized coal furnace, Fuel 156 (2015) 177–189.

[187] A. A. F. Peters, R. Weber, Mathematical Modeling of a 2.4 MW Swirling Pulverized Coal Flame, Combust. Sci. Technol. 122 (1997) 131–182.

[188] B. M. Franchetti, F. C. Marincola, S. Navarro-Martinez, A. M. Kempf, Large Eddy Simulation of a 100 kWth swirling oxy-coal furnace, Fuel 181 (2016) 491–502.

[189] H. Nicolai, X. Wen, F. C. Miranda, D. Zabrodiec, A. Massmeyer, F. di Mare, A. Dreizler, C. Hasse, R. Kneer, J. Janicka, Numerical investigation of swirl-stabilized pulverized coal flames in air and oxy-fuel atmospheres by means of large eddy simulation coupled with tabulated chemistry, Fuel 287 (2021) 119429.

[190] J. Guo, A. C. Lua, Kinetic study on pyrolytic process of oil-palm solid waste using two-step consecutive reaction model, Biomass Bioenergy 20 (3) (2001) 223–233.

[191] X. Shuangning, L. Zhihe, L. Baoming, Y. Weiming, B. Xueyuan, Devolatilization characteristics of biomass at flash heating rate, Fuel 85 (2006) 664–670.

[192] J. Li, G. Bonvicini, L. Tognotti, W. Yang, W. Blasiak, High-temperature rapid devolatilization of biomasses with varying degrees of torrefaction, Fuel 122 (2014) 261–269.

[193] F. Tabet, I. Gökalp, Review on CFD based models for co-firing coal and biomass, Renew. Sustain. Energy Rev. 51 (2015) 1101–1114.

[194] J. Li, M. C. Paul, P. L. Younger, I. Watson, M. Hossain, S. Welch, Prediction of high-temperature rapid combustion behaviour of woody biomass particles, Fuel 165 (2016) 205–214.

[195] M. A. Gómez, C. Álvarez Bermúdez, S. Chapela, A. Anca-Couce, J. Porteiro, Study of the effects of thermally thin and thermally thick particle approaches on the Eulerian modeling of a biomass combustor operating with wood chips, Energy 281 (2023) 128243.

[196] Y. B. Yang, V. N. Sharifi, J. Swithenbank, L. Ma, L. I. Darvell, J. M. Jones, M. Pourkashanian, A. Williams, Combustion of a Single Particle of Biomass, Energy Fuels 22 (2008) 306–316.

[197] J. M. Johansen, P. A. Jensen, P. Glarborg, M. Mancini, R. Weber, R. E. Mitchell, Extension of apparent devolatilization kinetics from thermally thin to thermally thick particles in zero dimensions for woody biomass, Energy 95 (2016) 279–290.

[198] T. Li, H. Thunman, H. Ström, A fast-solving particle model for thermochemical conversion of biomass, Combust. Flame 213 (2020) 117–131.

[199] A. Galgano, C. Di Blasi, Modeling the propagation of drying and decomposition fronts in wood, Combust. Flame 139 (2004) 16–27.

[200] R. Mehrabian, S. Zahirovic, R. Scharler, I. Obernberger, S. Kleditzsch, S. Wirtz, V. Scherer, H. Lu, L. L. Baxter, A CFD model for thermal conversion of thermally thick biomass particles, Fuel Process.Technol. 95 (2012) 96–108.

[201] Y. Haseli, J. A. van Oijen, L. P. H. de Goey, A Simplified Pyrolysis Model of a Biomass Particle Based on Infinitesimally Thin Reaction Front Approximation, Energy Fuels 26 (2012) 3230–3243.

[202] E. Russo, J. G. M. Kuerten, B. J. Geurts, Delay of biomass pyrolysis by gas–particle interaction, J. Anal. Appl. Pyrolysis 110 (2014) 88–99.

[203] A. Awasthi, J. G. M. Kuerten, B. J. Geurts, Direct Numerical Simulation of biomass pyrolysis and combustion with gas phase reactions, J. Phys. Conf. Ser. 745 (2016) 032119.

[204] T. Chen, X. Ku, J. Lin, L. Fan, New Pyrolysis Model for Biomass Particles in a Thermally Thick Regime, Energy Fuels 32 (9) (2018) 9399–9414.

[205] J. C. Wurzenberger, S. Wallner, H. Raupenstrauch, J. G. Khinast, Thermal conversion of biomass: Comprehensive reactor and particle modeling, AIChE Journal 48 (2002) 2398–2411.

[206] K. M. Bryden, M. J. Hagge, Modeling the combined impact of moisture and char shrinkage on the pyrolysis of a biomass particle, Fuel 82 (2003) 1633–1644.

[207] H. Lu, W. Robert, G. Peirce, B. Ripa, L. L. Baxter, Comprehensive Study of Biomass Particle Combustion, Energy Fuels 22 (2008) 2826–2839.

[208] H. Fatehi, F. S. Schmidt, X. S. Bai, Gas phase combustion in the vicinity of a biomass particle during devolatilization - Model development and experimental verification, Combust. Flame 196 (2018) 351–363.

[209] H. Ström, H. Thunman, A computationally efficient particle submodel for CFD-simulations of fixed-bed conversion, Appl. Energy 112 (2013) 808–817.

[210] F. Shafizadeh, P. P. S. Chin, Thermal Deterioration of Wood, American Chemical Society (1977) 57–81

[211] W.-C. R. Chan, M. Kelbon, B. B. Krieger, Modelling and experimental verification of physical and chemical processes during pyrolysis of a large biomass particle, Fuel 64 (1985) 1505–1513.

[212] F. Thurner, U. Mann, Kinetic investigation of wood pyrolysis, Ind. Eng. Chem. Process. Des. Dev. 20 (1981) 482–488.

[213] A. G. Liden, F. Berruti, D. S. Scott, Kinetic model for the production of liquids from the flash pyrolysis of biomass, Chem. Eng. Commun. 65 (1987) 207–221.

[214] H. Tolvanen, R. Raiko, An experimental study and numerical modeling of combusting two coal chars in a drop-tube reactor: A comparison between N_2/O_2, CO_2/O_2, and $N_2/CO_2/O_2$ atmospheres, Fuel 124 (2014) 190–201.

[215] P. S. Nobel, Effective Thickness and Resistance of the Air Boundary Layer Adjacent to Spherical Plant Parts, J. Exp. Botany 26 (1975) 120–130.

[216] X. Wen, M. Rieth, A. Scholtissek, O. T. Stein, H. Wang, K. Luo, A. M. Kempf, A. Kro-

nenburg, J. Fan, C. Hasse, A comprehensive study of flamelet tabulation methods for pulverized coal combustion in a turbulent mixing layer — Part I: A priori and budget analyses, Combust. Flame 216 (2020) 439–452.

[217] C. Meißner, H. Schneider, E. Sidiropoulos, J. I. Hölzer, T. Heckmann, B. Böhm, A. Dreizler, T. Seeger, Investigation on wall and gas temperatures inside a swirled oxy-fuel combustion chamber using thermographic phosphors, O_2 rotational and vibrational CARS, Fuel 289 (2021) 119787.

[218] J. Emmert, H. Schneider, C. Meißner, E. Sidiropoulos, J. I. Hölzer, T. Seeger, B. Böhm, A. Dreizler, S. Wanger, Characterization of temperature distributions in a swirled oxy-fuel coal combustor using tomographic absorption spectroscopy with fluctuation modelling, Appl. Energy Combust. Sci. 6 (2021) 100025.

[219] L. G. Becker, H. Kosaka, B. Böhm, S. Doost, R. Knappstein, M. Habermehl, R. Kneer, J. Janicka, A. Dreizler, Experimental investigation of flame stabilization inside the quarl of an oxyfuel swirl burner, Fuel 201 (2017) 124–135.

[220] M. Ihme, Y. C. See, LES flamelet modeling of a three-stream MILD combustor: Analysis of flame sensitivity to scalar inflow condition, Proc. Combust. Inst. 33 (2011) 1309–1317.

[221] S. Popp, F. Hunger, S. Hartl, D. Messig, B. Coriton, J. H. Frank, F. Fuest, C. Hasse, LES flamelet-progress variable modeling and measurements of a turbulent partially-premixed dimethyl ether jet flame, Combust. Flame 162 (2015) 3016–3029.

[222] M. Vascellari, G. L. Tufano, O. T. Stein, A. Kronenburg, A. M. Kempf, A. Scholtissek, C. Hasse, A flamelet/progress variable approach for modeling coal particle ignition, Fuel 201 (2017) 29–38.

[223] L. J. Dorigon, G. Duciak, R. Brittes, F. Cassol, M. Galarça, F. H. R. França, WSGG correlations based on HITEMP2010 for computation of thermal radiation in non-isothermal, non-homogeneous H_2O/CO_2 mixtures, Int. J. Heat Mass Transfer 64 (2013) 863–873.

[224] M. Bini, W. P. Jones, Large-eddy simulation of particle-laden turbulent flows, J. Fluid Mech. 614 (2008) 207–252.

[225] X. Wen, H. Wang, Y. Luo, K. Luo, J. Fan, Evaluation of flamelet/progress variable model for laminar pulverized coal combustion, Phys. Fluids 29 (2017) 083607.

[226] D. Messig, M. Vascellari, C. Hasse, Flame structure analysis and flamelet progress variable modelling of strained coal flames, Combust. Theo. Mod. 21 (2017) 700–721.

[227] C. D. Pierce, P. Moin, A dynamic model for subgrid-scale variance and dissipation rate of a conserved scalar, Phys. Fluids 10 (1998) 3041–3044.

[228] S. Weise, D. Messig, B. Meyer, C. Hasse, An abstraction layer for efficient memory management of tabulated chemistry and flamelet solutions, Combust. Theo. Mod. 17

(2013) 411–430.

[229] D. Ning, Y. Shoshin, J. A. van Oijen, G. Finotello, de Goey L. P. H., Burn time and combustion regime of laser-ignited single iron particle, Combust. Flame 230 (2021) 111424.

[230] P. Julien, J. M. Bergthorson, Enabling the metal fuel economy: green recycling of metal fuels, Sustain. Energy Fuels 1 (2017) 615–625.

[231] S. Goroshin, J. Palečka, J. M. Bergthorson, Some fundamental aspects of laminar flames in nonvolatile solid fuel suspensions, Prog. Energy Combust. Sci. 91 (2022) 100994.

[232] S. Goroshin, M. Bidabadi, J. H. S. Lee, Quenching distance of laminar flame in aluminum dust clouds, Combust. Flame 105 (1996) 147–160.

[233] S. Goroshin, M. Kolbe, J. H. S. Lee, Flame speed in a binary suspension of solid fuel particles, Proc. Combust. Inst. 28 (2000) 2811–2817.

[234] J. Palečka, S. Goroshin, J. M. Bergthorson, Propagation and quenching of dual-front flames in binary-fuel mixtures, Combust. Sci. Technol. 190 (2018) 1557–1579.

[235] A. E. Sidorov, V. G. Shevchuk, Laminar flame in fine-particle dusts, Combust. Explos. Shock Waves 47 (2011) 518–522.

[236] S. Goroshin, F.-D. Tang, A. J. Higgins, Reaction-diffusion fronts in media with spatially discrete sources, Phys. Rev. E 84 (2011) 027301.

[237] F.-D. Tang, A. J. Higgins, S. Goroshin, Propagation limits and velocity of reaction-diffusion fronts in a system of discrete random sources, Phys. Rev. E 85 (2012) 036311.

[238] F. Lam, X. Mi, A. J. Higgins, Front roughening of flames in discrete media, Phys. Rev. E 96 (2017) 013107.

[239] D. Ning, Y. Shoshin, J. A. van Oijen, G. Finotello, L. P. H. de Goey, Critical temperature for nanoparticle cloud formation during combustion of single micron-sized iron particle, Combust. Flame 244 (2022) 112296.

[240] S. Li, J. Huang, W. Weng, Y. Qian, X. Lu, M. Aldén, Z. Li, Ignition and combustion behavior of single micron-sized iron particle in hot gas flow, Combust. Flame 241 (2022) 112099.

[241] T. Li, F. Heck, F. Reinauer, B. Böhm, A. Dreizler, Visualizing particle melting and nanoparticle formation during single iron particle oxidation with multi-parameter optical diagnostics, Combust. Flame 245 (2022) 112357.

[242] A. Fujinawa, L. C. Thijs, J. Jean-Philyppe, A. Panahi, D. Chang, M. Schiemann, Y. A. Levendis, J. M. Bergthorson, X. Mi, Combustion behavior of single iron particles, Part II: A theoretical analysis based on a zero-dimensional model, Appl. Energy Combust. Sci. 14 (2023) 100145.

[243] A. Panahi, D. Chang, M. Schiemann, A. Fujinawa, X. Mi, J. M. Bergthorson, Y. A.

Levendis, Combustion behavior of single iron particles-part I: An experimental study in a drop-tube furnace under high heating rates and high temperatures, Appl. Energy Combust. Sci. 13 (2023) 100097.

[244] D. Ning, T. Li, J. Mich, A. Scholtissek, B. Böhm, A. Dreizler, Multi-stage oxidation of iron particles in a flame-generated hot laminar flow, Combust. Flame 256 (2023) 112950.

[245] F.-D. Tang, S. Goroshin, A. Higgins, J. Lee, Flame propagation and quenching in iron dust clouds, Proc. Combust. Inst. 32 (2009) 1905–1912.

[246] S. Goroshin, F.-D. Tang, A. J. Higgins, J. H. S. Lee, Laminar dust flames in a reduced-gravity environment, Acta Astronautica 68 (2011) 656–666.

[247] F.-D. Tang, S. Goroshin, A. J. Higgins, Modes of particle combustion in iron dust flames, Proc. Combust. Inst. 33 (2011) 1975–1982.

[248] P. Julien, S. Whiteley, S. Goroshin, M. J. Soo, D. L. Frost, J. M. Bergthorson, Flame structure and particle-combustion regimes in premixed methane-iron-air suspensions, Proc. Combust. Inst. 35 (2015) 2431–2438.

[249] A. Wright, A. J. Higgins, S. Goroshin, The Discrete Regime of Flame Propagation in Metal Particulate Clouds, Combust. Sci. Technol. 188 (2016) 2178–2199.

[250] M. McRae, P. Julien, S. Salvo, S. Goroshin, D. L. Frost, J. M. Bergthorson, Stabilized, flat iron flames on a hot counterflow burner, Proc. Combust. Inst. 37 (2019) 3185–3191.

[251] J. Palečka, J. Sniatowsky, S. Goroshin, A. J. Higgins, J. M. Bergthorson, A new kind of flame: Observation of the discrete flame propagation regime in iron particle suspensions in microgravity, Combust. Flame 209 (2019) 180–186.

[252] N. I. Poletaev, M. Y. Khlebnikova, Combustion of Iron Particles Suspension in Laminar Premixed and Diffusion Flames, Combust. Sci. Technol. 194 (2022) 1356–1377.

[253] M. Fedoryk, B. Stelzner, S. Harth, D. Trimis, Experimental investigation of the laminar burning velocity of iron-air flames in a tube burner, Appl. Energy Combust. Sci. 13 (2023) 100111.

[254] X. Mi, A. J. Higgins, S. Goroshin, J. M. Bergthorson, The influence of spatial discreteness on the thermo-diffusive instability of flame propagation with infinite Lewis number, Proc. Combust. Inst. 36 (2017) 2359–2366.

[255] A. Ravi, P. de Goey, J. van Oijen, Flame structure and burning velocity of flames propagating in binary iron aerosols, Proc. Combust. Inst. 39 (2023) 3573–3581.

[256] S. S. Hemamalini, S. Guhathakurta, J. A. van Oijen, B. Cuenot, X. C. Mi, On the Interaction between Burning Iron Particles and Turbulence: A Study via Mesoscale-resolved Simulations, in: Proc. Euro. Combust. Meet., 2023.

[257] G. K. Burgess, P. D. Foote, The Emissivity of Metals and Oxides: IV. Iron Oxide, 1st Edition, Vol. 12, U.S. Government Printing Office, Washington, 1916.

[258] J. O'Brien, J. Urzay, M. Ihme, P. Moin, A. Saghafian, Subgrid-scale backscatter in reacting and inert supersonic hydrogen-air turbulent mixing layers, J. Fluid Mech. 743 (2014) 554–584.

[259] M. Baigmohammadi, W. Prasidha, N. C. Stevens, Y. L. Shoshyn, T. Spee, P. de Goey, Towards utilization of iron powders for heating and power, Appl. Energy Combust. Sci. 13 (2023) 100116.

[260] M. Klein, A. Sadiki, J. Janicka, A digital filter based generation of inflow data for spatially developing direct numerical or large eddy simulations, J. Comput. Phys. 186 (2003) 652–665.

[261] A. Kempf, S. Wysocki, M. Pettit, An efficient, parallel low-storage implementation of Klein's turbulence generator for LES and DNS, Comput. Fluids 60 (2012) 58–60.

[262] A. Abdelsamie, G. Lartigue, C. E. Frouzakis, D. Thévenin, The Taylor–Green vortex as a benchmark for high-fidelity combustion simulations using low-Mach solvers, Computers Fluids 223 (2021) 104935.

[263] T. Zirwes, M. Sontheimer, F. Zhang, A. Abdelsamie, F. E. H. Pérez, O. T. Stein, H. G. Im, A. Kronenburg, H. Bockhorn, Assessment of Numerical Accuracy and Parallel Performance of OpenFOAM and its Reacting Flow Extension EBIdnsFoam, Flow Turbul. Combust. 111 (2023) 567–602.

[264] E. Komen, A. Shams, L. Camilo, B. Koren, Quasi-DNS capabilities of OpenFOAM for different mesh types, Computers Fluids 96 (2014) 87–104.

[265] T. Zirwes, F. Zhang, P. Habisreuther, M. Hansinger, H. Bockhorn, M. Pfitzner, D. Trimis, Quasi-DNS Dataset of a Piloted Flame with Inhomogeneous Inlet Conditions, Flow Turbul. Combust. 104 (4) (2019) 997–1027.

[266] C. H. Rycroft, VORO++: A three-dimensional Voronoi cell library in C++, Chaos: An Interdisciplinary Journal of Nonlinear Science 19 (2009) 041111.

[267] J. Jean-Philyppe, A. Fujinawa, J. M. Bergthorson, X. Mi, The ignition of fine iron particles in the Knudsen transition regime, Combust. Flame. 255 (2023) 112869.

[268] B.-D. Nguyen, D. Braig, A. Scholtissek, D. Ning, T. Li, A. Dreizler, C. Hasse, Ignition and kinetic-limited oxidation analysis of single iron microparticles in hot laminar flows, Fuel 371 (2024) 131866.

A Data Storage

Paper 1: *Luu et al., Fuel 368:31600, 2024* [178]

The LaTeX source files of the paper, all necessary post-processing routines, and the path to the data storage for the OpenFOAM case files are provided in the following Git repository:

LaTeX source files	https://gitlab.kit.edu/kit/ebi/tfs/publications/journal/2024_luu_fuel
OF - Case files	ebi-vbt-nas07.ebi.kit.edu/TFS/PUBLICATIONS/JOURNAL/2024_Luu_Fuel
Code version	cfe57431

Paper 2: *Luu et al., Proc. Combust. Inst. 39:3249-3258, 2023* [179]

The LaTeX source files of the paper, all necessary post-processing routines, and the path to the data storage for the OpenFOAM case files are provided in the following Git repository:

LaTeX source files	https://gitlab.kit.edu/kit/ebi/tfs/publications/journal/2023_luu_proci
OF - Case files	ebi-vbt-nas07.ebi.kit.edu/TFS/PUBLICATIONS/JOURNAL/2023_Luu_PROCI
Code version	d695d0a2

Paper 3: *Luu et al., Flow Turb. Combust. 112:1083-1103, 2024* [180]

The LaTeX source files of the paper, all necessary post-processing routines, and the path to the data storage for the OpenFOAM case files are provided in the following Git repository:

LaTeX source files	https://gitlab.kit.edu/kit/ebi/tfs/publications/journal/2024_luu_ftac
OF - Case files	ebi-vbt-nas07.ebi.kit.edu/TFS/PUBLICATIONS/JOURNAL/2024_Luu_FTaC
Code version	d3593767

Paper 4: *Luu et al., Proc. Combust. Inst. 40:105297, 2024* [181]

The LaTeX source files of the paper, all necessary post-processing routines, and the path to the data storage for the OpenFOAM case files are provided in the following Git repository:

LaTeX source files	https://gitlab.kit.edu/kit/ebi/tfs/publications/journal/2024_luu_proci
OF - Case files	ebi-vbt-nas07.ebi.kit.edu/TFS/PUBLICATIONS/JOURNAL/2024_Luu_PROCI
Code version	4ef0bbba

B Complete list of publications

Journal papers

1. **Luu T. D.**, Shamooni A., Stein O. T., Kronenburg A., Popp S., Nicolai H., Schneider H., Wen X. and Hasse C. *Flame characterisation of gas-assisted pulverised coal combustion using FPV-LES.* Proceedings of the Combustion Institute 39 (2023) 3249-3258. https://doi.org/10.1016/j.proci.2022.07.080

2. **Luu T. D.**, Shamooni A., Kronenburg A., Braig D., Mich J., Nguyen B.-D., Scholtissek A., Hasse C., Thäter G., Carbone M., Frohnapfel B. and Stein O. T. *Carrier-Phase DNS of Ignition and Combustion of Iron Particles in a Turbulent Mixing Layer.* Flow, Turbulence and Combustion 112 (2024) 1083-1103. https://doi.org/10.1007/s10494-023-00526-y

3. **Luu T. D.**, Zhang J., Gärtner J. W., Meng S., Kronenburg A., Li T., Løvås T. and Stein O. T. *Single particle conversion of woody biomass using fully-resolved and Euler–Lagrange coarse-graining approaches.* Fuel 368 (2024) 131600. https://doi.org/10.1016/j.fuel.2024.131600

4. **Luu T. D.**, Shamooni A., Kronenburg A., Braig D., Mich J., Nguyen B.-D., Scholtissek A., Hasse C., Thäter G., Carbone M., Frohnapfel B. and Stein O. T. *Carrier-phase DNS study of particle size distribution effects on iron particle ignition in a turbulent mixing layer.* Proceedings of the Combustion Institute 40 (2024) 105297. https://doi.org/10.1016/j.proci.2024.105297

5. Shamooni A., Debiagi P., Wang B., **Luu T. D.**, Stein O. T., Kronenburg A., Bagheri G., Stagni A., Frassoldati A., Faravelli T., Kempf A. M., Wen X. and Hasse C. *Carrier-phase DNS of detailed* NO_x *formation in early-stage pulverized coal combustion with fuel-bound nitrogen.* Fuel 291 (2021) 119998. https://doi.org/10.1016/j.fuel.2020.119998

6. Thäter G., Carbone M., **Luu T. D.**, Stein O. T. and Frohnapfel B. *The influence of clustering in homogeneous isotropic turbulence on the ignition behavior of iron particles.* Proceedings of the Combustion Institute 40 (2024) 105348. https://doi.org/10.1016/j.proci.2024.105348

Conference oral presentations

1. **Luu T. D.**, Shamooni A., Stein O. T., Kronenburg A., Popp S., Nicolai H., Schneider H., Wen X. and Hasse C. *Analysis of heat transfer effects in flamelet/progress variable LES of gas-assisted pulverised coal flames.* 30. Deutscher Flammentag (2021), Hannover, Germany, 28.-29. September 2021.

2. **Luu T. D.**, Shamooni A., Stein O. T., Kronenburg A., Popp S., Nicolai H., Schneider H., Wen X. and Hasse C. *Flame characterisation of gas-assisted pulverised coal combustion using FPV-LES.* 39th International Symposium on Combustion (2022), Vancouver, Canada, 24.-29. July 2022.

3. **Luu T. D.**, Zhang J., Gärtner J. W., Meng S., Kronenburg A., Li T., Løvås T. and Stein O. T. *Single particle conversion of woody biomass using fully-resolved and Euler–Lagrange approaches.* 4th International Workshop on Oxy-Fuel Combustion (2023), Naples, Italy, 22.-23. March 2023.

4. **Luu T. D.**, Shamooni A., Kronenburg A., Braig D., Mich J., Nguyen B.-D., Scholtissek A., Hasse C., Thäter G., Carbone M., Frohnapfel B. and Stein O. T. *Carrier-phase DNS on micron-sized iron particles in a turbulent reacting mixing layer.* 31. Deutscher Flammentag (2023), Berlin, Germany, 27.-28. September 2023.

5. **Luu T. D.**, Zhou Y., Shamooni A., Kronenburg A. and Stein O. T. *Analysis of the Overlap of Devolatilisation and Char Conversion during Single Coal Particle Burning using a Detailed Multi-Step Kinetic Approach.* 5th International Workshop on Oxy-Fuel Combustion (2025), Aachen, Germany, 19.-20. March 2025.

6. Thäter G., Carbone M., Venugopal V., **Luu T. D.**, Stein O. T. and Frohnapfel B. *The influence of turbulence on micron-sized iron particle combustion.* 31. Deutscher Flammentag (2023), Berlin, Germany, 27.-28. September 2023.

7. Hartmann N., Märker D., **Luu T. D.**, Zirwes, T., Kronenburg A. and Stein O. T. *Numerical Analysis of Nanoparticle Dynamics and Deposition in Iron Particle Combustion.* 2nd Metal-enabled Cycle of Renewable Energy MeCRE (2024), Darmstadt, Germany, 13.-15. November 2024.

Conference poster presentations

1. **Luu T. D.**, Shamooni A., Kronenburg A., Braig D., Mich J., Nguyen B.-D., Scholtissek A., Hasse C., Thäter G., Carbone M., Frohnapfel B. and Stein O. T. *Carrier-phase DNS study of particle size distribution effects on iron particle ignition in a turbulent mixing layer.* 40th International Symposium "Emphazing Energy Transition" CI's (2024), Milan, Italy, 21.-26. July 2024.

2. **Luu T. D.**, Göhringer M., Märker D. and Stein O. T. *Characterisation of multi-stage self-ignition of iron particle clouds in sheared turbulence.* 12th European Combustion Meeting ECM (2025), Edinburgh, United Kingdom, 7.-10. April 2025.

3. Thäter G., Carbone M., **Luu T. D.**, Stein O. T. and Frohnapfel B. *The influence of clustering in homogeneous isotropic turbulence on the ignition behavior of iron particles.* 40th International Symposium "Emphazing Energy Transition" CI's (2024), Milan, Italy, 21.-26. July 2024.

4. Thäter G., Carbone M., **Luu T. D.**, Stein O. T. and Frohnapfel B. *The influence of clustering on particle cloud combustion in homogeneous isotropic turbulence.* 2nd Metal-enabled Cycle of Renewable Energy MeCRE (2024), Darmstadt, Germany, 13.-15. November 2024.

5. Märker D., Hartmann N., **Luu T. D.**, Nguyen B.-D., Scholtissek A., Hasse C., Kronenburg A. and Stein O. T. *Modelling nanoparticle formation and deposition in burning iron microparticle arrays.* 12th European Combustion Meeting ECM (2025), Edinburgh, United Kingdom, 7.-10. April 2025.